NCL201701A

Physicochemical Characterization of Engineered Nanomaterials

prepared for

US Army Center for Environmental Health Research

Nanotechnology Characterization Laboratory
Frederick National Laboratory for Cancer Research
Leidos Biomedical Research, Inc.
Frederick, MD 21702
(301) 846-6939 • ncl@mail.nih.gov
http://ncl.cancer.gov

TABLE OF CONTENTS

OBJECTIVE

An Interagency Agreement was executed between the US Army's Center for Environmental Health Research (CEHR) and the National Cancer Institute's Nanotechnology Characterization Laboratory (NCL). As part of this agreement, the CEHR supplied 26 nanomaterials for sterility and endotoxin testing and physicochemical characterization. Some of the parameters investigated included size/size distribution, shape, metal concentrations, metal release kinetics, purity, surface coatings, and zeta potential. The overall goal for CEHR was to align nanomaterial physicochemical properties to biological toxicities using a zebra fish model. The zebra fish studies were conducted by a third party and were not covered under this agreement

NANOMATERIAL DESCRIPTIONS

A list of the materials supplied by CEHR is provided in Table A on the following page. Each sample was assigned a reference number, CEHR-#, for ease of tracking and reporting. These CEHR numbers are used throughout the report. The materials characterized included cerium dioxide (CEHR-1), nanocellulose (CEHR-2), silica (CEHR-8 to CEHR-12), silver (CEHR-13 to CEHR-15), zinc oxide (CEHR-16 to CEHR-17), iron oxide (CEHR-18 to CEHR-19), aluminum oxide (CEHR-20 to CEHR-22), and titanium dioxide (CEHR-23 to CEHR-26). These materials were all provided in solution. Other materials supplied to NCL, but not characterized, included powder versions of titanium dioxide (CEHR-3), silver (CEHR-4), nickel oxide (CEHR-5), multi-walled carbon nanotubes (CEHR-6), and carbon black (CEHR-7). These materials could not be characterized due to their insolubility

Table A. Nanomaterial List. A summary of all the nanomaterial samples received by the NCL. All information in this table was provided by CEHR. Each sample was assigned a reference number for ease of tracking and reporting. These CEHR numbers are used throughout the report.

Reference Number	Nanoparticle Description	Nominal size reported by manufacturer	Manufacturer, Lot/Catalog No.	Date Received	Storage	Amount Received
CEHR-1	CeO_2 10% wt in water	< 25 nm	Sigma Aldrich, Lot 643009	10/02/2015	room temp.	15 mL
CEHR-2	NCCS-1 reference material 5% in water	-	-	10/02/2015	room temp.	2 vials of~20 mL each; plus powder
CEHR-3	TiO_2	-	-	10/02/2015	room temp.	300 mg
CEHR-4	Ag	~20 nm		10/02/2015	room temp.	1.38 g
CEHR-5	NiO	-	-	10/02/2015	room temp.	300 mg
CEHR-6	MWCNT	-	Mitsui 7, Lot 05072001K28	10/02/2015	room temp.	249 mg
CEHR-7	Carbon black	-	Printex 90	10/02/2015	room temp.	400 mg
CEHR-8	SiO_2 nanospheres 10 mg/mL	20 ± 4 nm	nanoComposix, Lot JEA0156	02/11/2016	4°C	5 mL, 10 mg/mL
CEHR-9	SiO_2 nanospheres 10 mg/mL	50 ± 4 nm	nanoComposix, Lot JEA0088	02/11/2016	4°C	5 mL, 10 mg/mL
CEHR-10	SiO_2 nanospheres 10 mg/mL	100 ± 4 nm	nanoComposix, Lot JEA0167	02/11/2016	4°C	5 mL, 10 mg/mL
CEHR-11	SiO_2 nanospheres 10 mg/mL	200 ± 7nm	nanoComposix, Lot JEA0113	02/11/2016	4°C	5 mL, 10 mg/mL
CEHR-12	SiO_2 nanospheres 10 mg/mL	400 ± 40 nm	nanoComposix, Lot ECP1362	02/11/2016	4°C	5 mL, 10 mg/mL

Reference Number	Nanoparticle Description	Nominal size reported by manufacturer	Manufacturer, Lot/Catalog No.	Date Received	Storage	Amount Received
CEHR-13	Ag nanospheres with PVP 5 mg/mL	5 ± 2 nm	nanoComposix, Lot KJW1980A	02/11/2016	4°C	5 mL, 5 mg/mL
CEHR-14	Ag nanospheres with PVP 5 mg/mL	25 ± 5 nm	nanoComposix, Lot CLF0494A	02/11/2016	4°C	5 mL, 5 mg/mL
CEHR-15	Ag nanospheres with PVP 5 mg/mL	75 ± 5 nm	nanoComposix, Lot DMW0382	02/11/2016	4°C	5 mL, 5 mg/mL
CEHR-16	ZnO nanopowder, 20 wt% dispersion	30-40 nm	US Nano, Catalog US7100	02/11/2016	4°C	60 g (in solution)
CEHR-17	ZnO nanopowder, 20 wt% dispersion	50-80 nm	US Nano, Catalog US7290	02/11/2016	4°C	60 g (in solution)
CEHR-18	Fe_3O_4 nanopowder, 20 wt% water dispersion	15-20 nm	US Nano, Catalog US7568	02/11/2016	4°C	30 g (in solution)
CEHR-19	Fe_2O_3 gamma, 10 wt% water dispersion	20 nm	US Nano, Catalog US7558	02/11/2016	4°C	30 g (in solution)
CEHR-20	Al_2O_3 gamma, 20 wt% dispersion	10 nm	US Nano, Catalog US7020	02/11/2016	4°C	120 g (in solution)
CEHR-21	Al_2O_3 alpha, 20 wt% dispersion	30 nm	US Nano, Catalog US7010	02/11/2016	4°C	120 g (in solution)
CEHR-22	Al_2O_3 gamma, 20 wt% dispersion	30 nm	US Nano, Catalog US7030	02/11/2016	4°C	120 g (in solution)
CEHR-23	TiO_2 anatase, 15 wt% dispersion	5 -15 nm	US Nano, Catalog US7080	02/11/2016	4°C	120 g (in solution)
CEHR-24	TiO_2 rutile, 15 wt% dispersion	5 -15 nm	US Nano, Catalog US7050	02/11/2016	4°C	120 g (in solution)
CEHR-25	TiO_2 anatase, 40 wt% dispersion	30 -50 nm	US Nano, Catalog US7071	02/11/2016	4°C	120 g (in solution)
CEHR-26	TiO_2 rutile, 20 wt% dispersion	30 -50 nm	US Nano, Catalog US7070	02/11/2016	4°C	120 g (in solution)

The initial set of materials supplied to NCL was CEHR-1 to CEHR-7. Of these, CEHR-1 and CEHR-2 were supplied in liquid suspension, while the remaining materials were powder. Many of the techniques used for physicochemical analysis require an aqueous suspension of the nanomaterials. Multiple attempts were made to resuspend these materials; however, none of the powder materials could be resuspended in a reproducible manner. After discussion of these difficulties with CEHR, it was mutually decided to discontinue characterization of CEHR-3 to CEHR-7. No data on these five materials is presented in this report.

The second set of materials supplied to NCL, CEHR-8 to CEHR-26, were all metal/metal oxide nanomaterials. These materials were all purchased from either nanoComposix or US Nano and were all supplied as aqueous suspensions. These materials were much easier to work with, but have the added complexity of aggregation/agglomeration in solution, which could impact analysis of “nano” sized materials. In addition, many manufacturers also add a surface coating or other excipients to aid in solubility and/or stability. This too confounds toxicity testing, as it’s often unclear as to whether toxicities stem from the nanomaterial or from free coating in solution. Often times, especially for proprietary mixtures, this information is not disclosed to the consumer. It is important to consider these aspects when analyzing biological data.

EXECUTIVE SUMMARY

Twenty-one (21) different nanomaterials were characterized as part of this collaboration. All of the materials were aqueous suspensions, and all but one were metal or metal oxide materials. The non-metal nanomaterial was nanocrystalline cellulose (CEHR-2), a reference standard material from National Research Council Canada. The NCL evaluated sterility, endotoxin contamination and a variety of physicochemical parameters, including size/size distribution, shape, metal concentrations, purity, surface chemistry, and stability. Size and polydispersity were evaluated using transmission electron microscopy (TEM), dynamic light scattering (DLS), and asymmetric flow field-flow fractionation (AF4) coupled with DLS detection. Nanoparticle concentrations were measured using inductively coupled plasma mass spectrometry (ICP-MS) and thermogravimetric analysis (TGA). ICP-MS was also used to assess purity by detection of trace metal impurities, and stability by monitoring the level of free metal ions released in solution over time. Surface chemistry was evaluated by TGA to detect the presence of a surface coating or other excipient, and surface charge was indirectly evaluated by measuring the zeta potential. Importantly, while TGA could provide an indication of a coating and/or other excipients in the formulation, it could not identify the coatings/excipients. This is an important consideration for biological testing of these materials, as the coating/excipient may elicit a biological response or toxicity unrelated to the nanomaterial.

An overview, along with a tabular summary, of the most significant findings for each of these materials is provided here in the Executive Summary. Greater details, including methods used for the analyses, are provided in their respective sections.

I. Cerium Oxide Nanoparticles (CEHR-1)

Reference Number	Nanoparticle Description	Nominal size reported by manufacturer
CEHR-1	CeO_2 10% wt in water	< 25 nm

Cerium oxide nanoparticles from Sigma Aldrich, with a nominal size of <25 nm, were characterized for several physicochemical parameters, including size, ceria concentration, and zeta potential. By TEM, the sample showed significant aggregation/agglomeration and accurate size information was not obtainable (Figure I-1). DLS also suggested aggregation, with an intensity-weighted hydrodynamic diameter of approximately 260 nm, more than 10 times the reported size (Figure 1-2). Of note, the reported size was calculated by BET (per the Sigma Aldrich website). BET is not a suitable technique for size, especially for non-uniform particles. BET measures the surface area and makes several assumptions to calculate a size.

Ceria concentration was measured by ICP-MS and TGA. However, over time the sample showed signs of evaporation and eventually became a paste-like substance. As a result, the concentrations were not consistent between runs. The gradual change in concentration is evident by the large standard deviation for the ICP-MS *cerium* concentration, 141 ± 42 mg/g (Table I-3). Furthermore, the average *ceria* concentration by ICP-MS was 17% wt. and the average TGA concentration was 20% wt., nearly double the reported 10% wt. concentration (Table I-4). Because of the compromise in sample stability, characterization was halted on this material.

Prior to stopping characterization, ICP-MS showed there were no other metal impurities in the sample (Figure I-3), and zeta potential analysis revealed a positive zeta potential (Table I-5). A positive zeta potential is unexpected for uncoated cerium oxide nanoparticles and suggests that they may be coated with a positively-charged surface moiety. Additional discussion on the characterization of CEHR-1 is described in Section I.

Cerium Oxide Nanoparticle Summary

Ceria Nanoparticles:	CEHR-1
Manufacturer Reported Values	
Vendor, Lot No.	Sigma Aldrich 643009
Nominal Size	<25 nm
Concentration	10% wt.
Sterility & Endotoxin	
Sterility	Not Tested
Endotoxin	Not Tested
Size	
Particle Diameter by TEM	Aggregates/ Agglomerates
Hydrodynamic Diameter by Batch-mode DLS	257 ± 11 nm
Polydispersity Index by Batch-mode DLS	0.15 ± 0.02
Hydrodynamic Diameter by Flow-mode DLS	Not Tested
Concentration	
Total [Ce] by ICP-MS	141 ± 42 mg/g
Total [CeO_2] by ICP-MS	17% wt.
Total [CeO_2] by TGA	20% wt.
Surface Characterization	
Zeta Potential	18 ± 2 mV
Purity	
Metal Impurities by ICP-MS	None

II. Nanocellulose (CEHR-2)

Reference Number	Nanoparticle Description	Nominal size reported by manufacturer
CEHR-2	NCCS-1 reference material 5% in water	-

Nanocrystalline cellulose (NCC) is a reference standard material from National Research Council Canada. Additional information, including the previous characterization of this standard material can be found here: http://www.nrc-cnrc.gc.ca/eng/solutions/advisory/crm/certificates/cncs_1.html.
The material was evaluated for morphology by TEM, size/size distribution by DLS, analysis of metal impurities by ICP-MS, concentration by TGA, and zeta potential. TEM confirmed the crystalline needle-like structures reminiscent of NCC (Figure II-1). NCL had previously characterized this material and measured 84 ± 35 nm and 5 ± 2 nm for the length and width, respectively, consistent with the reported values. The DLS measured hydrodynamic diameter was 87 nm, in agreement with the TEM size (Table II-1). The needle-like shape of these particles were not amenable to separation by AF4 for additional size distribution/polydispersity analysis.

The concentration was measured by TGA. This technique used the assumption that all material decomposed, with the exception of water, as well as the residual material mass was NCC. This afforded a measured concentration of 67 mg/mL (Figure II-4). This was in complete agreement with the reported concentration. The measured zeta potential was -27 mV (Table II-2). The reference site also states a negative zeta potential for NCC. Although the values were different, this was expected due to differences between the measurement conditions. Finally, six metal impurities were detected in the sample by semi-quantitative ICP-MS analysis, namely Al, Fe, Cu, Zn, Se, and Mo. Iron and copper were also listed as metal impurities on the reference site. A complete quantitative ICP-MS analysis would be required to verify their presence and determine concentration.

In general, all of measurements made were in good agreement with the theoretical values as described on the website noted above. Additional details on the characterization of NCC is described in Section II.

Nanocellulose Summary

Nanocrystalline Cellulose:	CEHR-2
Manufacturer Reported Values	
Vendor, Lot No.	NCCS-1 Reference Material
Nominal Size	84 nm x 5.6 nm
Concentration	5% wt.
Sterility & Endotoxin	
Sterility	Not Tested
Endotoxin	Not Tested
Size	
Particle Diameter by TEM	84 ± 35 nm x 5 ± 2 nm
Hydrodynamic Diameter by Batch-mode DLS	87 ± 1 nm
Polydispersity Index by Batch-mode DLS	0.18 ± 0.01
Hydrodynamic Diameter by Flow-mode DLS	Not Tested
Concentration	
Total [NCC] by TGA	67 mg/mL
Surface Characterization	
Zeta Potential	-27 ± 0 mV
Purity	
Metal Impurities by ICP-MS	Al, Fe, Zn, Cu, Se, Mo

III. Silica Nanoparticles (CEHR-8 to CEHR-12)

Reference Number	Nanoparticle Description	Nominal size reported by manufacturer
CEHR-8	SiO_2 nanospheres 10 mg/mL	20 ± 4 nm
CEHR-9	SiO_2 nanospheres 10 mg/mL	50 ± 4 nm
CEHR-10	SiO_2 nanospheres 10 mg/mL	100 ± 4 nm
CEHR-11	SiO_2 nanospheres 10 mg/mL	200 ± 7nm
CEHR-12	SiO_2 nanospheres 10 mg/mL	400 ± 40 nm

Five silica nanoparticles from nanoComposix with nominal TEM sizes of 20, 50, 100, 200, and 400 nm (CEHR-8 to CEHR-12, respectively) were evaluated for sterility and physicochemical properties including size distribution, silica concentration, zeta potential, and evaluation of possible surface coatings on the nanoparticles. In general, the silica nanoparticles' sizes were in good agreement with the vendor-reported values. The TEM measured diameters for CEHR-8 to CEHR-12 were 23, 48, 103, 188, and 410 nm, respectively (Table III-3). The DLS measured hydrodynamic diameters were 29, 58, 135, 229, and 448 nm for CEHR-8 to CEHR-12, respectively (Table III-4). The DLS measured sizes are expected to be slightly larger than the TEM sizes. TEM measures the electron dense diameter, while DLS provides the hydrodynamic diameter. Flow-mode DLS using AF4 separation also afforded similar size distributions for CEHR-10, CEHR-11, and CEHR-12 (Figures III-12 to III-14). Interestingly, CEHR-8 showed two populations by AF4-DLS (Figure III-11). The major peak was in agreement with the batch-mode DLS, but a second minor population was noted at 174-184 nm. CEHR-9 was not analyzed by AF4 due to possible mold contamination in the sample.

All five particles had a reported concentration of 10 mg/mL. Analysis of SiO_2 concentration by thermogravimetric analysis (TGA) revealed concentrations of 4.0, 9.1, 7.5, 8.5, and 10.2 mg/mL, respectively (Table III-12). Thus, CEHR-12 was in agreement with the reported concentration, CEHR-9, CEHR-10 and CEHR-11 were 10-25% lower than theoretical, and CEHR-8 had less than half the SiO_2 as reported.

TGA was also used to detect possible coatings on the nanoparticle. While a clear weight loss event was observed for CEHR-8 and CEHR-9, only gradual weight loss events were noted for CEHR-10 to CEHR-12. The percent mass coating per mass nanoparticle was 13% and 19% for CEHR-8 and CEHR-9, respectively, and only 3-6% for CEHR-10 to CEHR-12 (Table III-13). Thus, while TGA appeared to denote a possible coating loss on all five particles, NCL could not identify or confirm the presence of a coating beyond this test. Importantly, no surface modification was specified by the manufacturer for these materials. The zeta potentials for all five particles were negative (Table III-14). Negative zeta potentials would be expected for uncoated silica nanoparticles or those with a negatively charged coating.

A summary of all data acquired on these materials is provided in the table that follows. A more complete description of the analyses conducted is provided in Section III of this report. Importantly, CEHR-9 tested positive for low-grade contamination with mold. As such, this material is not recommended for biological evaluation.

Silica Nanoparticle Summary

Silica Nanoparticles:	CEHR-8	CEHR-9	CEHR-10	CEHR-11	CEHR-12
Manufacturer Reported Values					
Vendor, Lot No.	nanoComposix JEA0156	nanoComposix JEA0088	nanoComposix JEA0167	nanoComposix JEA0113	nanoComposix ECP1362
Nominal Size	20 ± 4 nm	50 ± 4 nm	100 ± 4 nm	200 ± 7 nm	400 ± 40 nm
Theoretical Concentration	10 mg/mL	10 mg/mL	10 mg/mL	10 mg/mL	10 mg/mL
Sterility & Endotoxin					
Sterility	Negative	Mold	Negative	Negative	Negative
Endotoxin	3.1 EU/mg	<0.005 EU/mg	0.05 EU/mg	<0.005 EU/mg	0.009 EU/mg
Size					
Particle Diameter by TEM	23 ± 4 nm	48 ± 5 nm	103 ± 7 nm	188 ± 24 nm	410 ± 29 nm
Hydrodynamic Diameter by Batch-mode DLS	29 ± 0 nm	58 ± 0 nm	135 ± 1 nm	229 ± 2 nm	448 ± 6 nm
Polydispersity Index by Batch-mode DLS	0.11 ± 0.01	0.02 ± 0.01	0.06 ± 0.01	0.02 ± 0.01	0.02 ± 0.01
Hydrodynamic Diameter by Flow-mode DLS	Major: 25-37 nm Minor: 174-184 nm	Not Tested	96-129 nm	183-235 nm	416-465 nm
Concentration					
Total [SiO_2] by TGA	4.0 mg/mL	9.1 mg/mL	7.5 mg/mL	8.5 mg/mL	10.2 mg/mL
Surface Characterization					
Coating Detected	Possible	Possible	Possible	Possible	Possible
Coating Identity	Unknown	Unknown	Unknown	Unknown	Unknown
Coating Concentration by TGA (mass coating per mass NP)	13%	19%	3%	6%	5%
Zeta Potential	-27 ± 1 mV	-53 ± 4 mV	-49 ± 1 mV	-55 ± 1 mV	-68 ± 1 mV

IV. Silver Nanoparticles (CEHR-13 to CEHR-15)

Reference Number	Nanoparticle Description	Nominal size reported by manufacturer
CEHR-13	Ag nanospheres with PVP 5 mg/mL	5 ± 2 nm
CEHR-14	Ag nanospheres with PVP 5 mg/mL	25 ± 5 nm
CEHR-15	Ag nanospheres with PVP 5 mg/mL	75 ± 5 nm

Three silver nanoparticles, stabilized with a polyvinylpyrrolidone (PVP) coating, were supplied from nanoComposix. The nominal TEM sizes of the formulations were 5, 25, and 75 nm (CEHR-13 to CEHR-15, respectively). All three samples were evaluated for sterility and physicochemical properties including size distribution, total and free silver concentrations, PVP concentration, and zeta potential.

As seen with the silica nanoparticles purchased from nanoComposix, the silver nanoparticles were, generally, in good agreement with the manufacturer reported sizes and concentrations. The TEM measured diameters for CEHR-13 and CEHR-15 were 5 and 83 nm, respectively (Table IV-3). Of note however, CEHR-14 showed two distinct populations by TEM, one at approximately 7 nm and the other very close the nominal size at 24 nm (Figure IV-2). Size by DLS and AF4-DLS showed two populations for CEHR-13. The major population in CEHR-13 was approximately 15 nm, in agreement with a TEM nominal diameter of 5 nm (Figures IV-4 and IV-7). The DLS measured sizes are expected to be slightly larger than the TEM sizes, especially for surface-coated nanoparticles in which the surface coating is not visualized by negative-stain TEM. DLS and AF4-DLS also showed 2 populations for CEHR-14. The major population for CEHR-14 was 5 nm by batch-mode DLS (in agreement with the small size seen by TEM) and 25 nm by AF4-DLS (in agreement with the large size seen by TEM) (Figures IV-5 and IV-8). The small size population noted for CEHR-14 could indicate sample stability issues such as nanoparticle degradation, while the 25 nm AF4-DLS population could indicate coating instability. DLS and AF4-DLS were in good agreement for CEHR-15. The major peak was approximately 121 nm and was in good agreement with the theoretical size (Figures IV-6 and IV-9).

ICP-MS was used to quantitate the total silver in each sample. All three samples had a theoretical concentration of 5 mg/mL. CEHR-13, CEHR-14, and CEHR-15 had total silver concentrations of 4.6, 4.5, and 4.5 mg/mL, respectively, in good agreement with the reported concentrations (Table IV-10). Silver release was also measured by ICP-MS. By August 2016, CEHR-13 had 18%, CEHR-14 had 13%, and CEHR-15 had 2.5% free silver (Table IV-11). This is an important parameter to monitor because an increase in the free silver content can be an indication of particle instability, and in high enough concentrations can interfere with the proper interpretation of certain biological assays. Nanoparticle concentrations were also measured by TGA; however, TGA results were not consistent with the ICP-MS data, suggesting TGA is not an appropriate method for measuring nanoparticle concentration for these materials.

PVP concentrations were determined by TGA, and were approximately 29%, 5%, and 15% (mass coating per mass nanoparticle) for CEHR-13, CEHR-14, and CEHR-15, respectively (Table IV-13). Theoretical PVP concentrations were not provided by the manufacturer. Zeta

potentials were negative for all three particles (Table IV-14). PVP, a neutral functionality, is not covalently linked to the surface of the nanoparticle, and thus neutral zeta potentials are *not* expected for these materials.

Additional details on the analyses conducted on the silver nanoparticles are provided in Section IV of this report. A summary of all data acquired on these materials is provided in the table that follows. In general, these materials had physicochemical properties in good agreement with the reported values. Importantly though, CEHR-14 showed signs of instability by the three sizing techniques and all three formulations showed increasing levels of free silver ions suggesting a limited shelf-life stability.

Silver Nanoparticle Summary

Silver Nanoparticles:	CEHR-13	CEHR-14	CEHR-15
Manufacturer Reported Values			
Vendor, Lot No.	nanoComposix KJW1980A	nanoComposix CLF0494A	nanoComposix DMW0382
Nominal Size	5 ± 2 nm	25 ± 5 nm	75 ± 5 nm
Concentration	5 mg/mL	5 mg/mL	5 mg/mL
Sterility & Endotoxin			
Sterility	Negative	Negative	Negative
Endotoxin	1.9 EU/mg	<5 EU/mg	2.5 EU/mg
Size			
Particle Diameter by TEM	5 ± 1 nm	7 ± 2 nm & 24 ± 5 nm	83 ± 9 nm
Hydrodynamic Diameter by Batch-mode DLS	14 ± 3 nm	5 ± 0 nm	121 ± 2 nm
Polydispersity Index by Batch-mode DLS	0.45 ± 0.02	0.56 ± 0.01	0.08 ± 0.02
Hydrodynamic Diameter by Flow-mode DLS	Major: 14-23 nm Minor: 46-160 nm	Major: 25-26 nm Minor: 12-15 nm	103-139 nm
Concentration			
Total [Ag] by ICP-MS	4.62 ± 0.05 mg/mL	4.51 ± 0.05 mg/mL	4.49 ± 0.04 mg/mL
Total [Ag] by TGA	7.8 mg/mL	3.5 mg/mL	2.2 mg/mL
Surface Characterization			
Coating Detected	Yes	Yes	Yes
Coating Identity	Polyvinylpyrrolidone (per manufacturer; size unknown)	Polyvinylpyrrolidone (per manufacturer; size unknown)	Polyvinylpyrrolidone (per manufacturer; size unknown)
Coating Concentration by TGA (mass coating per mass NP)	29%	5%	15%
Zeta Potential	-33 ± 0 mV	-20 ± 1 mV	-24 ± 1 mV
Purity			
Metal Impurities by ICP-MS	Zn	Zn, Cu	Zn
Stability			
Free [Ag ions] by ICP-MS (01 June 2016)	5.1%	1.2%	0.4%
Free [Ag ions] by ICP-MS (31 August 2016)	18%	13%	2.5%

V. Zinc Oxide Nanoparticles (CEHR-16 and CEHR-17)

Two zinc nanoparticles from US Nano, with nominal size ranges of 30-40 and 50-80 nm (CEHR-16 and CEHR-17, respectively), were characterized for sterility and physicochemical properties. CEHR-16 was found to be contaminated with bacteria (Table V-1). As such, this material is not recommended for use in follow-on biological assays. No contamination was detected in CEHR-17.

Reference Number	Nanoparticle Description	Nominal size reported by manufacturer
CEHR-16	ZnO nanopowder, 20 wt% dispersion	30-40 nm
CEHR-17	ZnO nanopowder, 20 wt% dispersion	50-80 nm

The reported sizes were presumed to be TEM diameters, although the measurement technique was not disclosed by the manufacturer. TEM analysis showed some degree of aggregation/agglomeration, but the individual particles were still generally discernable at high magnification (Figures V-1 and V-2). The TEM diameters were 35 nm and 25 nm for CEHR-16 and CEHR-17, respectively (Table V-3). Thus, the TEM size of the individual particles was consistent with the reported size for CEHR-16, but was only half the reported size for CEHR-17. Consistent with aggregation/agglomeration seen in the TEM images, the batch-mode and flow-mode DLS showed much larger sizes, suggesting the nanoparticles have aggregated/agglomerated in solution (Table V-8). The batch-mode DLS diameters were 668 and 318 nm for CEHR-16 and CEHR-17, respectively. The flow-mode DLS showed two populations, 127-215 nm and 260-290 nm for CEHR-17. Flow-mode DLS was not completed on CEHR-16 due to the bacterial contamination.

The nanoparticle stock concentration was reported to be 20% by weight. Despite issues with sample heterogeneity (described below), both ICP-MS and TGA measurements averaged to afford concentrations in good agreement with the reported values (Table V-11). ICP-MS concentrations were 23% and 22%, respectively, and TGA provided 20% and 16%, respectively. Large standard deviations (see table that follows), however, highlight the issues with consistent sampling of both materials.

Purity and stability were also evaluated by ICP-MS. ICP-MS showed iron, manganese, and strontium impurities in CEHR-17, but no metal impurities in CEHR-16 (Figure V-6). Very little free zinc was detected initially in the samples, <0.1%. These values slowly increased to 1.2% for CEHR-16 and 1.3% for CEHR-17 (Table V-10) by November 2016. TGA revealed what may be a coating or other undisclosed excipient in both formulations (Figures V-10 and V-11). The amounts were 2% and 8% (mass coating per mass nanoparticle) for CEHR-16 and CEHR-17, respectively. Also of note, the TGA showed a different decomposition pattern for the two samples, suggesting whatever the coating/excipients are, they are likely different between the two samples. The zeta potential was negative for both samples, which would be expected for either uncoated nanoparticles or those modified with a negatively charged surface coating.

A summary of all data acquired on the zinc nanomaterials is provided in the table that follows. A more complete description of all analyses conducted is provided in Section V. Importantly, CEHR-16 tested positive for bacterial contamination, and is not recommended for biological evaluation. The particles were aggregated/agglomerated in solution and may have an unknown surface coating which could confound toxicity testing. Furthermore, both materials settle fairly rapidly, leading to sampling inconsistency. This is depicted in the photograph on the right. The samples must be thoroughly mixed prior to use to ensure a more homogenous sampling.

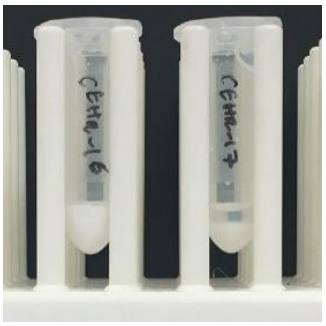

Zinc Oxide Nanoparticle Summary

Zinc Nanoparticles:	CEHR-16	CEHR-17
Manufacturer Reported Values		
Vendor, Catalog No.	US Nano US7100	US Nano US7290
Nominal Size	30-40 nm	50-80 nm
Concentration	20%wt.	20% wt.
Sterility & Endotoxin		
Sterility	Bacteria 2200 CFU/mg	Negative
Endotoxin	1.4 EU/mg	<0.5 EU/mg
Size		
Particle Diameter by TEM	35 ± 9 nm	25 ± 9 nm
Hydrodynamic Diameter by Batch-mode DLS	668 ± 36 nm	318 ± 12 nm
Polydispersity Index by Batch-mode DLS	0.17 ± 0.02	0.14 ± 0.02
Hydrodynamic Diameter by Flow-mode DLS	Not Tested	Major: 127-215 nm Minor: 260-290 nm
Concentration		
Total [Zn] by ICP-MS	187 ± 49 mg/g	176 ± 49 mg/g
Total [ZnO] by ICP-MS	23% wt.	22% wt.
Total [ZnO] by TGA	20% wt.	16% wt.
Surface Characterization		
Coating Detected	Possible	Possible
Coating Identity	Unknown	Unknown
Coating Concentration by TGA (mass coating per mass NP)	2%	8%
Zeta Potential	-22 ±1 mV	-35 ±1 mV
Purity		
Metal Impurities by ICP-MS	None	Mn, Fe, Sr
Stability		
Free [Zn ion] by ICP-MS (06 June 2016)	<0.1%	<0.1%
Free [Zn ion] by ICP-MS (07 September 2016)	<0.1%	1.3%
Free [Zn ion] by ICP-MS (30 November 2016)	1.2%	0.9%

VI. Iron Oxide Nanoparticles (CEHR-18 and CEHR-19)

Two iron oxide nanoparticles were supplied from US Nano, CEHR-18 (Fe_3O_4) and CEHR-19 (Fe_2O_3 gamma). The samples had nominal sizes of 15-20 nm and 20 nm, respectively. CEHR-18 and CEHR-19 were characterized for sterility and physicochemical properties. CEHR-18 had no detectable bacteria or endotoxin. However, CEHR-19 was found to be contaminated with bacteria and had endotoxin levels >6000 EU/mg; thus, this sample is not recommended for biological testing (Table VI-1).

Reference Number	Nanoparticle Description	Nominal size reported by manufacturer
CEHR-18	Fe_3O_4 nanopowder, 20 wt% water dispersion	15-20 nm
CEHR-19	Fe_2O_3 gamma, 10 wt% water dispersion	20 nm

The vendor-reported sizes were presumed to be TEM diameters of the individual particles, although the sizing technique was not disclosed by the vendor. TEM analysis revealed significant agglomeration/aggregation for both materials (Figures VI-1 and VI-2). There were enough individually discernable particles to allow for sizing of CEHR-18, but not for CEHR-19. The TEM measured size for CEHR-18 was 12 nm, just slightly smaller than the reported diameter range. DLS hydrodynamic diameters of >200 nm for both materials also suggested aggregation/agglomeration, in agreement with the TEM images (Figures VI-3 and VI-4). Sample polydispersity was also evident upon AF4 separation. CEHR-18 had a very broad size range with peaks up to 260 nm (Figure VI-5). CEHR-19 was not analyzed by AF4 due to the bacterial contamination.

Iron concentrations were also different than that reported by the vendor, 20% and 10% by weight for CEHR-18 and CEHR-19, respectively. ICP-MS and TGA provided similar values of 9% and 11%, respectively, for CEHR-18, showing the sample concentration was approximately only half of the theoretical concentration. ICP-MS and TGA concentrations for CEHR-19 were 15% and 26% (Table VI-11). While the measurements are not completely in agreement, both suggest the sample is more concentrated than the theoretical value. The difference between the ICP-MS and TGA measurements likely stems from inconsistent sampling. The nanoparticles settle rapidly, especially for CEHR-19, as can be seen in the picture.

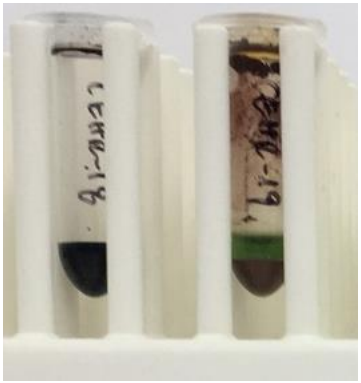

Release of free iron was also monitored by ICP-MS. A maximum of 1.2% and 2.5% free iron was detected in CEHR-18 and CEHR-19, respectively (Table VI-10). The results fluctuated over the course of the stability study, but are attributed to the sample heterogeneity issues. ICP-MS also identified possible traces of manganese and zinc in both formulations (Figure VI-6), and TGA revealed the presence of a coating or other added excipients (Figures VI-10 and VI-11). The mass coating per mass nanoparticle was 15% and 17% for CEHR-18 and CEHR-19, respectively. This material could not be identified through TGA. The zeta potential was negative for both samples, -36 mV (Table VI-13). Negative zeta potentials would be expected for either uncoated iron oxide nanoparticles or those with a negatively charged surface coating.

Additional details on the characterization of the iron oxide nanoparticle samples is described in Section VI. A summary of the relevant findings is presented in the table that follows. Of note, CEHR-19 had bacterial contamination and is not recommended for biological testing. The particles were aggregated/agglomerated in solution and may have an unknown surface coating which could confound toxicity testing. Furthermore, both materials settle fairly rapidly, leading to sampling inconsistency. The samples must be thoroughly mixed prior to use to ensure a more homogenous sampling.

Iron Oxide Nanoparticle Summary

Iron Nanoparticles:	CEHR-18	CEHR-19
Manufacturer Reported Values		
Vendor, Catalog No.	US Nano US7568	US Nano US7558
Nominal Size	15-20 nm	20 nm
Concentration	20% wt.	10% wt.
Sterility & Endotoxin		
Sterility	Negative	Bacteria 72,000 CFU/mg
Endotoxin	<0.05 EU/mg	6170 EU/mg
Size		
Particle Diameter by TEM	12 ± 4 nm	Aggregation/ Agglomeration
Hydrodynamic Diameter by Batch-mode DLS	238 ± 15 nm	242 ± 26 nm
Polydispersity Index by Batch-mode DLS	0.25 ± 0.01	0.34 ± 0.02
Hydrodynamic Diameter by Flow-mode DLS	Major: 34-100 nm Minor: 100-260 nm	Not Tested
Concentration		
Total [Fe] by ICP-MS	68 ± 12 mg/g	107 ± 38 mg/g
Total [Fe_xO_y] by ICP-MS	9% wt.	15% wt.
Total [Fe_xO_y] by TGA	11% wt.	26% wt.
Surface Characterization		
Coating Detected	Possible	Possible
Coating Identity	Unknown	Unknown
Coating Concentration by TGA (mass coating per mass NP)	15%	17%
Zeta Potential	-36 ± 0 mV	-36 ± 1 mV
Purity		
Metal Impurities by ICP-MS	Mn, Zn	Mn, Zn
Stability		
Free [Fe ion] by ICP-MS (09 June 2016)	0.8%	2.5%
Free [Fe ion] by ICP-MS (26 August 2016)	1.2%	1.8%
Free [Fe ion] by ICP-MS (21 November 2016)	0.3%	1.8%

VII. Aluminum Oxide Nanoparticles (CEHR-20 to CEHR-22)

Reference Number	Nanoparticle Description	Nominal size reported by manufacturer
CEHR-20	Al_2O_3 gamma, 20 wt% dispersion	10 nm
CEHR-21	Al_2O_3 alpha, 20 wt% dispersion	30 nm
CEHR-22	Al_2O_3 gamma, 20 wt% dispersion	30 nm

Three aluminum oxide nanoparticles from US Nano, with nominal sizes of 10, 30 and 30 nm for CEHR-20, CEHR-21, and CEHR-22, respectively, were characterized for sterility and relevant physicochemical parameters. CEHR-20 and CEHR-22 are gamma phase Al_2O_3, while CEHR-21 is alpha phase Al_2O_3. None of the three formulations had detectable bacterial or endotoxin contamination (Table VII-1 and VII-2).

TEM analysis revealed rod-like structures for CEHR-20 and flake-like structures for CEHR-21 and CEHR-22. Diameters of the individually dispersed structures were 24, 30, and 15 nm, respectively, although the images clearly depict sample aggregation/agglomeration and a polydispersity in the particle sizes (Figures VII-1 to VII-3). DLS also suggested aggregation, with diameters much larger than the TEM diameters. CEHR-20 and CEHR-21 were monomodal and had diameters of 122 and 194 nm, respectively (Tables III-4 and III-5). CEHR-22 had a very broad bimodal distribution. The average size was 171 nm although the peak spanned <10 nm to >500 nm (Figure VII-6). AF4 separation was unsuccessful for these materials. Because the samples were highly positive, they stuck to the membrane and resulted in very low recoveries.

The aluminum concentrations were determined by both ICP-MS and TGA. The ICP-MS measured concentrations were 10, 15, and 22% by weight, respectively (Table VII-8). The TGA-measured concentrations were 16, 19, and 19% by weight, respectively (Table VII-10). While the TGA concentrations agree reasonably well with the vendor reported concentrations, the difference between the two methods highlights the heterogeneity of the sample and inconsistent sampling difficulties. CEHR-20, for example, was very gelatinous as shown in the picture.

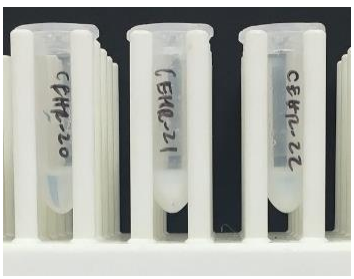

ICP-MS and TGA were also used to assess the purity and stability of the formulations. No considerable free aluminum was detected in any of the samples (Table VII-9). Semi-quantitative ICP-MS revealed the possible presence of zinc impurities in CEHR-20 and yttrium, zirconium and hafnium impurities in CEHR-21 (Figure VII-7). Further analysis would be required to confirm these impurities. TGA revealed the presence of a coating and/or other added excipients in the samples (Figures VII-12 to VII-14). Although TGA could not identify this material, a difference in decomposition temperatures suggest the added material is different for CEHR-20 as compared to CEHR-21 and CEHR-22. Zeta potential analysis also suggested a coating was present on the materials, as all three samples had a positive zeta potential (Table VII-12). A negative zeta potential would be expected for uncoated aluminum oxide nanoparticles.

A summary of all data acquired on the aluminum oxide nanomaterials is provided in the table that follows. A more complete description of all analyses conducted is provided in Section VII. Importantly, the samples showed signs of aggregation/agglomeration in solution and may have an unknown surface coating which could confound toxicity testing. Furthermore, the samples—especially CEHR-20—are very heterogeneous, leading to sampling inconsistency. The samples must be thoroughly mixed prior to use to ensure a more homogenous sampling.

Aluminum Oxide Nanoparticle Summary

Aluminum Nanoparticles:	CEHR-20	CEHR-21	CEHR-22
Manufacturer Reported Values			
Vendor, Catalog No.	US Nano US7020	US Nano US7010	US Nano US7030
Nominal Size	10 nm	30 nm	30 nm
Concentration	20% wt.	20% wt.	20% wt.
Sterility & Endotoxin			
Sterility	Negative	Negative	Negative
Endotoxin	<0.5 EU/mg	<0.5 EU/mg	<5 EU/mg
Size			
Particle Diameter by TEM	24 ± 7 nm	30 ± 17 nm	15 ± 5 nm
Hydrodynamic Diameter by Batch-mode DLS	122 ± 2 nm	194 ± 2 nm	171 ± 2 nm
Polydispersity Index by Batch-mode DLS	0.14 ± 0.01	0.07 ± 0.01	0.25 ± 0.01
Hydrodynamic Diameter by flow-mode DLS	*AF4 was unsuccessful for these materials.*		
Particle Diameter by TEM	24 ± 7 nm	30 ± 17 nm	15 ± 5 nm
Concentration			
Total [Al] by ICP-MS	53 ± 28 mg/g	79 ± 20 mg/g	119 ± 71 mg/g
Total [Al_2O_3] by ICP-MS *(calc.)*	10% wt.	15% wt.	22% wt.
Total [Al_2O_3] by TGA	16% wt.	19% wt.	19% wt.
Surface Characterization			
Coating Detected	Possible	Possible	Possible
Coating Identity	Unknown, but different than CEHR-21 and CEHR-22	Unknown	Unknown
Coating Concentration by TGA (mass coating per mass NP)	23%	5%	14%
Zeta Potential	45 ± 1 mV	25 ± 2 mV	48 ± 1 mV
Purity			
Metal Impurities by ICP-MS	Zn	Y, Zr, Hf	None
Stability			
Free [Al ion] by ICP-MS (15 June 2016)	0.1%	<0.1%	<0.1%
Free [Al ion] by ICP-MS (30 August 2016)	<0.1%	<0.1%	<0.1%
Free [Al ion] by ICP-MS (30 November 2016)	<0.1%	0.3%	<0.1%

VIII. Titanium Oxide Nanoparticles (CEHR-23 to CEHR-26)

Four titanium oxide nanoparticles with nominal size ranges of 5-15 nm for CEHR-23 and CEHR-24 and 30-50 nm CEHR-25 and CEHR-26 were supplied from US Nano. CEHR-23 and CEHR-25 are anatase TiO_2 while CEHR-24 and CEHR-26 are rutile TiO_2. All four materials were characterized for sterility and relevant physicochemical parameters. Sterility screening revealed that CEHR-24 contained bacterial contamination (Table VIII-1). For this reason, this sample is not recommended for biological testing. CEHR-23, CEHR-25, and CEHR-26 showed no detectable bacteria contamination and had undetectable levels of endotoxin (Table VIII-2).

Reference Number	Nanoparticle Description	Nominal size reported by manufacturer
CEHR-23	TiO_2 anatase, 15 wt% dispersion	5 -15 nm
CEHR-24	TiO_2 rutile, 15 wt% dispersion	5 -15 nm
CEHR-25	TiO_2 anatase, 40 wt% dispersion	30 -50 nm
CEHR-26	TiO_2 rutile, 20 wt% dispersion	30 -50 nm

The TEM measured diameters for CEHR-25 and CEHR-26 were 41 and 55 nm, respectively, and were similar to the reported size ranges (Table VIII-3). CEHR-24 was roughly five times larger than the reported size by TEM. CEHR-23 was too aggregated/agglomerated to obtain sizing data on individual particles. By DLS, all four samples were considerably larger than the TEM and/or reported sizes (Table VIII-4), suggesting the samples have aggregated/agglomerated in solution, as evidenced in the TEM images (Figures VIII-1 to VIII-4). AF4 separation also showed polydispersity for CEHR-25, with peaks ranging from 43 nm to greater than 300 nm (Figure VIII-9). AF4 was unsuccessful for CEHR-23 and CEHR-26. These two samples stuck to the membrane, resulting in very low recoveries. CEHR-24 was not subjected to AF4 analysis due to the bacterial contamination detected in the sample.

Nanoparticle concentrations were measured by ICP-MS and TGA. The nanoparticle concentrations for CEHR-23, CEHR-24, CEHR-25, and CEHR-26 were 11%, 12%, 39%, and 7% by weight, respectively, as measured by ICP-MS (Table VIII-11). The TGA measured concentrations were very similar and were 13%, 15%, 36%, and 9% by weight, respectively (Table VIII-13). In general, CEHR-23, CEHR-24, and CEHR-25 aligned well with the reported concentrations. CEHR-26, on the other hand, was less than half the reported concentration. All samples showed visible signs of settling, but CEHR-26 was the most prominent. The heterogeneous samples were prone to inconsistent sampling, making accurate concentration determination difficult.

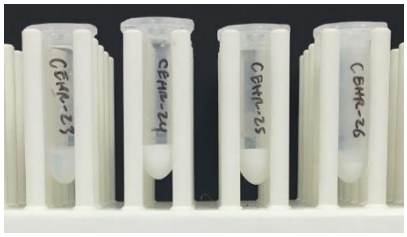

Negligible free titanium content (≤0.1%) was seen in all four samples (Table VIII-12). ICP-MS was also used to detect metal impurities in the samples. CEHR-23 and CEHR-24 contained zinc and hafnium (Figure VIII-10). CEHR-26 contained zinc, zirconium, and tin. CEHR-25 contained the most metal impurities with zinc, iron, strontium, manganese, vanadium, lead, uranium, and cerium all detected (Figure VIII-10). TGA also showed the presence of unknown coatings or other added excipients in all four samples (Table VIII-14). The zeta potentials were variable among the various samples, with CEHR-23 being positive, CEHR-24 being negative, CEHR-25 being borderline negative, and CEHR-26 being neutral (Table VIII-15). These results also

suggest the presence of other components on the nanoparticle surface. Different decomposition patterns in TGA and different zeta potential ranges suggest the coatings/excipients may be different among the four samples.

Greater details on the titanium oxide nanoparticle characterization is described in Section VIII. A table summarizing all the measured parameters is provided on the next page. Notably, the samples appeared to have aggregated/agglomerated in solution and may have an unknown surface coating which could confound toxicity testing. The samples, especially CEHR-26, are very heterogeneous, leading to sampling inconsistency. Furthermore, CEHR-24 had bacterial contamination and is not recommended for biological testing. The samples must be thoroughly mixed prior to use to ensure a more homogenous sampling.

Titanium Oxide Nanoparticle Summary

Titanium Nanoparticles	CEHR-23	CEHR-24	CEHR-25	CEHR-26
Manufacturer Reported Values				
Vendor, Catalog No.	US Nano US7080	US Nano US7050	US Nano US7071	US Nano US7070
Nominal Size	5-15 nm	5-15 nm	30-50 nm	30-50 nm
Concentration	15% wt.	15% wt.	40% wt.	20% wt.
Sterility & Endotoxin				
Sterility	Negative	310 CFU/mg	Negative	Negative
Endotoxin	<5 EU/mg	28 EU/mg	<0.5 EU/mg	<0.05 EU/mg
Size				
Particle Diameter by TEM	Aggregates/ Agglomerates	63 ± 19 nm	41 ± 14 nm	55 ± 15 nm
Hydrodynamic Diameter by Batch-mode DLS	47 ± 4 nm	683 ± 209 nm	219 ± 36 nm	780 ± 68 nm
Polydispersity Index by Batch-mode DLS	0.29 ± 0.02	0.29 ± 0.06	0.28 ± 0.03	0.22 ± 0.03
Hydrodynamic Diameter by flow-mode DLS	Unsuccessful	Not Tested	Major: 43-200 nm 285-320 nm	Unsuccessful
Concentration				
Total [Ti] by ICP-MS	63 ± 8 mg/g	72 ± 20 mg/g	231 ± 66 mg/g	42 ± 22 mg/g
Total [TiO_2] by ICP-MS	11% wt.	12% wt.	39% wt.	7% wt.
Total [TiO_2] by TGA	13% wt.	15% wt.	36% wt.	9% wt.
Surface Characterization				
Coating Detected	Possible	Possible	Possible	Possible
Coating Identity	Unknown	Unknown	Unknown	Unknown
Coating Concentration by TGA (mass coating per mass NP)	9%	10%	10%	1%
Zeta Potential	40 ± 2 mV	-20 ± 1 mV	-12 ± 0 mV	7 ± 1 mV
Purity				
Metal Impurities by ICP-MS	Zn, Hf	Zn, Hf	V, Mn, Fe, Zn, Sr, Ce, Pb, U	Zn, Zr, Sn
Stability				
Free [Ti ion] by ICP-MS (28 September 2016)	0%	0%	0%	0%
Free [Ti ion] by ICP-MS (29 November 2016)	<0.1%	<0.1%	<0.1%	0.1%

Important Notes for Interpreting Summary Tables

- The reported batch-mode DLS diameter is from the most abundant population (i.e., some are intensity averages and some are volume averages).
- The reported flow-mode DLS diameter is the range of DLS peak averages (i.e., this is not the range of particle sizes).
- The ICP-MS metal oxide concentration was calculated assuming all metal exists in the oxidation state reported by the manufacturer/vendor.
- The TGA metal oxide concentration assumes that all residual weight is that of the metal oxide, and that all metal exists in the oxidation state reported by the manufacturer/vendor. Oxidation state could not be confirmed.
- TGA weight loss events for the metal/metal oxide nanoparticles, with the exception of water, were assumed to stem from a possible coating. However, it is possible these could be from other added excipients. TGA cannot differentiate between the two.
- Metal impurities identified are noted only as *possible* impurities; they were not qualitatively confirmed. (Peak heights in the semi-quantitative ICP-MS plots may not be representative of metal concentrations/ratios.)
- Free ion concentrations assumed that no nanoparticles passed through the stirred cell membrane.

I. Cerium Oxide

I. Cerium Oxide

A. Section Summary

Cerium oxide with a nominal size of <25 nm (CEHR-1) was characterized for size by dynamic light scattering (DLS) and transmission electron microscopy (TEM) measurements, zeta potential, and total cerium oxide concentration by inductively-coupled plasma mass spectrometry (ICP-MS) and thermogravimetric analysis (TGA).

Size analysis of the cerium oxide nanomaterial was conducted by DLS and TEM. However, by TEM, the sample was significantly aggregated and reliable size measurements were not possible (Figure I-1). By DLS, the intensity-weighted hydrodynamic diameter was approximately 260 nm (Figure 1-2). Both techniques indicated the sample had significant aggregation/agglomeration in solution.

Total cerium oxide concentration was measured by ICP-MS and TGA. The ICP-MS cerium concentration was converted to a weight percent cerium oxide to facilitate comparison with the vendor-specified value of 10% by weight. The ICP-MS and TGA-measured concentrations were 17% and 20% by weight, respectively (Table I-4). These results were nearly double the reported concentration. With time, the sample showed clear signs of evaporation, and the change in sample concentration was evident between runs. Eventually, the sample became paste-like and was difficult to obtain consistent data.

ICP-MS was also used to assess the purity of the formulation; no metal impurities were detected in CEHR-1 (Figure I-3). The zeta potential was positive (Table I-5). This was inconsistent with the predicted range for uncoated cerium oxide nanoparticles and suggests they may be coated with a positively-charged surface moiety. However, because of the compromise in sample integrity, further characterization was halted on this material. No evaluation of sterility, endotoxin, surface coating analysis, size polydispersity by AF4, or free cerium concentrations were conducted.

B. Transmission Electron Microscopy

Design and Methods

Transmission electron microscopy (TEM) was conducted to assess the size and morphology of the nanomaterials. Stock solutions were diluted 1000-fold with ultrapure water, and 2 µL was applied to a glow discharged carbon film grid (Electron Microscopy Sciences). The grid was washed three times with ultrapure water, blotted, and allowed to air dry before imaging. Images were taken using a T-20 TEM (FEI) equipped with a LαB6 thermoionic gun at 80 V acceleration voltage.

Results and Discussion

Figure I-1 contains representative images for CEHR-1. The sample was significantly aggregated, and while individual some particles could be seen within the aggregates, there were too few clearly discernable individual particles to be sized accurately. The reported size for CEHR-1 was <25 nm, according to the Sigma Aldrich website. By visual inspection, there appeared to be individual particles (contained within aggregates) that were less than 25 nm, consistent with the theoretical value. Importantly however, the vendor states that BET was used to obtain the size of the ceria particle. BET analysis is not an ideal technique for size, especially for non-uniform particles. BET measures the surface area and makes several assumptions to calculate a size. Thus, this may not provide an accurate representation of the true size of the sample in solution.

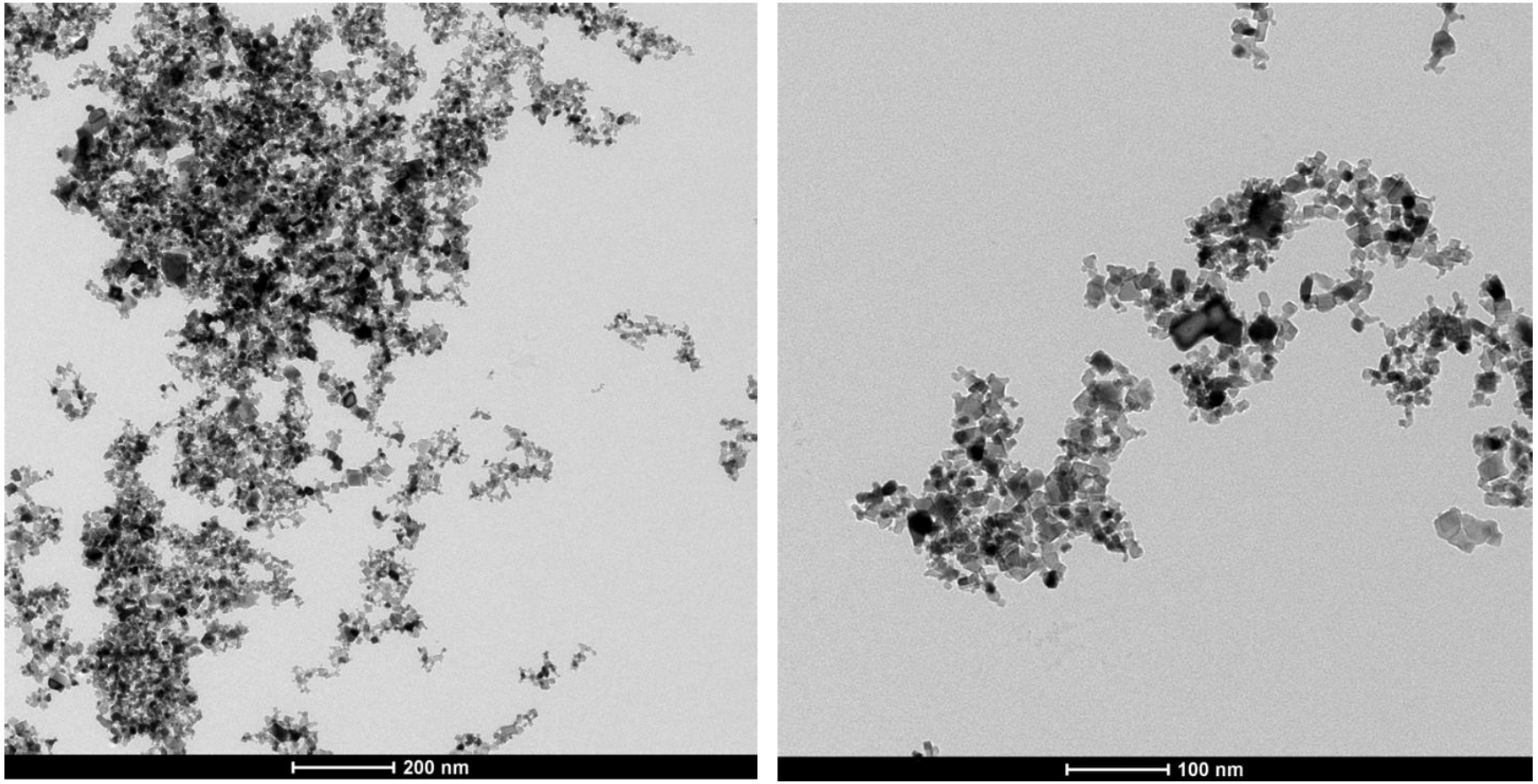

Figure I-1. Representative TEM images of CEHR-1. Two representative images are shown for CEHR-1. The sample was too aggregated/agglomerated for accurate sizing of the individual particles.

C. Hydrodynamic Size/Size Distribution via Dynamic Light Scattering

Design and Methods

A Malvern Zetasizer Nano ZS instrument (Southborough, MA) with back scattering detector (173°) was used for measuring the hydrodynamic size (diameter) in batch mode. NIST-NCL joint protocol PCC-1 was followed (https://ncl.cancer.gov/resources/assay-cascade-protocols). Stock samples were diluted 100- and 1,000-fold in water. Samples were measured at 25°C in a quartz microcuvette. Traces in the figures represent the average of at least twelve measurements.

Hydrodynamic diameters are reported as the intensity-weighted average and as the volume-weighted average over a particular range of size populations corresponding to the most prominent peak. The Int-Peak value is used as the hydrodynamic diameter of a particular species. The Vol-Peak and %Vol values are used to approximate relative amounts of various species in the formulation.

Results and Discussion

The intensity and volume distribution plots for the ceria nanoparticles are provided in Figure I-2. The averaged intensity distribution was approximately 260 nm. This large hydrodynamic diameter could be indiciative of aggregation, and supports the TEM analysis. Our previous experience with similar ceria particles also showed these particles tend to aggregate/agglomerate in solution.

Table I-1. Comparison of sizes.

Reference Number	Nominal size reported by manufacturer	TEM Measured Size	DLS Measured Size (Int-Peak)
CEHR-1	< 25 nm	Aggregated/Agglomerated	257 ± 11 nm

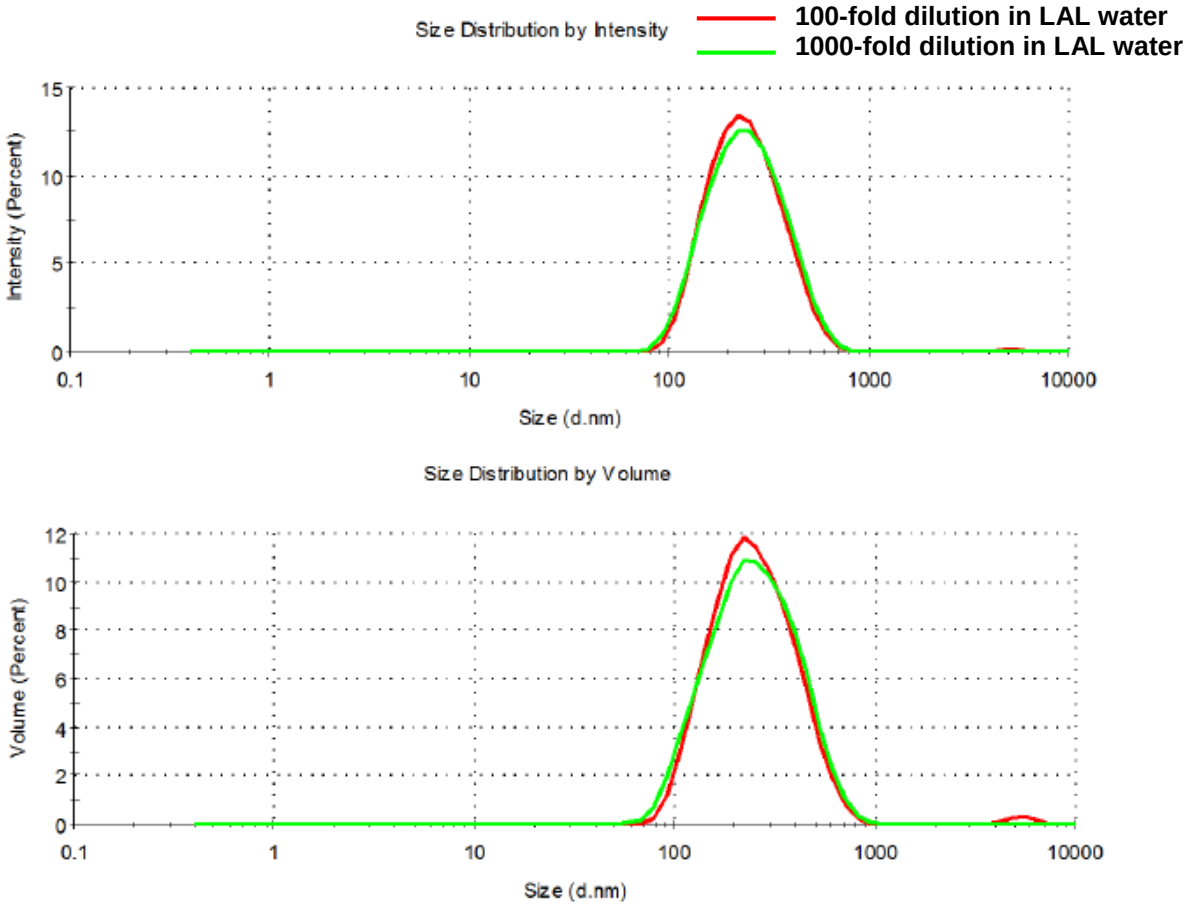

Figure I-2. The averaged intensity and volume distribution plots for CEHR-1 diluted in water.

Table I-2. Summary of the hydrodynamic size for CEHR-1 diluted in water.

Dispersing Medium	Dilution	Z-Avg, nm	PdI	Int-Peak, nm	% Int	Vol-Peak, nm	% Vol
DI water	100-fold	224 ± 2	0.15 ± 0.02	257 ± 11	100 ± 1	228 ± 14	99 ± 2
DI water	1000-fold	222 ± 3	0.15 ± 0.02	263 ± 4	100 ± 0	274 ± 8	100 ± 0

Note: Results are the average of at least 12 measurements. Z-Avg is the intensity-weighted average. PdI is the polydispersity index. Int-Peak is the intensity-weighted average over the primary peak. % Int is the percentage of the intensity spectra occupied by the primary peak. Vol-Peak is the volume-weighted average over the primary peak. % Vol is the percentage of the volume spectra occupied by the primary peak.

D. Inductively Coupled Plasma Mass Spectrometry

Design and Methods

The cerium concentration of CEHR-1 was determined by inductively coupled plasma mass spectrometry (ICP-MS). An Agilent ICP-MS 7500CX equipped with a micro-mist nebulizer, standard sample introduction system, and integrated auto-sampler, operated in "no gas" mode in Agilent's proprietary ORS (Octopole Reaction System) was used. Tuning of the instrument was performed daily prior to sample testing.

Semi-Quantitative Analysis

A semi-quantitative analysis was performed on the sample prior to quantitative determination of the ceria concentration. The semi-quantitative analysis was performed to help determine the proper dilution range for the sample, as well as to detect the presence of other metals in the sample. Only metals with counts two times greater than the background were denoted.

The samples (10 µL) were initially digested using 3.99 mL of a 5:1:2 mixture of HNO_3: HCl: 30% H_2O_2. This sample was then diluted with 2% nitric acid to target a 10 to 200 ppb concentration. The listed weight percent for CEHR-1 (10 wt%) was used as a guide for the dilution. For 10 wt% of CeO_2, the estimated cerium weight would be 8.1% or 0.081 mg Ce / g sample, assuming a 1 g/mL density.

Total Metal Concentration

Using the data from the semi-quantitative analysis, the appropriate dilution was determined for the ICP-MS full quantitative analysis. The dilution target for the samples was 5 to 200 ppb. Samples (10-100 µL) were initially digested with a 5:1:2 mixture of HNO_3: HCl: 30% H_2O_2. The acid digested samples were then further diluted to approximately 30-50 mL total volume with 2% nitric acid. A second dilution was then performed in which 10-100 µL of the first dilution was diluted to 10-50 mL using 2% nitric acid.

The metal concentration in the samples was determined by comparing against a series of calibration standards prepared from NIST SRM 3110. A series of concentrations ranging 5 to 200 ng/g (ppb) were prepared. The dilutions were made using 2% nitric acid. Specifically, a dilution of 5000 ng Ce / g 2% HNO_3 was used to make a 1000 ng Ce / g solution, which was then used to create standards for the calibration curve in a range of 5 to 200 ng/g in 10 mL volumes. In addition, an internal standard, indium, was used to track the signal response of the ICP-MS. The internal standard was diluted to approximately 50 ppb and was mixed with the sample using a sample T. A simple linear regression was used for calculation of the metal concentrations.

The sequence for the ICP-MS runs consisted of five blanks, the calibration curve standards ordered from lowest to highest, five more blanks, then the ceria nanoparticle samples. Each sample was run in duplicate with three blanks between each sample. After the last sample was measured, five blanks were run, followed by the calibration standards once again. Three blanks were run following completion of the ICP-MS runs to flush the sample introduction system.

Results and Discussion

Semi-Quantitative Analysis

The results from the semi-quantitative analysis of CEHR-1 are shown in Figure I-3. Only cerium was detected in CEHR-1. No other metal impurities were detected in the sample. In the initial data, indium (^{115}In) was also present, due to its use as an internal standard for the instrument run, but was omitted in the figure for clarity.

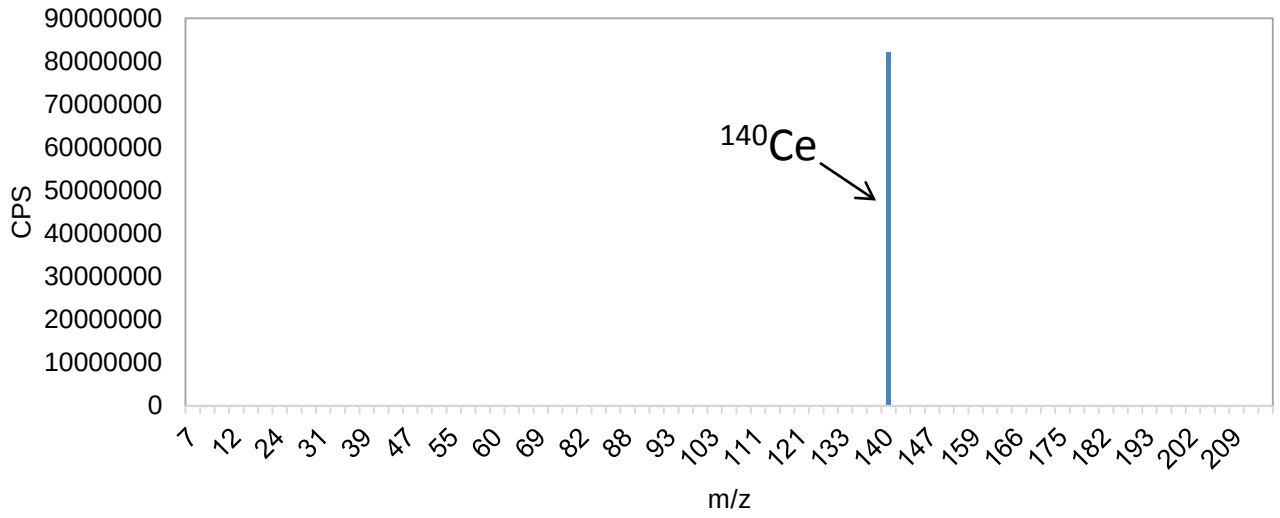

Figure I-3. **Plot of CPS vs m/z.** Semi-quantitative analysis of CEHR-1. The sample was analyzed on 7 September 2016. Note ^{12}C was removed to better visualize any smaller peaks. The internal standard peak for ^{115}In was also omitted.

Full Quantitative Analysis: Total Cerium Concentration
The calibration curve used for total cerium quantitation was constructed from NIST SRM 3110. Quantitative total cerium concentration for CEHR-1 is summarized in Table I-3. The ICP-MS cerium concentration, in units of mg/g, was converted to weight percent. To do so, the cerium mass was converted to CeO_2, using cerium oxide's molecular weight of 172.115 g/mol. To calculate the cerium oxide weight percent, the cerium oxide mass was divided by the mass of the solution to output the nanoparticle percent. The percent weight of the cerium oxide nanoparticles was 17%, nearly double the vendor-specified value of 10% wt.

Note, over time the CEHR-1 sample became very viscous and lost water due to evaporation leaving a paste rather than a liquid. Because of this, measurement of free cerium concentratio. was not pursued.

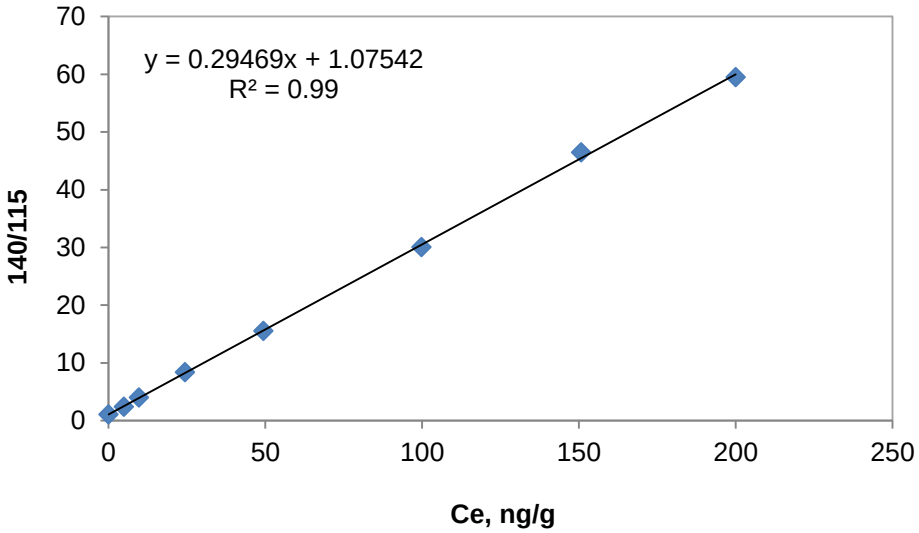

Figure I-4. Cerium Calibration Curve. A typical calibration curve ranging from 0 to 200 Ce ng/g, used to calculate the cerium concentration in CEHR-1. The calibration curve was constructed from NIST SRM 3110 cerium standard.

Table I-3. Total cerium concentration in CEHR-1 as determined by ICP-MS.

Reference Number	Reported Concentration	Total [Ce]	Total [CeO_2]
CEHR-1	10% wt.	141 ± 42 mg/g (n=3)	17% by weight

E. Thermogravimetric Analysis

Design and Methods

CEHR-1 was analyzed via thermogravimetric analysis (TGA) to determine the concentration of the metallic nanomaterial by measuring the residual material remaining after combustion of water and any coatings or other excipients added. The sample was measured in liquid form (as-received). CEHR-1, 50 µL, was transferred to an aluminum oxide crucible (150 µL crucible with lid, Mettler Toledo) for TGA measurement (TGA/DSC 1, Mettler Toledo). The sample was held at 25˚C for 5 min, then ramped to 1000˚C at a heating rate of 20˚C/min under nitrogen gas. The empty crucible was subjected to the TGA method prior to loading the sample to serve as a background correction.

TGA can also be used to assess whether coatings are present on the nanoparticles and in what concentration. However, the sample quantity for CEHR-1 was very limited and had undergone significant evaporation before this analysis could be completed. Therefore, this analysis was not conducted.

Results and Discussion

The TGA curve (top panel; weight loss versus temperature) for CEHR-1 is shown in Figure I-5. The first derivative of this curve (bottom panel) was used to highlight the weight loss events. The major weight loss event was observed between 50-180˚C, corresponding to the loss of water. The total mass cerium oxide was determined by using the amount of mass remaining at the end of the TGA run. However, this analysis assumes that, at the end of the run, all that remained was the cerium oxide; the water would have evaporated and any organic coating present would have combusted. The TGA-measured nanoparticle concentration for CEHR-1 was 20% (by weight, Table I-4). This value was nearly double the vendor-specified value of 10 wt%. This was expected, as the sample showed clear loss of water due to evaporation, leaving a paste rather than a liquid. Because of the compromise in sample integrity, other measurements to determine a coating presence/concentration were not pursued.

Table I-4. Comparison of TGA Measured Concentration to ICP-MS Measured and Reported Nanoparticle Concentrations.

Reference Number	Reported Concentration	Measured Concentration via ICP-MS	Measured Concentration via TGA of Liquid Sample
CEHR-1	10% wt.	17% wt.	20% wt.

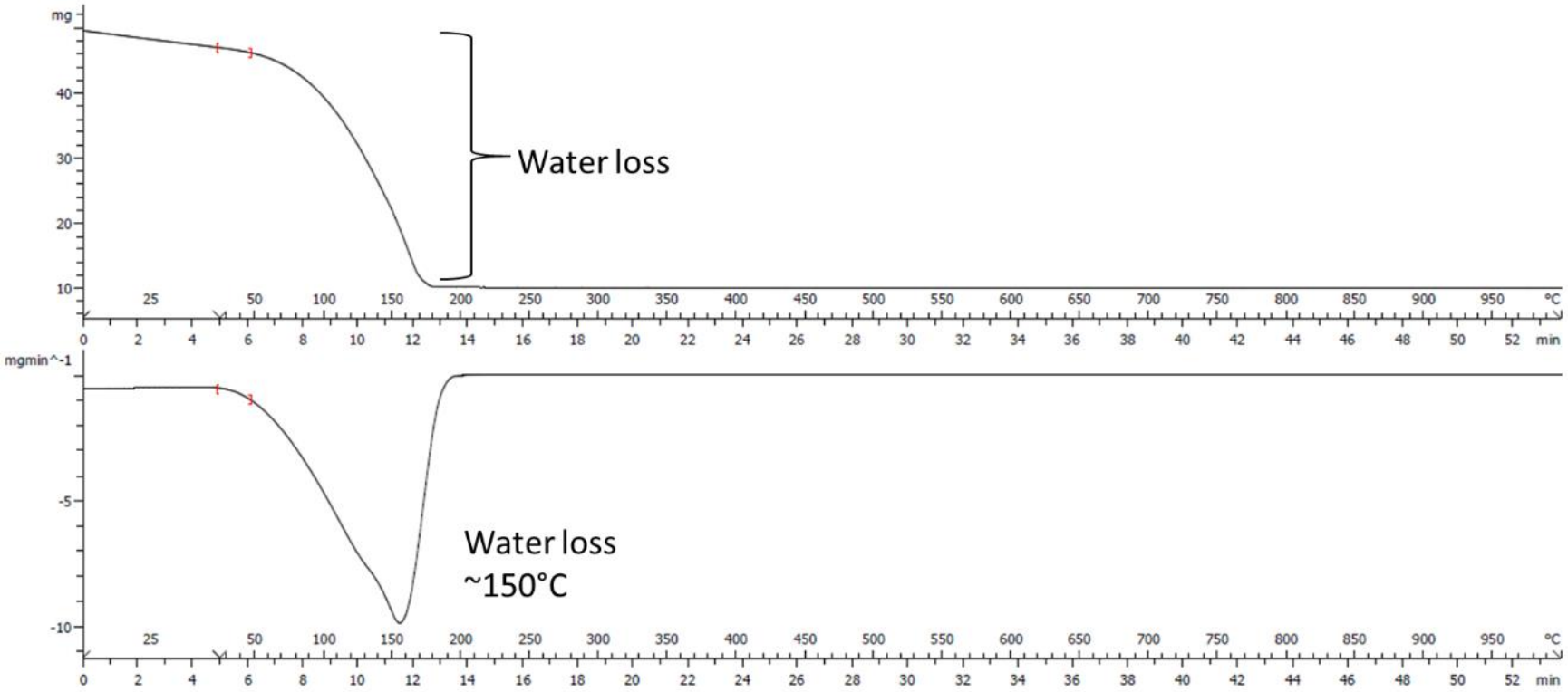

Reference Number	Volume (µL)	Starting Mass (mg)	Total Mass Loss (mg)	Residue mass (mg)
CEHR-1	50	49.380	39.647	9.729

Figure I-5. TGA thermogram of CEHR-1. The top panel is the weight loss versus temperature (and time) curve, while the bottom panel is the first derivative of the curve.

F. Zeta Potential

Design and Methods

A Malvern Zetasizer Nano ZS instrument was used to measure zeta potential at 25°C for CEHR-1. NCL protocol PCC-2 was followed (https://ncl.cancer.gov/resources/assay-cascade-protocols). The sample was diluted 10,000-fold in 10 mM NaCl. Sample pH was measured before loading into a pre-rinsed folded capillary cell. An applied voltage of 150 V was used. Traces in the figures represent the average of three measurements.

The instrument was validated by running an appropriate standard (Zeta Potential Transfer Standard, DTS0050, zeta potential value of -42 ± 4 mV at 25°C, Malvern Instruments) before all zeta potential measurements.

Results and Discussion

The zeta potential distribution for CEHR-1 is shown in Figure I-6. The sample, when dispersed in 10 mM NaCl and at native pH, exhibited a positive zeta potential. This is in contrast to the expected range for these materials and could indicate the presence of an unknown positively-charged coating on the nanoparticles. As the sample was compromised with time, i.e. solution began to evaporate and sample became a paste, further analysis was halted. TGA was not be performed to verify the presence of any coating.

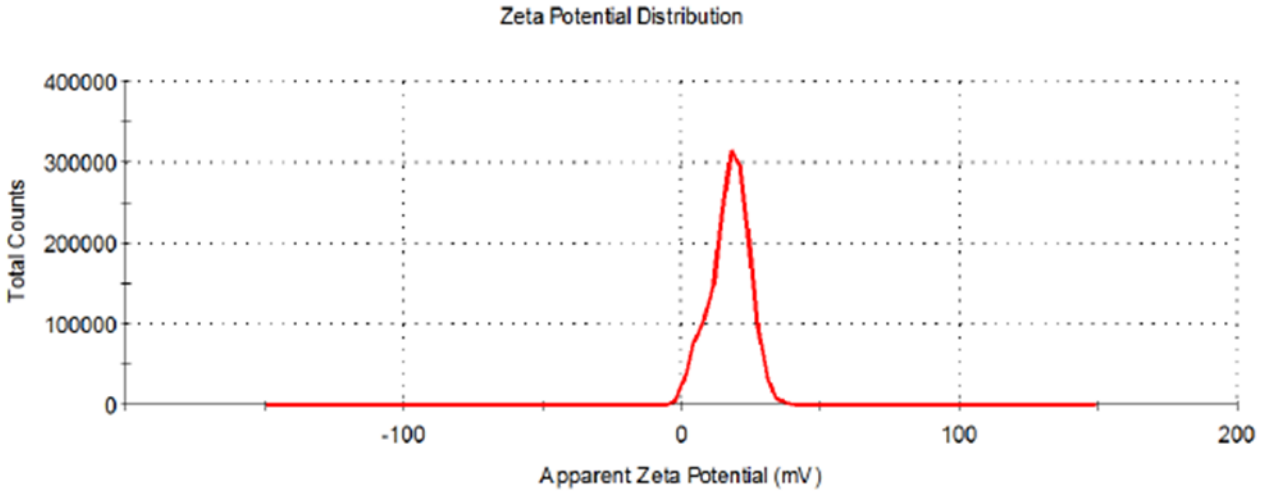

Figure I-6. The averaged zeta potential distributions for CEHR-1 diluted 10,000-fold in 10 mM NaCl.

Table I-5. Summary of the zeta potential for CEHR-1 diluted 10,000-fold in 10 mM NaCl.

Sample	pH	Zeta Potential
CEHR-1	6.9	18 ± 2 mV

II. Nanocrystalline Cellulose

II. Nanocrystalline Cellulose

A. Section Summary

Nanocrystalline cellulose (NCC) is a reference standard material from National Research Council Canada. Information on this material, including the previous characterization of this standard material can be found here: http://www.nrc-cnrc.gc.ca/eng/solutions/advisory/crm/certificates/cncs_1.html.
NCL performed several measurements on this material to verify the integrity of the sample, including NCC morphology by transmission electron microscopy (TEM), size/size distribution by dynamic light scattering (DLS), analysis of metal impurities by inductively-coupled plasma mass spectrometry (ICP-MS), concentration by thermogravimetric analysis (TGA), and measurement of zeta potential.

TEM analysis confirmed the presence of the crystalline needle-like structures (Figure II-1). Due to the crystal bundling, an extensive length and width analysis of the individual crystals was not performed. However, a limited analysis confirmed the sizes were consistent with theoretical values of 84 ± 14 nm and 5.6 ± 1.1 nm for the length and width, respectively. Furthermore, the NCL had previously characterized this material (supplied directly from NRCC) and obtained similar TEM measurements of 84 ± 35 nm and 5 ± 2 nm for the length and width, respectively. The DLS measured size was also in agreement with the theoretical value, with a Z-average hydrodynamic diameter of 87 nm (Table II-1). The needle-like shape of these particles were not amenable to separation by AF4 for size polydispersity analysis.

Several metal impurities were detected in CEHR-2 by ICP-MS: Al, Fe, Cu, Zn, Se, and Mo, (Figure II-3). Iron and copper were also noted as impurities in the reference material according to the above-noted website. The other four metals were not listed. Interestingly, Ni was not detected in the semi-quantitative analysis. Nickel and iron were the two highest concentration metal impurities noted on the reference site; all other metals were at least an order of magnitude lower in concentration. A more thorough, quantitative analysis of these minor impurities was not carried out.

TGA analysis showed a decomposition temperature of approximately 300°C (Figure II-4 and II-5). This was in close agreement with the reported temperature of 261°C. The differences between the two measurements were expected due to different heating rates. A second decomposition temperature at 480°C was also noted for NCC on the website linked above. However, this second loss was not detected in our analyses. TGA afforded an NCC concentration of 67 mg/mL, in complete agreement with the reported concentration of 67.9 ± 0.3 mg/g.

The measured zeta potential was negative (Table II-2). Although the value of the zeta potential (-27 mV) was different than the reported value (-46.7 mV), this was expected due to differences between the two measurement conditions. Zeta potential is sensitive to changes in pH and ionic strength, and the two measurements were made in different dispersing media. Importantly, the zeta potentials were both negative.

Overall, the measurements for CEHR-1 were in good agreement with the reported values.

B. Transmission Electron Microscopy

Design and Methods

Transmission electron microscopy (TEM) was conducted to assess the size and morphology of the nanomaterials. Stock solutions were diluted 10-fold with ultrapure water, and 2 µL was applied to a glow discharged carbon film grid (Electron Microscopy Sciences). The grid was washed three times with ultrapure water, blotted, treated with 2 µL 0.7% uranyl formate and allowed to air dry before imaging. Images were taken using a T-12 TEM (FEI) equipped with a LαB6 thermoionic gun at 80 V acceleration voltage.

Results and Discussion

Representative TEM images for CEHR-2 are shown in Figures II-1. The sample consisted of needle-like structures of varying lengths, with bundling. The bundling makes it more difficult to accurately measure the dimensions of the individual particles. This however, may just be an artifact of sample processing for TEM. NCL has worked with this material previously, acquired directly from NRCC, and obtained measurements of 84 ± 35 nm and 5 ± 2 nm for the length and width, respectively. These are in good agreement with the theoretical values. The reported measurements for this reference material are 84 ± 14 nm for length and 5.6 ± 1.1 nm for width.

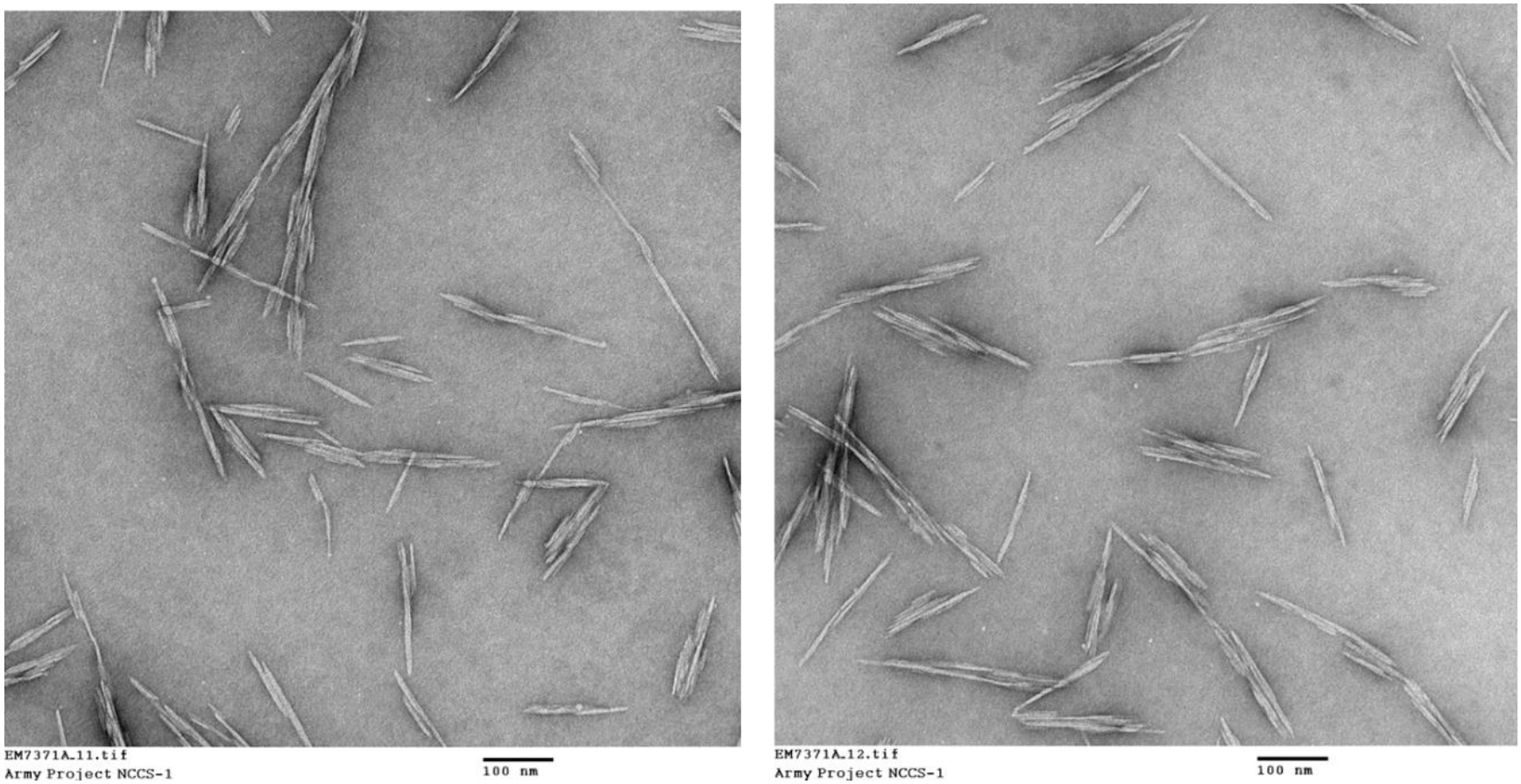

Figure II-1. Representative TEM images for CEHR-2.

C. Hydrodynamic Size/Size Distribution via Dynamic Light Scattering

Design and Methods

A Malvern Zetasizer Nano ZS instrument (Southborough, MA) with back scattering detector (173°) was used for measuring the hydrodynamic size (diameter) in batch mode. NIST-NCL joint protocol PCC-1 was followed (https://ncl.cancer.gov/resources/assay-cascade-protocols). The stock sample of CEHR-2 was measured at 25°C in a quartz microcuvette. Traces in the figures represent the average of at least twelve measurements.

Hydrodynamic diameters are reported as the intensity-weighted average and as the volume-weighted average over a particular range of size populations corresponding to the most prominent peak. The Int-Peak value is used as the hydrodynamic diameter of a particular species. The Vol-Peak and %Vol values are used to approximate relative amounts of various species in the formulation. Z-Avg values are generally used to assess batch-to-batch variability of a sample.

Results and Discussion

The intensity and volume distribution plots for CEHR-2 are provided in Figure II-2, and the size data is tabulated in Table II-1. The Z-average hydrodynamic diameter for CEHR-2 was 87 nm. This is in very good agreement with the reported Z-average of 80.1 ± 5.6 nm and matched very well with the TEM length of the crystals.

Note however, that DLS is not an ideal technique for size determination for this material due to its non-spherical nature. DLS assumes a spherical shape when calculating average sizes. TEM is the better method for size analysis of this type of material. DLS can be used for qualitative assessments, such as batch-to-batch comparisons.

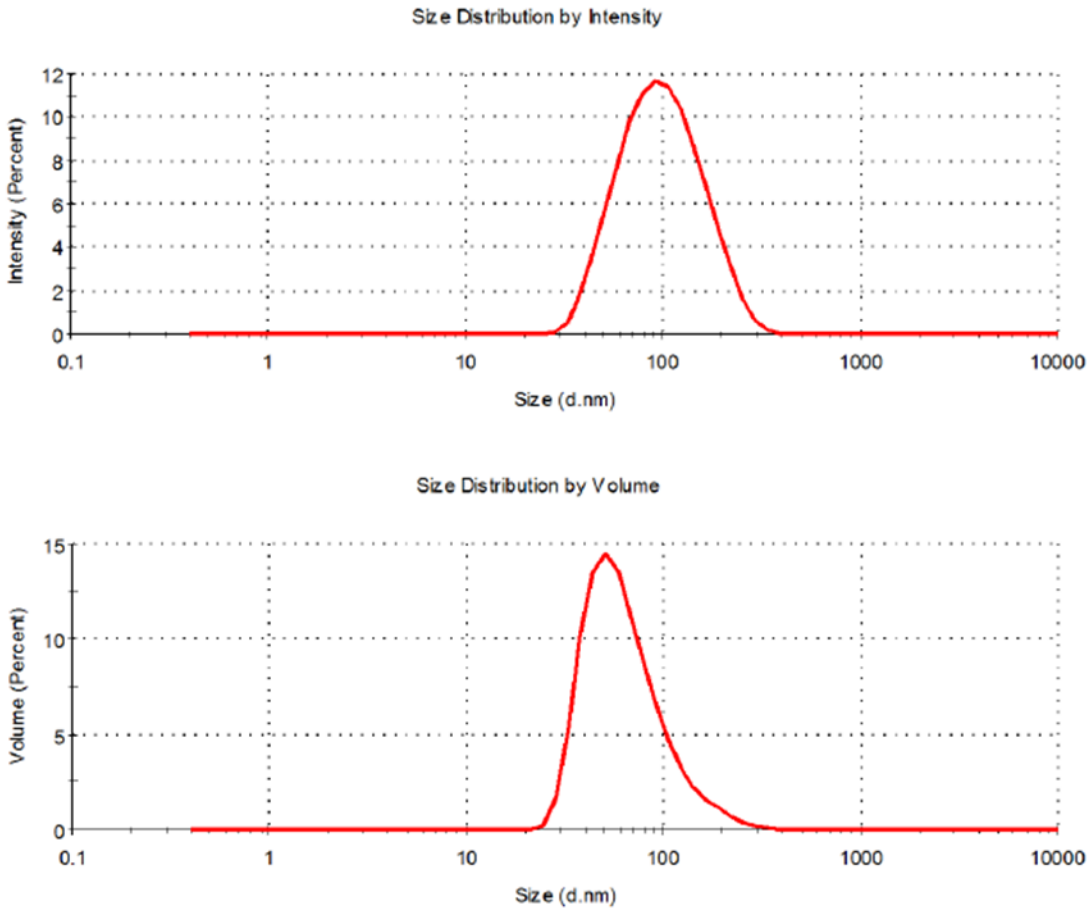

Figure II-2. The averaged intensity and volume distribution plots for stock CEHR-2.

Table II-1. Summary of the hydrodynamic size for stock CEHR-2.

Z-Avg, nm	PdI	Int-Peak, nm	% Int	Vol-Peak, nm	% Vol
87 ± 1	0.18 ± 0.01	107 ± 2	100 ± 0	68 ± 2	100 ± 0

Note: Results are the average of at least 12 measurements. Z-Avg is the intensity-weighted average. PdI is the polydispersity index. Int-Peak is the intensity-weighted average over the primary peak. % Int is the percentage of the intensity spectra occupied by the primary peak. Vol-Peak is the volume-weighted average over the primary peak. % Vol is the percentage of the volume spectra occupied by the primary peak.

D. Inductively Coupled Plasma Mass Spectrometry

Design and Methods

A semi-quantitative analysis was performed on CEHR-2 to estimate the amounts of any trace metals in the sample. An Agilent ICP-MS 7500CX equipped with a micro-mist nebulizer, standard sample introduction system, and integrated auto-sampler, operated in "no gas" mode in Agilent's proprietary ORS (Octopole Reaction System) was used. Tuning of the instrument was performed daily prior to sample testing.

A 25 µL aliquot of the nanocellulose stock solution was digested using 200 µL concentrated nitric acid. After 10 minutes, this digested sample was vortexed for 10 seconds and then diluted with water to target a 30 mL dilution. An internal standard, indium, was used to track the signal response of the ICP-MS. The internal standard was diluted to approximately 50 ppb and was mixed with the sample using a sample T. Only metals with counts two times greater than the background were denoted.

Results and Discussion

The results from the semi-quantitative analysis of CEHR-2, are shown in Figure II-3. There were six metal impurities detected in the sample: Al, Fe, Cu, Zn, Se, and Mo. Of these, only iron and copper were listed as impurities on the reference site. Notably absent was detection of Ni; Ni was the most abundant metal impurity noted for NCC according to the specifications on the website. There were several other metal impurities noted on the reference site that were noted detected here, but were all at least an order of magnitude lower in concentration.

This was only an analysis to detect potential metal impurities. For an accurate determination of concentrations, quantitative analysis compared to a standard would be required.

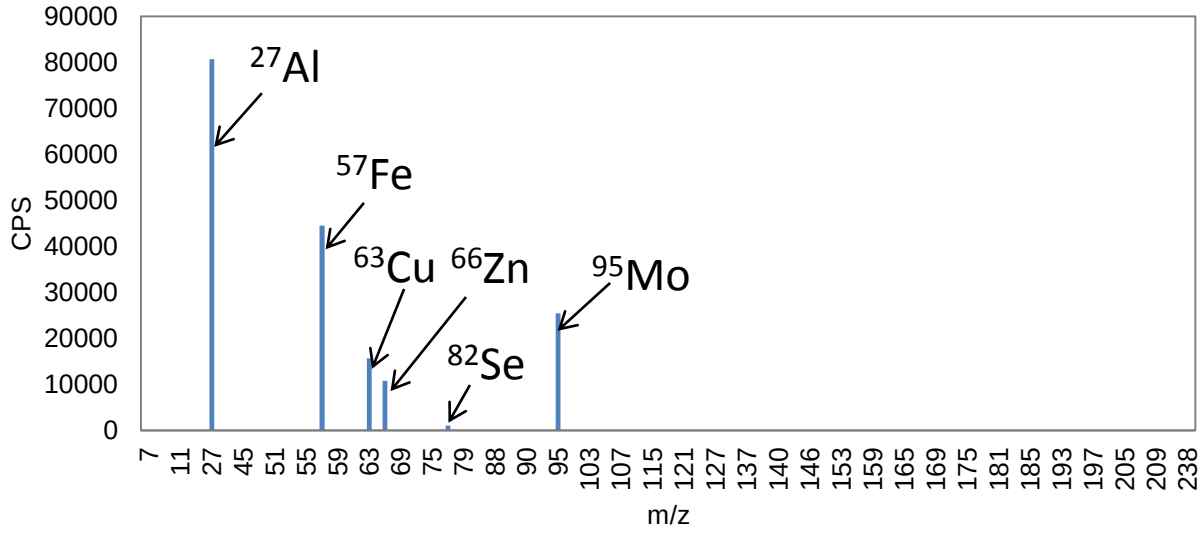

Figure II-3. Semi-quantitative analysis for CEHR-2. Plot of CPS vs m/z for CEHR-2. Sample was analyzed on 7 September 2016. Note ^{12}C, ^{23}Na, ^{29}Si, ^{31}P, ^{34}S, ^{35}Cl, ^{39}K were removed to better visualize the smaller peaks. The internal standard peak for ^{115}In was also omitted.

E. Thermogravimetric Analysis

Design and Methods

Samples were analyzed via thermogravimetric analysis (TGA) to determine the concentration of the nanocellulose by measuring the residual material remaining after evaporation of water and oxidation. NCL received samples in solution and in powder form. Both samples were measured by TGA.

For the liquid sample, 50 µL was transferred to an aluminum oxide crucible (150 µL crucible with lid, Mettler Toledo) for TGA measurement (TGA/DSC 1, Mettler Toledo). The powder sample was run as is. Both samples were subjected to the same TGA heating gradient. Samples were held at 25˚C for 5 min, then ramped to 1000˚C at a heating rate of 20˚C/min under nitrogen gas. The empty crucible was subjected to the TGA method prior to loading the sample to serve as a background correction.

Results and Discussion

The TGA thermograms for both the liquid and powder forms of CEHR-2 are provided in Figures II-4 and II-5, respectively. Figure II-4 is dominated by the loss of water from the sample, but a second loss was seen at approximately 290°C corresponding to the decomposition of NCC. The thermogram for the dry powder had minor water loss and an NCC decomposition temperature 310°C. Residual mass was observed for both samples at the end of the TGA run, suggesting the nanocellulose was not completely combusted at 1000˚C. Assuming all of the weight loss at approximately 300°C and all the residual mass were attributed to NCC, this afforded an NCC concentration of 67 mg/mL (Figure II-4).

These results are in close agreement with the referenced data. Two decomposition temperatures are indicated for NCC, 261°C and 480°C, and a 50 mg/g residual mass is noted following the TGA run. The 261°C NCC decomposition temperature is lower than observed here; however, this temperature can shift with changes in the TGA heating rates. The higher 480°C decomposition temperature was not observed in our analyses. However, it is unclear from the reference site how predominant this second peak is. The reported concentration is 67.9 ± 0.3 mg/g, in complete agreement with the measured results.

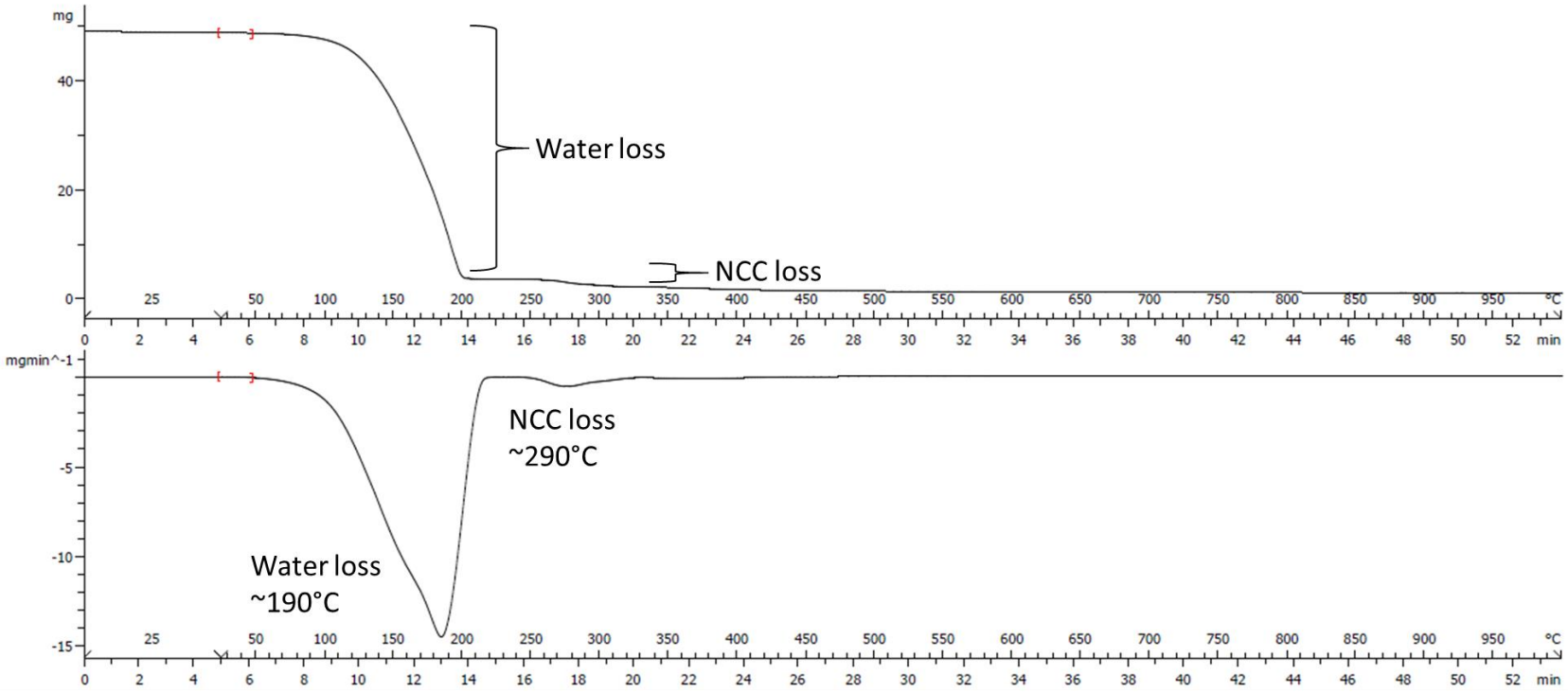

Reference Number (form)	Volume (µL)	Starting Mass (mg)	Water Loss mass (mg)	NCC Loss Mass (mg)	Residual Mass (mg)	Residual Mass per Dry Mass (mg/g)
CEHR-2 (liquid)	50	48.8128	45.4813	2.5075	0.8239	247

Figure II-4. TGA thermogram of CEHR-2, liquid form. The top panel is the weight loss versus temperature (and time) curve. The bottom panel is the first derivative of that curve.

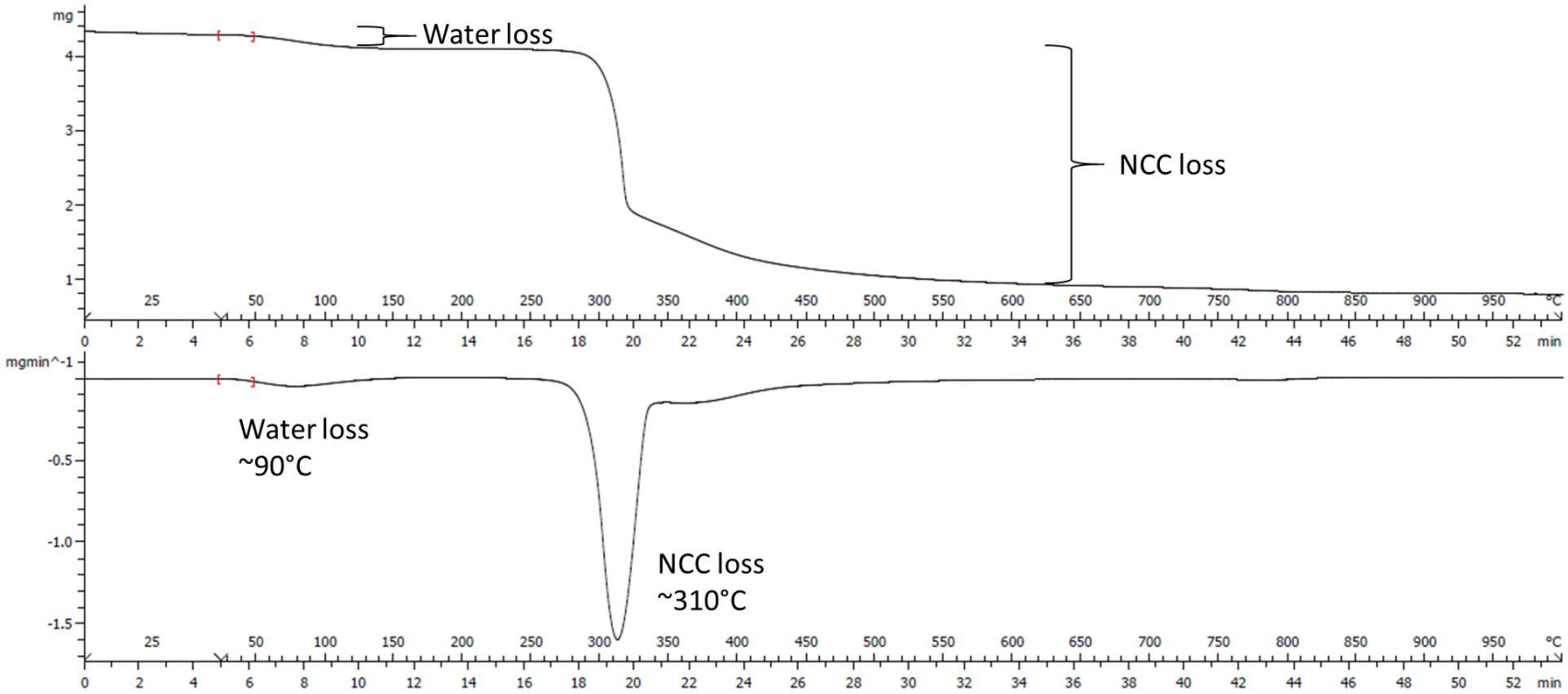

Reference Number (form)	Starting Mass (mg)	Water Loss mass (mg)	NCC Loss Mass (mg)	Residue mass (mg)	Residual Mass per Dry Mass (mg/g)
CEHR-2 (solid)	4.3212	0.2441	3.2928	0.7814	192

Figure II-5. TGA thermogram of CEHR-2, solid form. The top panel is the weight loss versus temperature (and time) curve. The bottom panel is the first derivative of that curve.

F. Zeta Potential

Design and Methods

A Malvern Zetasizer Nano ZS instrument was used to measure zeta potential at 25°C. NCL protocol PCC-2 was followed (https://ncl.cancer.gov/resources/assay-cascade-protocols). CEHR-2 was initially diluted 250-fold in water and then further diluted 2-fold in 10 mM NaCl (500-fold final dilution in 5 mM NaCl). Sample pH was measured before loading into a pre-rinsed folded capillary cell. An applied voltage of 150 V was used. Traces in the figures represent the average of four measurements.

The instrument was validated by running an appropriate standard (Zeta Potential Transfer Standard, DTS0050, zeta potential value of -42 ± 4 mV at 25˚C, Malvern Instruments) before all zeta potential measurements.

Results and Discussion

The zeta potential distribution for CEHR-2 is shown in Figure II-6. The sample exhibited a negative zeta potential, -27 mV, under the given measurement conditions. The reported zeta potential value is -46.7 mV, as measured in water. Zeta potential values will vary to some degree with pH and ionic strength of the dispersing medium. Therefore, the difference between our results and the theoretical zeta potential can be explained by a difference in measurement conditions (i.e., 5 mM NaCl versus water). Importantly, both measurements showed a negative zeta potential for the material.

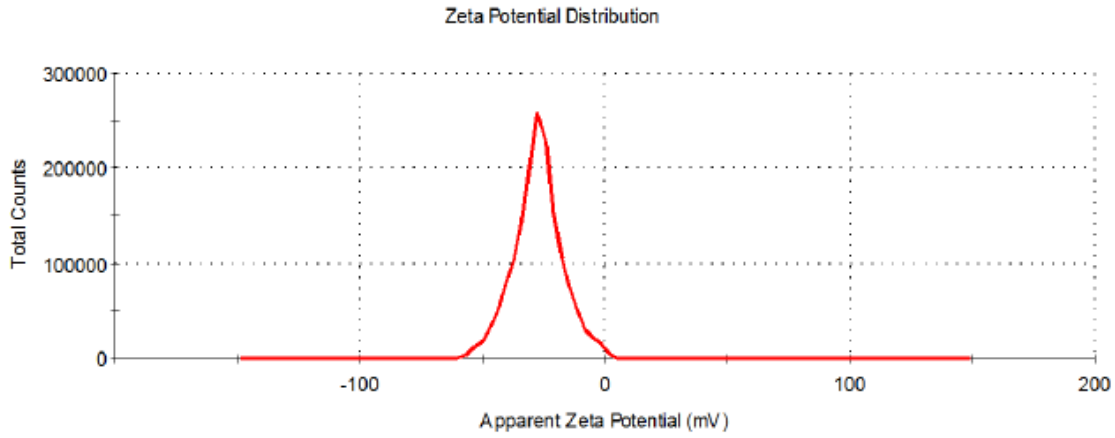

Figure II-6. The averaged zeta potential distributions for CEHR-2 diluted 500-fold in 10 mM NaCl.

Table II-2. Summary of the zeta potential for CEHR-2 diluted 500-fold in 10 mM NaCl.

Sample	pH	Zeta Potential
CEHR-2	6.9	-27 ± 0 mV

III. Silica

III. Silica

A. Section Summary

Five silica nanospheres with nominal sizes of 20, 50, 100, 200, and 400 nm (CEHR-8 to CEHR-12, respectively) were characterized for sterility and relevant physicochemical parameters. This included size (DLS and TEM) and polydispersity (AF4-DLS) measurements, zeta potential, and detection and quantification of possible surface coatings on the nanoparticles (TGA).

Sterility screening of the silica nanoparticles showed that CEHR-8, CEHR-10, CEHR-11, and CEHR-12 were free of bacterial contamination. CEHR-9 appeared to show low grade contamination with mold, and therefore is not recommended for biological testing (Table III-1). Endotoxin levels were quantitated by the Limulus Amebocyte Lysate (LAL) assay. Analysis revealed that CEHR-9, CEHR-10, CEHR-11, and CEHR-12 had endotoxin values ≤0.05 EU/mg. CEHR-8 had an average endotoxin value of 3.1 EU/mg (Table III-2). The potential implication of this level of endotoxin is unknown; the effects would depend on the test being conducted and the dose of the material being used. Considerations of endotoxin impact on environmental studies involving engineered nanomaterials are reviewed in detail elsewhere (Petersen EJ, et al., Environ Sci Technol. 2014;48(8):4226-46).

Size analysis of the five silica nanomaterials was conducted by dynamic light scattering (DLS) and transmission electron microscopy (TEM). Both methods revealed sizes generally consistent with those reported by the manufacturer. The TEM measured diameters for CEHR-8 to CEHR-12 were 23, 48, 103, 188, and 410 nm, respectively (Table III-3). These are in good agreement with the manufactured-reported TEM sizes. The DLS hydrodynamic diameters for CEHR-8 to CEHR-12 were 29, 58, 135, 229, and 448 nm, respectively (Table III-4). The DLS results are expected to deviate somewhat (i.e., be larger) from the TEM sizes, as TEM measures the electron dense diameter, while DLS provides a measure of the hydrodynamic size. The difference between the two measurements was within an expected range.

Asymmetric-flow field flow fractionation (AF4) was used to examine the size polydispersity of the silica nanoparticles. Peaks ranging from approximately 25-37 nm for CEHR-8 (Figure III-11), 96-129 nm for CEHR-10 (Figure III-12), 183-235 nm for CEHR-11 (Figure III-13), and from 416-465 nm for CEHR-12 (Figure III-14) were observed. In general, the AF4-DLS results coincided with the batch-mode DLS results. The only exception was the presence of a second peak in CEHR-8 which was not detected by batch-mode DLS. Note, CEHR-9 was not analyzed by AF4 due to the possible mold contamination in the sample.

The total mass silica concentrations were determined by thermogravimetric analysis (TGA). Silica concentrations could not be measured by inductively coupled plasma-mass spectrometry (ICP-MS) due to our instrument setup (glass nebulizer). All five formulations had a reported concentration of 10 mg/mL. CEHR-12 was very close to the reported concentration, with 10.2 mg/mL. CEHR-9 to CEHR-11 were approximately 10-25% lower than the theoretical concentrations, with concentrations ranging 7.5-9.1 mg/mL (Table III-12). CEHR-8 had the lowest concentration, 4.1 mg/mL, and was less than half of the reported-concentration.

The presence of a coating was also assessed by TGA. All five formulations showed a weight loss which could be indicative of a coating on the nanoparticle. CEHR-8 and CEHR-9 showed a definitive peak in the second derivative curve at 225-250°C, while the remaining formulations showed only a gradual weight loss. The percent mass ratio of possible coatings on the silica nanoparticles are summarized in Table III-13. CEHR-8 and CEHR-9 had 13% and 19%, while

the other three materials had 3-6% possible coating. Note, the identity of the coating could not be determined by TGA and was not reported by the vendor. The weight loss events could also stem from other excipients in the formulation. TGA cannot differentiate between surface coatings and other added excipients. The surface charge of the nanoparticles was assessed by measuring the zeta potential. All five nanoparticles had negative zeta potentials (Tables III-14). This is in line with the anticipated range for either uncoated silica nanoparticles or those with a negatively-charged coating.

B. Sterility

Design and Methods

Sterility, i.e. bacterial contamination, of the five silica nanospheres was assessed using NCL protocol STE-2.2 (https://ncl.cancer.gov/resources/assay-cascade-protocols). In brief, samples were plated onto LB agar plates at several dilutions (10-, 100-, and 1000-fold) and allowed to incubate at 37°C for 72 hours. The plates were then visually inspected for colony formation.

Results & Conclusions

CEHR-8, CEHR-10, CEHR-11, and CEHR-12 showed no visible colony formation after 72 hrs. The CEHR-9 test sample showed approximately 10 CFU/mg. However, upon repeating this assay, a second aliquot of CEHR-9 showed no contamination. CEHR-9 may have low grade contamination with mold, and therefore, it is recommended that CEHR-9 not be used in biological assays. A summary of the sterility findings from the silica nanomaterials is provided in the table below.

Table III-1. Summary of the sterility testing results for the silica nanospheres.

Reference Number	Nanoparticle Description	Nominal size reported by manufacturer	Sterility (agar plate)
CEHR-8	SiO_2 nanospheres 10 mg/mL	20 ± 4 nm	Negative
CEHR-9	SiO_2 nanospheres 10 mg/mL	50 ± 4 nm	**Low-grade mold contamination**
CEHR-10	SiO_2 nanospheres 10 mg/mL	100 ± 4 nm	Negative
CEHR-11	SiO_2 nanospheres 10 mg/mL	200 ± 7nm	Negative
CEHR-12	SiO_2 nanospheres 10 mg/mL	400 ± 40 nm	Negative

C. Endotoxin

Design and Methods

The objective of this experiment was to evaluate potential endotoxin contamination in the five silica nanoparticles. NCL's protocol for the kinetic turbidity Limulus Amebocyte Lysate (LAL) assay was used (STE-1.2; https://ncl.cancer.gov/resources/assay-cascade-protocols). All samples were initially diluted to 1 mg/mL theoretical concentration and tested at 1:5, 1:50, and 1:500 dilutions in water.

Results and Discussion

Four of the five silica nanoparticles, CEHR-9 through CEHR-12, had very low or undetectable levels of endotoxin, ≤ 0.05 EU/mg. CEHR-8 had endotoxin levels of 3.14 EU/mg. The impact, i.e. potential biological consequences, of endotoxin in this formulation will be dependent on the test being conducted and the dose of the formulation used. The potential impact of endotoxin on environmental studies involving engineered nanomaterials are reviewed here: Petersen EJ, et al., Environ Sci Technol. 2014;48(8):4226-46.

Table III-2. Endotoxin levels detected by the LAL assay. Results are shown as endotoxin units (EU) per mg of nanoparticle (vendor-supplied concentration).

Reference Number	Nanoparticle Description	Nominal size reported by manufacturer	Endotoxin Turbidity LAL
CEHR-8	SiO_2 nanospheres 10 mg/mL	20 ± 4 nm	**3.1 EU/mg**
CEHR-9	SiO_2 nanospheres 10 mg/mL	50 ± 4 nm	<0.005 EU/mg
CEHR-10	SiO_2 nanospheres 10 mg/mL	100 ± 4 nm	0.05 EU/mg
CEHR-11	SiO_2 nanospheres 10 mg/mL	200 ± 7nm	<0.005 EU/mg
CEHR-12	SiO_2 nanospheres 10 mg/mL	400 ± 40 nm	0.009 EU/mg

D. Transmission Electron Microscopy

Design and Methods

Transmission electron microscopy (TEM) was conducted to assess the size and morphology of the nanomaterials. Stock solutions (2 µL) were applied to a glow discharged carbon film grid (Electron Microscopy Sciences). The grid was washed three times with ultrapure water, blotted, and allowed to air dry before imaging. Images were taken using a T-12 TEM (FEI) equipped with a LαB6 thermoionic gun at 80 V acceleration voltage.

Particle size analysis was performed using ImageJ (https://imagej.nih.gov/ij/). Only particles that were individually dispersed were included in the sizing analysis.

Results and Discussion

Representative TEM images and size histograms for each of the silica nanoparticles are shown in Figures III-1 to III-5 for CEHR-8, -9, -10, -11, and -12, respectively. All samples appeared to be monodisperse and the measured diameter via TEM was in good agreement with the expected diameter. Table III-3 summarizes our measured sizes in comparison to the nominal TEM sizes reported by the manufacturer.

Table III-3. Comparison of vendor-reported TEM size and NCL-measured TEM size.

Reference Number	Nanoparticle Description	Nominal size reported by manufacturer	TEM Measured Size
CEHR-8	SiO_2 nanospheres 10 mg/mL	20 ± 4 nm	23 ± 4 nm
CEHR-9	SiO_2 nanospheres 10 mg/mL	50 ± 4 nm	48 ± 5 nm
CEHR-10	SiO_2 nanospheres 10 mg/mL	100 ± 4 nm	103 ± 7 nm
CEHR-11	SiO_2 nanospheres 10 mg/mL	200 ± 7nm	188 ± 24 nm
CEHR-12	SiO_2 nanospheres 10 mg/mL	400 ± 40 nm	410 ± 29 nm

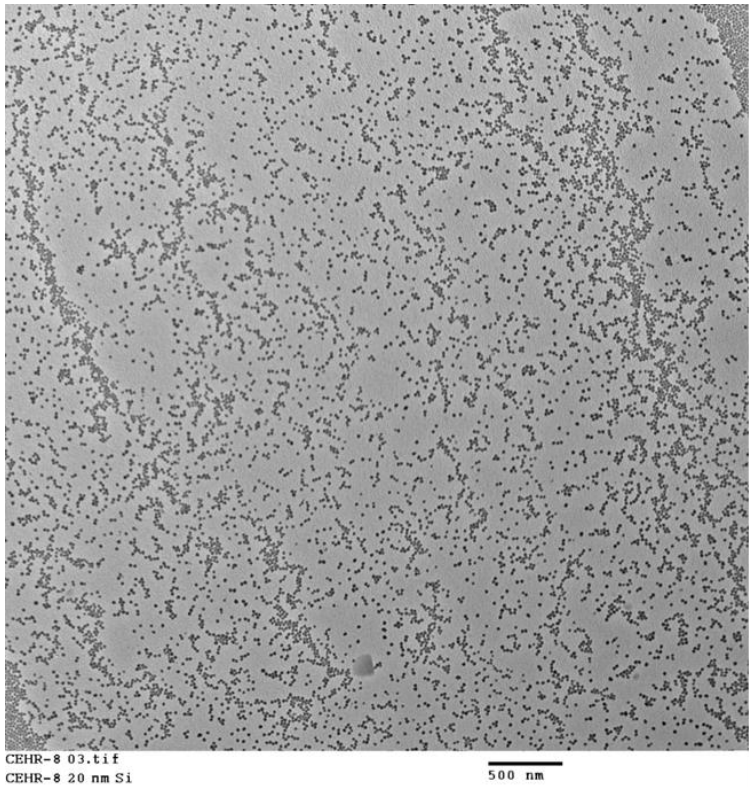

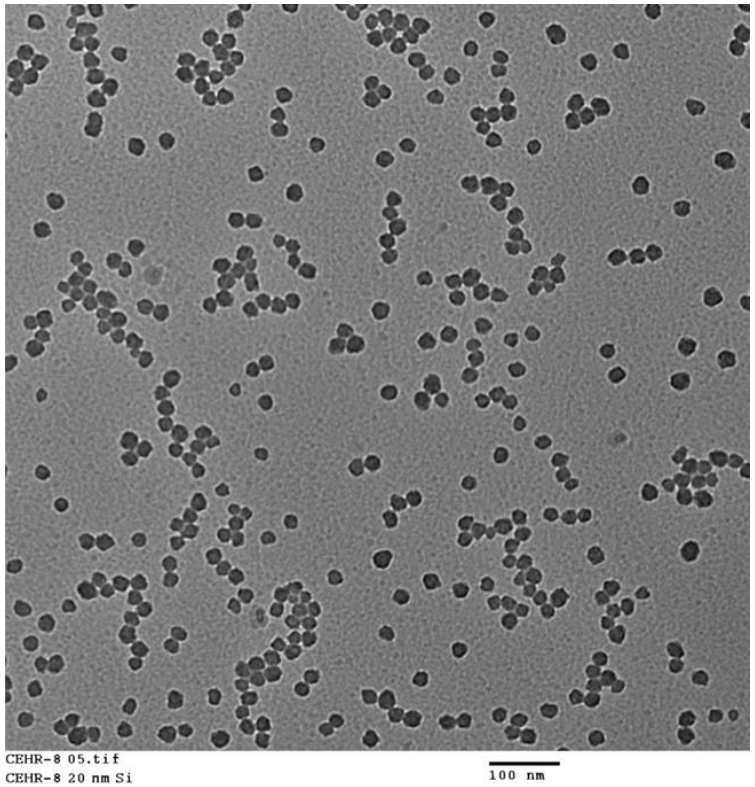

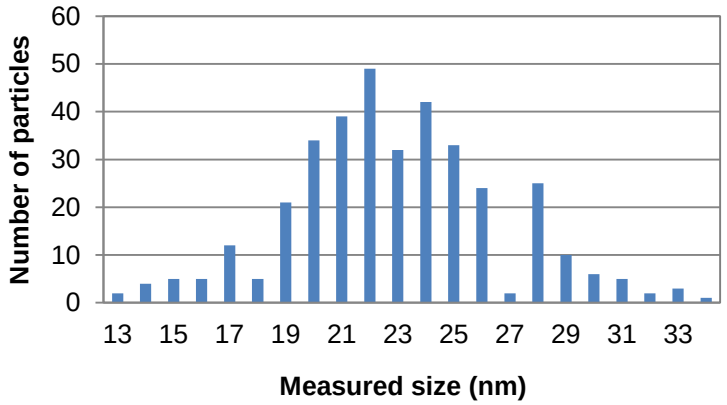

Figure III-1. Representative TEM Images of CEHR-8. Two representative images are shown for CEHR-8, showing the range of average diameters spanning 23 ± 4 nm (n = 361).

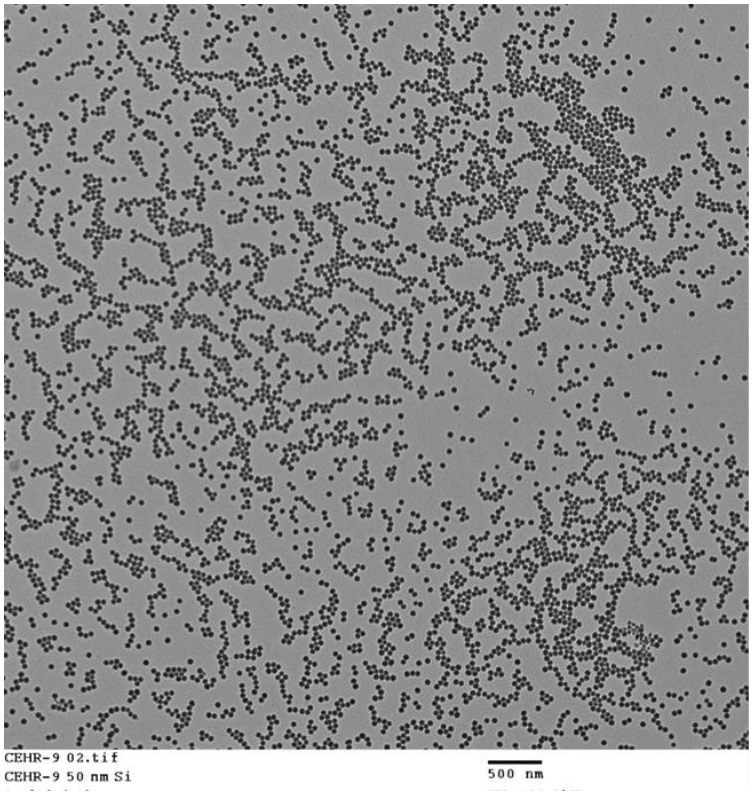

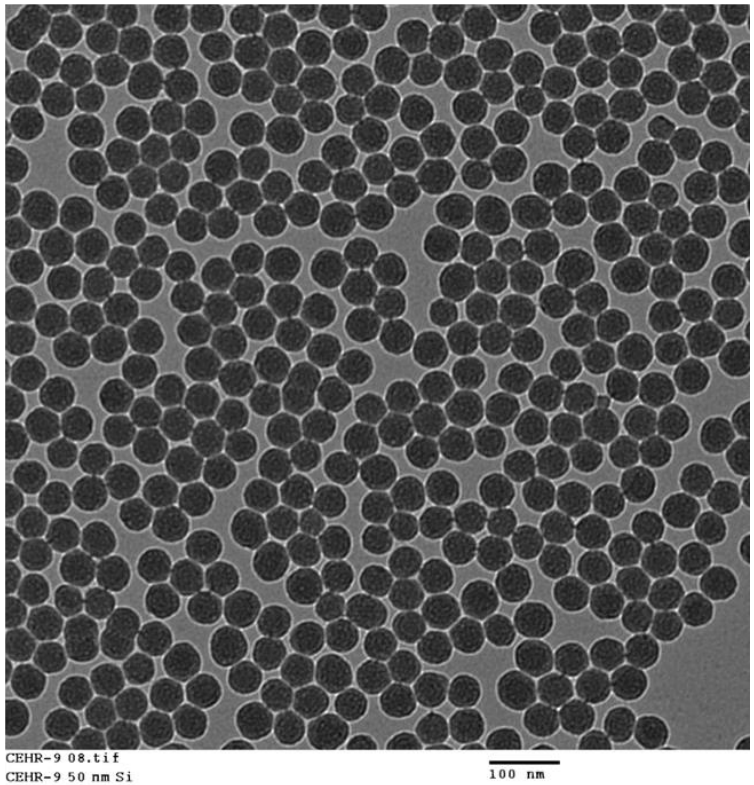

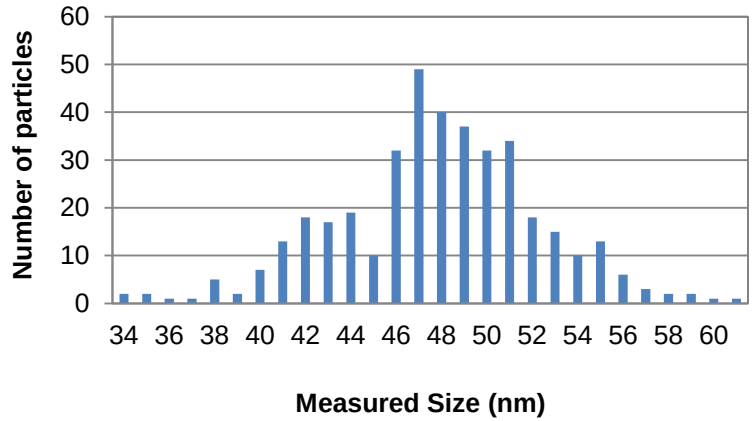

Figure III-2. Representative TEM Images of CEHR-9. Two representative images are shown for CEHR-9, showing the range of average diameters spanning 48 ± 5 nm (n = 392).

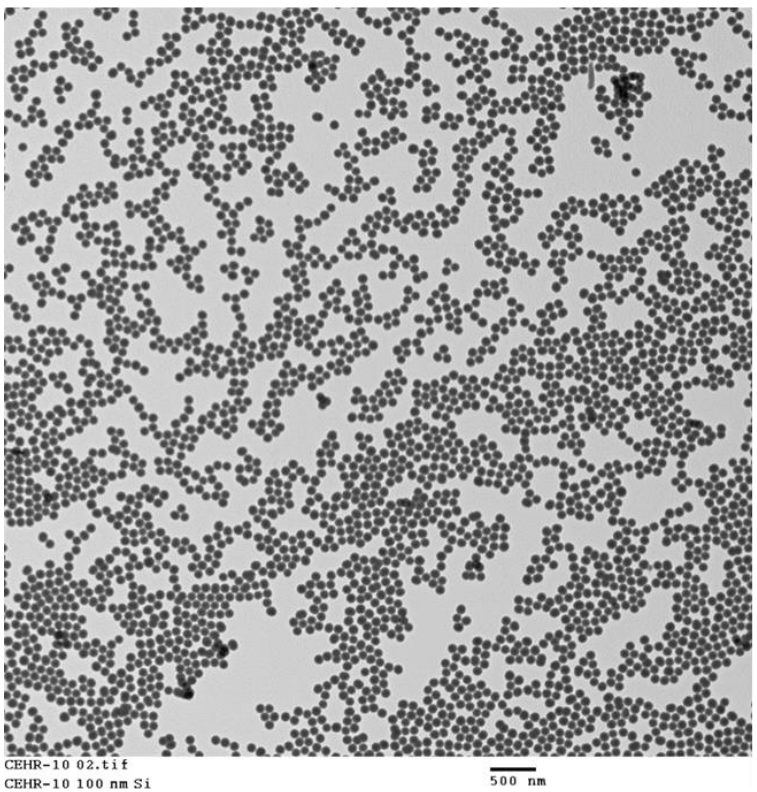

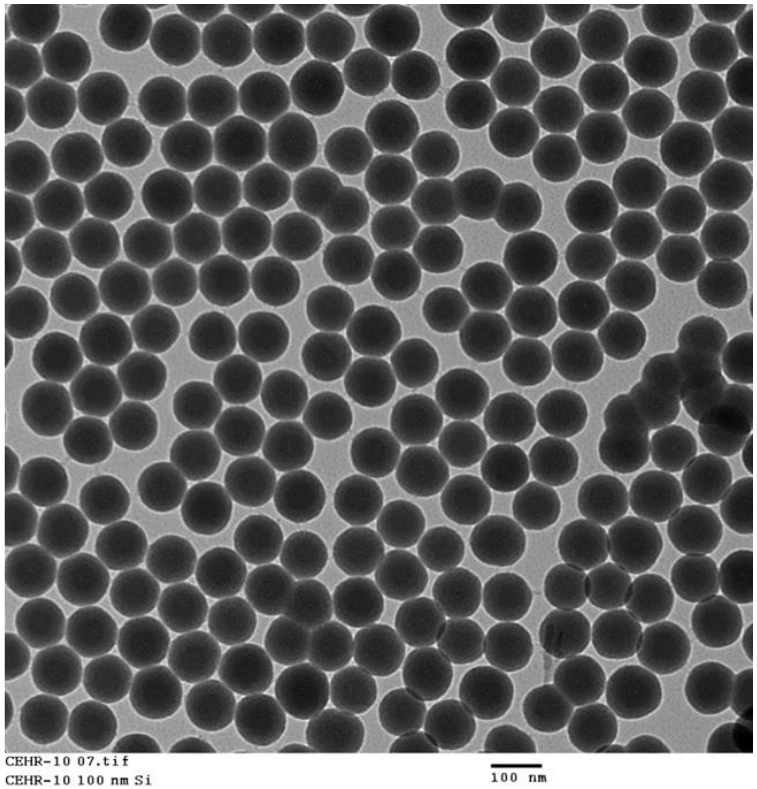

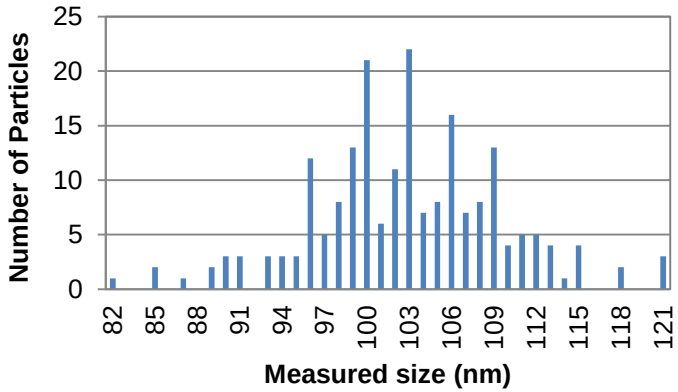

Figure III-3. Representative TEM Images of CEHR-10. Two representative images are shown for CEHR-10, showing the range of average diameters spanning 103 ± 7 nm (n = 206).

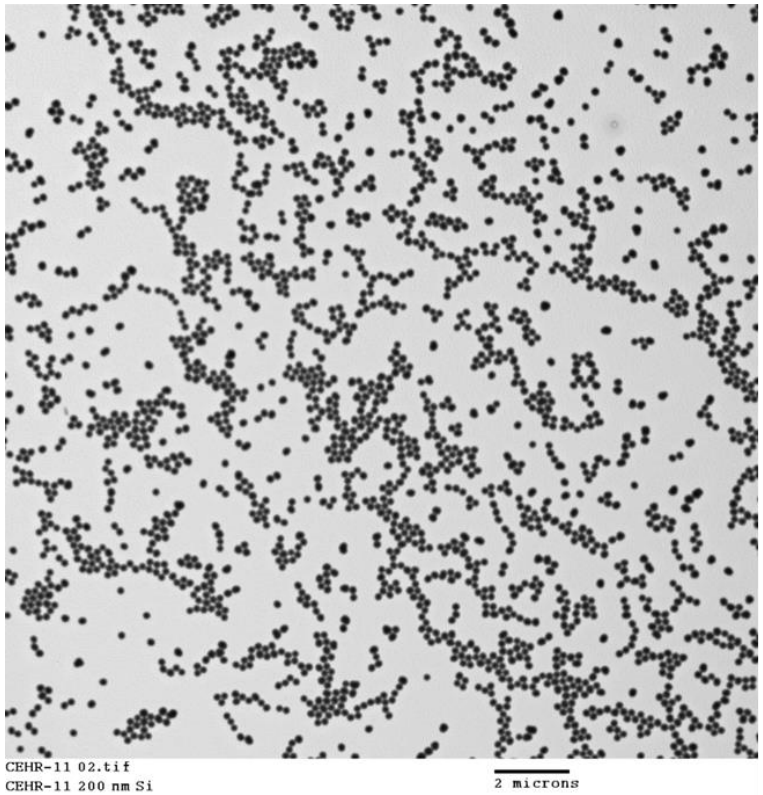

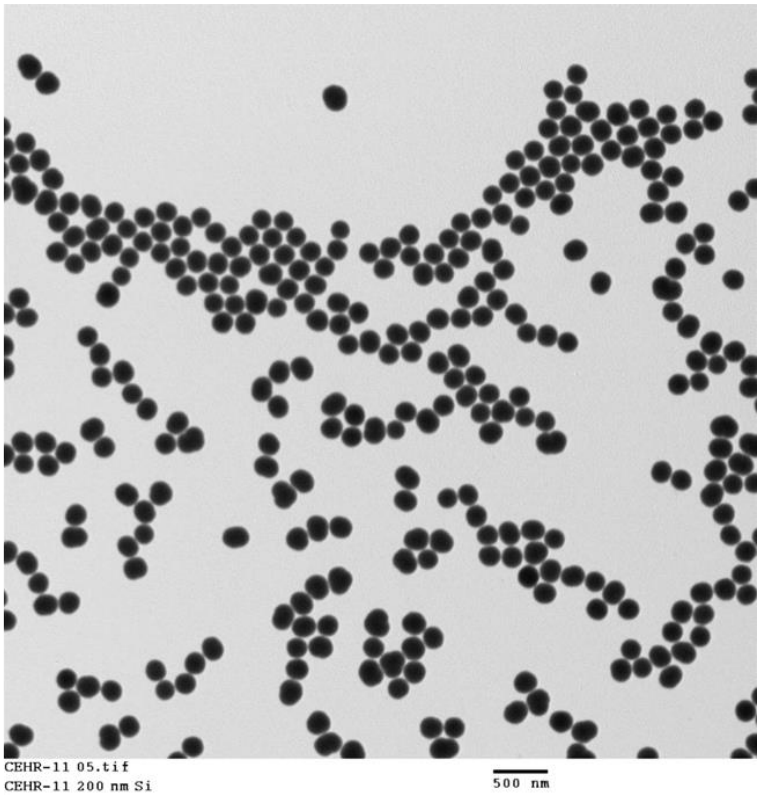

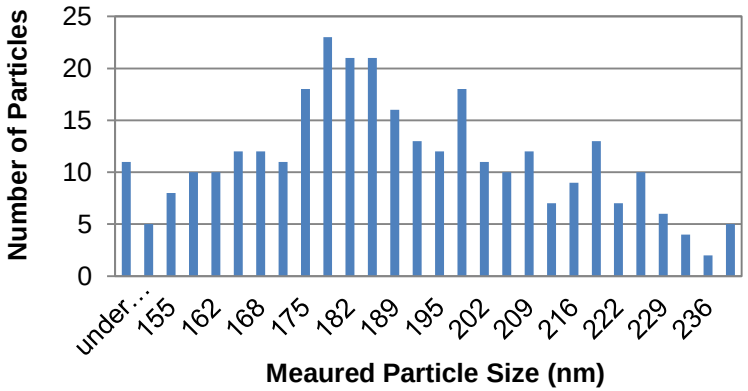

Figure III-4. Representative TEM Images of CEHR-11. Two representative images are shown for CEHR-10, showing the range of average diameters spanning 190 ± 24 nm (n = 317).

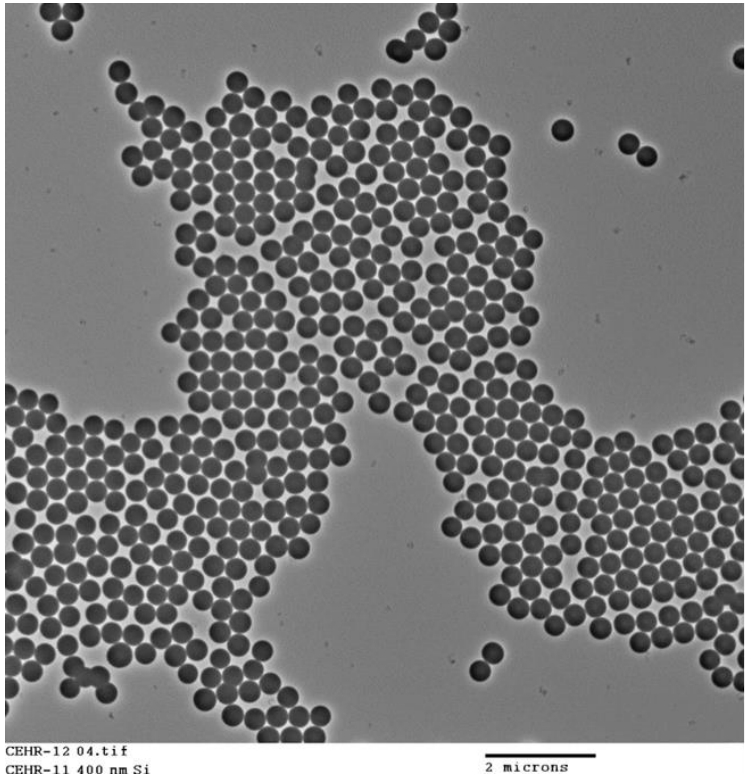

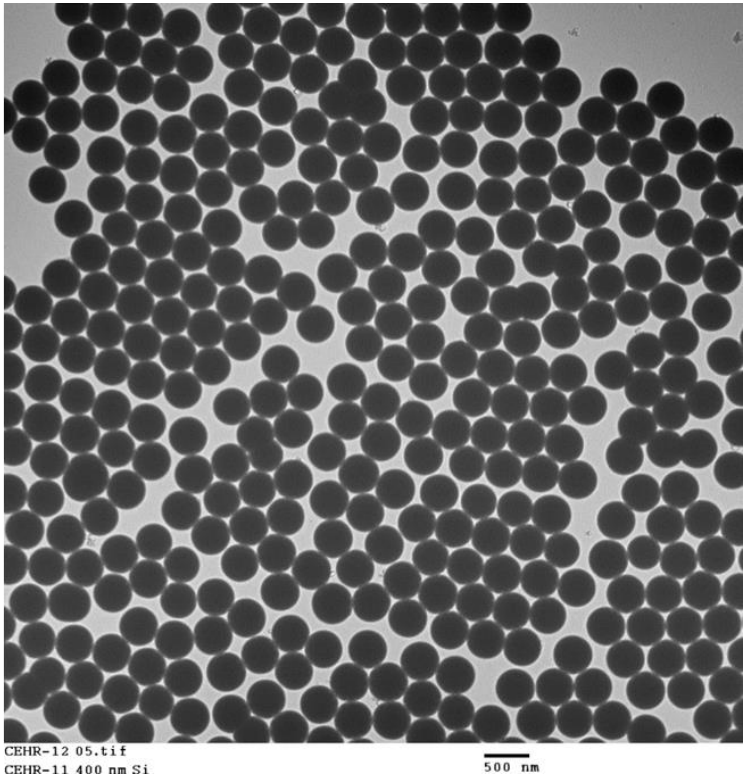

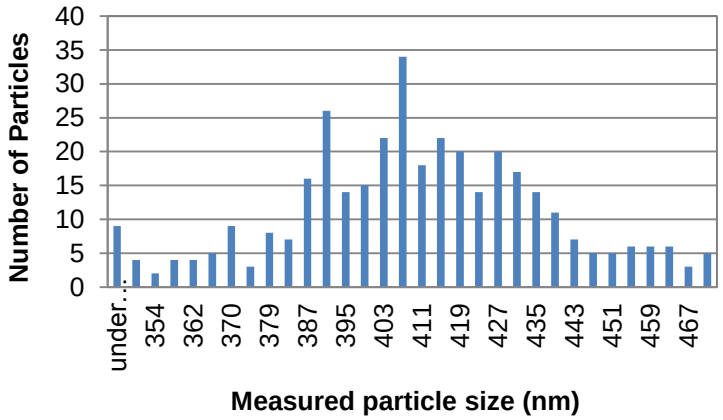

Figure III-5. Representative TEM Images of CEHR-12. Two representative images are shown for CEHR-12, showing the range of average diameters spanning 410 ± 29 nm (n = 361).

E. Hydrodynamic Size/Size Distribution via Dynamic Light Scattering

Design and Methods

A Malvern Zetasizer Nano ZS instrument (Southborough, MA) with back scattering detector (173°) was used for measuring the hydrodynamic size (diameter) in batch mode. NIST-NCL joint protocol PCC-1 was followed (https://ncl.cancer.gov/resources/assay-cascade-protocols). Stock samples of CEHR-8 through CEHR-12 were diluted 10-, 100-, or 1,000-fold in water. At least two dilutions were measured for each sample. Measurements were made at 25°C in a quartz microcuvette. Traces in the figures represent the average of at least twelve measurements.

Hydrodynamic diameters are reported as the intensity-weighted average and as the volume-weighted average over a particular range of size populations corresponding to the most prominent peak. The Int-Peak value is used as the hydrodynamic diameter of a particular species. The Vol-Peak and %Vol values are used to approximate relative amounts of various species in the formulation. Z-Avg values are generally used to assess batch-to-batch variability of a sample.

Results and Discussion

The silica nanosphere samples from nanoComposix were diluted in water and measured by DLS for hydrodynamic diameter. The intensity and volume distribution plots are provided in Figures III-6 to III-10. A summary of the sizes is provided in the table below (Table III-4), and more detailed size distribution data is summarized in the corresponding tables below each figure. In general, the DLS measured sizes were in close agreement with the theoretical sizes provided by the manufacturer. The manufacturer sizes are derived from TEM, and thus are expected to deviate somewhat from the DLS measured sizes. TEM measures the electron dense diameters, while DLS provides a measure of the hydrodynamic size.

Table III-4. Comparison of TEM and DLS sizes.

Reference Number	Nominal size reported by manufacturer	TEM Measured Size	DLS Measured Size (Int-Peak)
CEHR-8	20 ± 4 nm	23 ± 4 nm	29 ± 0 nm
CEHR-9	50 ± 4 nm	48 ± 5 nm	58 ± 0 nm
CEHR-10	100 ± 4 nm	103 ± 7 nm	135 ± 1 nm
CEHR-11	200 ± 7nm	188 ± 24 nm	229 ± 2 nm
CEHR-12	400 ± 40 nm	410 ± 29 nm	448 ± 6 nm

CEHR-8 (20 nm theoretical by TEM) had an Int-Peak diameter of 30 nm. The formulation was monodisperse and showed no significant change in size upon dilution. CEHR-9 had a DLS diameter of approximately 60 nm, again slightly larger than the TEM reported diameter of 50 nm. This sample was also monodisperse and showed no change in size upon dilution. A similar trend was seen for CEHR-10 and CEHR-11. The 100 nm (TEM) CEHR-10 silica nanoparticle had a DLS diameter of approximately 130 nm, and the 200 nm CEHR-11 particle had a 225 nm DLS diameter. Both samples were monodisperse and did not change significantly upon dilution.

CEHR-12 had a reported TEM diameter of 400 nm. When measured at 100-fold dilution, the sample had a 448 nm DLS diameter. However, when diluted further to 1000-fold, a significant increase in size was observed, 527 nm. Both traces were monodisperse, but the increase in size upon dilution could indicate stability issues with the sample. This should be considered when diluting the material for use in biological assays.

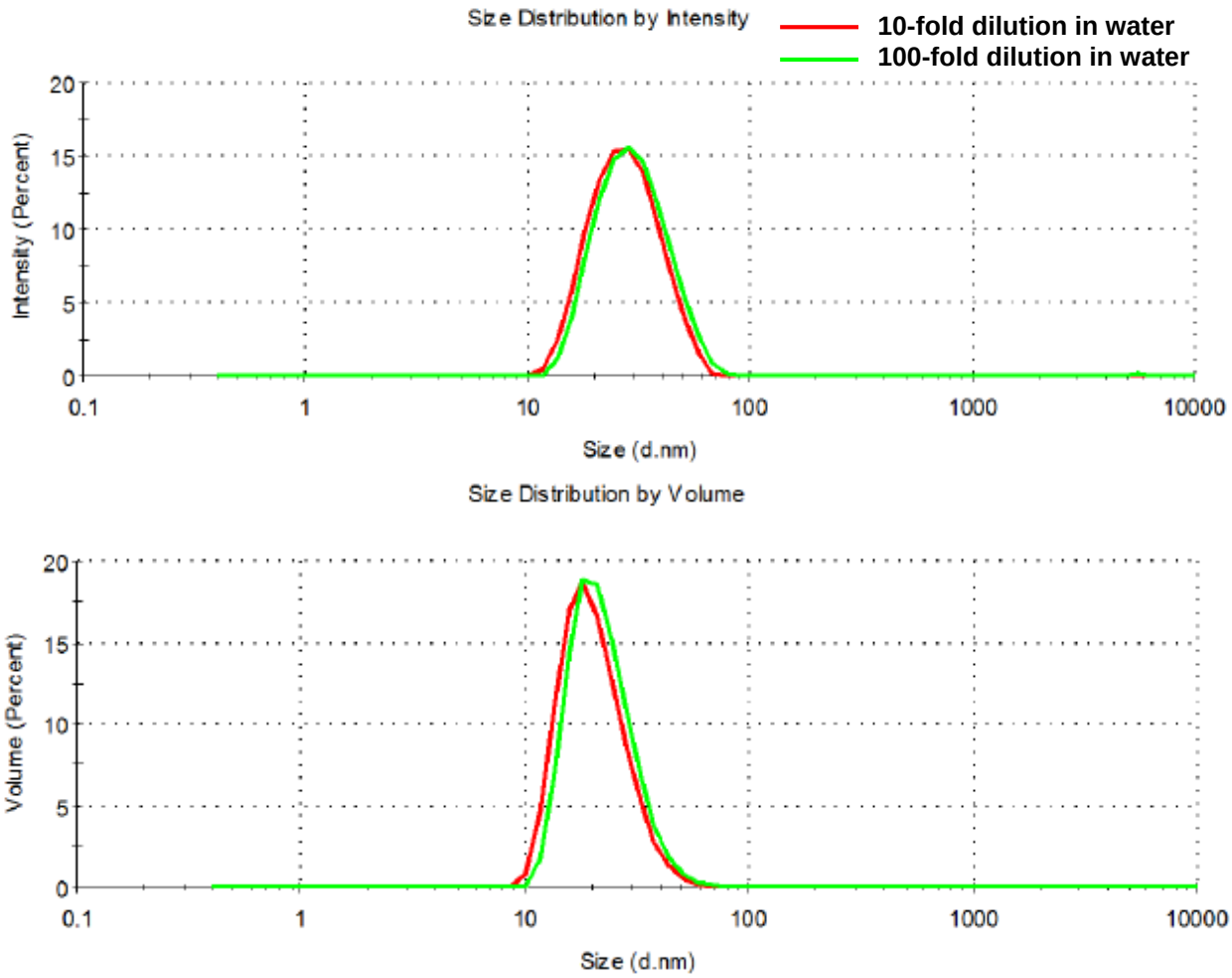

Figure III-6. The averaged intensity and volume distribution plots for CEHR-8 diluted in water.

Table III-5. Summary of the hydrodynamic size for CEHR-8 diluted in water

Dispersing Medium	Dilution	Z-Avg, nm	PdI	Int-Peak, nm	% Int	Vol-Peak, nm	% Vol
DI water	10-fold	26 ± 0	0.11 ± 0.01	29 ± 0	100 ± 0	20 ± 1	100 ± 0
DI water	100-fold	28 ± 0	0.13 ± 0.01	31 ± 1	99 ± 1	23 ± 0	100 ± 0

Note: Results are the average of at least 12 measurements. Z-Avg is the intensity-weighted average. PdI is the polydispersity index. Int-Peak is the intensity-weighted average over the primary peak. % Int is the percentage of the intensity spectra occupied by the primary peak. Vol-Peak is the volume-weighted average over the primary peak. % Vol is the percentage of the volume spectra occupied by the primary peak.

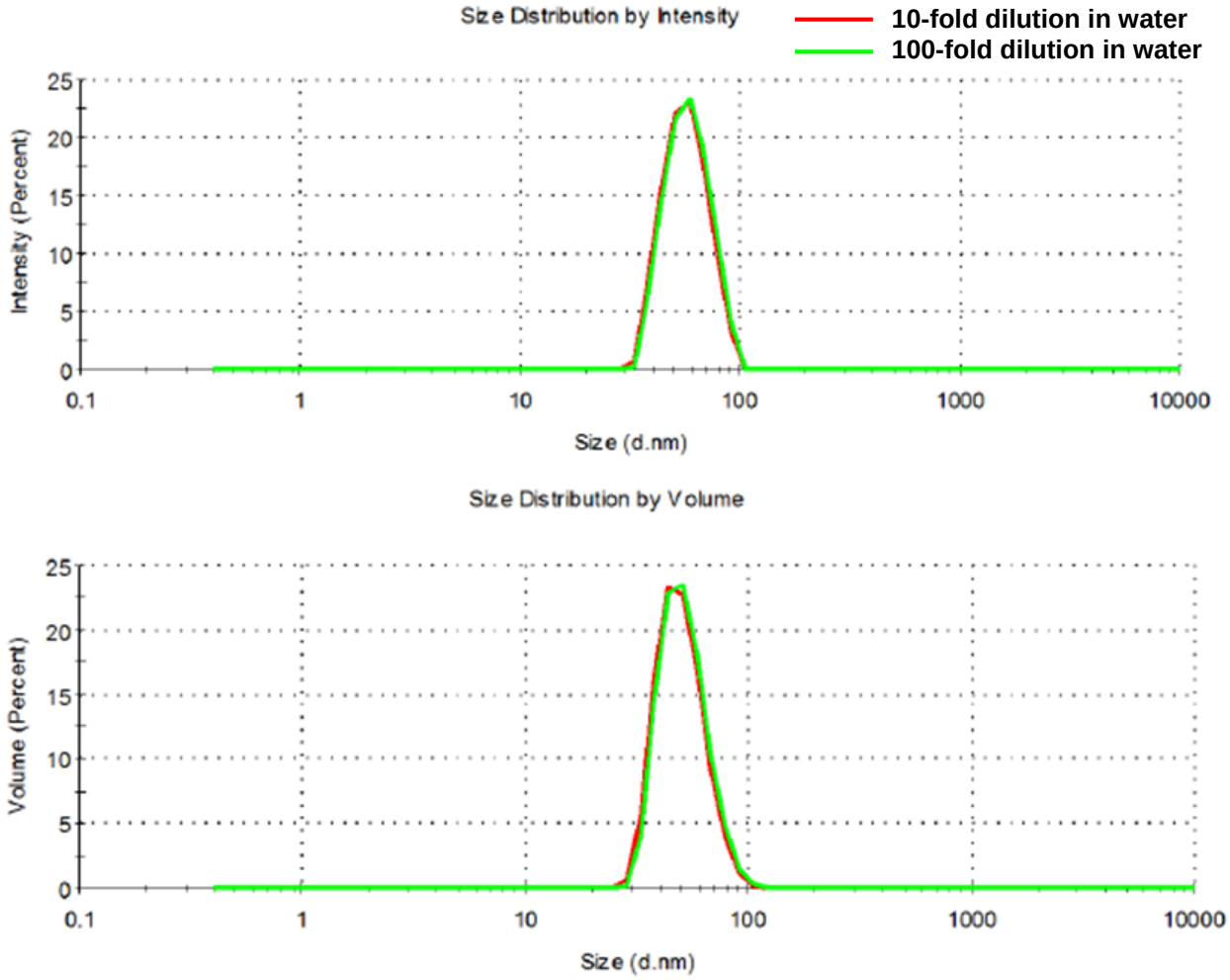

Figure III-7. The averaged intensity and volume distribution plots for CEHR-9 diluted in water.

Table III-6. Summary of the hydrodynamic size for CEHR-9 diluted in water

Dispersing Medium	Dilution	Z-Avg, nm	PdI	Int-Peak, nm	% Int	Vol-Peak, nm	% Vol
DI water	10-fold	55 ± 0	0.02 ± 0.01	58 ± 0	100 ± 0	51 ± 1	100 ± 0
DI water	100-fold	57 ± 0	0.02 ± 0.01	59 ± 0	100 ± 0	52 ± 0	100 ± 0

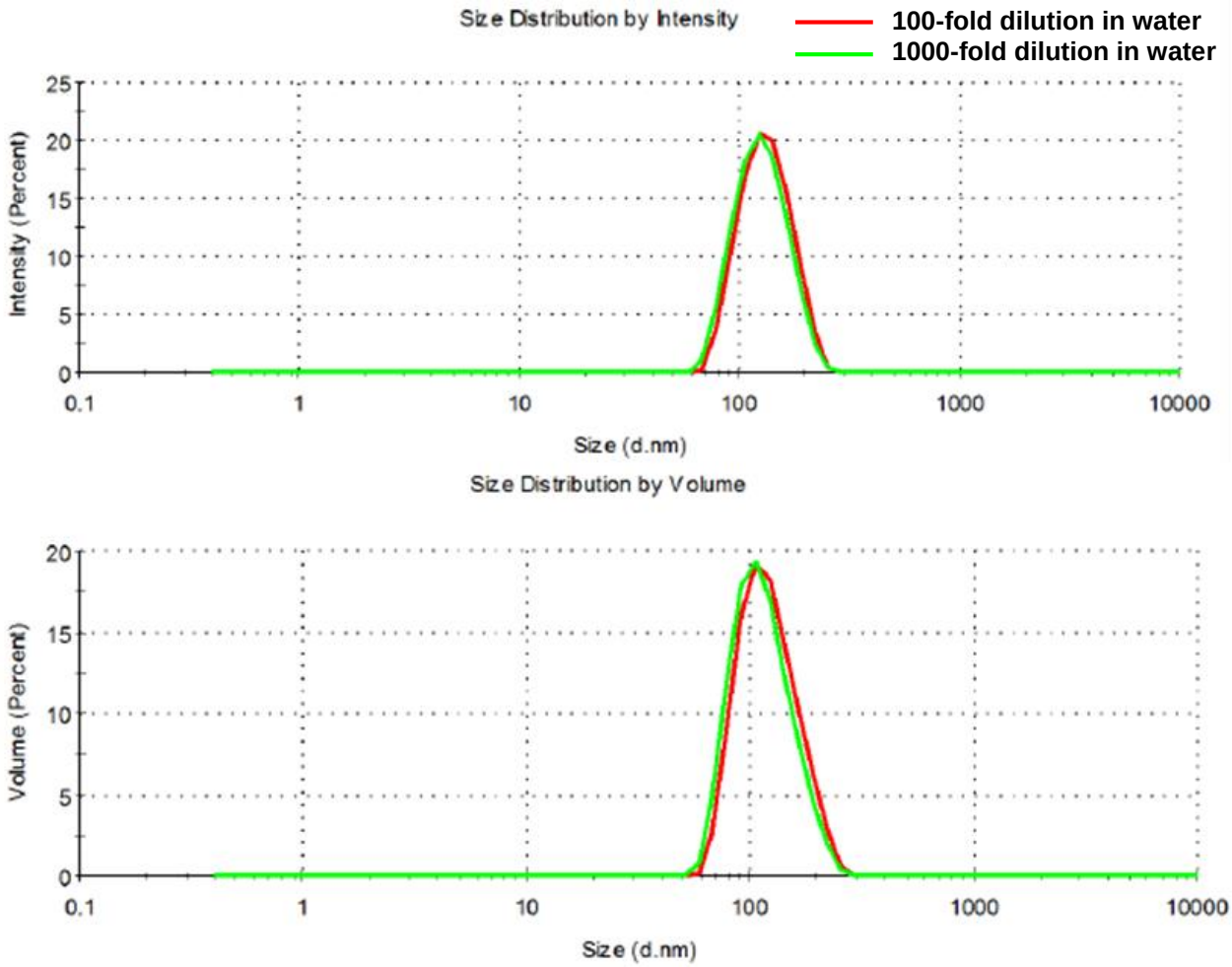

Figure III-8. The averaged intensity and volume distribution plots for CEHR-10 diluted in water.

Table III-7. Summary of the hydrodynamic size for CEHR-10 diluted in water

Dispersing Medium	Dilution	Z-Avg, nm	PdI	Int-Peak, nm	% Int	Vol-Peak, nm	% Vol
DI water	100-fold	126 ± 1	0.06 ± 0.01	135 ± 1	100 ± 0	124 ± 1	100 ± 0
DI water	1000-fold	121 ± 1	0.06 ± 0.02	129 ± 2	100 ± 0	117 ± 1	100 ± 0

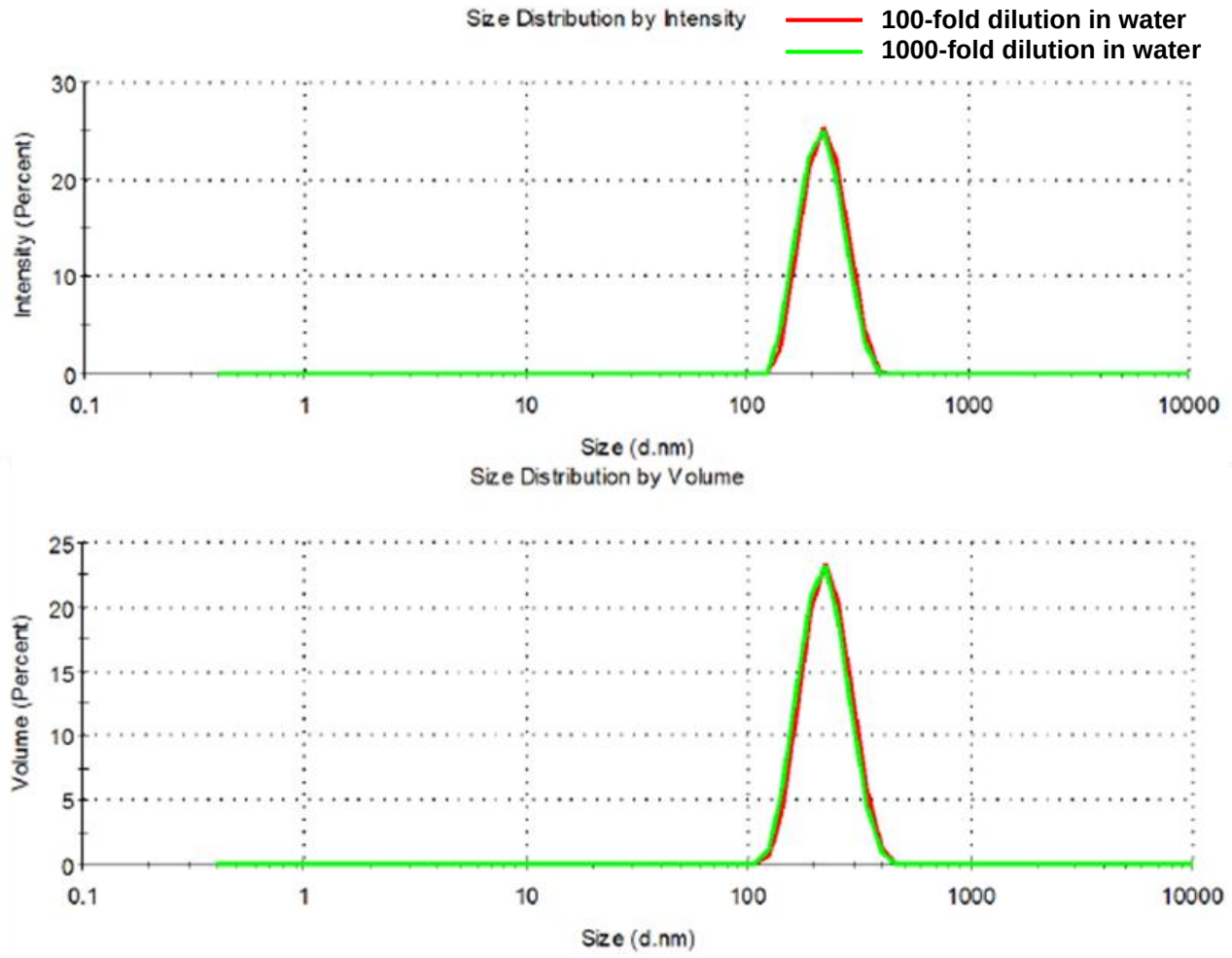

Figure III-9. The averaged intensity and volume distribution plots for CEHR-11 diluted in water.

Table III-8. Summary of the hydrodynamic size for CEHR-11 diluted in water

Dispersing Medium	Dilution	Z-Avg, nm	PdI	Int-Peak, nm	% Int	Vol-Peak, nm	% Vol
DI water	100-fold	221 ± 2	0.02 ± 0.01	229 ± 2	100 ± 0	124 ± 1	100 ± 0
DI water	1000-fold	214 ± 2	0.02 ± 0.01	222 ± 2	100 ± 0	117 ± 1	100 ± 0

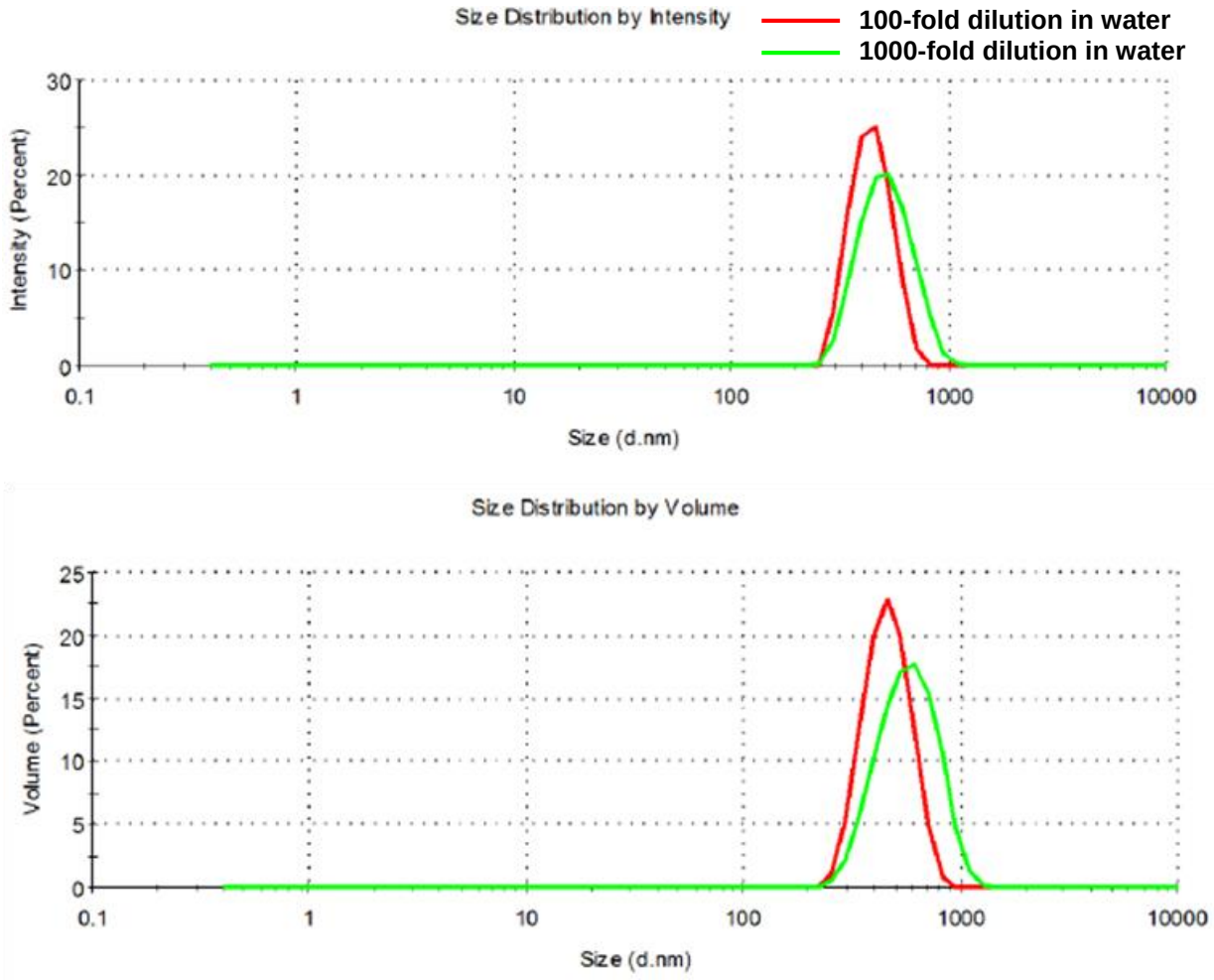

Figure III-10. The averaged intensity and volume distribution plots for CEHR-12 diluted in water.

Table III-9. Summary of the hydrodynamic size for CEHR-12 diluted in water

Dispersing Medium	Dilution	Z-Avg, nm	PdI	Int-Peak, nm	% Int	Vol-Peak, nm	% Vol
DI water	100-fold	432 ± 5	0.02 ± 0.01	448 ± 6	100 ± 0	490 ± 9	100 ± 0
DI water	1000-fold	494 ± 9	0.09 ± 0.04	527 ± 9	100 ± 0	593 ± 25	100 ± 0

F. Asymmetric-Flow Field Flow Fractionation

Design and Methods

The silica nanospheres were separated using asymmetric-flow field-flow fractionation (AF4) with multiple in-line detectors to evaluate the polydispersity of the samples. AF4 provides a more thorough understanding of the various populations present in the sample over other batch-mode measurement techniques such as DLS alone. The AF4 system consisted of an isocratic pump (Agilent G1310A, Palo Alto, CA), well-plate autosampler (Agilent G1329A), AF4 separation channel (Eclipse DualTec; Wyatt Technology, Santa Barbara, CA), multi-angle light scattering detector (HELEOS II; Wyatt Technology), diode array detector (DAD, Agilent G1315B), and a DLS detector (Malvern Zetasizer Nano ZS; Southborough, MA). The separation channel had a length of 275 mm and a 350 μm spacer. A 10 kDa regenerated cellulose membrane was used for all separations.

The elution profile is provided in Table III-10. The cross flow was controlled by an Eclipse flow controller. CEHR-8 was run as is (stock, no dilution), CEHR-10 was diluted 10-fold, CEHR-11 was diluted 20-fold, and CEHR-12 was diluted 20-fold. All samples were run in 0.05% (v/v) SDS filtered through a 0.2 μm regenerated cellulose membrane prior to use. The nanoparticles did not interact/stick to the FFF membrane under these conditions. A 100 μL sample injection volume used for all samples and the chromatographic traces were monitored by DLS detection and UV at 280 nm. The hydrodynamic size is plotted across the eluted peaks. The UV absorbance at 280 nm was monitored to track relative abundance of each size population.

Note, CEHR-9 was not analyzed by AF4 due to the possible mold contamination in the sample.

Table III-10. AF4 Elution Profile.

Start Time (min)	End Time (min)	Duration (min)	Mode	Starting Cross-flow Rate (mL/min)	Ending Cross-flow Rate (mL/min)
0	2	2	Elution	1	1
2	4	2	Focus	-	-
4	9	5	Focus + Inject	-	-
9	19	10	Focus	-	-
19	29	10	Elution	1	1
29	31	2	Elution	1	0.5
31	41	10	Elution	0.5	0
41	61	20	Elution	0	0
61	65	4	Elution + Inject	0	0
65	66	1	Elution	0	0

Results and Discussion

The fractograms for CEHR-8 are shown in Figure III-11. The light scattering (top and bottom panel) signals showed two major peaks (peak at roughly 20 minutes is the void peak). The first peak corresponded to the major population in the sample (as evidenced by its strong UV signal) and had a fairly constant hydrodynamic diameter of 25–37 nm. This was in good agreement with the batch-mode DLS result of 29 nm (Table III-5). The second peak had an approximate size of 174-184 nm. This population was not detected by other sizing techniques (batch-mode DLS and TEM), highlighting the importance of running multiple methods for a more complete picture of the size distribution within the sample.

The CEHR-10 fractograms are shown in Figure III-12. The light scattering signals showed a single peak with a slight shoulder, and had a hydrodynamic size of 96–129 nm. This was in good agreement with the batch-mode DLS result of 135 nm (Table III-7). The light scattering signals for CEHR-11 (Figure III-13) showed a single peak with a hydrodynamic size of 183–235 nm. Again, this flow-mode DLS size was in good agreement with the batch-mode DLS result of 229 nm (Table III-8). CEHR-12 also showed a single peak. The hydrodynamic size was 416–465 nm (Figure III-14). The batch-mode DLS for CEHR-12 was 448 nm (Table III-9).

In general, the flow mode DLS results were in good agreement with the batch-mode DLS results (Table III-11). The only exception was the presence of a second peak in CEHR-8 which was not detected by batch-mode DLS. These DLS sizes are also in good agreement with the vendor-reported sizes (TEM diameters). The DLS measured sizes are slightly larger, but this is expected as DLS measures the hydrodynamic size; whereas TEM measures the electron dense size.

Table III-11. Comparison of Batch-mode and Flow-mode DLS sizes.

Reference Number	Batch-mode DLS Measured Size (Int-Peak)	Flow-mode DLS Measured Size: Major peak	Flow-mode DLS Measured Size: Minor peak
CEHR-8	29 ± 0 nm	25-37 nm	174-184 nm
CEHR-9	58 ± 0 nm	Not Tested	-
CEHR-10	135 ± 1 nm	96-129 nm	-
CEHR-11	229 ± 2 nm	183-235 nm	-
CEHR-12	448 ± 6 nm	416-465 nm	-

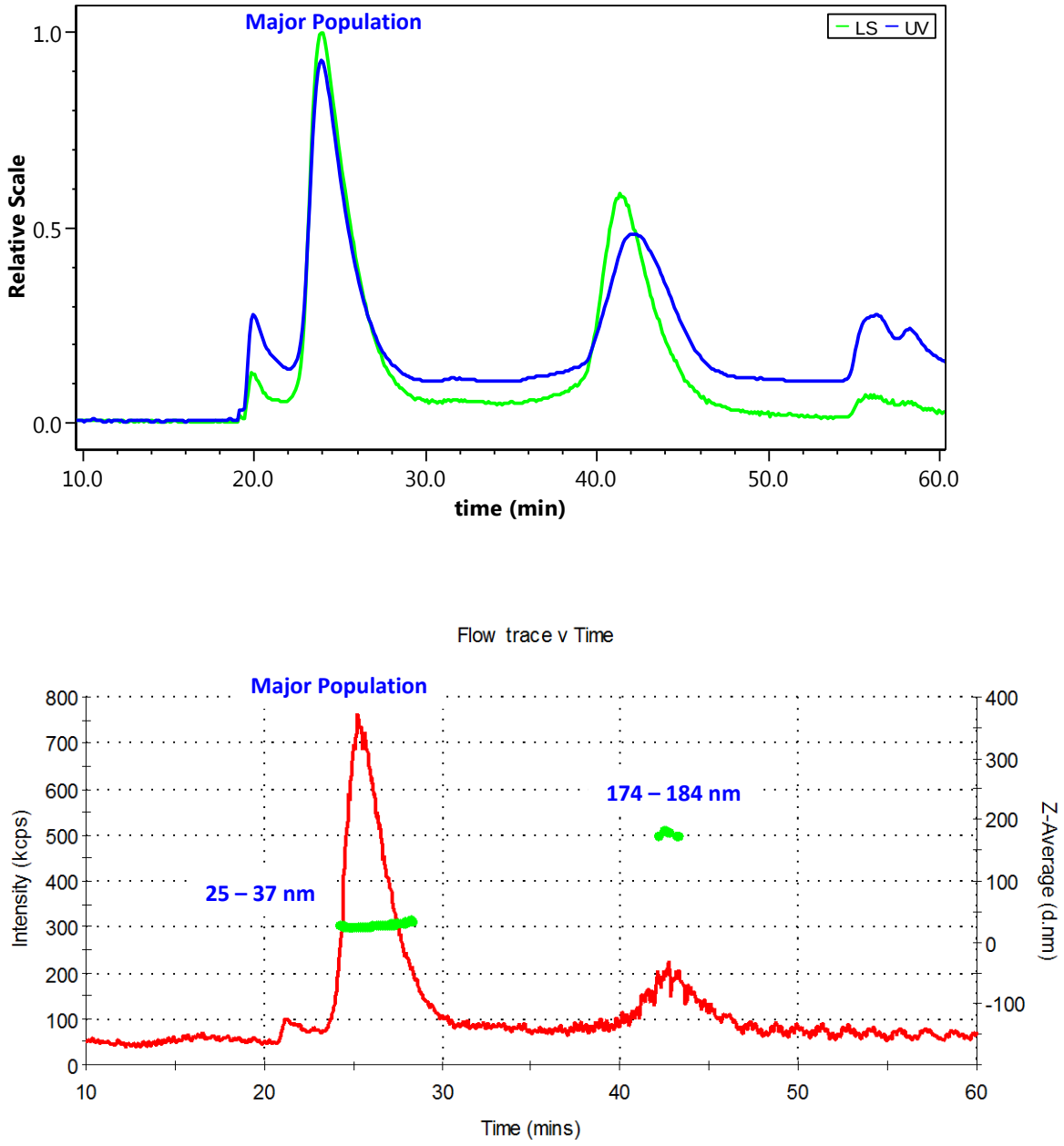

Figure III-11. AF4 fractograms for CEHR-8. The top panel shows the UV (280 nm) and LS (light scattering) signals while the bottom panel shows the hydrodynamic size distributions across the eluted peaks.

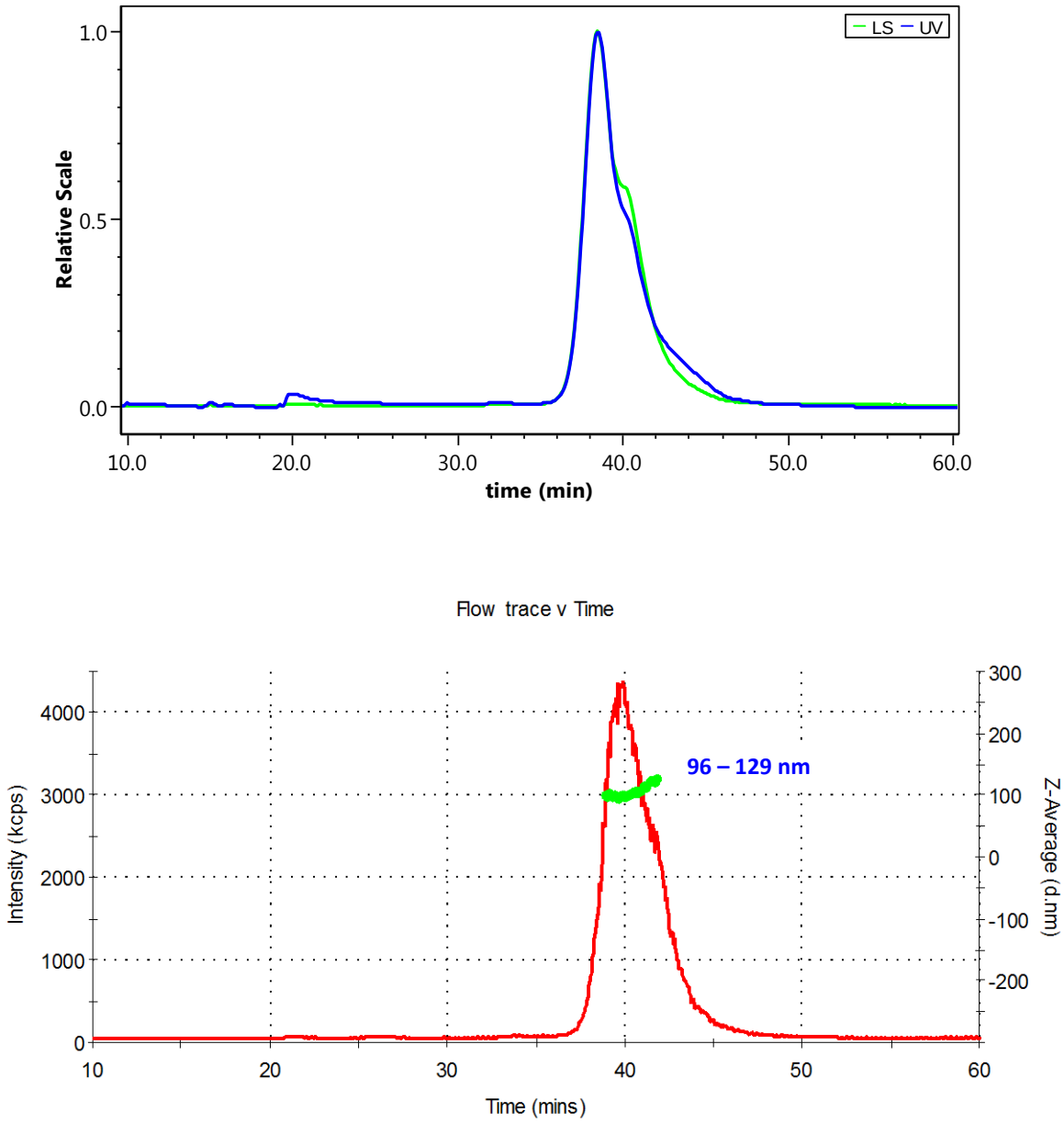

Figure III-12. AF4 fractograms for CEHR-10. The top panel shows the UV (280 nm) and LS (light scattering) signals while the bottom panel shows the hydrodynamic size distributions across the eluted peaks.

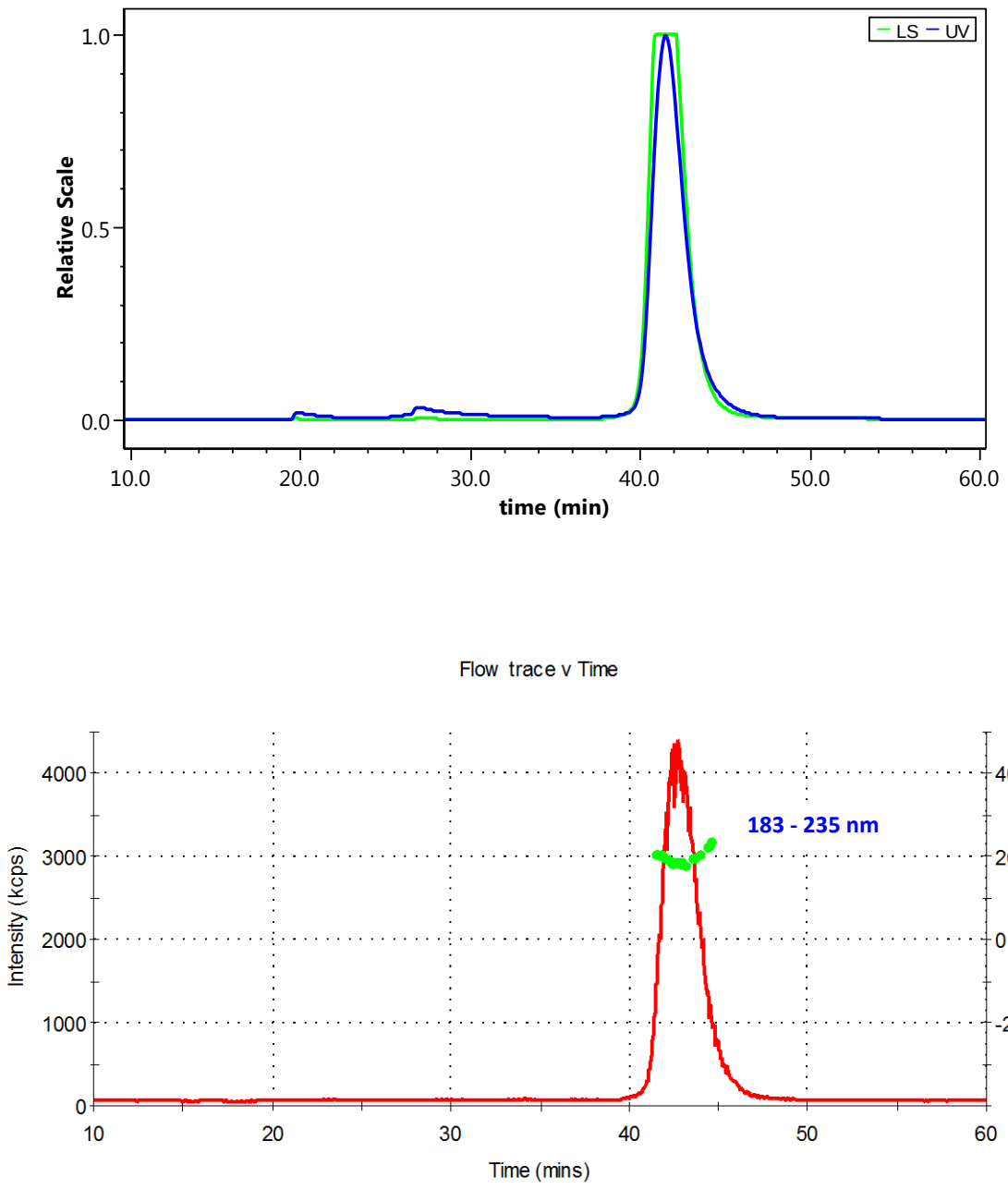

Figure III-13. AF4 fractograms for CEHR-11. The top panel shows the UV (280 nm) and LS (light scattering) signals while the bottom panel shows the hydrodynamic size distributions across the eluted peaks.

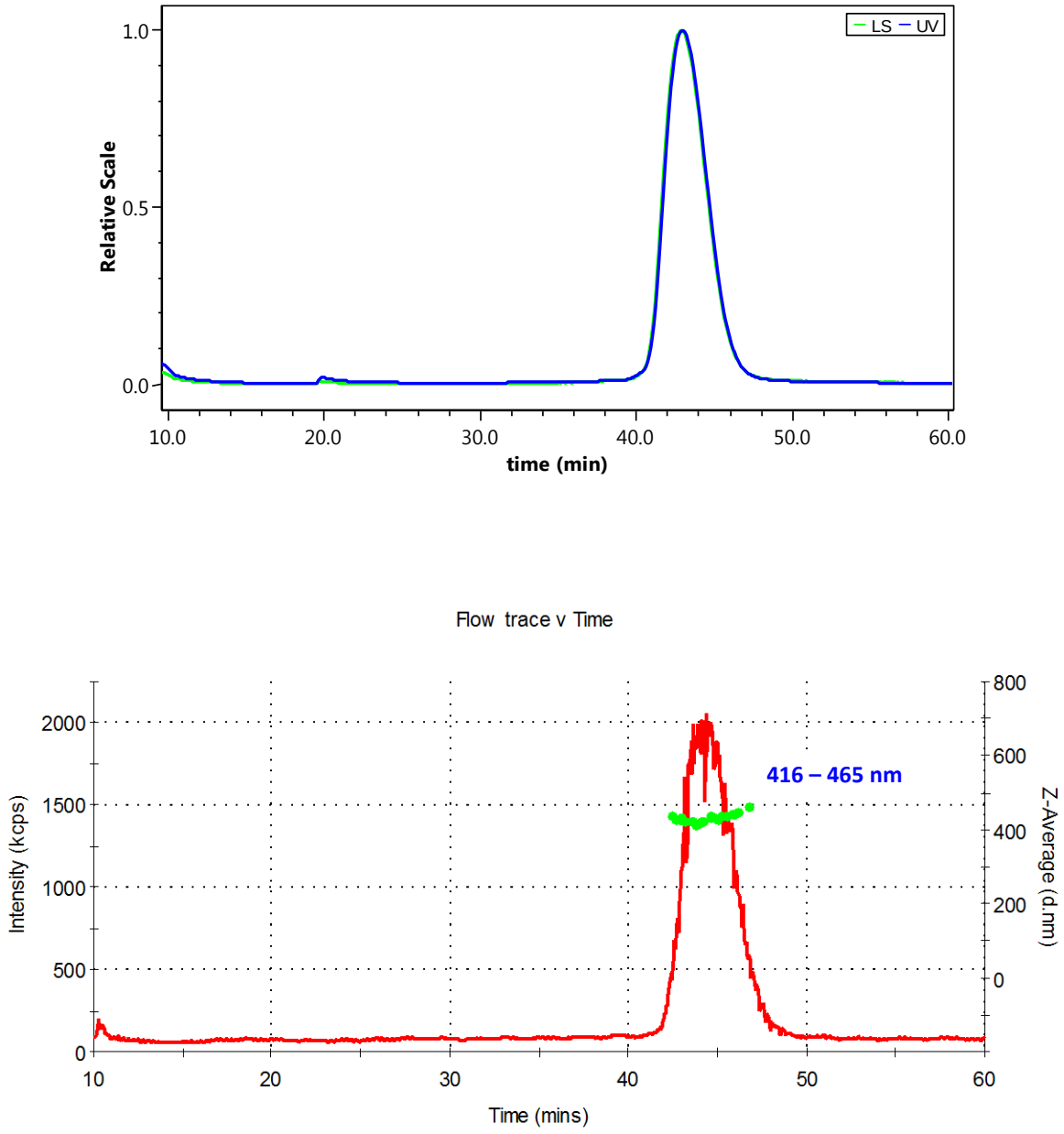

Figure III-14. AF4 fractograms for CEHR-12. The top panel shows the UV (280 nm) and LS (light scattering) signals while the bottom panel shows the hydrodynamic size distributions across the eluted peaks.

G. Thermogravimetric Analysis

Design and Methods

Samples were analyzed via thermogravimetric analysis (TGA) to assess whether coatings were present on the nanoparticles and in what concentration. TGA was also used to determine the concentration of the metallic nanomaterial by measuring the residual material remaining after combustion of any coatings. For measurement of the metallic nanoparticle concentration, the samples were measured in their liquid (as-received) forms. For detection and measurement of coating concentrations, the samples were lyophilized prior to the TGA run. The signal from the water loss had the potential to swamp out a small amount of loss from any coating present, and thus was removed/minimized by lyophilization. Using lyophilized samples allowed for better sensitivity (total weight measured >1 mg) and hence a more accurate coating determination.

Nanoparticle Concentration

For each liquid sample, 50 μL was transferred to an aluminum oxide crucible (150 μL crucible with lid, Mettler Toledo) for TGA measurement (TGA/DSC 1, Mettler Toledo). Samples were held at 25˚C for 5 min, then ramped to 1000˚C at a heating rate of 20˚C/min under nitrogen gas. A new crucible was used for each sample. The empty crucible was subjected to the TGA method prior to loading the sample to serve as a background correction.

TGA cannot confirm the oxidation state of the material. Concentrations are reported using the manufacturer-reported oxidation state.

Coating Detection and Concentration

To determine coating content of the samples, samples were lyophilized overnight after being frozen in an ultra-low temperature freezer (-80˚C) for at least 3 hours. Typically, 500 μL of sample solution yielded 5 mg of lyophilized powder. About 1 mg was the typical amount added for TGA analysis, allowing for repeat runs, if necessary. The dried samples were added to aluminum oxide crucibles and subjected to the same temperature program as described above for the liquid samples.

Results and Discussion

Nanoparticle Concentration

The TGA curves (top panel; weight loss versus temperature) for CEHR-8 through CEHR-12, the silica nanosphere samples, are shown in Figures III-15 through III-19, respectively. To aid with the analysis, the first derivative of this curve was taken to highlight the weight loss event (bottom panel). For all samples, a single weight loss event was observed occurring between 50-180˚C, corresponding to the loss of water (top panels). The total mass silica was determined using the mass left at the end of the TGA run. A comparison of the vendor-reported concentrations to the TGA-measured concentrations is provided in Table III-12. CEHR-12 was very close to the reported concentration. CEHR-9 to CEHR-11 were approximately 10-25% lower than the theoretical concentrations. CEHR-8 was less than half of the reported-concentration.

Importantly, this analysis assumes that, at the end of the run, all that remained was the silica nanoparticles; the water would have evaporated and any organic coating present would have combusted. In some instances, combustion of a coating may leave residual mass, which would increase the nanoparticle concentration. It is not possible to determine this without subjecting the coating alone (not in nanosolution) to the TGA method. Since the coating identity is unknown, this control could not be performed.

While ICP-MS is the more sensitive and accurate technique for measuring metal concentrations, silicon concentrations could not be measured by ICP-MS due to our instrument setup (glass nebulizer). TGA is a good alternative when ICP-MS is unavailable, although ideally TGA results should be confirmed with a second technique. TGA results rely on several assumptions (e.g., only the nanoparticle weight remains at the end of the run) that could affect the results, i.e. increase or decrease the presumed nanoparticle concentration.

Table III-12. Comparison of Reported Nanoparticle Concentration to TGA Calculated Nanoparticle Concentrations.

Reference Number	Reported Concentration	Calculated Concentration via TGA of Liquid Sample
CEHR-8	10 mg/mL	4.0 mg/mL
CEHR-9	10 mg/mL	9.1 mg/mL
CEHR-10	10 mg/mL	7.5 mg/mL
CEHR-11	10 mg/mL	8.5 mg/mL
CEHR-12	10 mg/mL	10.2 mg/mL

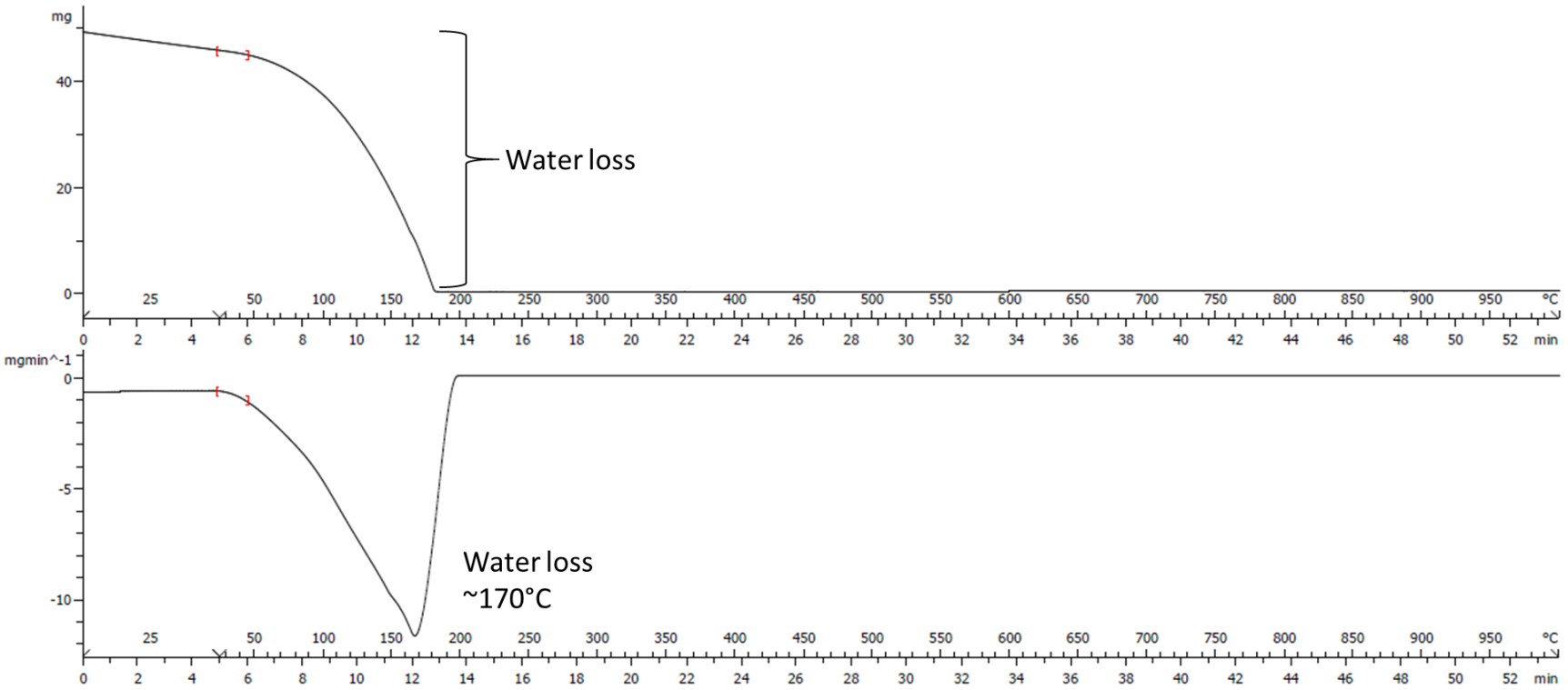

Reference Number	Volume (µL)	Starting Mass (mg)	Total Mass Loss (mg)	Residue mass (mg)
CEHR-8	50	48.885	48.684	0.200

Figure III-15. TGA thermogram of CEHR-8. The top panel is the weight loss versus temperature (and time) curve. The bottom panel is the first derivative of that curve.

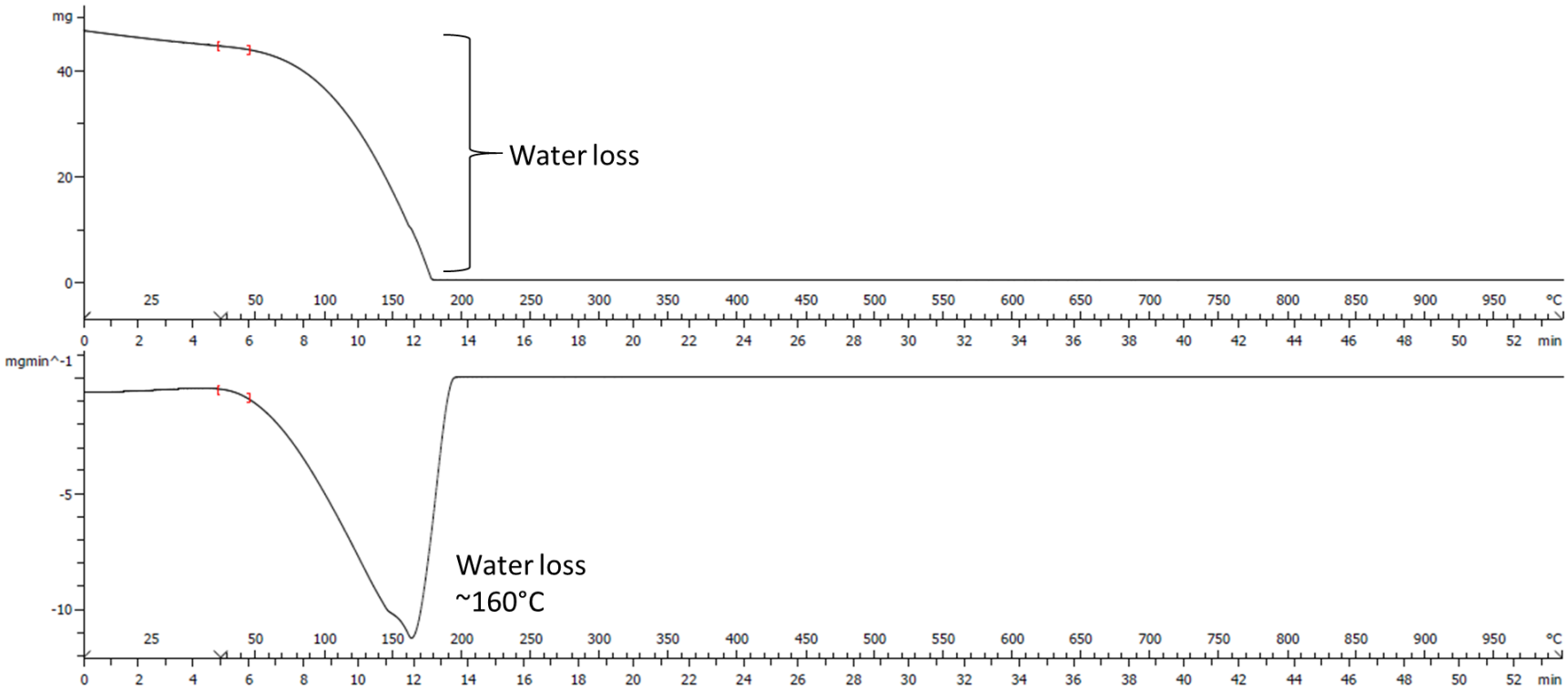

Reference Number	Volume (µL)	Starting Mass (mg)	Total Mass Loss (mg)	Residue mass (mg)
CEHR-9	50	47.364	46.908	0.456

Figure III-16. TGA thermogram of CEHR-9. The top panel is the weight loss versus temperature (and time) curve. The bottom panel is the first derivative of that curve.

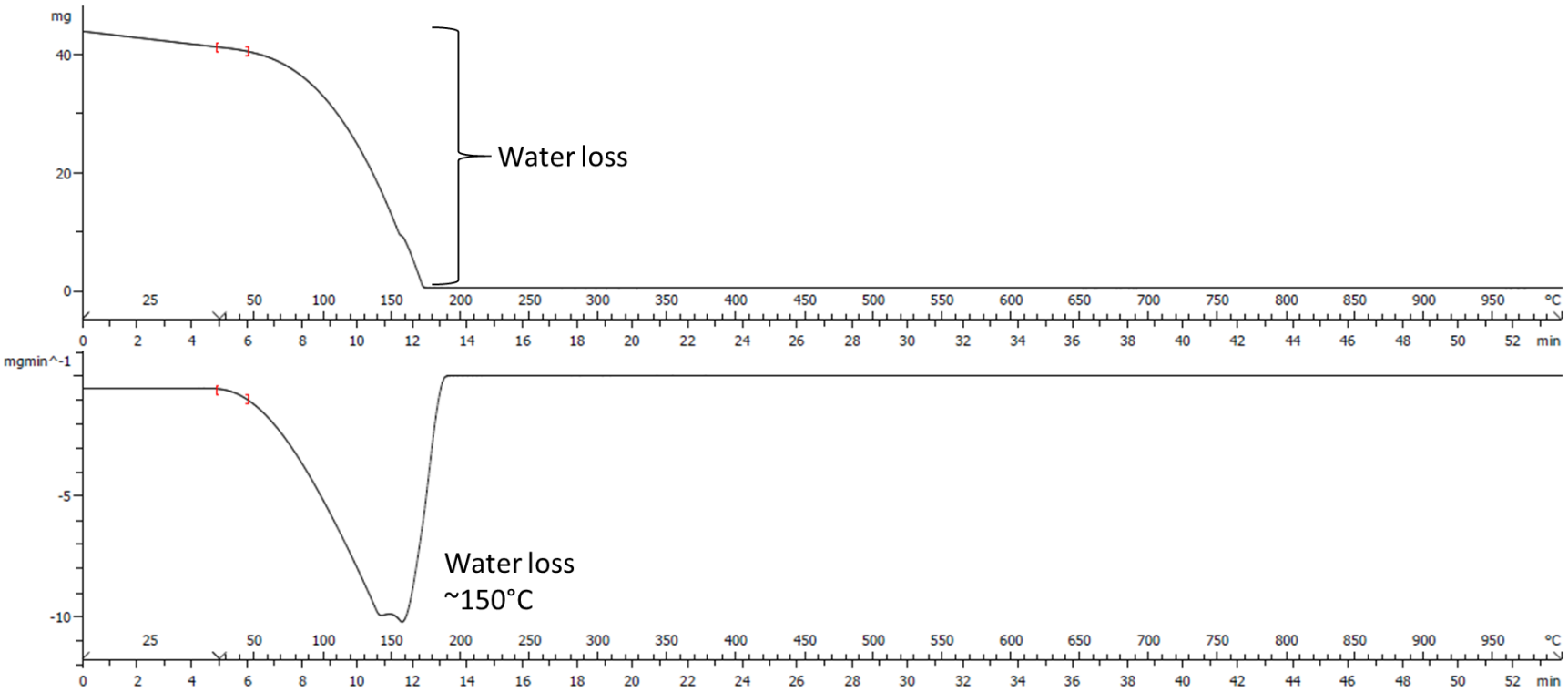

Reference Number	Volume (µL)	Starting Mass (mg)	Total Mass Loss (mg)	Residue mass (mg)
CEHR-10	50	43.815	43.443	0.372

Figure III-17. TGA thermogram of CEHR-10. The top panel is the weight loss versus temperature (and time) curve. The bottom panel is the first derivative of that curve.

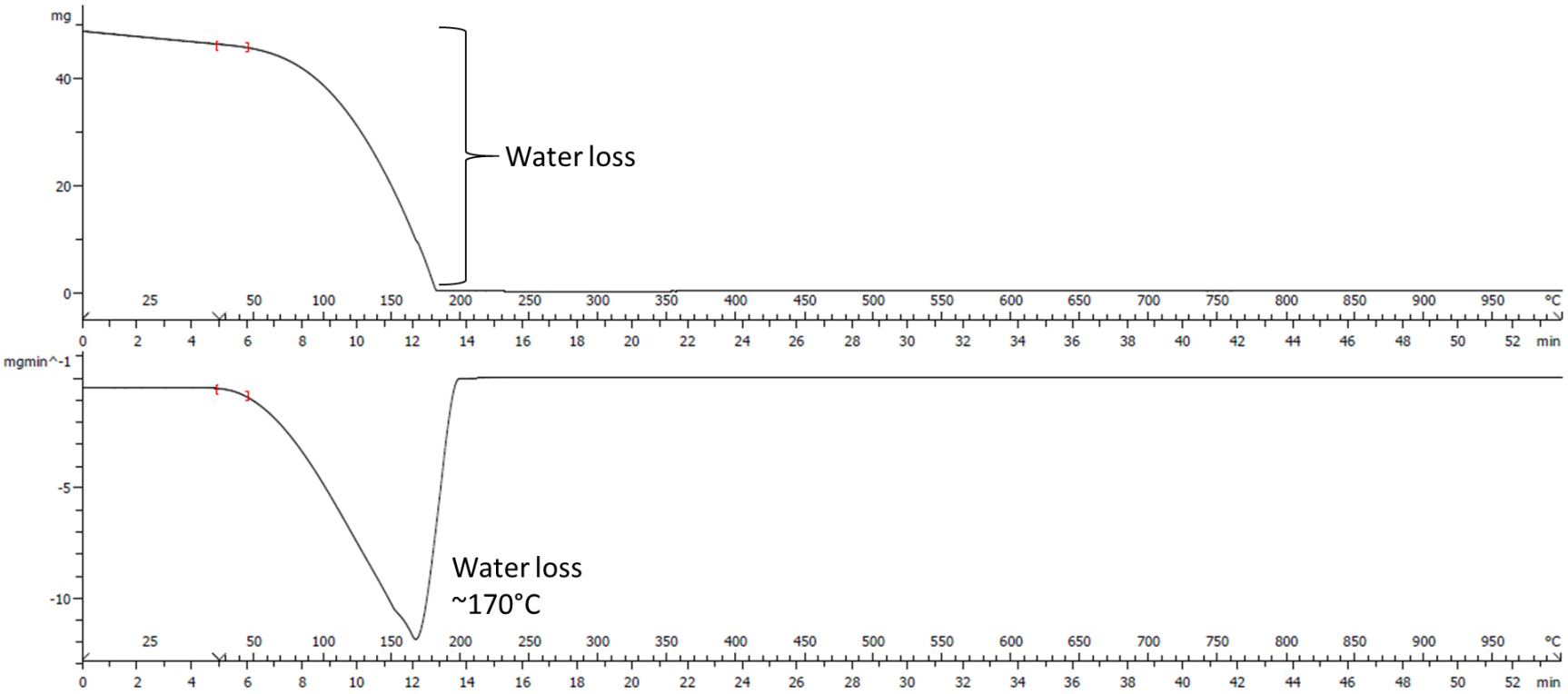

Reference Number	Volume (µL)	Starting Mass (mg)	Total Mass Loss (mg)	Residue mass (mg)
CEHR-11	50	48.787	48.363	0.423

Figure III-18. TGA thermogram of CEHR-11. The top panel is the weight loss versus temperature (and time) curve. The bottom panel is the first derivative of that curve.

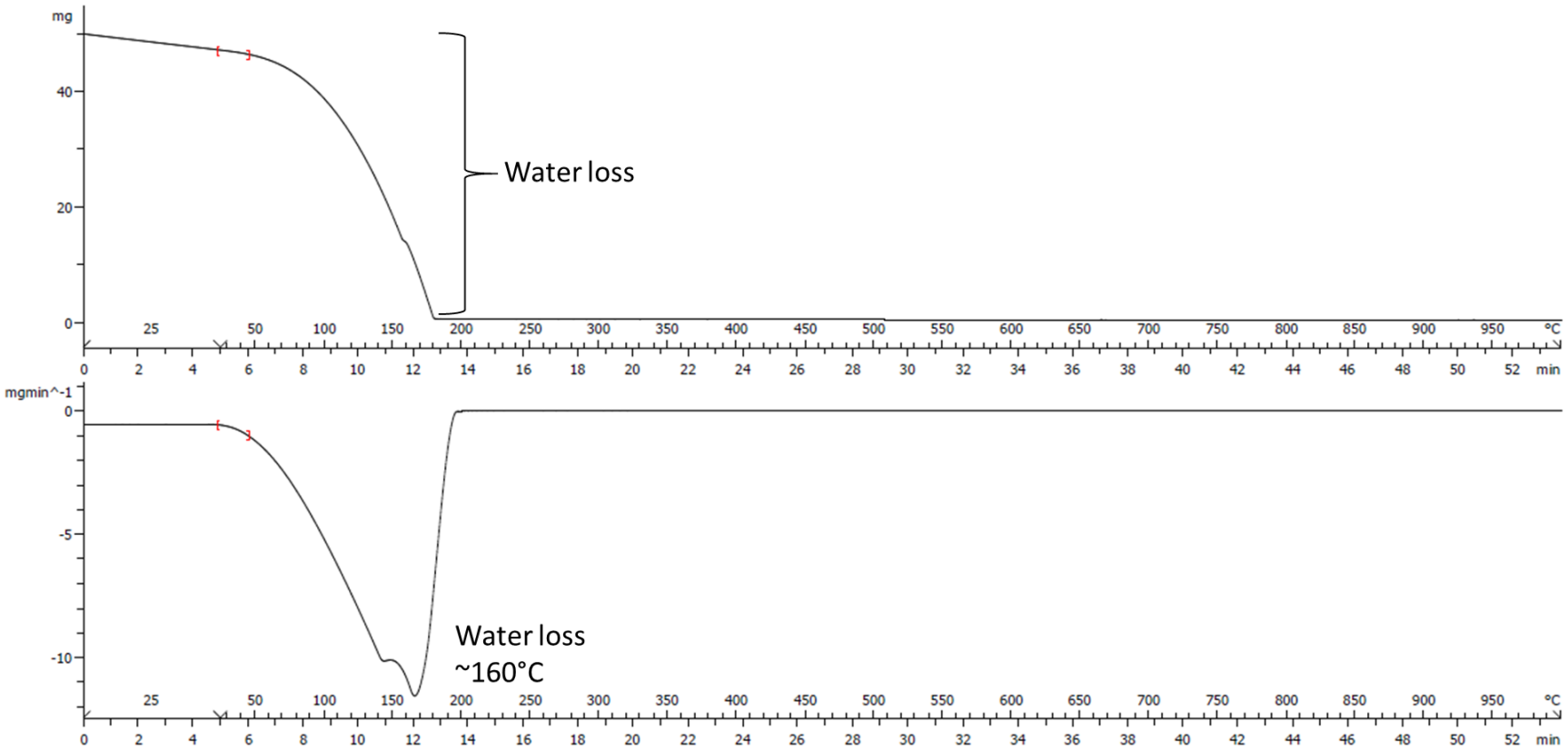

Reference Number	Volume (µL)	Starting Mass (mg)	Total Mass Loss (mg)	Residue mass (mg)
CEHR-12	50	49.787	49.275	0.512

Figure III-19. TGA thermogram of CEHR-12. The top panel is the weight loss versus temperature (and time) curve. The bottom panel is the first derivative of that curve.

Coating Detection and Concentration

The amount of any possible coating contained in the samples was assumed to be very low. Since the water peak dominated the TGA curves, all samples were lyophilized to remove the water and improve sensitivity for coating detection. Typical TGA curves for the lyophilized CEHR-8 to CEHR-12 samples are shown in Figures III-20 to III-24, respectively.

In all samples, the first weight loss event corresponded to the loss of residual water and occurred between 50-180˚C. The mass at this temperature (180˚C) was defined as the mass total construct (after water loss). Based on the first derivative curves, CEHR-8 and CEHR-9 displayed a distinct second weight loss, indicative of a possible coating on the nanoparticles. The remaining samples showed only a gradual decrease in weight up to the final temperature, and did not show a distinct peak in the derivative curves. This gradual weight loss may represent a possible coating on the silica nanoparticles, but is less clear than CEHR-8 and CEHR-9. The observed weight losses could also stem from other excipients in the formulation, and not necessarily a nanoparticle surface coating. TGA cannot differentiate between surface coatings and other added excipients.

The coating mass loss was defined as the difference between masses at 180˚C (the mass total construct after water loss) and 1000˚C (residual mass). Importantly, this assumes that the weight of any residual decomposed coating is negligible relative to the weight of silica. The percent mass ratio of possible coatings on the silica nanoparticles was then calculated for each sample and is summarized in Table III-13. The calculated percent coatings ranged from 3.3% to 18.7%. Note, the identity of the coating could not be determined by TGA, and was not reported by the vendor.

Table III-13. Summary of Percent Coating Mass per Mass Silica detected in each of the silica nanoparticles.

Reference Number	Reported Coating	%Mass Coating per Mass Silica
CEHR-8	None	13%
CEHR-9	None	19%
CEHR-10	None	3%
CEHR-11	None	6%
CEHR-12	None	5%

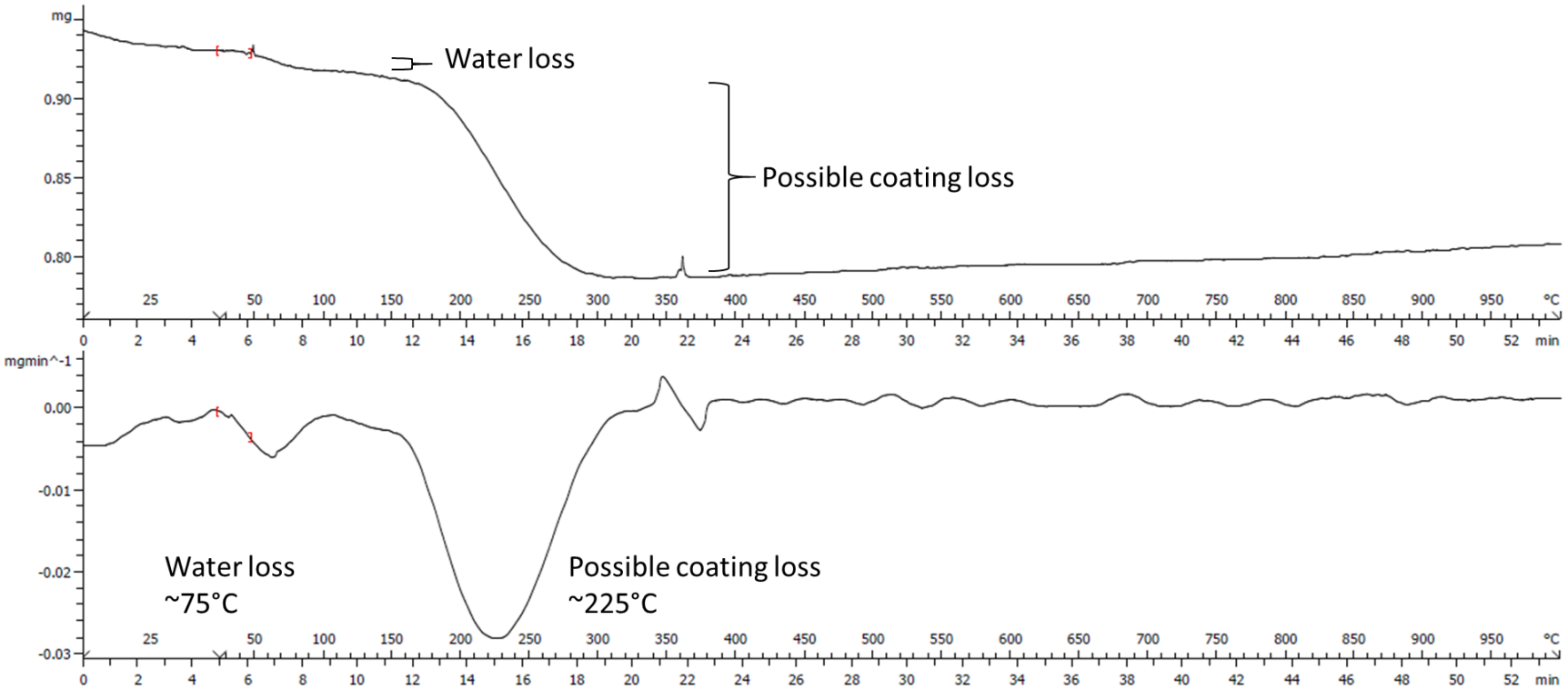

Reference Number	Starting Mass (mg)	Water Loss (mg)	Coating Loss (mg)	Residue (mg)	%Mass Coating per Mass Silica
CEHR-8	0.943	0.027	0.108	0.808	13%

Figure III-20. TGA thermogram of CEHR-8 (lyophilized). The top panel is the weight loss versus temperature (and time) curve. The bottom panel is the first derivative of that curve.

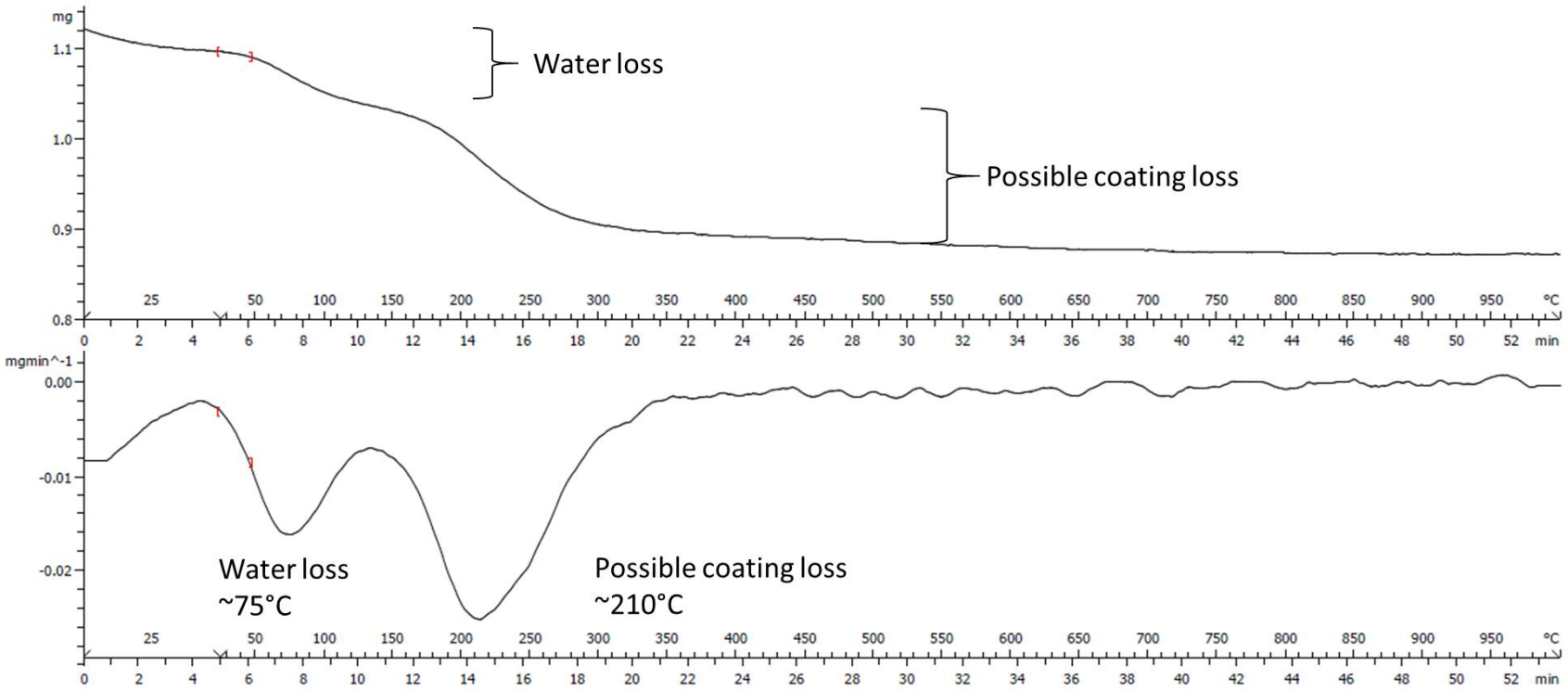

Reference Number	Starting Mass (mg)	Water Loss (mg)	Coating Loss (mg)	Residue (mg)	%Mass Coating per Mass Silica
CEHR-9	1.121	0.086	0.163	0.872	19%

Figure III-21. TGA thermogram of CEHR-9 (lyophilized). The top panel is the weight loss versus temperature (and time) curve. The bottom panel is the first derivative of that curve.

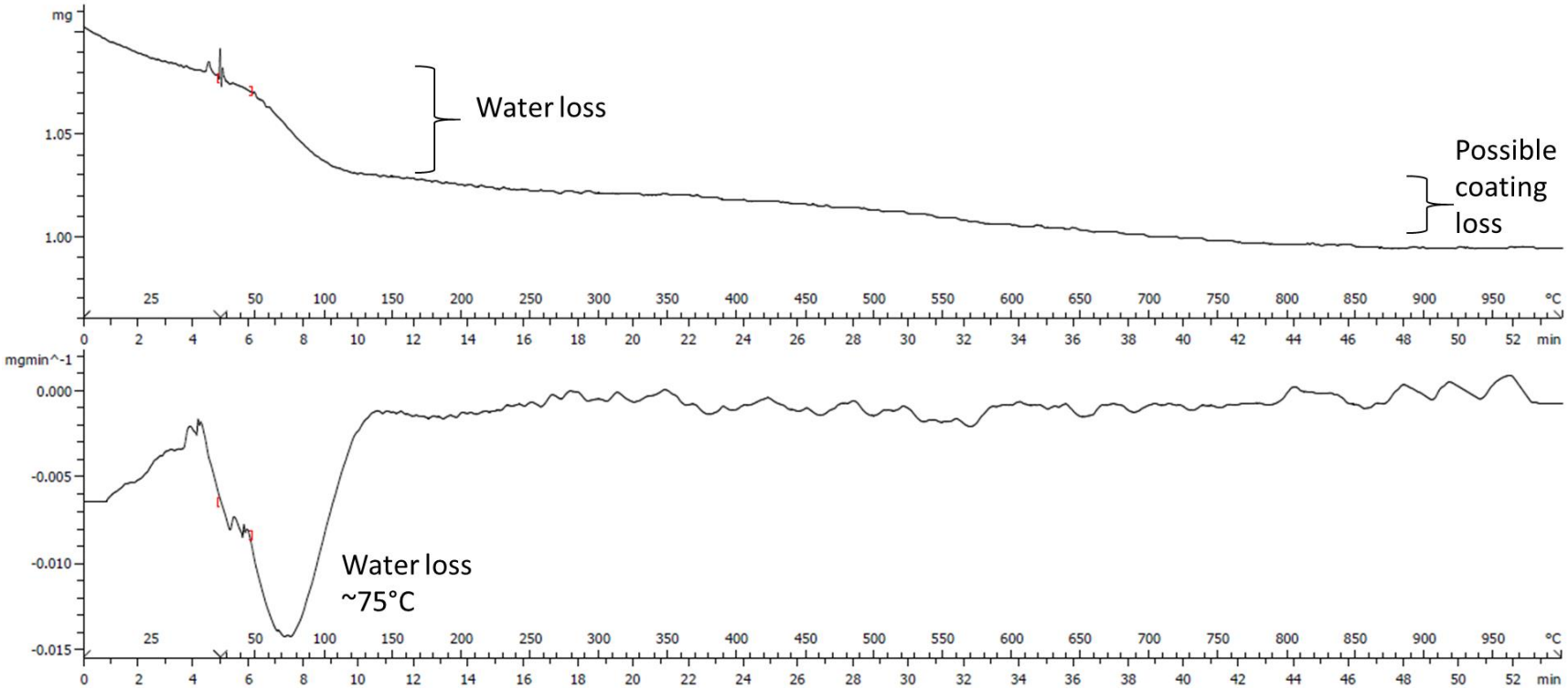

Reference Number	Starting Mass (mg)	Water Loss (mg)	Coating Loss (mg)	Residue (mg)	%Mass Coating per Mass Silica
CEHR-10	1.102	0.0750	0.033	0.994	3%

Figure III-22. TGA thermogram of CEHR-10 (lyophilized). The top panel is the weight loss versus temperature (and time) curve. The bottom panel is the first derivative of that curve.

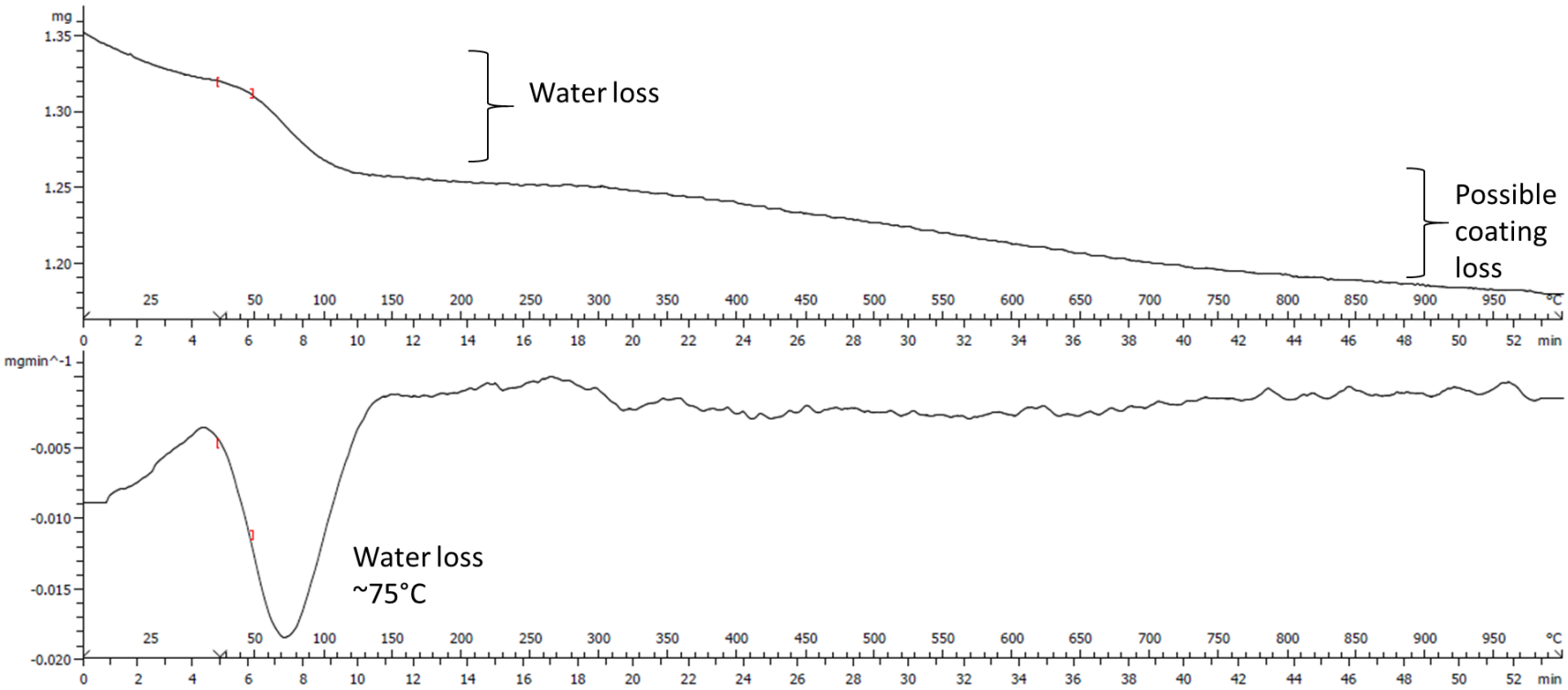

Reference Number	Starting Mass (mg)	Water Loss (mg)	Coating Loss (mg)	Residue (mg)	%Mass Coating per Mass Silica
CEHR-11	1.352	0.098	0.076	1.179	6%

Figure III-23. TGA thermogram of CEHR-11 (lyophilized). The top panel is the weight loss versus temperature (and time) curve. The bottom panel is the first derivative of that curve.

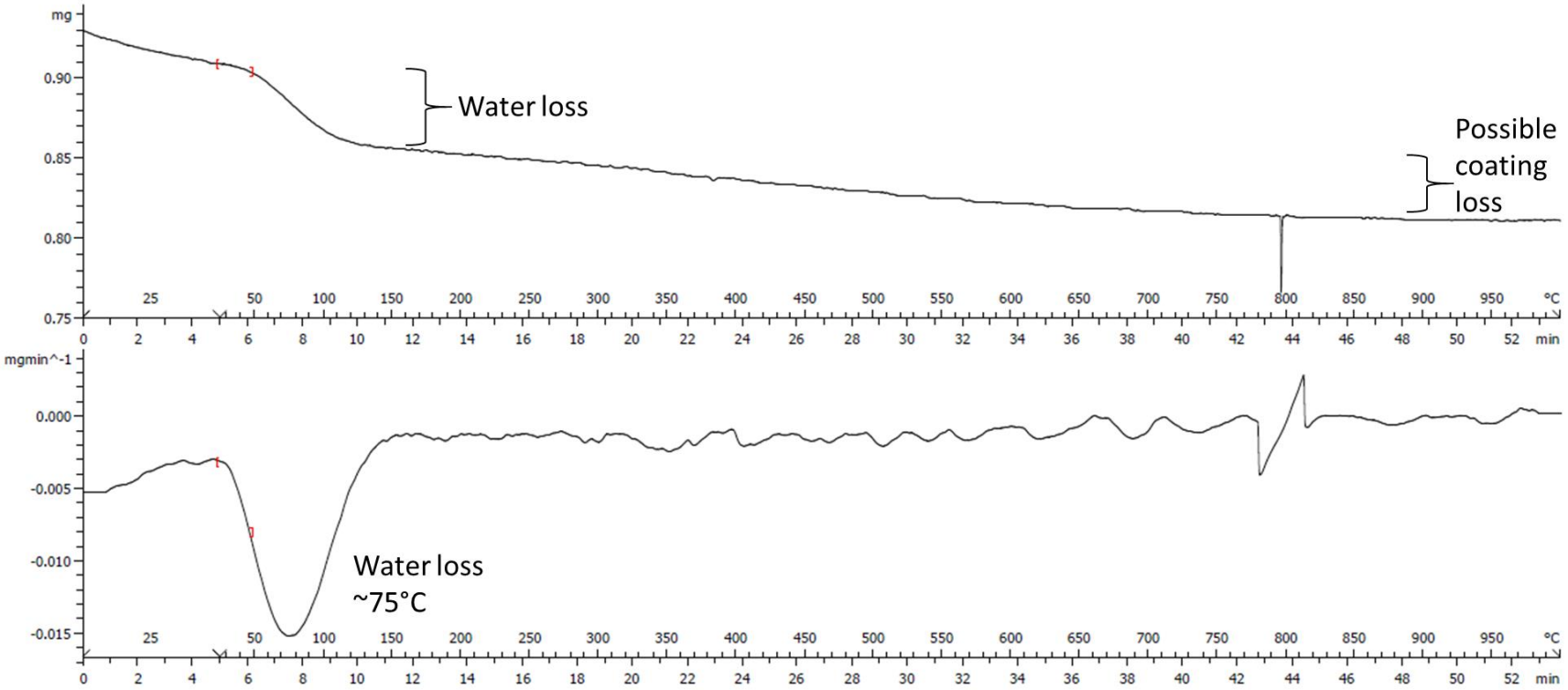

Reference Number	Starting Mass (mg)	Water Loss (mg)	Coating Loss (mg)	Residue (mg)	%Mass Coating per Mass Silica
CEHR-12	0.929	0.075	0.043	0.810	5%

Figure III-24. TGA thermogram of CEHR-12 (lyophilized). The top panel is the weight loss versus temperature (and time) curve. The bottom panel is the first derivative of that curve.

H. Zeta Potential

Design and Methods

A Malvern Zetasizer Nano ZS instrument was used to measure zeta potential at 25°C for all samples. NCL protocol PCC-2 was followed (https://ncl.cancer.gov/resources/assay-cascade-protocols). Samples were diluted either 10- or 100-fold in deionized water. Sample pH was measured before loading into a pre-rinsed folded capillary cell. An applied voltage of 150 V was used. Traces in the figures represent the average of four measurements.

The instrument was validated by running an appropriate standard (Zeta Potential Transfer Standard, DTS0050, zeta potential value of -42 ± 4 mV at 25°C, Malvern Instruments) before all zeta potential measurements.

Results and Discussion

All five silica nanomaterials, CEHR-8 through CEHR-12, had negative zeta potentials. CEHR-8 had a value of -27 mV, while CEHR-9 through CEHR-12 had zeta potentials ≤ -49 mV (Table III-14). These values were in line with the expected values for unfunctionalized silica nanoparticles or those coated with a negatively charged surface coating.

Table III-14. Summary of the zeta potentials for CEHR-8 to CEHR-12.

Sample	pH	Zeta Potential
CEHR-8	7.3	-27 ± 1 mV
CEHR-9	7.4	-53 ± 4 mV
CEHR-10	7.4	-49 ± 1 mV
CEHR-11	7.5	-55 ± 1 mV
CEHR-12	7.5	-68 ± 1 mV

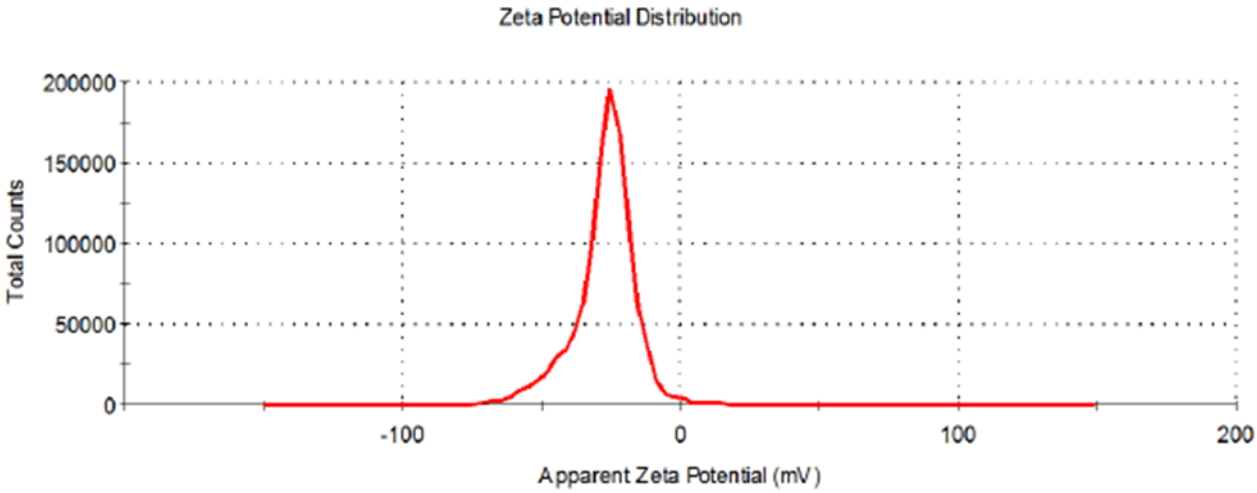

Sample	pH	Zeta Potential
CEHR-8	7.3	-27 ± 1 mV

Figure III-25. The averaged zeta potential distributions for CEHR-8 diluted 10-fold in deionized water.

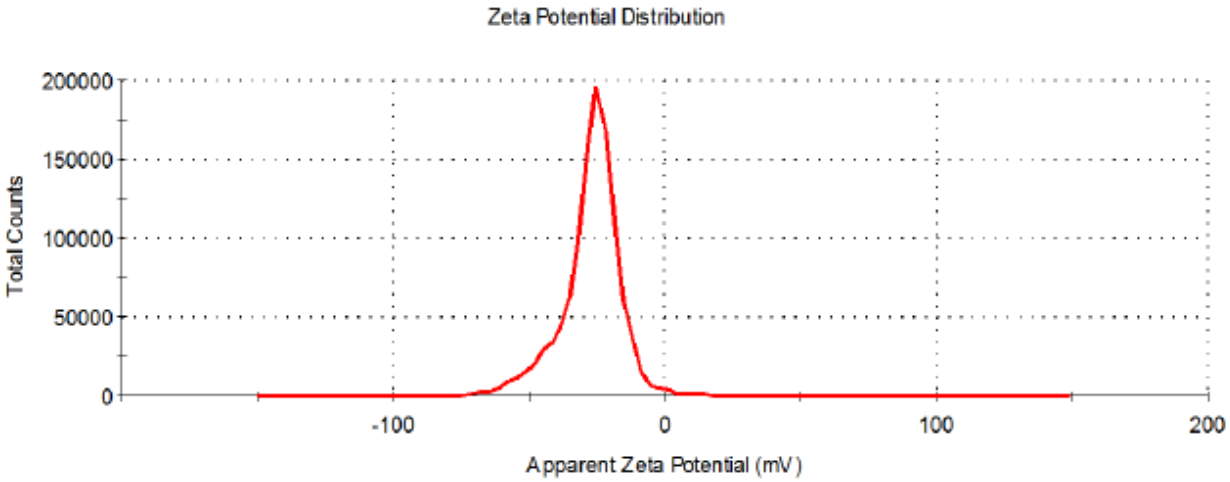

Sample	pH	Zeta Potential
CEHR-9	7.4	-53 ± 4 mV

Figure III-26. The averaged zeta potential distributions for CEHR-9 diluted 10-fold in deionized water.

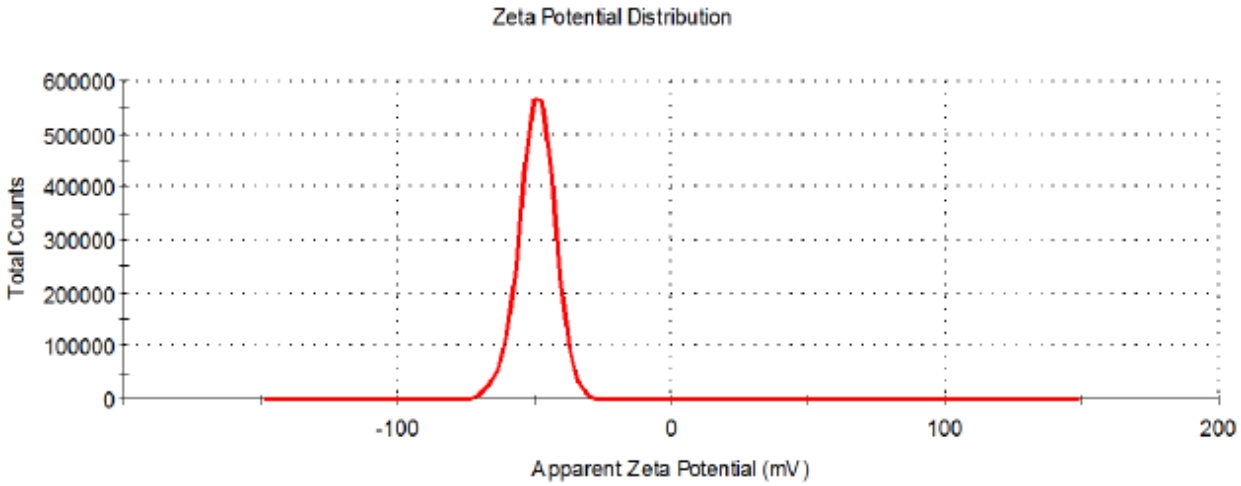

Sample	pH	Zeta Potential
CEHR-10	7.4	-49 ± 1 mV

Figure III-27. The averaged zeta potential distributions for CEHR-10 diluted 100-fold in deionized water.

Table III-17. Summary of the zeta potential for CEHR-10 diluted 100-fold in deionized water.

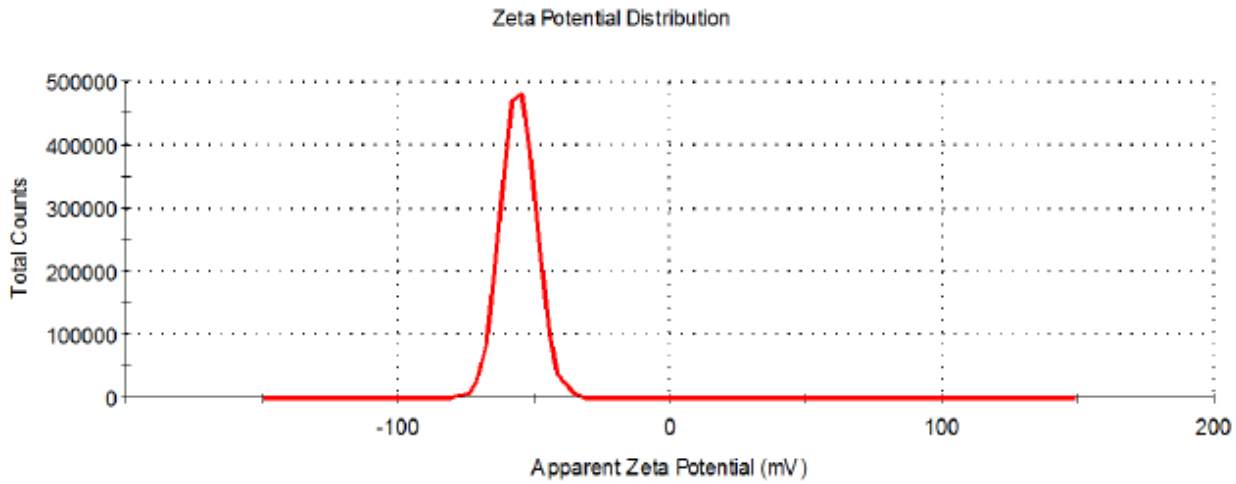

Sample	pH	Zeta Potential
CEHR-11	7.5	-55 ± 1 mV

Figure III-28. The averaged zeta potential distributions for CEHR-11 diluted 100-fold in deionized water.

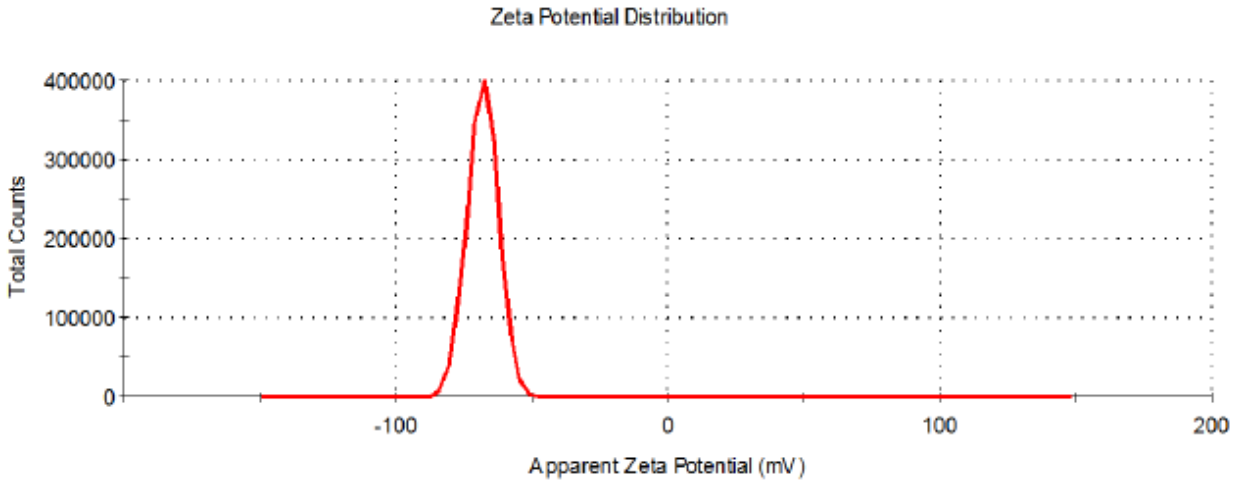

Sample	pH	Zeta Potential
CEHR-12	7.5	-68 ± 1 mV

Figure III-29. The averaged zeta potential distributions for CEHR-12 diluted 100-fold in deionized water.

IV. Silver

IV. Silver

A. Section Summary

Three silver nanoparticles with nominal sizes of 5, 25, and 75 nm (CEHR-13 to CEHR-15, respectively) stabilized with polyvinylpyrrolidone (PVP) were characterized for sterility and endotoxin contamination, as well as several physicochemical parameters. These included size (DLS and TEM) and polydispersity (AF4-DLS) measurements, zeta potential, total and free silver concentrations by inductively-coupled plasma mass spectrometry (ICP-MS) and quantitation of the PVP coating (TGA).

Sterility screening of CEHR-13 to CEHR-15 showed that all samples were free of bacterial contamination (Table IV-1). Endotoxin analysis revealed that all samples had approximately 2-5 EU/mg of endotoxin (Table IV-2). It is not known whether these levels of endotoxin would be problematic for subsequent biological studies; the effects of detected endotoxin would be dependent upon the tests being conducted and the dose of the material being used. Considerations of endotoxin impact on environmental studies involving engineered nanomaterials are reviewed in detail elsewhere (Petersen EJ, et al., Environ Sci Technol. 2014;48(8):4226-46).

Size analysis of the three silver nanoparticles was conducted using both dynamic light scattering (DLS) and transmission electron microscopy (TEM). The TEM measured sizes were fairly consistent with sizes reported by the manufacturer, whereas the DLS measured sizes were slightly larger. This is expected, as the manufacturer reported sizes are derived from TEM. The TEM analysis of CEHR-13 revealed a size of 5 nm, consistent with the manufacturer reported size (Table IV-3). By DLS, CEHR-13 showed two peaks in the intensity distribution; the major peak was approximately 100 nm, while the minor peak was approximately 15 nm (Table IV-4). However, by the volume distribution, the 15 nm peak was the predominant population in the sample. This hydrodynamic size range would be consistent with a TEM diameter of 5 nm. The TEM analysis of CEHR-14 revealed two distinct size populations in the sample, 7 nm and 24 nm (Figure IV-2). The 24 nm particles matched the theoretical size. The presence of the smaller particles suggests sample instability. By DLS, CEHR-14 also showed two peaks, one was approximately 47 nm, while the other was approximately 5 nm (Figure IV-5). The volume distribution suggested the 5 nm size was the predominant population in the formulation. CEHR-15 showed a TEM size of 83 nm, consistent with the manufacturer reported size (Table IV-3). By DLS, CEHR-15 showed a single peak approximately 120 nm (Table IV-4), in line with the expected size for a coated nanoparticle.

Asymmetric-flow field flow fractionation (AF4) was used to examine the size polydispersity of the silver nanoparticles. CEHR-13 and CEHR-14 contained two size populations while CEHR-15 only one, in agreement with the batch-mode DLS results. The major size population for CEHR-13 had a hydrodynamic size of 14-23 nm while the minor size population ranged from 46-160 nm (Figure IV-7), in good agreement with the batch mode DLS data. The major size population for CEHR-14 had a fairly constant hydrodynamic size of 25-26 nm while the minor size population ranged from 12-14 nm (Figure IV-8). This was in contrast to the batch-mode DLS in which a 5 nm population appeared to be the dominant population in the sample. The major 25 nm population was in agreement with the theoretical TEM size of the formulation, and may suggest the coating was dissociating from the silver nanoparticles. CEHR-15 had a hydrodynamic size range of 103-139 nm (Figure IV-9), in good agreement with the batch-mode DLS. Of note, a second peak was detected in CEHR-15; however, it contained only a UV signal and no detectable light scattering signal. The strong UV signal suggests it is dominant in the

solution, but the lack of a light scattering signal suggests it is very small. It is not known what this sample is; it was not detected by other sizing techniques.

Silver concentration, both total and free silver, as well as metal impurities in the samples, were measured by inductively coupled plasma-mass spectrometry (ICP-MS). Semi-quantitative analysis for all three samples revealed minor metal impurities (Figure IV-11), namely zinc (present in all three samples) and copper (only present in CEHR-14). The total silver concentrations for CEHR-13, CEHR-14, and CEHR-15 were 4.6, 4.5, and 4.5 mg/mL (Table IV-10), respectively. These are in good agreement with the manufacturer value of 5 mg/mL. The free silver content of each nanoparticle was also measured by ICP-MS. An increase in the free silver content can be an indication of particle instability, and in high enough concentrations can interfere with the proper interpretation of certain biological assays. The initial measurements showed some free silver in all three samples. CEHR-13 had the highest amount of free silver at 5% (Table IV-11). CEHR-14 and CEHR-15 had ≤ 1.2% free silver. By August 2016, all three samples exhibited an increase in the amount of free silver. CEHR-13 had the highest amount of free silver at 18%, CEHR-14 had 13%, and CEHR-15 had 2.5% free silver (Table IV-11).

The total mass silver concentrations were also determined using thermogravimetric analysis (TGA, Table IV-12). The TGA-measured silver concentration for CEHR-13 was about 50% higher than the theoretical value, while CEHR-14 and CEHR-15 silver concentrations were about 50% lower. This is in contrast to the ICP-MS results which showed very good agreement with the theoretical silver concentrations, suggesting that TGA, in this case, is not an ideal technique to measure total silver concentrations.

TGA was also used to determine the amount of coating (PVP, as reported by the manufacturer) on each of the silver nanoformulations. The percent mass ratios of coating to silver are summarized in Table IV-13 and were approximately 29%, 5%, and 15% for CEHR-13, CEHR-14, and CEHR-15, respectively. TGA could not confirm the identity of the coating or molecular weight of polymer. The surface charge of the nanoparticles was assessed by measuring the zeta potential. All three nanoparticles had negative zeta potentials (Table IV-14). This was in agreement with the expected range for PVP-stabilized silver nanoparticles, based on our prior experiences with similar particles.

B. Sterility

Design and Methods

Sterility, i.e. bacterial contamination, of the three silver nanoparticles was assessed using NCL protocol STE-2.2 (https://ncl.cancer.gov/resources/assay-cascade-protocols). In brief, samples were plated onto LB agar plates at several dilutions (10-, 100-, and 1000-fold) and allowed to incubate at 37°C for 72 hours. The plates were then visually inspected for colony formation.

Results & Conclusions

None of the three silver samples, CEHR-13, CEHR-14, or CEHR-15, showed visible colony formation after 72 hrs. A summary of these findings is provided in the table below.

Table IV-1. Summary of the sterility testing results for the silver nanoparticles.

Reference Number	Nanoparticle Description	Nominal size reported by manufacturer	Sterility (agar plate)
CEHR-13	Ag nanospheres with PVP 5 mg/mL	5 ± 2 nm	Negative
CEHR-14	Ag nanospheres with PVP 5 mg/mL	25 ± 5 nm	Negative
CEHR-15	Ag nanospheres with PVP 5 mg/mL	75 ± 5 nm	Negative

C. Endotoxin

Design and Methods

The objective of this experiment was to evaluate potential endotoxin contamination in the three silver nanoparticles. NCL's protocol for the kinetic turbidity Limulus Amebocyte Lysate (LAL) assay was used (STE-1.2; https://ncl.cancer.gov/resources/assay-cascade-protocols). All samples were initially diluted to 1 mg/mL theoretical concentration and tested at 1:5, 1:50, and 1:500 dilutions in water.

Results and Discussion

All three formulations had detectable endotoxin, approximately 2-5 EU/mg. The significance, i.e. biological consequence, of endotoxin in these formulations will depend on the test being conducted and the dose of the formulation used. The potential impact of endotoxin on environmental studies involving engineered nanomaterials are reviewed here: Petersen EJ, et al., Environ Sci Technol. 2014;48(8):4226-46.

Table IV-2. Endotoxin levels detected by the LAL assay. Results are shown as endotoxin units (EU) per mg of nanoparticle (vendor-supplied concentration).

Reference Number	Nanoparticle Description	Nominal size reported by manufacturer	Endotoxin Turbidity LAL
CEHR-13	Ag nanospheres with PVP 5 mg/mL	5 ± 2 nm	**1.9 EU/mg**
CEHR-14	Ag nanospheres with PVP 5 mg/mL	25 ± 5 nm	<5 EU/mg
CEHR-15	Ag nanospheres with PVP 5 mg/mL	75 ± 5 nm	**2.5 EU/mg**

D. Transmission Electron Microscopy

Design and Methods

Transmission electron microscopy (TEM) was conducted to assess the size and morphology of the nanomaterials. Stock solutions (2 µL) were applied to a glow discharged carbon film grid (Electron Microscopy Sciences). The grid was washed three times with ultrapure water, blotted, and allowed to air dry before imaging. Images were taken using a T-12 TEM (FEI) equipped with a LαB6 thermoionic gun at 80 V acceleration voltage.

Particle size analysis was performed using ImageJ (https://imagej.nih.gov/ij/). Only particles that were individually dispersed were included in the sizing analysis.

Results and Discussion

Representative TEM images and size histograms for each of the silver nanoparticles are shown in Figures IV-1 to IV-3 for CEHR-13, -14, and -15, respectively. For both CEHR-13 and CEHR-15, the measured size agreed well with the reported size (Table IV-1). CEHR-14, on the other hand, had two distinct size populations in the sample (Figure IV-2). One population was 24 nm, in good agreement with the theoretical size. The second population was smaller particles (7 nm) that were similar in size to CEHR-13. It is possible that these small particles have "shed" from the larger particles, and may be an indication of particle instability. A more extensive analysis of the TEM images would be required to better quantitate the ratio of these two populations. DLS analysis, however, suggests the smaller particles are the dominant species (see next section, Figure IV-6).

Additionally, CEHR-15 appeared to have hexagonal particles (Figure IV-3). The edges of the particles in this sample were straighter and many clearly six-sided shapes were present in this sample (rather than spheres as seen in CEHR-13 and CEHR-14). Table IV-1 summarizes the measured sizes in comparison to the nominal sizes.

Table IV-3. Comparison of vendor reported size and TEM-measured size.

Reference Number	Nanoparticle Description	Nominal size reported by manufacturer	TEM Measured Size
CEHR-13	Ag nanospheres with PVP 5 mg/mL	5 ± 2 nm	5 ± 1 nm
CEHR-14	Ag nanospheres with PVP 5 mg/mL	25 ± 5 nm	7 ± 2 nm & 24 ± 5 nm
CEHR-15	Ag nanospheres with PVP 5 mg/mL	75 ± 5 nm	83 ± 9 nm

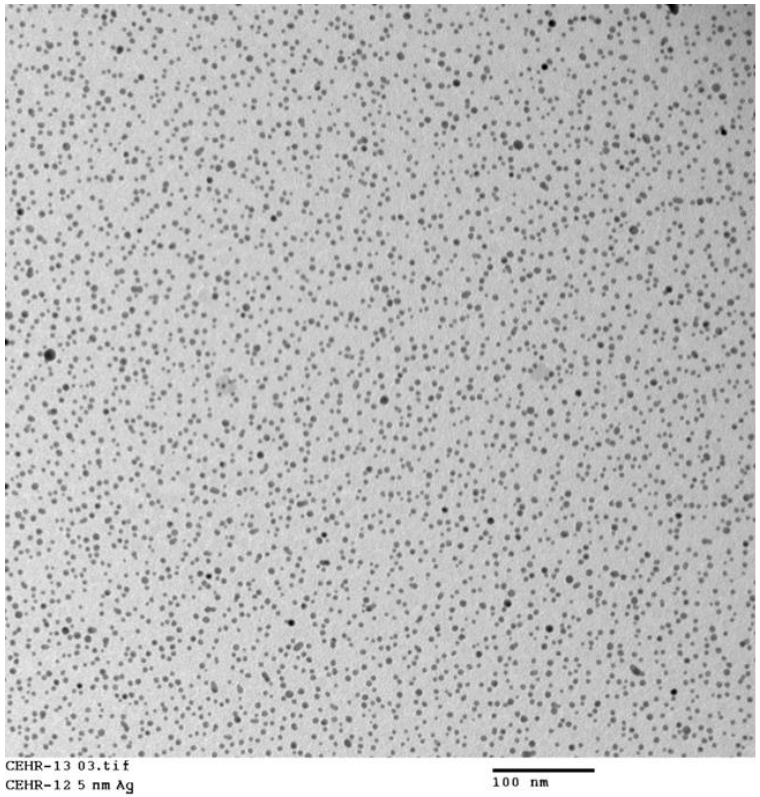

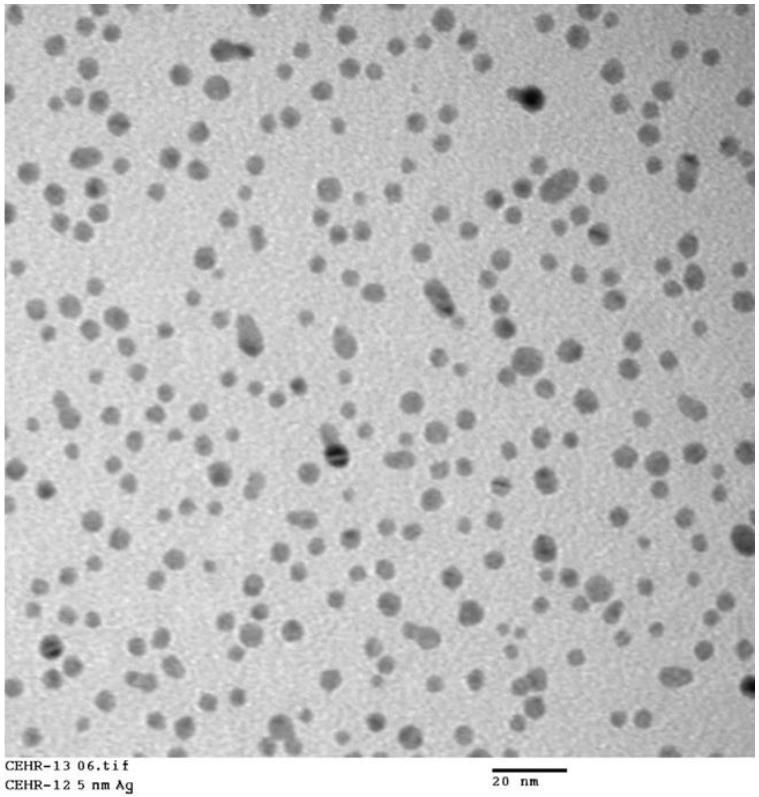

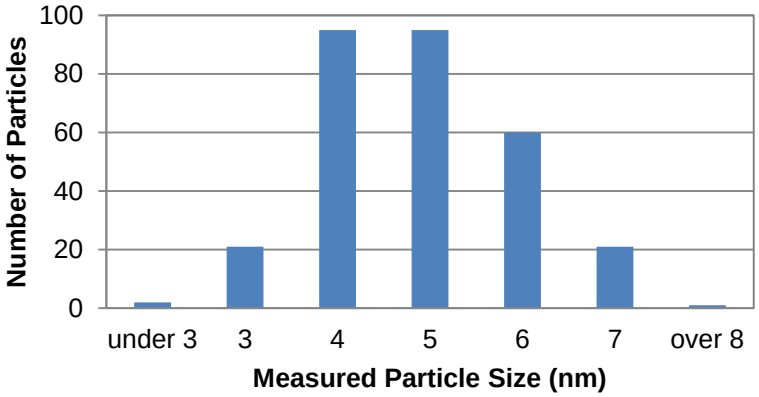

Figure IV-1. Representative TEM Images of CEHR-13. Two representative images are shown for CEHR-13, showing the range of average diameters spanning 5 ± 1 nm (n = 291).

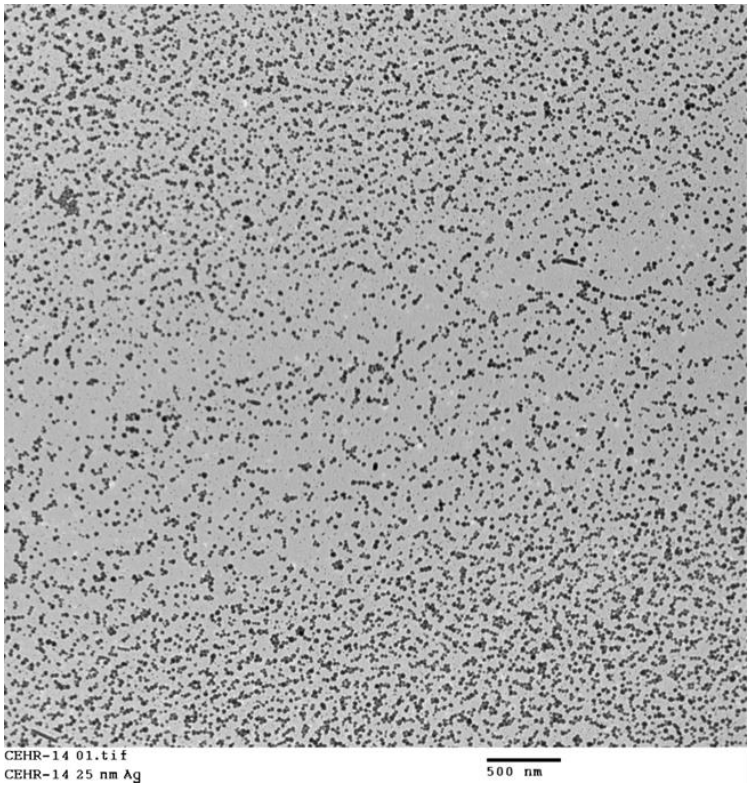

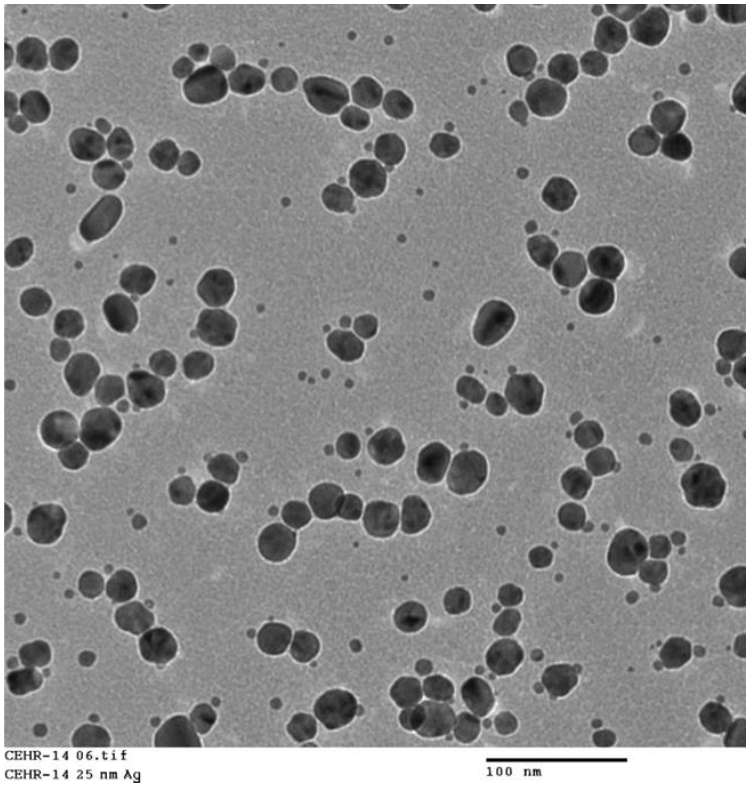

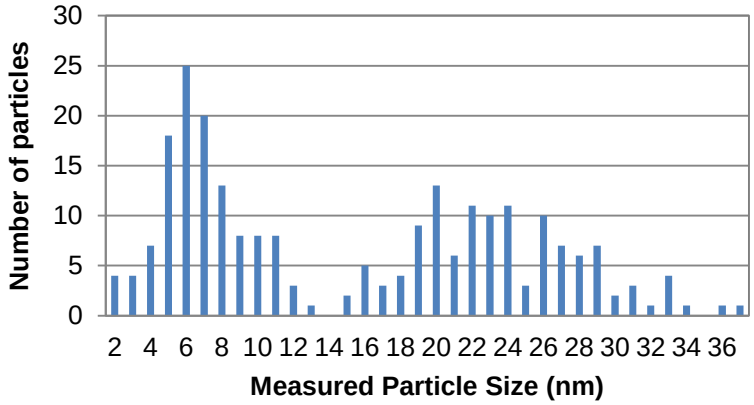

Figure IV-2. Representative TEM Images of CEHR-14. Two representative images are shown for CEHR-14, showing two distinct populations. The average diameter of the smaller population was 7 ± 2 nm (n = 119), while the average diameter of the larger population was 24 ± 5 nm (n = 120). The overall average diameter for the entire sample population was 16 ± 9 nm (n = 239).

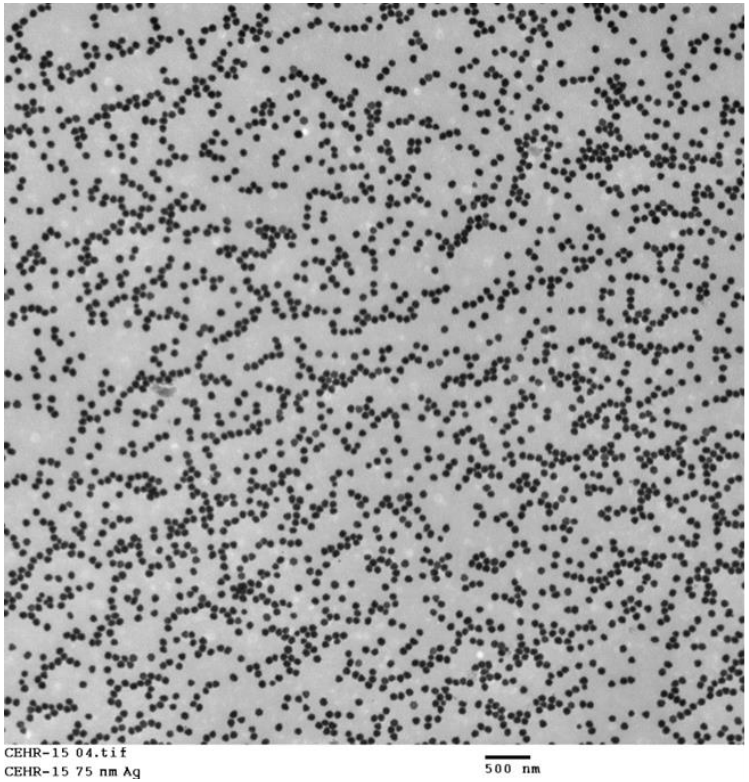

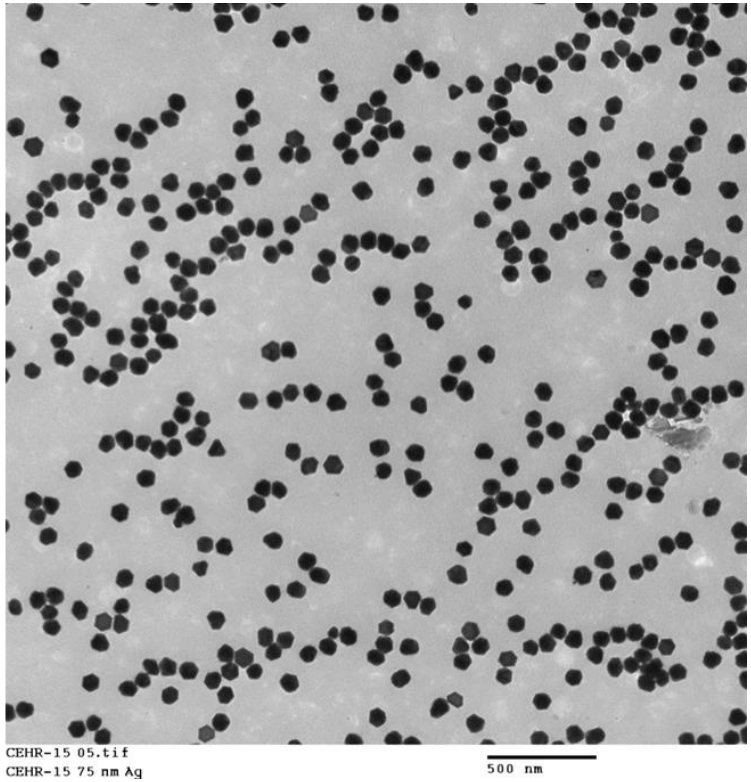

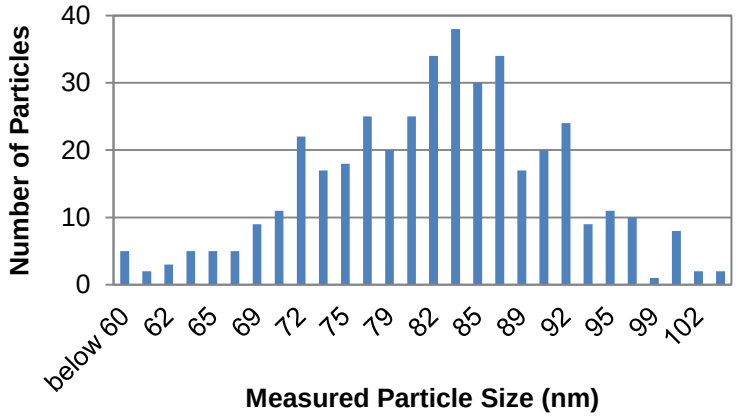

Figure IV-3. Representative TEM Images of CEHR-15. Two representative images are shown for CEHR-15, showing the range of average diameters spanning 83 ± 9 nm (n = 412).

E. Hydrodynamic Size/Size Distribution via Dynamic Light Scattering

Design and Methods

A Malvern Zetasizer Nano ZS instrument (Southborough, MA) with back scattering detector (173°) was used for measuring the hydrodynamic size (diameter) in batch mode. NIST-NCL joint protocol PCC-1 was followed (https://ncl.cancer.gov/resources/assay-cascade-protocols). Stock samples of CEHR-13 through CEHR-15 were diluted 10-, 100-, or 1,000-fold in water. At least two dilutions were measured for each sample. Measurements were made at 25°C in a quartz microcuvette. Traces in the figures represent the average of at least twelve measurements.

Hydrodynamic diameters are reported as the intensity-weighted average and as the volume-weighted average over a particular range of size populations corresponding to the most prominent peak. The Int-Peak value is used as the hydrodynamic diameter of a particular species. The Vol-Peak and %Vol values are used to approximate relative amounts of various species in the formulation. Z-Avg values are generally used to assess batch-to-batch variability of a sample.

Results and Discussion

The PVP-coated silver nanoparticles from nanoComposix were diluted in water and measured by DLS for hydrodynamic diameter. The intensity and volume distribution plots are provided in Figures IV-4 to IV-6, and a summary of the sizes is provided in the corresponding tables below each figure. A comparison of the DLS measured sizes to the measured and theoretical TEM sizes is provided in Table IV-4 below.

CEHR-13 is reported to have a 5 nm TEM diameter by the manufacturer. The volume distribution of the DLS measurement showed a peak close to the theoretical size, at about 15 nm. DLS hydrodynamic sizes are expected to be larger than TEM-measured sizes; thus, 15 nm appeared to be in line with the expected size for this nanoparticle. However, the Int-Peak distribution showed two peaks. The major peak was approximately 100 nm, while the minor peak was approximately 15 nm (Figure IV-4). The presence of the roughly 100 nm peak suggests the sample may be aggregating either in the stock solution itself or upon dilution. Although the 100 nm peak was the dominate species in the intensity distribution, the volume distribution suggests the smaller 15 nm peak was the major population. Larger particles scatter more light and will dominate the DLS distribution signal, as evidenced in the comparison between the intensity and volume distribution plots.

CEHR-14 is reported to have a 25 nm TEM diameter by the manufacturer. Similar to the previous sample, this sample had a single peak in the volume distribution and two major peaks in the intensity distribution. The intensity distribution had a major peak at approximately 47 nm and a minor peak at approximately 5 nm (Figure IV-5). The major peak in the intensity distribution was somewhat larger than expected for a PVP-coated particle of this size (based on our prior experiences with similar particles), but was not entirely unrealistic. The volume distribution showed a single 5 nm peak, and was the dominate species in the formulation. This smaller particle was also evident in the TEM analysis of the sample (see Figure IV-2).

CEHR-15 is the 75 nm silver nanoparticle. This measured DLS size was approximately 120 nm by Int-Peak and 102 nm by Vol-Peak. Both distributions were monodisperse and showed no change in size upon dilution. The Int-Peak size was again somewhat larger than anticipated

based on our prior experience but was not improbable depending on the size of the PVP polymer coating. The size of the PVP was not disclosed by the manufacturer and sample quantities were too limited to measure.

Table IV-4. Comparison of TEM and DLS sizes.

Reference Number	Nominal size reported by manufacturer	TEM Measured Size	DLS Measured Size (Int-Peak)
CEHR-13	5 ± 2 nm	5 ± 1 nm	117 ± 3 nm
CEHR-14	25 ± 5 nm	7 ± 2 nm & 24 ± 5 nm	47 ± 1 nm
CEHR-15	75 ± 5 nm	83 ± 9 nm	121 ± 2 nm

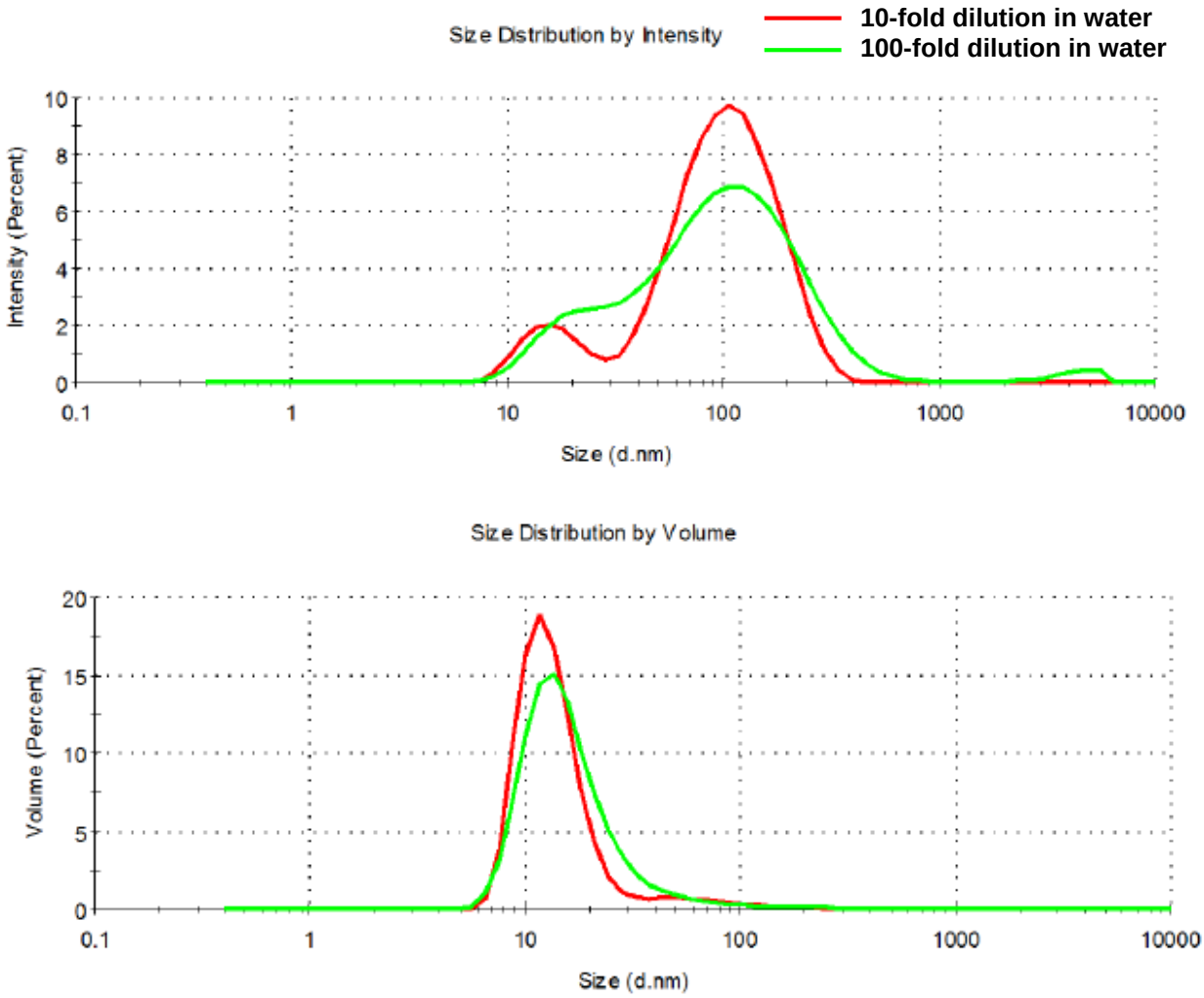

Figure IV-4. The averaged intensity and volume distribution plots for CEHR-13 diluted in water.

Table IV-5. Summary of the hydrodynamic size for CEHR-13 diluted in water.

Dispersing Medium	Dilution	Z-Avg, nm	PdI	Int-Peak, nm	% Int	Vol-Peak, nm	% Vol
DI water	10-fold	65 ± 1	0.45 ± 0.02	117 ± 3	88 ± 2	14 ± 3	96 ± 2
DI water	100-fold	62 ± 6	0.50 ± 0.02	128 ± 9	87 ± 13	19 ± 3	100 ± 0

Note: Results are the average of at least 12 measurements. Z-Avg is the intensity-weighted average. PdI is the polydispersity index. Int-Peak is the intensity-weighted average over the primary peak. % Int is the percentage of the intensity spectra occupied by the primary peak. Vol-Peak is the volume-weighted average over the primary peak. % Vol is the percentage of the volume spectra occupied by the primary peak.

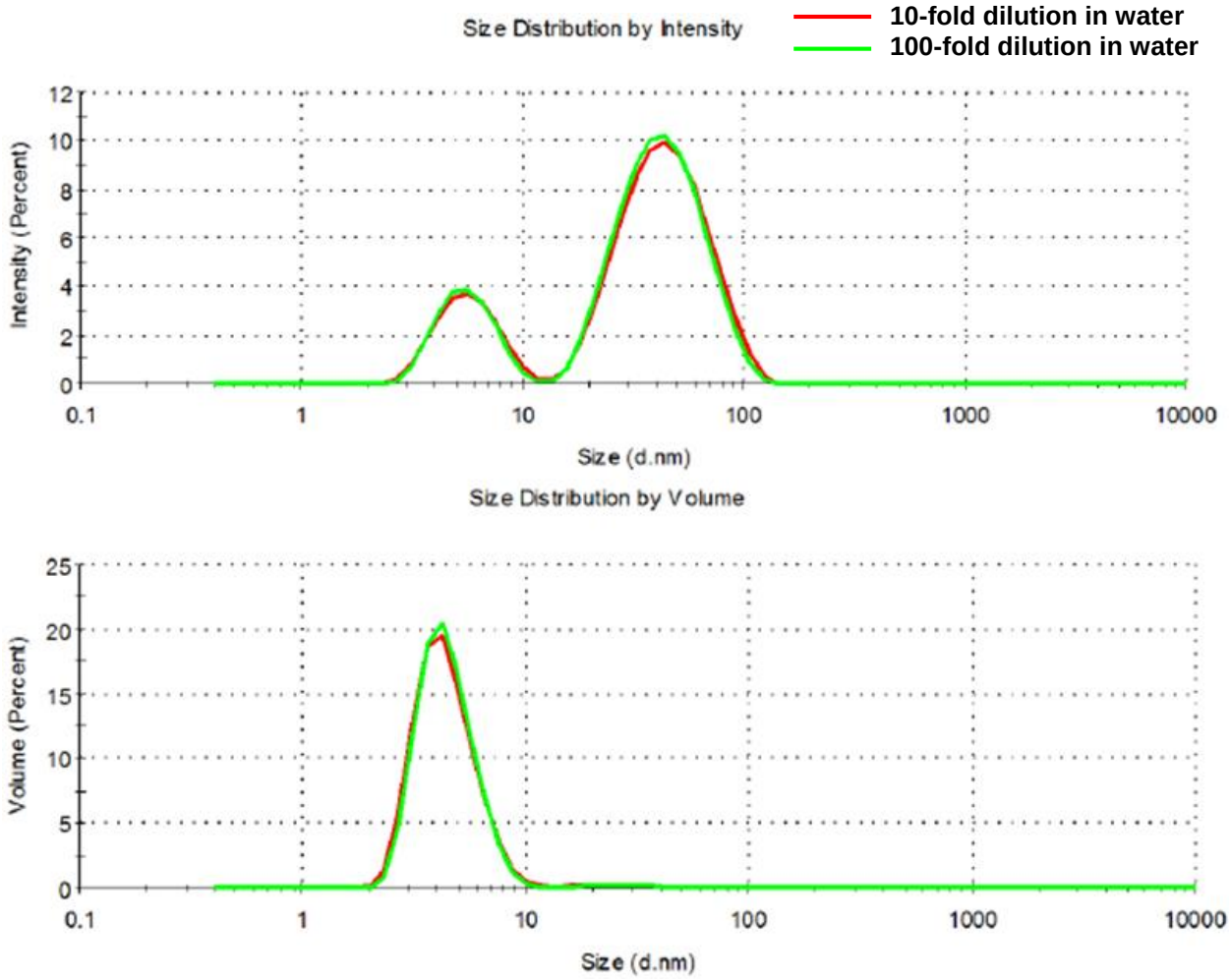

Figure IV-5. The averaged intensity and volume distribution plots for CEHR-14 diluted in water.

Table IV-6. Summary of the hydrodynamic size for CEHR-14 diluted in water

Dispersing Medium	Dilution	Z-Avg, nm	PdI	Int-Peak, nm	% Int	Vol-Peak, nm	% Vol
DI water	100-fold	20 ± 0	0.56 ± 0.01	47 ± 1	79 ± 1	5 ± 0	99 ± 0
DI water	1000-fold	20 ± 0	0.55 ± 0.01	46 ± 1	79 ± 1	5 ± 0	99 ± 0

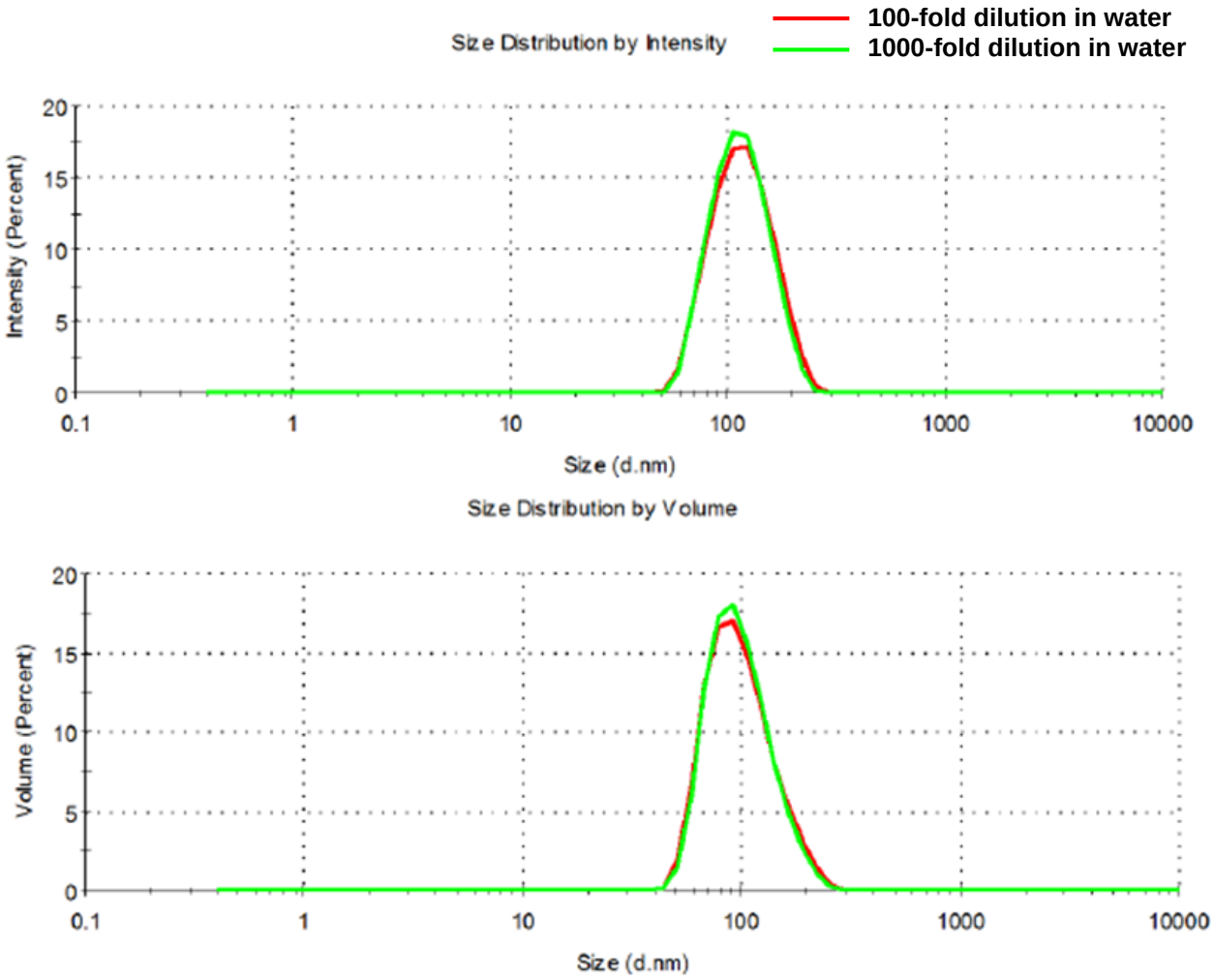

Figure IV-6 The averaged intensity and volume distribution plots for CEHR-15 diluted in water.

Table IV-7. Summary of the hydrodynamic size for CEHR-15 diluted in water

Dispersing Medium	Dilution	Z-Avg, nm	PdI	Int-Peak, nm	% Int	Vol-Peak, nm	% Vol
DI water	100-fold	110 ± 1	0.08 ± 0.02	121 ± 2	100 ± 0	103 ± 1	100 ± 0
DI water	1000-fold	109 ± 0	0.07 ± 0.02	118 ± 2	100 ± 0	102 ± 1	100 ± 0

F. Asymmetric-Flow Field Flow Fractionation

Design and Methods

The silver nanoparticles were separated using asymmetric-flow field-flow fractionation (AF4) with multiple in-line detectors to evaluate the polydispersity of the samples. AF4 provides a more thorough understanding of the various populations present in the sample over other batch-mode measurement techniques such as DLS alone. The AF4 system consisted of an isocratic pump (Agilent G1310A, Palo Alto, CA), well-plate autosampler (Agilent G1329A), AF4 separation channel (Eclipse DualTec; Wyatt Technology, Santa Barbara, CA), multi-angle light scattering detector (HELEOS II; Wyatt Technology), diode array detector (DAD, Agilent G1315B), and a DLS detector (Malvern Zetasizer Nano ZS; Southborough, MA). The separation channel had a length of 275 mm and a 350 µm spacer. A 10 kDa regenerated cellulose membrane was used for all separations.

The elution profile is provided in Table IV-8. The cross flow was controlled by an Eclipse flow controller. CEHR-13 was diluted 10-fold; CEHR-14 was diluted 20-fold; CEHR-15 was diluted 30-fold. All samples were diluted and run in 15 mM NaCl filtered through a 0.2 µm regenerated cellulose membrane prior to use. The nanoparticles did not interact/stick to the FFF membrane under these conditions. A sample injection of volume of 100 µL was used for all samples and the chromatographic traces were monitored by DLS detection and UV at 210 nm. The hydrodynamic size is plotted across the eluted peaks. The UV absorbance at 210 nm was monitored to track relative abundance of each size population.

Table IV-8. AF4 elution profile.

Start Time (min)	End Time (min)	Duration (min)	Mode	Starting Cross-flow Rate (mL/min)	Ending Cross-flow Rate (mL/min)
0	2	2	Elution	1	1
2	4	2	Focus	-	-
4	9	5	Focus + Inject	-	-
9	19	10	Focus	-	-
19	29	10	Elution	1	1
29	31	2	Elution	1	0.5
31	41	10	Elution	0.5	0
41	61	20	Elution	0	0
61	63	2	Elution + Inject	0	0
63	64	1	Elution	0	0

Results and Discussion

The fractograms for CEHR-13 are shown in Figure IV-7. The light scattering (top and bottom panel) signals showed two peaks. The first peak corresponded to the major population in the sample (as evidenced by its strong UV signal) and had a hydrodynamic size of 14-23 nm. The second peak had a polydispersed size distribution ranging from 46-160 nm. The flow-mode DLS results agreed with the batch-mode DLS results (Table IV-9). Although two peaks were seen in the batch-mode DLS intensity distribution, larger particles scatter more light and will dominant the batch-mode light scattering signal. By volume distribution, only one peak was observed at 14 nm, implying this was the dominant species in the formulation, in agreement with the flow-mode DLS. In both cases, the measured sizes were slightly larger than the nominal size of 5 nm. However, the nominal reported size is a TEM-measured size. The larger DLS hydrodynamic sizes are in line with the expected range for a 5 nm TEM particle.

The fractograms for CEHR-14 are shown in Figure IV-8. The light scattering signals showed two overlapping peaks. The first peak corresponded to the major population in the sample (as evidenced by its strong UV signal) and had a fairly constant hydrodynamic size of 25-26 nm. The second peak had a fairly uniform size distribution ranging from 12-15 nm. Note, this size population was present in very low amounts as evidenced by its almost non-existent UV signal. The flow-mode DLS results were not in complete agreement with the batch-mode DLS results (Figure IV-5). While batch-mode DLS showed two populations as well, the major species appeared to be 5 nm, while the minor species appeared to be 47 nm. The 25 nm major peak seen by flow-mode DLS was in agreement with the larger of the two TEM populations observed, but was expected to be a bit larger due to the surface coating. PVP is not conjugated to the surface of the silver nanoparticles, but merely coats the nanoparticles. It is possible the PVP is dissociating from the silver nanoparticles during the AF4 run, and hence decreasing the hydrodynamic diameter. This is not seen with the other two silver formulations, but CEHR-14 showed signs of instability from TEM (Figure IV-2) and hence may be more susceptible to this dissociation.

The CEHR-15 fractograms are shown in Figure IV-9. The light scattering signal showed one peak. This peak, eluting at about 40 min, had a polydispersed size distribution ranging from 103-139 nm. This agreed with the batch-mode DLS result of 121 nm (Table IV-4), and these hydrodynamic sizes are in the expected range for a TEM-measured size of 83 nm. The AF4-DLS also showed an additional peak by the UV signal, but had no detectable light scattering signal. The strong UV signal suggests this was the major population in the sample, whereas the lack of a light scattering signal suggests this population had a very small size. It is unclear what this population is, as it was undetected by other sizing techniques.

Table IV-9. Comparison of Batch-mode and Flow-mode DLS sizes.

Reference Number	Batch-mode DLS Measured Size (Int-Peak)	Flow-mode DLS Measured Size: Major peak	Flow-mode DLS Measured Size: Minor peak
CEHR-13	117 ± 3 nm	14-23 nm	46-160 nm
CEHR-14	47 ± 1 nm	25-26+ nm	12-15 nm
CEHR-15	121 ± 2 nm	103-139 nm	-

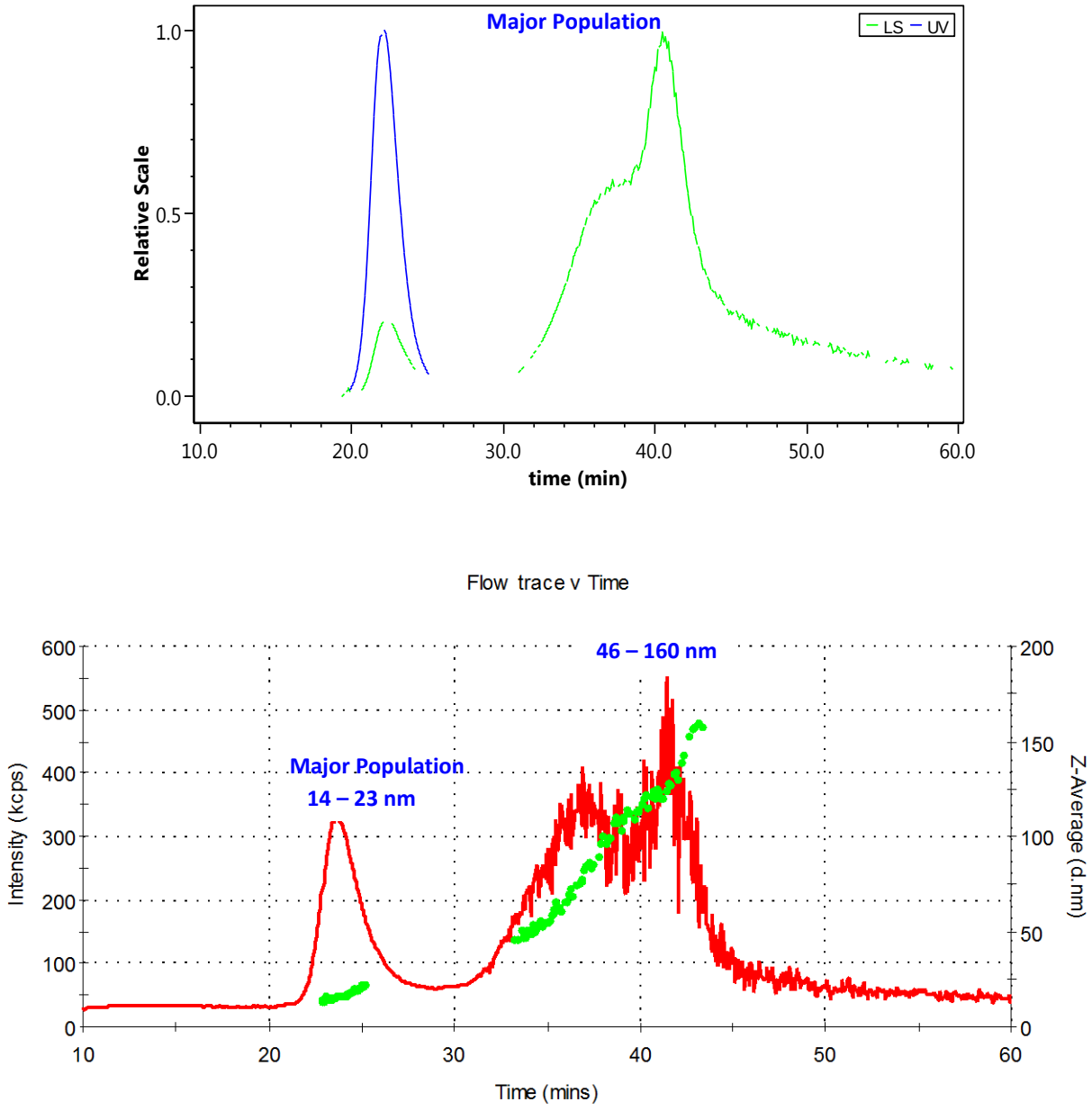

Figure IV-7. AF4 fractograms for CEHR-13. The top panel shows the UV (210 nm) and LS (light scattering) signals while the bottom panel shows the hydrodynamic size distributions across the eluted peaks.

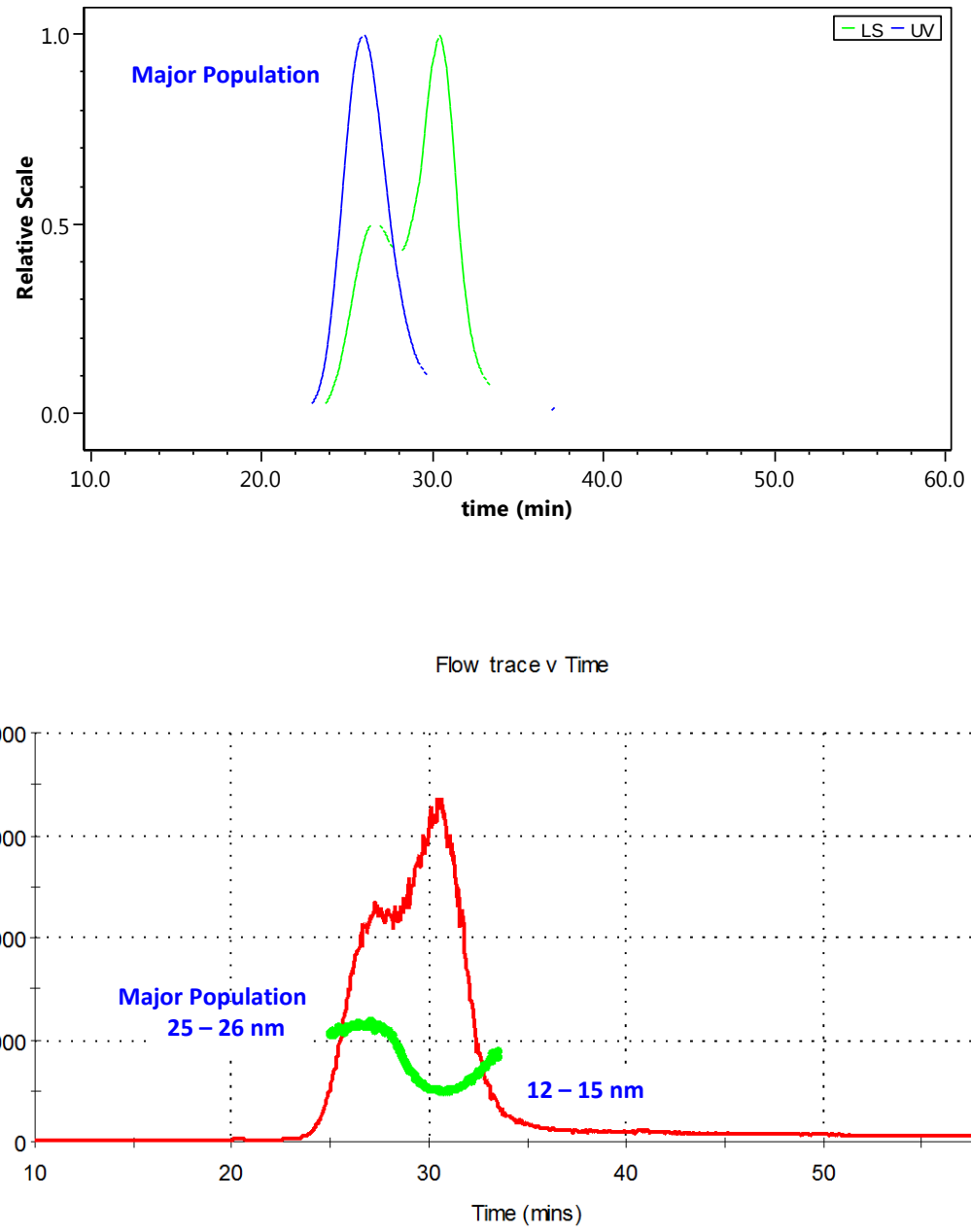

Figure IV-8. AF4 fractograms for CEHR-14. The top panel shows the UV (210 nm) and LS (light scattering) signals while the bottom panel shows the hydrodynamic size distributions across the eluted peaks.

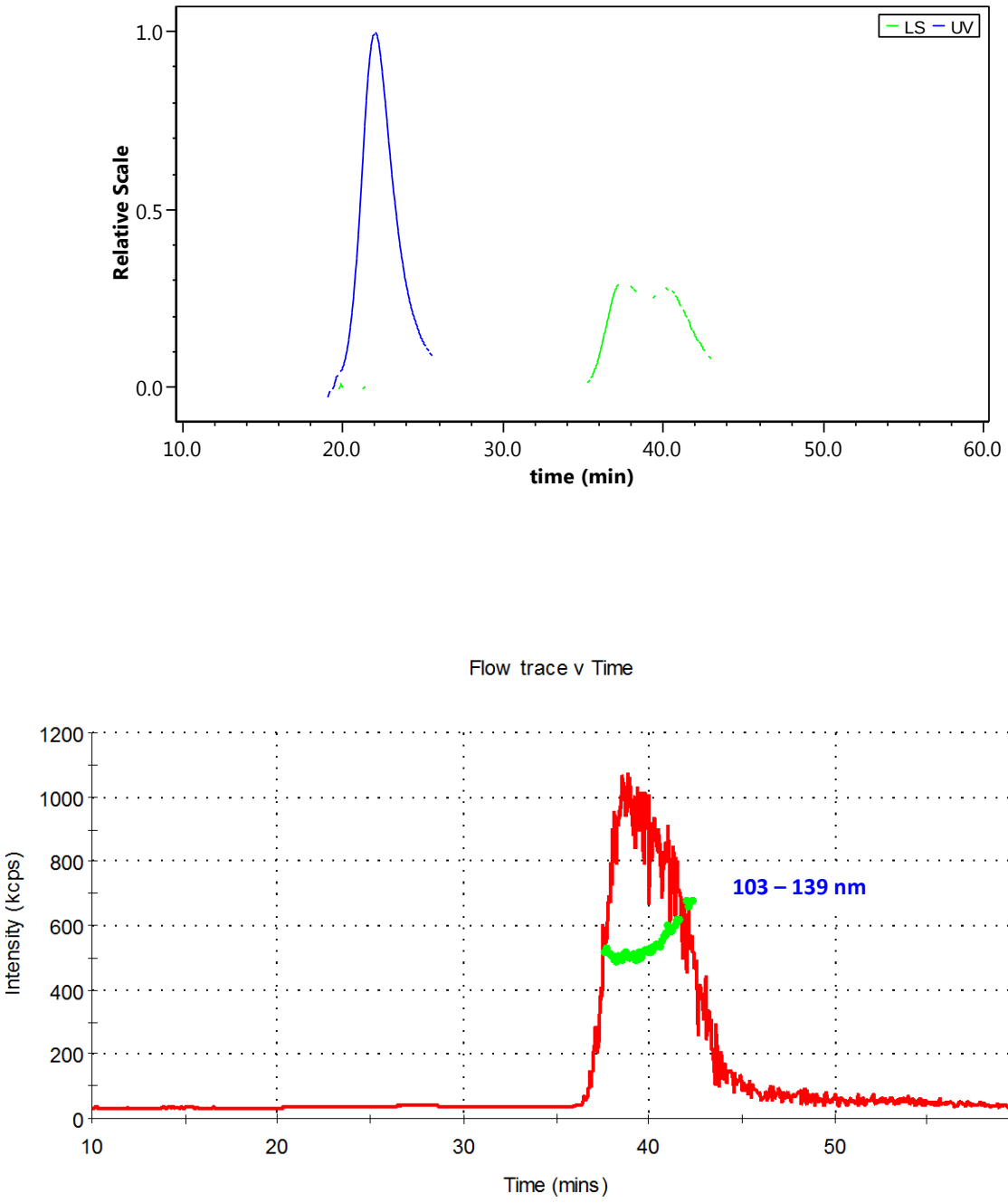

Figure IV-9. AF4 fractograms for CEHR-15. The top panel shows the UV (210 nm) and LS (light scattering) signals while the bottom panel shows the hydrodynamic size distributions across the eluted peaks.

G. Inductively Coupled Plasma Mass Spectrometry

Design and Methods

The silver concentrations of CEHR-13 through CEHR-15 were determined by inductively coupled plasma mass spectrometry (ICP-MS). An Agilent ICP-MS 7500CX equipped with a micro-mist nebulizer, standard sample introduction system, and integrated auto-sampler, operated in “no gas” mode in Agilent’s proprietary ORS (Octopole Reaction System) was used. Tuning of the instrument was performed daily prior to sample testing.

Semi-Quantitative Analysis

A semi-quantitative analysis was performed on each sample prior to quantitative determination of the silver concentrations. The semi-quantitative analysis was performed to help determine the proper dilution range for the samples, as well as to detect the presence of other metals in the sample. Only metals with counts two times greater than the background were denoted.

A 25 µL aliquot of the silver nanoparticle stock solution was digested using 200 µL concentrated nitric acid. After 10 minutes, this digested sample was vortexed for 10 seconds and then diluted with water to target a 30 mL first dilution. Next, a second dilution was performed by adding 10 mL of 2% nitric acid to 100 µL of the first dilution.

Total Metal Concentration

Using the data from the semi-quantitative analysis, the appropriate dilution was determined for the ICP-MS full quantitative analysis. The dilution target for the samples was 5 to 200 ppb. The total metal concentration was determined using the native formulation (i.e. not centrifuged or separated). Samples (10-100 µL) were initially digested with nitric acid. Typically, no more than a total of 1 mL of concentrated acid was used. The acid digested samples were then further diluted to approximately 30-50 mL total volume with 2% nitric acid. A second dilution was then performed in which 10-100 µL of the first dilution was diluted to 10-50 mL using 2% nitric acid. Samples were run in duplicate.

The metal concentration in the samples was determined by comparing against a series of calibration standards prepared from NIST SRM 3151. A dilution of 5000 ng Ag/g in 2% HNO_3 was used to make a 1000 ng Ag/g solution, which was then used to create standards for the calibration curve in a range of 5 to 200 ng/g in 10 mL volumes. The dilutions were made using 2% nitric acid. In addition, an internal standard, indium, was used to track the signal response of the ICP-MS. The internal standard was diluted to approximately 50 ppb and was mixed with the sample using a sample T. A simple linear regression was used for calculation of the metal concentrations.

The sequence for the ICP-MS runs consisted of five blanks, the calibration curve standards ordered from lowest to highest, five more blanks, then the silver nanoparticle samples. Each sample was run in duplicate with three blanks between each sample. After the last silver sample was measured, five blanks were run, followed by the calibration standards once again. Three blanks were run following completion of the ICP-MS runs to flush the sample introduction system.

Free Metal Concentration

In addition to determining the total metal concentration present in each sample, ICP-MS was also used to assess the amount of free metal ions present. The separation of free metal ions from the nanoparticles was carried out using stirred cell filtration. This technique was chosen because it allows for separation of a wide range of the supplied nanomaterials. The nanoparticles have variations in densities and coatings, which can affect the separation efficiency in other techniques such as centrifugation. Stirred cell filtration allows only small metal ions to pass through a membrane filter while larger nanoparticles are blocked from passing through the filter.

Free metal ions were separated from the nanoparticles using a Millipore 10 mL stirred cell apparatus and a 10 kDa molecular weight cut-off (MWCO; approximate pore size is 5-7 nm) regenerated cellulose membrane (Millipore) as depicted in Figure IV-10. To prepare the sample, the nanoparticle (25 µL) was diluted in 10 mL deionized water (18.2 MΩ-cm); 0.5 mL of the solution (or "reserved") was retained for analysis. The remaining solution (9.5 mL) was added to the stirred cell apparatus. The separation started with a constant stream of nitrogen to provide a downward pressure and force the liquid through the 10 kDa MWCO membrane. In addition, a magnetic stir bar was used to create a consistent solution and avoid buildup of nanoparticles on the membrane surface. The free metal ions freely passed through the membrane as the "permeate". The nanoparticles, which are larger than the pores of the membrane, are left behind as the "retentate."

The samples were prepared for ICP-MS by taking an aliquot of the reserved, retentate, and permeate solutions from the stirred cell separation. The reserved and retentate solutions were diluted to 10x and 100x dilutions in 2% HNO_3 to target the appropriate analysis range for ICP-MS quantitation. The permeate solution was used undiluted and diluted 10x in 2% HNO_3 to target the appropriate range. The dilution factors were based on prior calculation of the total metal concentration.

To calculate the percentage of free metal ions in the nanoparticle, the concentration of total metal in the reserved and permeate solutions were determined. To calculate the total metal concentration, the total dilution factor was calculated and the factor was applied to the ICP-MS result. The percent of free metal ions was calculated as follows:

$$\frac{Free\ metal\ ions\ from\ permeate\ (\frac{mg}{g})}{Total\ metal\ ions\ from\ reserved\ (\frac{mg}{g})} \times 100\% = \%\ free\ metal\ ions$$

Metal Release with Time

The stirred cell separation as described above was performed twice on each sample at different times. The purpose of this was to evaluate the release of free metal ions over time, providing a measure of the shelf-life stability of the materials. The dates are noted for each analysis.

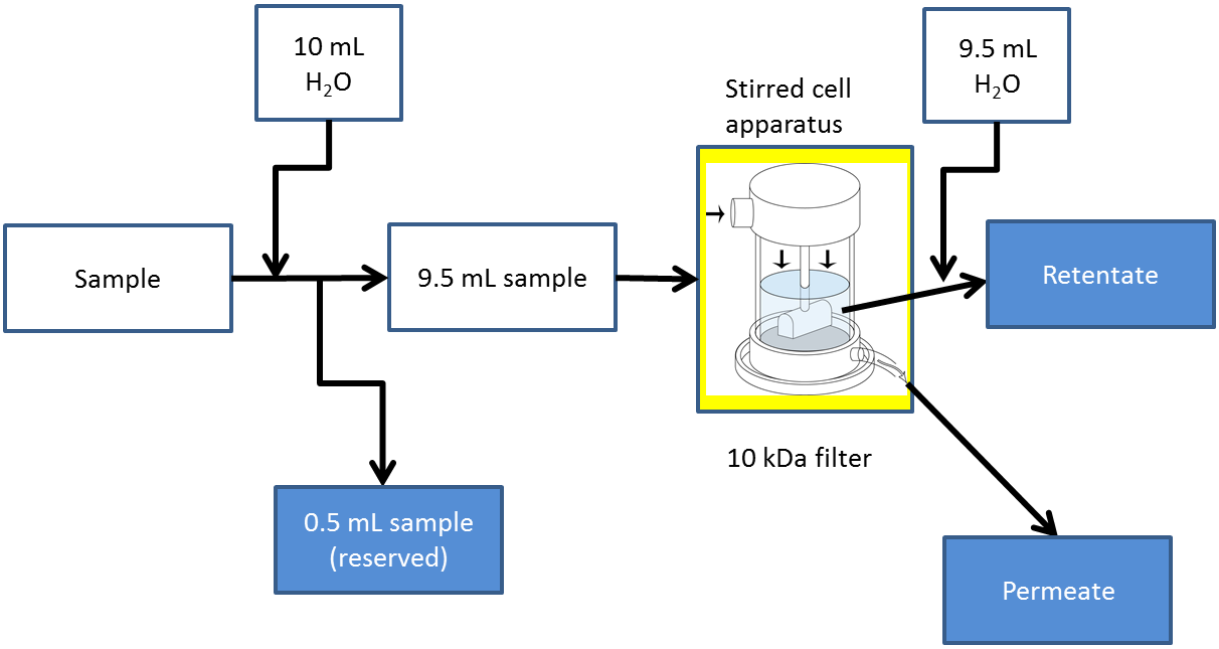

Figure IV-10. Illustration of the stirred cell technique used for quantitation of free metal ions.

Results and Discussion

Semi-Quantitative Analysis

The results from the semi-quantitative analysis of CEHR-13, -14, and -15 are shown in Figure IV-11. For all three samples, silver and zinc were detected by the semi-quantitative analysis. A third metal, copper, was detected in CEHR-14. The origin of the zinc and copper impurities is not known. This was only an analysis to detect potential metal impurities. For an accurate determination of their concentrations, quantitative analysis compared to a standard would be required.

A. CEHR-13

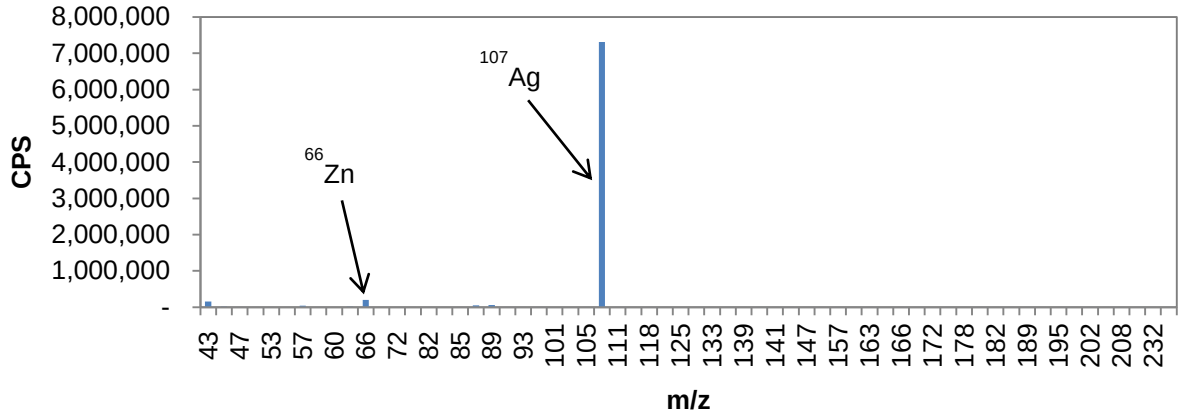

B. CEHR-14

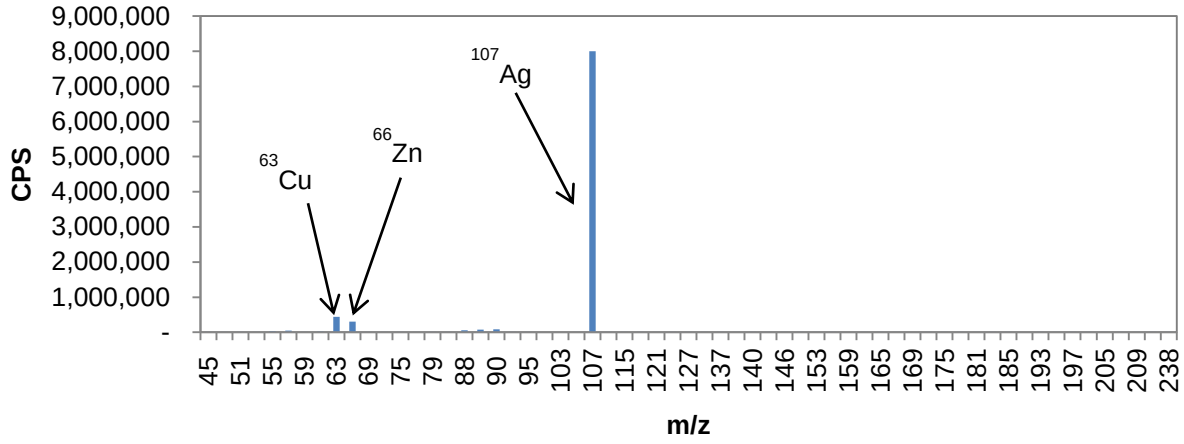

C. CEHR-15

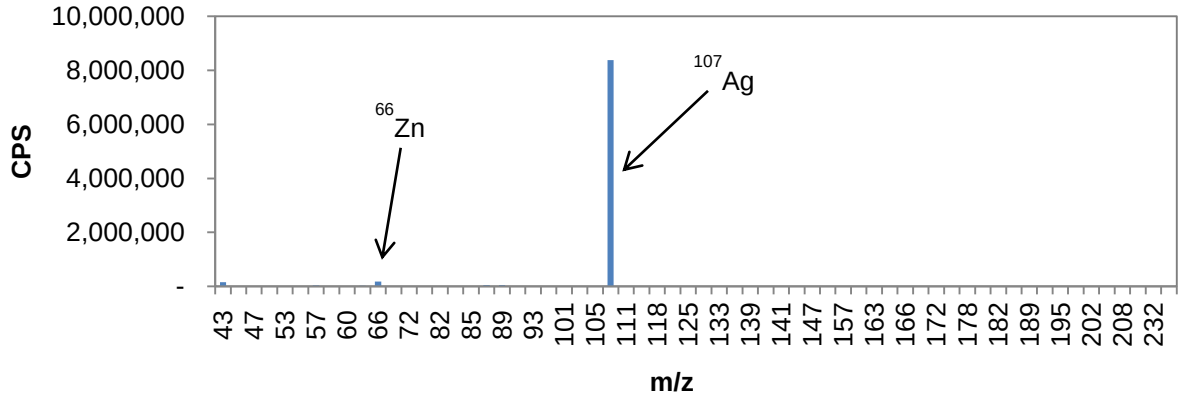

Figure IV-11. Plots of CPS vs m/z. (A) CEHR-13 semi-quantitative analysis plot. **(B)** CEHR-14 semi-quantitative analysis plot. **(C)** CEHR-15 semi-quantitative analysis plot. Samples were analyzed on 28 September 2016. Note ^{12}C, ^{24}Mg, ^{27}Al, ^{29}Si, ^{31}P, ^{34}S, ^{35}Cl, ^{39}K, and ^{43}Ca were removed in all three plots to better visualize the smaller peaks. The internal standard peak for ^{115}In was also omitted.

Full Quantitative Analysis: Total Silver Concentration
The calibration curve used for total silver quantitation was constructed from NIST SRM 3151 (Figure IV-12). Quantitative total silver concentrations for CEHR-13, CEHR-14, and CEHR-15 are summarized in Table IV-10. The ICP-MS silver concentrations, in units of mg/g, were converted to mg/mL by using the measured weight/volume for each sample. The silver concentrations for CEHR-13, CEHR-14, and CEHR-15 were 4.2, 4.3, and 4.8 mg/mL, respectively. The total silver concentration of CEHR-15 was in very good agreement with the theoretical concentration, whereas CEHR-13 and CEHR-14 were approximately 15% lower than theoretical. All three formulations had theoretical concentrations of 5 mg/mL.

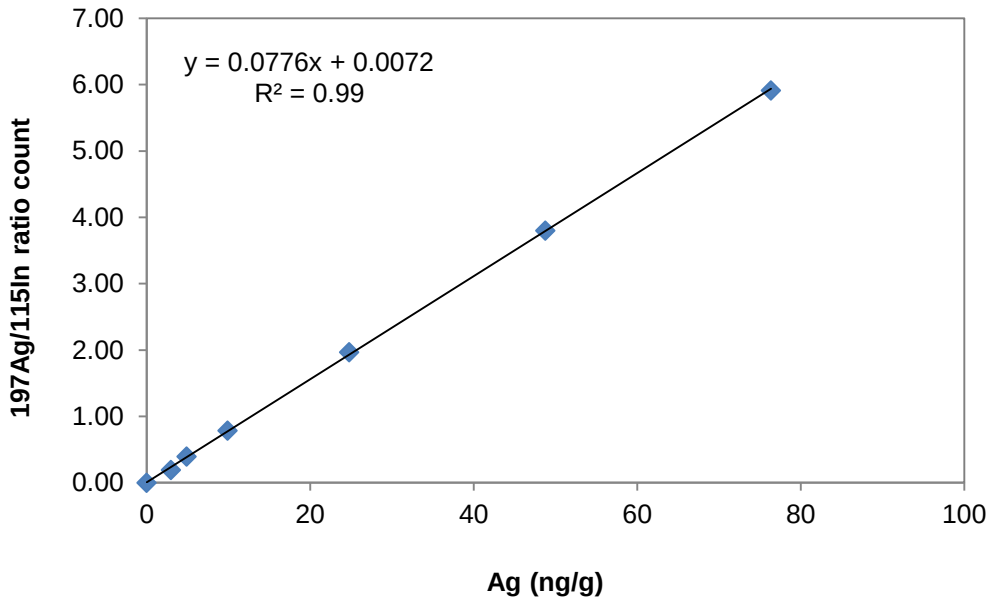

Figure IV-12. Silver Calibration Curve. A typical calibration curve ranging from 0 to 75 Ag ng/g, used to calculate the silver concentration in CEHR-13, CEHR-14, and CEHR-15. The calibration curve was constructed from NIST SRM 3151 silver standard.

Table IV-10. Summary of the total silver concentration in CEHR-13, CEHR-14, and CEHR-15 as determined by ICP-MS.

Reference Number	Reported Concentration	Total [Ag]	Total [Ag]*
CEHR-13	5 mg/mL	4.52 ± 0.05 mg/g (n=3)	4.62 ± 0.05 mg/mL
CEHR-14	5 mg/mL	4.54 ± 0.05 mg/g (n=3)	4.51 ± 0.05 mg/mL
CEHR-15	5 mg/mL	4.49 ± 0.04 mg/g (n=3)	4.49 ± 0.04 mg/mL

* Calculated from mg/g by using the measured weight/volume of each sample.

Free Silver Concentration

Stirred cell filtration was employed to separate any free silver ions from the silver nanoparticles. Repeat measurements were made approximately three months apart to assess silver release kinetics/stability of the formulation. The stock sample (prior to stirred cell filtration; designated as Total [Ag] in Table IV-11) was re-measured each time and used to calculate (normalize) the percent free silver (free [Ag] / total [Ag]) in each formulation.

The results for CEHR-13, CEHR-14, and CEHR-15 are shown in Table IV-11. The initial measurements (June 2016) showed some free silver in all three samples. CEHR-13 had the highest amount of free silver at 5.1%. CEHR-14 had 1.2% and CEHR-15 had the lowest free silver at 0.4%. After three months of additional storage at 4°C, all three samples showed an increase in the amount of free silver, indicating release over time. Relative to the initial free silver quantities detected, roughly 3.5-, 11-, and 6-fold increases in free silver were detected for CEHR-13, CEHR-14, and CEHR-15, respectively.

Importantly, the membrane used for separation of the free silver ions had a pore size of approximately 5-7 nm. It is possible that some amount of the CEHR-13 nanoparticles, as well as the small sized nanoparticles detected in CEHR-14, passed through the filter which would artificially increase the free silver concentrations. We did not evaluate these permeates by DLS or TEM to rule this out; however, our previous experience with similar particles dictates that very little, if any, of the nanoparticles pass through the membrane.

Table IV-11. Summary of Free Silver Concentrations as a Function of Time. Summary of the free silver detected by ICP-MS following stirred cell separation.

Reference Number	Date	Total [Ag] (Reserve)	Free [Ag] (Permeate)	% Free Ag
CEHR-13	01 June 2016	4.91 ± 0.08 mg/g	0.25 ± 0.01 mg/g	5.1 %
CEHR-13	31 August 2016	4.0 ± 0.2 mg/g	0.72 ± 0.05 mg/g	18 %
CEHR-14	01 June 2016	4.86 ± 0.04 mg/g	0.0576 ± 0.0009 mg/g	1.2 %
CEHR-14	31 August 2016	4.00 ± 0.01 mg/g	0.52 ± 0.02 mg/g	13 %
CEHR-15	01 June 2016	4.18 ± 0.08 mg/g	0.0170 ± 0.0001 mg/g	0.4 %
CEHR-15	31 August 2016	4.4 ± 0.8 mg/g	0.11 ± 0.01 mg/g	2.5 %

H. Thermogravimetric Analysis

Design and Methods

Samples were analyzed via thermogravimetric analysis (TGA) to assess whether coatings were present on the nanoparticles and in what concentration. TGA was also used to determine the concentration of the metallic nanomaterial by measuring the residual material remaining after combustion of any coatings. For measurement of the metallic nanoparticle concentration, the samples were measured in their liquid (as-received) forms. For detection and measurement of coating concentrations, the samples were lyophilized prior to the TGA run. The signal from the water loss had the potential to swamp out a small amount of loss from any coating present, and thus was removed/minimized by lyophilization. Using lyophilized samples allowed for better sensitivity (total weight measured >1 mg) and hence a more accurate coating determination.

Nanoparticle Concentration

For each liquid sample, 50 µL was transferred to an aluminum oxide crucible (150 µL crucible with lid, Mettler Toledo) for TGA measurement (TGA/DSC 1, Mettler Toledo). Samples were held at 25˚C for 5 min, then ramped to 1000˚C at a heating rate of 20˚C/min under nitrogen gas. A new crucible was used for each sample. The empty crucible was subjected to the TGA method prior to loading the sample to serve as a background correction.

TGA cannot confirm the oxidation state of the material. Concentrations are reported using the manufacturer-reported oxidation state.

Coating Detection and Concentration

To determine coating content of the samples, samples were lyophilized overnight after being frozen in an ultra-low temperature freezer (-80˚C) for at least 3 hours. Typically, 250 µL of sample solution yielded 6 mg of lyophilized powder. About 1 mg was the typical amount added for TGA analysis, allowing for repeat runs, if necessary. The dried samples were added to aluminum oxide crucibles and subjected to the same temperature program as described above for the liquid samples.

Results and Discussion

Nanoparticle Concentration

The TGA curves (top panel; weight loss versus temperature) for CEHR-13 through CEHR-15 are shown in Figures IV-13 through IV-15, respectively. The first derivative of this curve (bottom panel) was used to highlight the weight loss events. For all samples, a single weight loss event was observed between 50-180˚C, corresponding to the loss of water. The coating loss was small relative to the water peak, and thus is not clearly seen. The total mass silver was determined by using the amount of mass left at the end of the TGA run. A comparison of the vendor-reported concentrations to the TGA-measured concentrations is provided in Table IV-12. The TGA-measured value for CEHR-13 was about 50% higher than the theoretical concentration. The TGA concentrations for CEHR-14 and CEHR-15 were about 30% and 50% lower than theoretical, respectively. This is in contrast to the ICP-MS results which showed better agreement with the theoretical silver concentrations.

This analysis assumes that at the end of the run all that remained was the silver nanoparticles; the water would have evaporated and the organic coating (PVP in this case) present would have combusted. In some instances, combustion of a coating may leave residual mass, which would increase the nanoparticle concentration. It is not possible to determine this without subjecting the coating alone (not in nanosolution) to the TGA method. For many materials, TGA produces results in agreement with ICP-MS values. However, comparison of TGA silver concentrations to ICP-MS concentrations showed, in this case, that TGA is not an ideal method for calculating silver concentration for these materials. ICP-MS, with sensitivity down to the ppb range, will always be the more sensitive and more accurate technique. TGA is a good alternative when ICP-MS is unavailable, e.g. for silica nanoparticles.

Table IV-12. Comparison of TGA Measured Concentration to ICP-MS Measured and Reported Nanoparticle Concentrations.

Reference Number	Reported Concentration	Measured Concentration via ICP-MS	Measured Concentration via TGA of Liquid Sample
CEHR-13	5 mg/mL	4.62 ± 0.05 mg/mL	7.8 mg/mL
CEHR-14	5 mg/mL	4.51 ± 0.05 mg/mL	3.5 mg/mL
CEHR-15	5 mg/mL	4.49 ± 0.04 mg/mL	2.2 mg/mL

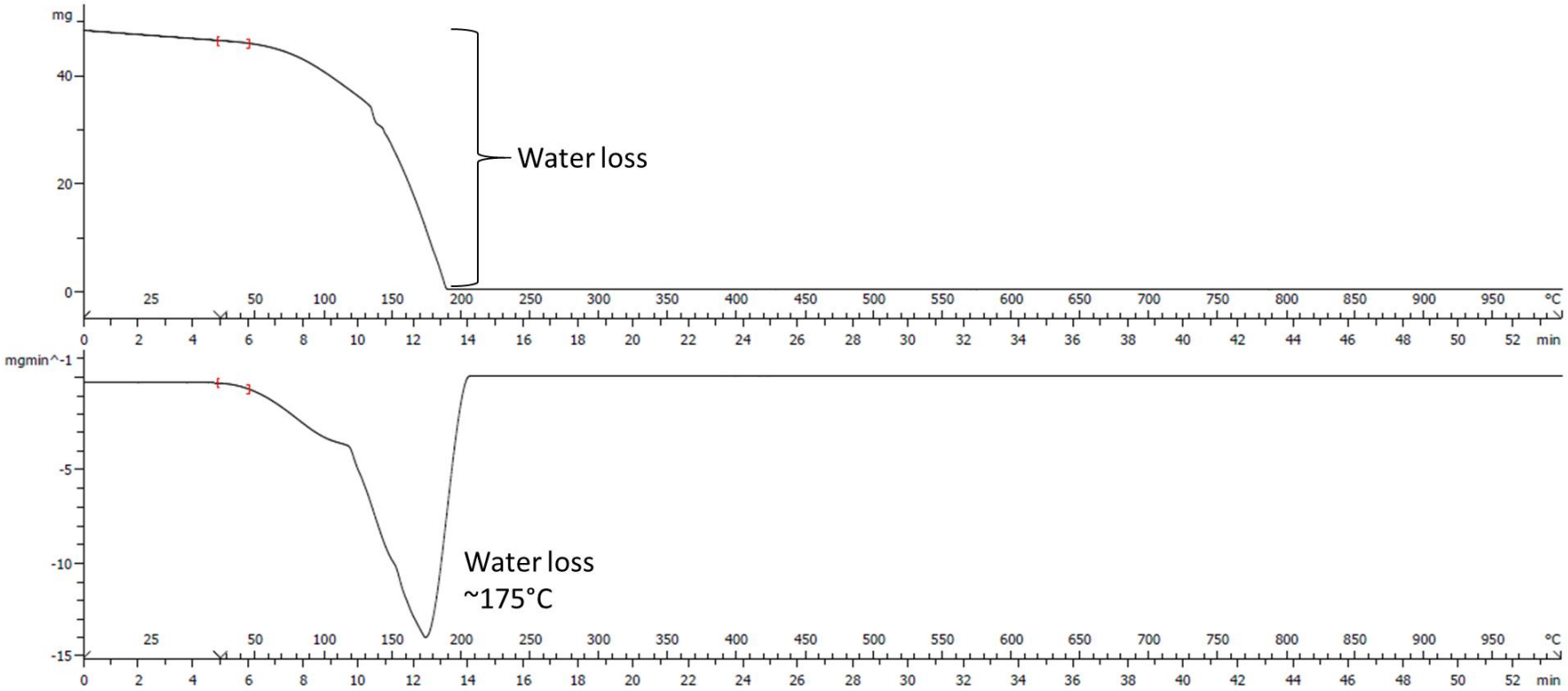

Reference Number	Volume (µL)	Starting Mass (mg)	Total Mass Loss (mg)	Residue mass (mg)
CEHR-13	50	48.165	47.777	0.389

Figure IV-13. TGA thermogram of CEHR-13. The top panel is the weight loss versus temperature (and time) curve. The bottom panel is the first derivative of that curve.

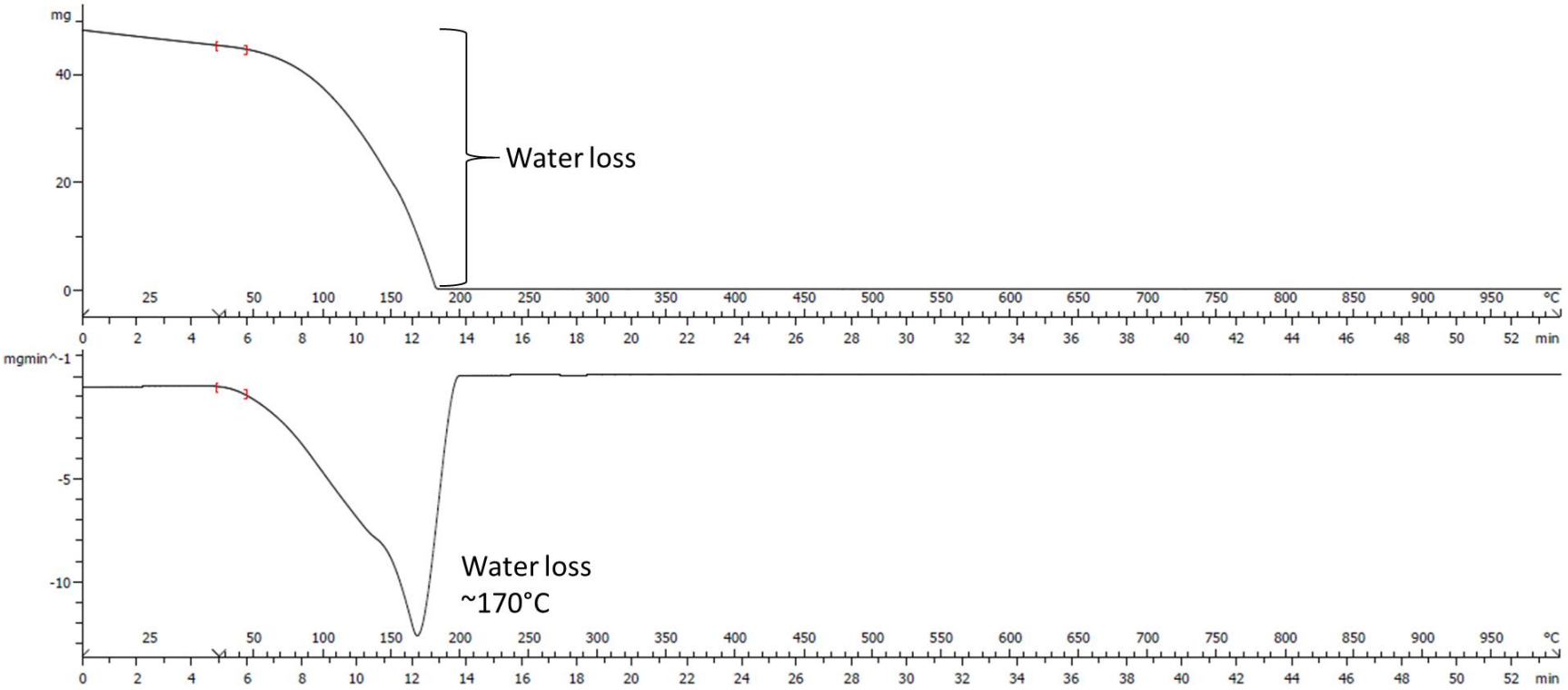

Reference Number	Volume (µL)	Starting Mass (mg)	Total Mass Loss (mg)	Residue mass (mg)
CEHR-14	50	48.110	47.935	0.175

Figure IV-14. TGA thermogram of CEHR-14. The top panel is the weight loss versus temperature (and time) curve. The bottom panel is the first derivative of that curve.

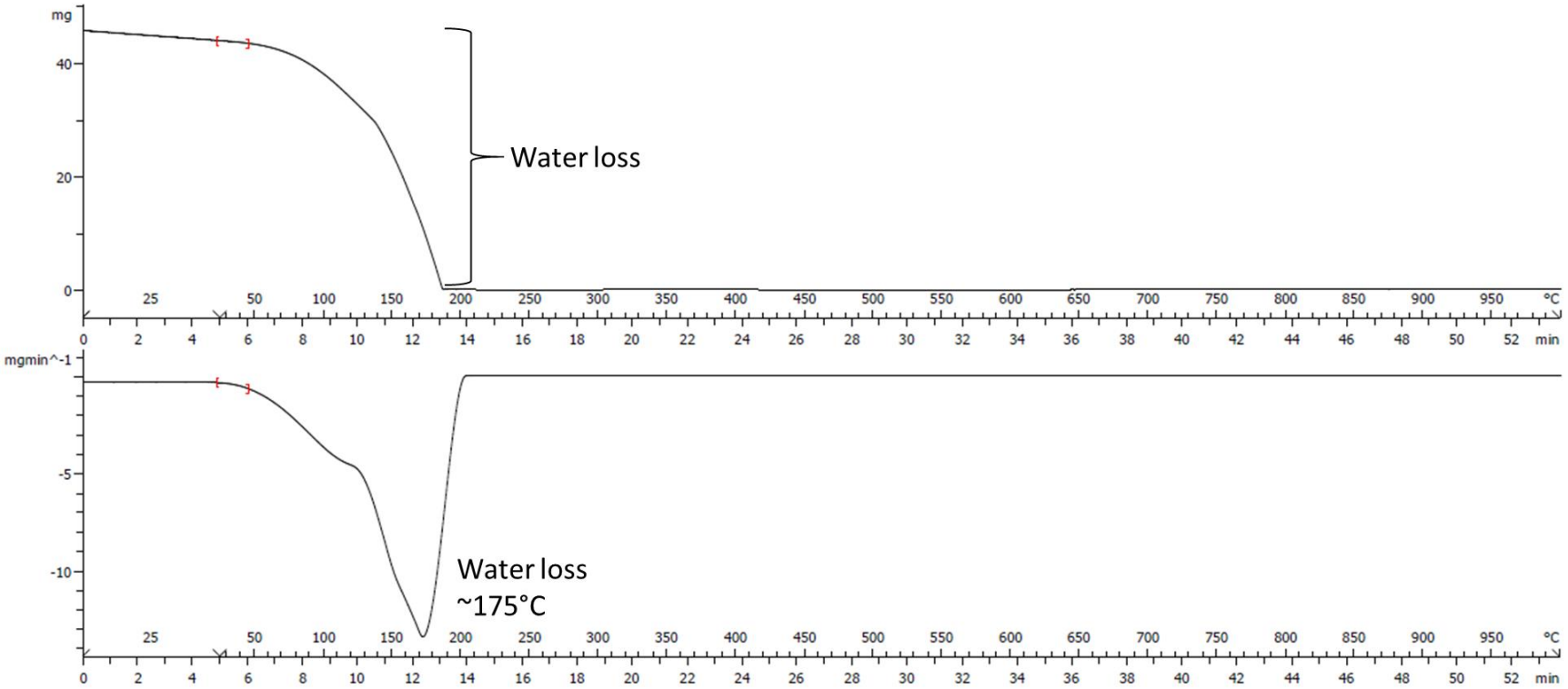

Reference Number	Volume (µL)	Starting Mass (mg)	Total Mass Loss (mg)	Residue mass (mg)
CEHR-15	50	45.699	45.587	0.112

Figure IV-15. TGA thermogram of CEHR-15. The top panel is the weight loss versus temperature (and time) curve. The bottom panel is the first derivative of that curve.

Coating Detection and Concentration

The manufacturers of the silver nanoparticles, nanoComposix, disclosed the presence of a polyvinylpyrrolidone (PVP) coating on the nanoparticles. The molecular weight of the polymer (each particle could have different molecular weight PVP) or the quantity in solution was not provided. PVP coats the nanoparticles but is not covalently bound to the surface. The amount of PVP contained in the samples was very low. Since the water peak dominated the TGA curves, all samples were lyophilized to remove the water and improve sensitivity for coating detection. Typical TGA curves for the lyophilized samples are shown in Figures IV-16 to IV-18, respectively.

In all samples, the first weight loss event occurred by 100˚C. This peak was assumed to be residual water loss, although typically water loss is noted slightly greater than 100˚C. The reason for this is not clear. Two additional weight loses were observed for CEHR-13 and CEHR-14, while CEHR-15 displayed only one additional weight loss event. Based off of the derivative curves, decomposition temperatures of 200 and 400°C were determined. From our previous experience with similar particles, PVP has a decomposition temperature of 400°C; the identity of the 200°C decomposition temperature was not determined and not included in the coating concentration determination.

For each run, the weight loss of PVP was calculated by using the first derivative analysis to mark the beginning and end of each weight loss event. The beginning and end was chosen where the derivative was constant (essentially zero). The final weight, as measured after the TGA run, was taken to be the silver nanoparticle amount ("Residue" mass denoted in Figures IV-16 to IV-18). This assumes that the weight of any residual decomposed PVP is negligible relative to the weight of silver. The mass ratio of PVP to Ag nanoparticle was then calculated for each independent run and is summarized in Table IV-13. The calculated percent coatings were 29%, 5%, and 15% for CEHR-13, CEHR-14, and CEHR-15, respectively.

Table IV-13. Summary of Percent Coating Mass per Mass Silver detected in each of the silver nanoparticles.

Reference Number	Reported Coating	%Mass Coating per Mass Silver
CEHR-13	PVP Conc. not reported	29%
CEHR-14	PVP Conc. not reported	5%
CEHR-15	PVP Conc. not reported	15%

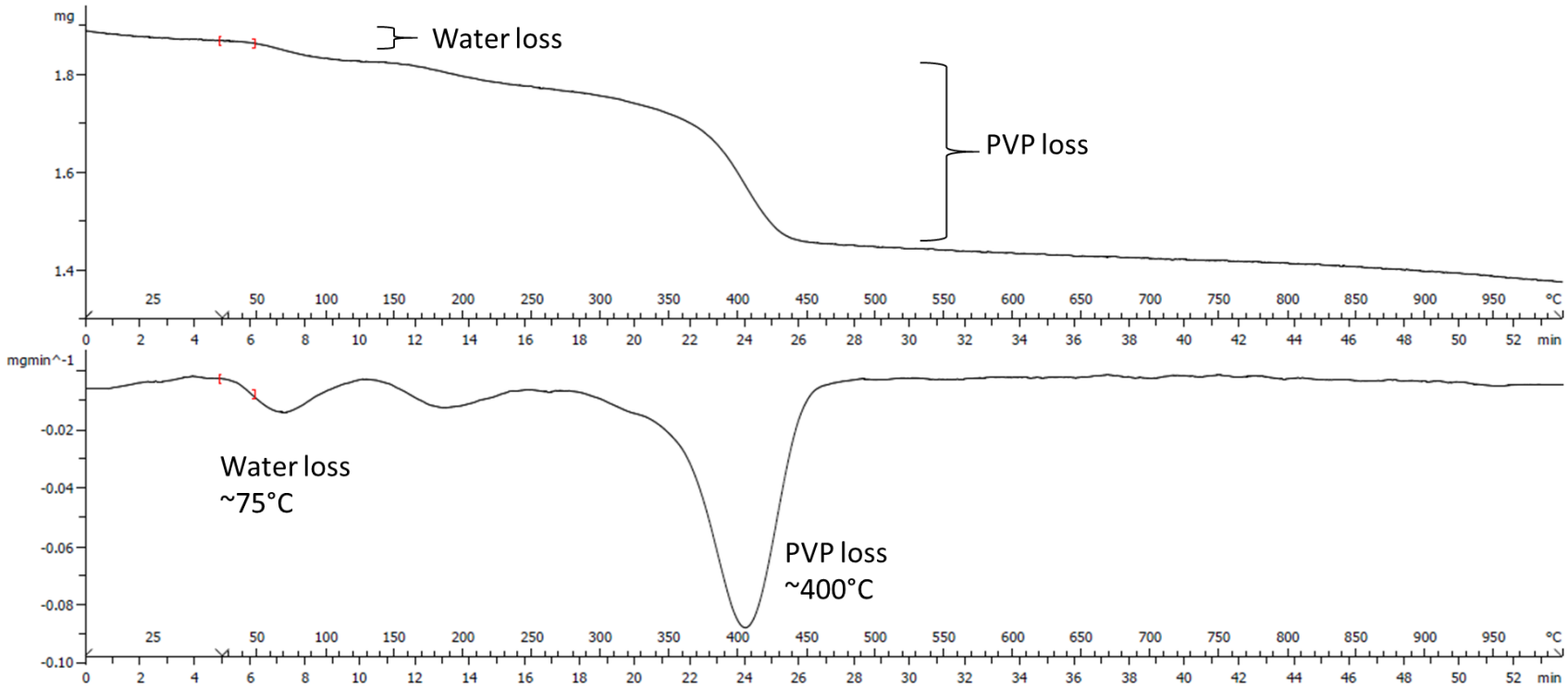

Reference Number	Starting Mass (mg)	Water Loss (mg)	Coating Loss (mg)	Residue (mg)	%Mass Coating per Mass Silver
CEHR-13	1.888	0.063	0.395	1.375	29%

Figure IV-16. TGA thermogram of CEHR-13 (lyophilized). The top panel is the weight loss versus temperature (and time) curve. The bottom panel is the first derivative of that curve.

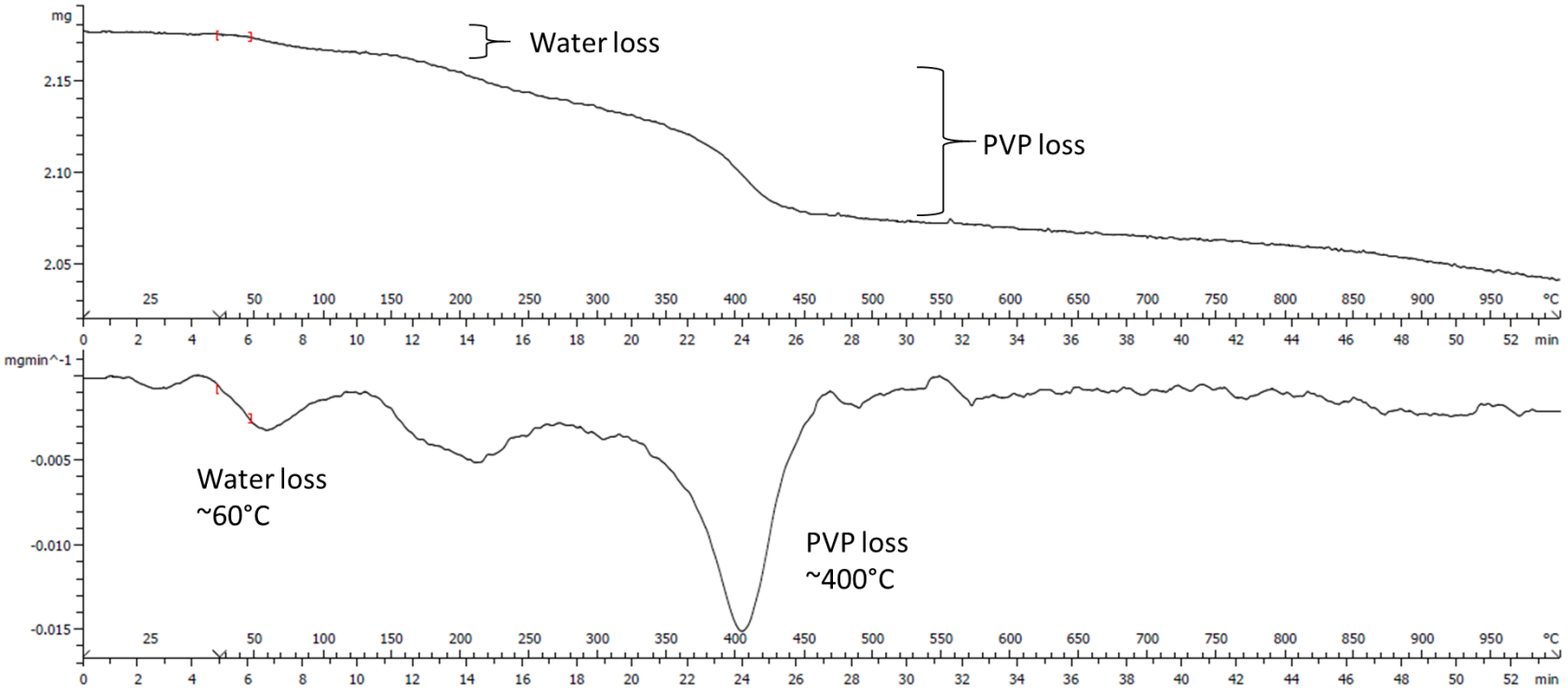

Reference Number	Starting Mass (mg)	Water Loss (mg)	Coating Loss (mg)	Residue (mg)	%Mass Coating per Mass Silver
CEHR-14	2.181	0.016	0.099	2.041	5%

Figure IV-17. TGA thermogram of CEHR-14 (lyophilized). The top panel is the weight loss versus temperature (and time) curve. The bottom panel is the first derivative of that curve.

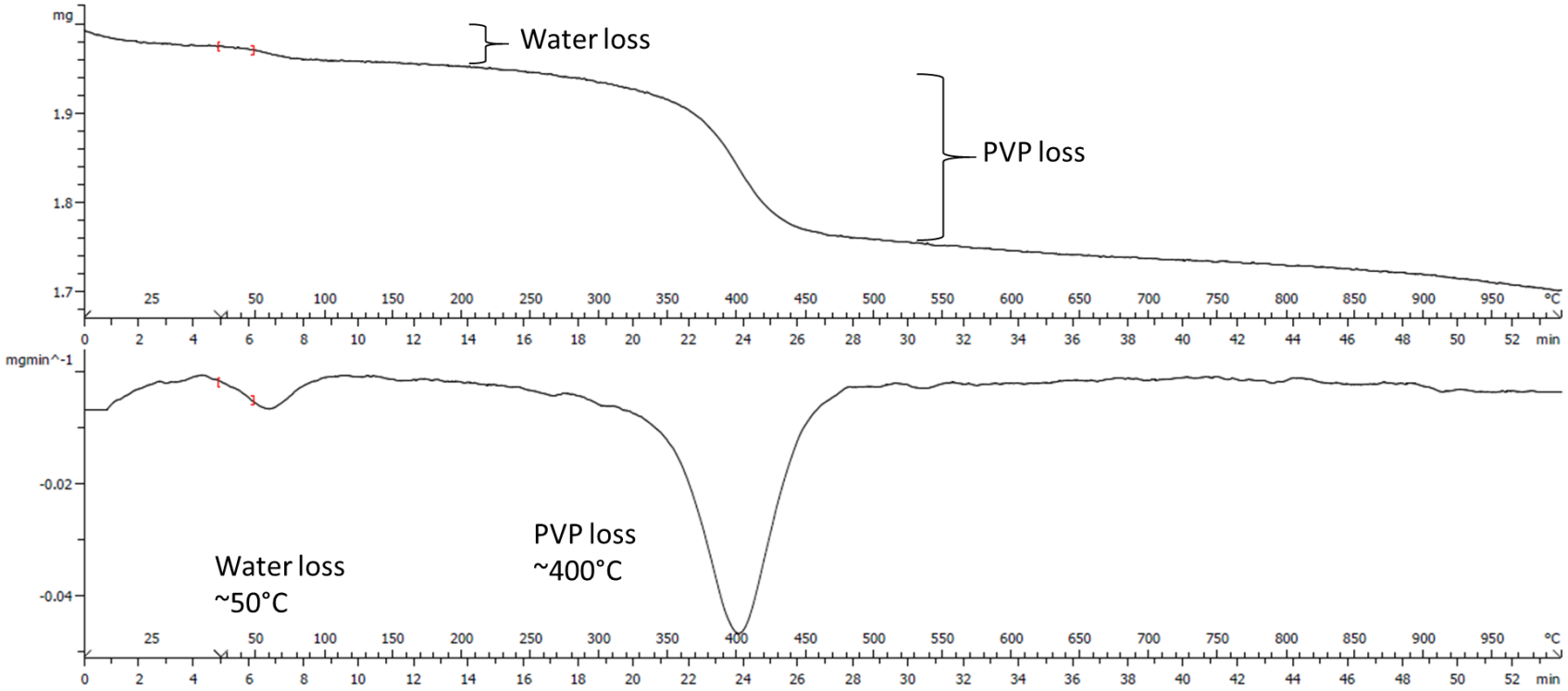

Reference Number	Starting Mass (mg)	Water Loss (mg)	Coating Loss (mg)	Residue (mg)	%Mass Coating per Mass Silver
CEHR-15	1.992	0.033	0.258	1.701	15%

Figure IV-18. TGA thermogram of CEHR-15 (lyophilized). The top panel is the weight loss versus temperature (and time) curve. The bottom panel is the first derivative of that curve.

I. Zeta Potential

Design and Methods

A Malvern Zetasizer Nano ZS instrument was used to measure zeta potential at 25°C for all samples. NCL protocol PCC-2 was followed (https://ncl.cancer.gov/resources/assay-cascade-protocols). Samples were diluted 100- or 1000-fold in deionized water. Sample pH was measured before loading into a pre-rinsed folded capillary cell. An applied voltage of 150 V was used. Traces in the figures represent the average of four measurements.

The instrument was validated by running an appropriate standard (Zeta Potential Transfer Standard, DTS0050, zeta potential value of -42 ± 4 mV at 25°C, Malvern Instruments) before all zeta potential measurements.

Results and Discussion

The three silver nanomaterials, CEHR-13 through CEHR-15, had negative zeta potential values. CEHR-13 was -33 mV, CEHR-14 was -20 mV, and CEHR-15 was -24 mV (Table IV-14). These values are in agreement with the expected values. It should be noted that while the silver nanoparticles contain PVP, it is not conjugated to the surface. Hence, PVP is not expected to generate a neutral zeta potential in this case. Some surface oxidation may have occurred (unconfirmed) which could impact the zeta potential, making them more negative.

Table IV-14. Summary of the zeta potentials for CEHR-8 to CEHR-12.

Sample	pH	Zeta Potential
CEHR-13	6.2	-33 ± 0 mV
CEHR-14	6.2	-20 ± 1 mV
CEHR-15	6.0	-24 ± 1 mV

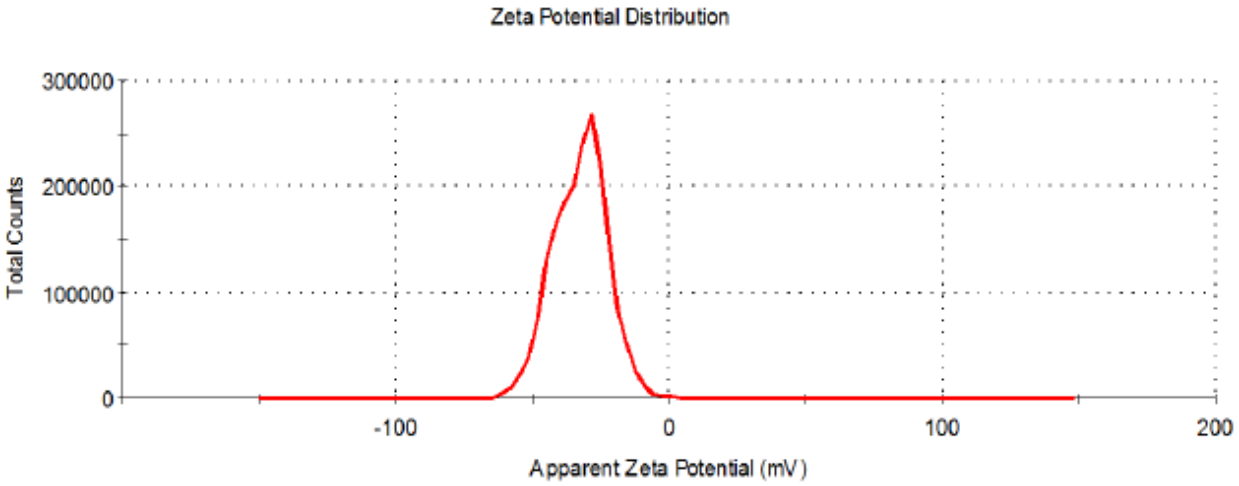

Sample	pH	Zeta Potential,
CEHR-13	6.2	-33 ± 0 mV

Figure IV-19. The averaged zeta potential distributions for CEHR-13 diluted 100-fold in deionized water.

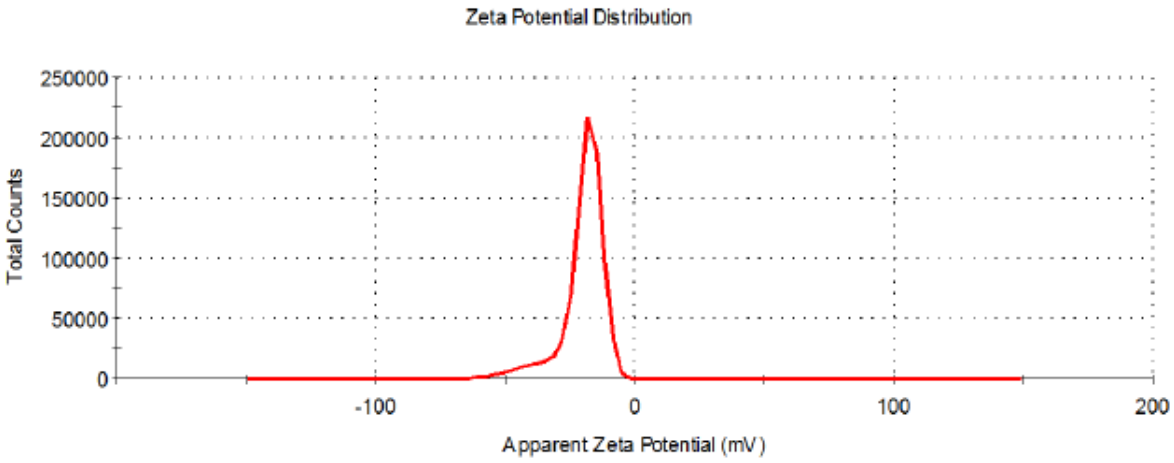

Sample	pH	Zeta Potential
CEHR-14	6.2	-20 ± 1 mV

Figure IV-20. The averaged zeta potential distributions for CEHR-14 diluted 1000-fold in deionized water.

Table IV-16. Summary of the zeta potential for CEHR-14 diluted 1000-fold in deionized water.

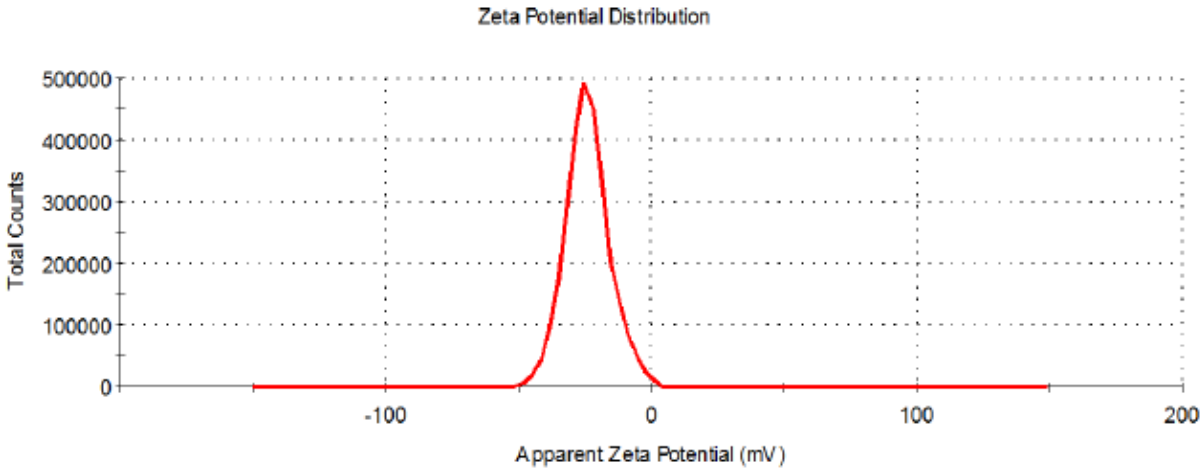

Sample	pH	Zeta Potential
CEHR-15	6.0	-24 ± 1 mV

Figure IV-21. The averaged zeta potential distributions for CEHR-15 diluted 1000-fold in deionized water.

V. Zinc Oxide

V. Zinc Oxide

A. Section Summary

Two zinc oxide nanoparticles with nominal size ranges of 30-40 and 50-80 nm (CEHR-16 and CEHR-17, respectively) were characterized for sterility and relevant physicochemical parameters. This included size (DLS and TEM) and polydispersity (AF4-DLS) measurements, zeta potential, total and free zinc concentrations by inductively-coupled plasma mass spectrometry (ICP-MS), and detection and quantification of possible surface coatings on the nanoparticles (TGA).

Sterility screening of the zinc oxide nanoparticles showed that CEHR-17 was free of bacterial contamination. CEHR-16, however, was contaminated with bacteria; therefore, this sample is not recommended for biological testing (Table V-1). Endotoxin analysis revealed that CEHR-17 had endotoxin values ≤0.5 EU/mg, while CEHR-16 had an average endotoxin value of 1.36 EU/mg (Table V-2). The bacterial contamination in CEHR-16 may have contributed to the endotoxin levels in this sample. Endotoxin is a component of the cell wall of gram negative bacteria. If the contamination found in CEHR-16 was due to gram-positive bacteria, the endotoxin would have originated from another source. Bacterial serotyping was not performed in this study, and thus the link between the bacterial contamination and endotoxin levels was not confirmed.

Size analysis of the two zinc oxide nanomaterials was conducted by dynamic light scattering (DLS) and transmission electron microscopy (TEM). As evidenced by TEM, both samples appeared to have formed aggregates, but individual particles were still clearly seen (Figures V-1 and V-2). The TEM measured diameters for the individual particles for CEHR-16 and CEHR-17 were 35 and 25 nm, respectively (Table V-3). The CEHR-16 particle size was in good agreement with the reported size; the reported size is believed to be a TEM diameter, although the manufacturer did not disclose the technique used. For CEHR-17, the measured size was approximately half of the reported size. The DLS measured diameters were considerably larger than the TEM sizes, suggesting the sample has aggregated/agglomerated in solution, as seen in the TEM images. The DLS diameters (Int-Peak) were 668 and 318 nm for CEHR-16 and CEHR-17, respectively (Figures V-3 and V-4).

Asymmetric-flow field flow fractionation (AF4) was used to examine the size polydispersity for CEHR-17. Two size populations were observed (Figure V-5). The dominant size population was approximately 127-215 nm. The second, minor population had a size range of approximately 260-290 nm. These results agreed with the batch-mode DLS data (318 nm). Larger particles scatter more light and will dominant a batch-mode DLS light scattering signal. Therefore, despite the 260-290 nm population being the minor species by AF4-DLS, this population will dominate the batch-mode DLS results, masking the 127-215 nm population. Note, CEHR-16 was not analyzed by AF4 due to the bacterial contamination in the sample.

Zinc concentrations were measured by inductively coupled plasma-mass spectrometry (ICP-MS) and thermogravimetric analysis (TGA). ICP-MS zinc concentrations were converted to a weight percent of zinc oxide for comparison to the manufacturer-reported sample concentrations. The total zinc oxide nanoparticle concentrations for CEHR-16 and CEHR-17 were 23 and 22% by weight (Table V-9), respectively. The TGA-measured concentrations for CEHR-16 and CEHR-17 were 20 and 16%, respectively. Both of these measurements were in very good agreement with the 20% reported concentration (Table V-11). Note however, the sample settles rapidly and requires a very thorough mixing to ensure homogeneous sampling.

ICP-MS and TGA were also used to assess the purity and stability of the formulations. ICP-MS was used to determine whether any metal impurities were present in the samples. CEHR-16 had no detectable metal impurities, while CEHR-17 contained iron, strontium, and manganese (Figure V-6). The free zinc content for each formulation was also measured by ICP-MS. An increase in the free zinc content can be an indication of particle instability. For CEHR-16 and CEHR-17, a maximum release of 1.2% and 1.3%, respectively, was detected by November 2016 (Table V-10). TGA revealed additional components thought to be a coating on the nanomaterials. The percent mass ratios of coating to zinc oxide are summarized in Table V-12 and were approximately 2% and 8% for CEHR-16 and CEHR-17, respectively. TGA could not confirm the identity of this material. Of note, the decomposition patterns were different between CEHR-16 and CEHR-17, suggesting the added coating/excipients may be different between the two samples. The zeta potentials of the nanoparticles were negative (Table V-13). These values are consistent for either uncoated zinc oxide nanoparticles or those coated with a negatively-charged surface moiety.

B. Sterility

Design and Methods

Sterility, i.e. bacterial contamination, of the two zinc oxide nanoparticles was assessed using NCL protocol STE-2.2 (https://ncl.cancer.gov/resources/assay-cascade-protocols). In brief, samples were plated onto LB agar plates at several dilutions (10-, 100-, and 1000-fold) and allowed to incubate at 37°C for 72 hours. The plates were then visually inspected for colony formation.

Results & Conclusions

CEHR-17 showed no visible colony formation. CEHR-16, however, was contaminated with bacteria; it showed 2200 CFU/mg after the 72 hr incubation period. It is recommended this sample not be used for any biological tests. A summary of these results is provided in the table below.

Table V-1. Summary of the sterility testing results for the zinc oxide nanoparticles.

Reference Number	Nanoparticle Description	Nominal size reported by manufacturer	Sterility (agar plate)
CEHR-16	ZnO nanopowder, 20 wt% dispersion	30-40 nm	**2200 CFU/mg**
CEHR-17	ZnO nanopowder, 20 wt% dispersion	50-80 nm	Negative

C. Endotoxin

Design and Methods

The objective of this experiment was to evaluate potential endotoxin contamination in the two zinc oxide formulations. NCL's protocols for the kinetic turbidity Limulus Amebocyte Lysate (LAL) assay was used (STE-1.2; https://ncl.cancer.gov/resources/assay-cascade-protocols. All samples were initially diluted to 1 mg/mL theoretical concentration and tested at 1:5, 1:50, and 1:500 dilutions in water.

Results and Discussion

CEHR-17 had undetectable levels of endotoxin (i.e., below the assay's lower limit of detection, <0.5), while CEHR-16 had endotoxin levels of 1.36 EU/mg (Table V-2). Due to the presence of bacterial contamination (Table V-I), it is recommended that CEHR-16 not be used in any biological tests.

Table V-2. Endotoxin levels detected by the LAL assay. Results are shown as endotoxin units (EU) per mg of nanoparticle.

Reference Number	Nanoparticle Description	Nominal size reported by manufacturer	Endotoxin Turbidity LAL
CEHR-16	ZnO nanopowder, 20 wt% dispersion	30-40 nm	**1.4 EU/mg**
CEHR-17	ZnO nanopowder, 20 wt% dispersion	50-80 nm	< 0.5 EU/mg

D. Transmission Electron Microscopy

Design and Methods

Transmission electron microscopy (TEM) was conducted to assess the size and morphology of the nanomaterials. Stock solutions were diluted to 5% with ultrapure water, and 2 µL were applied to a glow discharged carbon film grid (Electron Microscopy Sciences). The grid was washed three times with ultrapure water, blotted, and allowed to air dry before imaging. Images were taken using a T-12 TEM (FEI) equipped with a LαB6 thermoionic gun at 80 V acceleration voltage.

Particle size analysis was performed using ImageJ (https://imagej.nih.gov/ij/). Only particles that were individually dispersed were included in the sizing analysis.

Results and Discussion

Representative TEM images of CEHR-16 and CEHR-17 are shown in Figures V-1 and V-2, respectively. The measured size of the individual particles in CEHR-16 (35 nm) agreed well with the reported size (30-40 nm) for this sample. The particles have formed aggregates but individual particles were clearly seen. On the other hand, the measured size of the CEHR-17 particles (25 nm) was much smaller than the reported size. The measured size was approximately half of the manufacturer reported size with a relatively large standard deviation (36% of measured size).

Table V-3. Comparison of vendor reported size and TEM-measured size.

Reference Number	Nanoparticle Description	Nominal size reported by manufacturer	TEM Measured Size
CEHR-16	ZnO nanopowder, 20 wt% dispersion	30-40 nm	35 ± 9 nm
CEHR-17	ZnO nanopowder, 20 wt% dispersion	50-80 nm	25 ± 9 nm

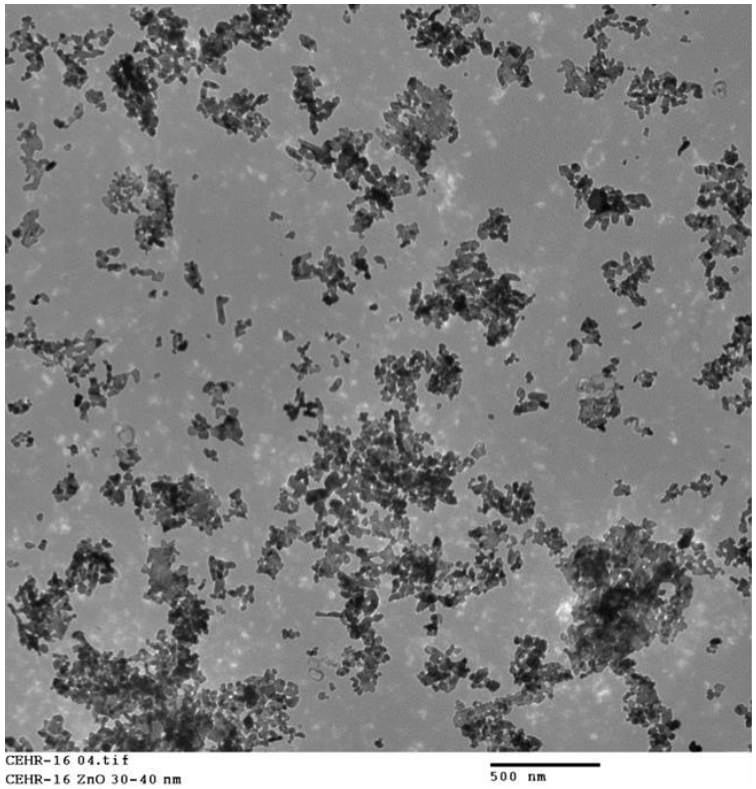

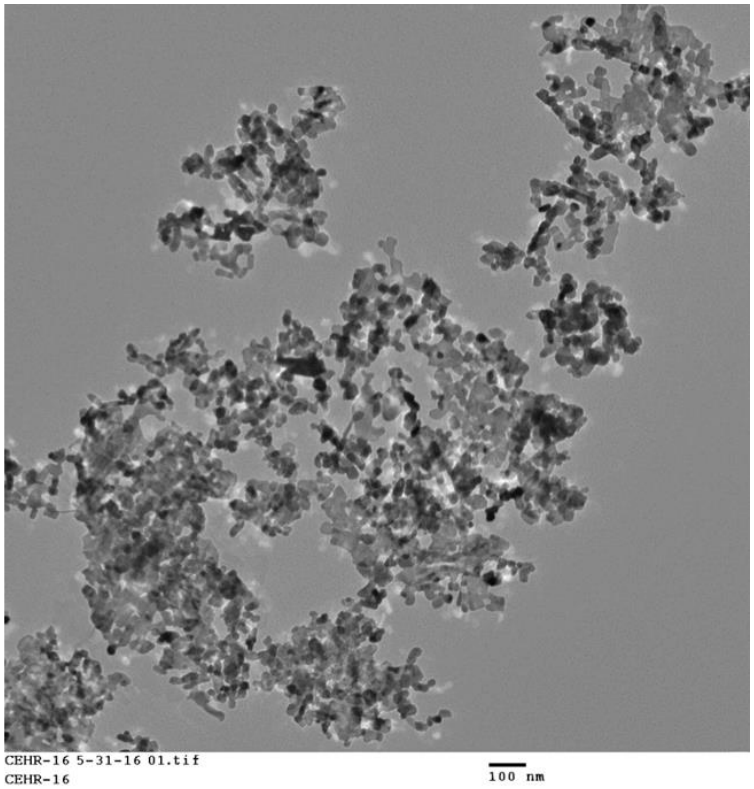

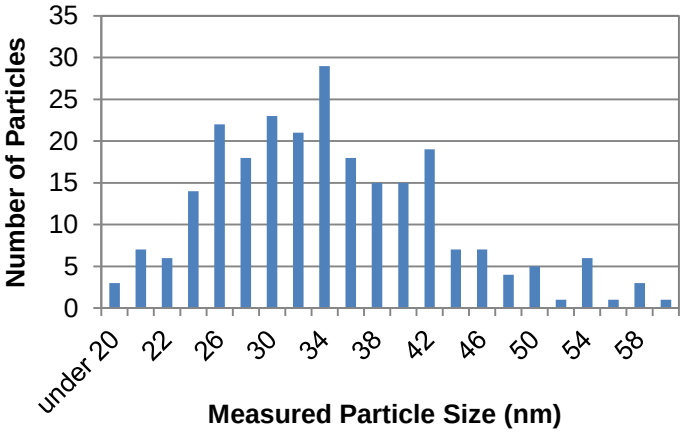

Figure V-1. Representative TEM Images of CEHR-16. Two representative images are shown for CEHR-16, showing the range of average diameters spanning 35 ± 9 nm (n = 244).

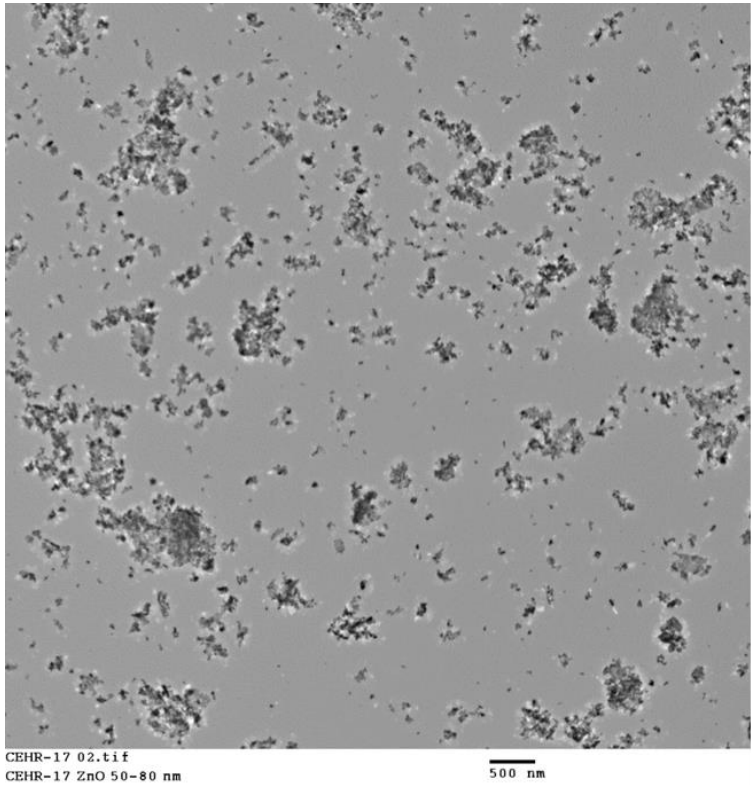

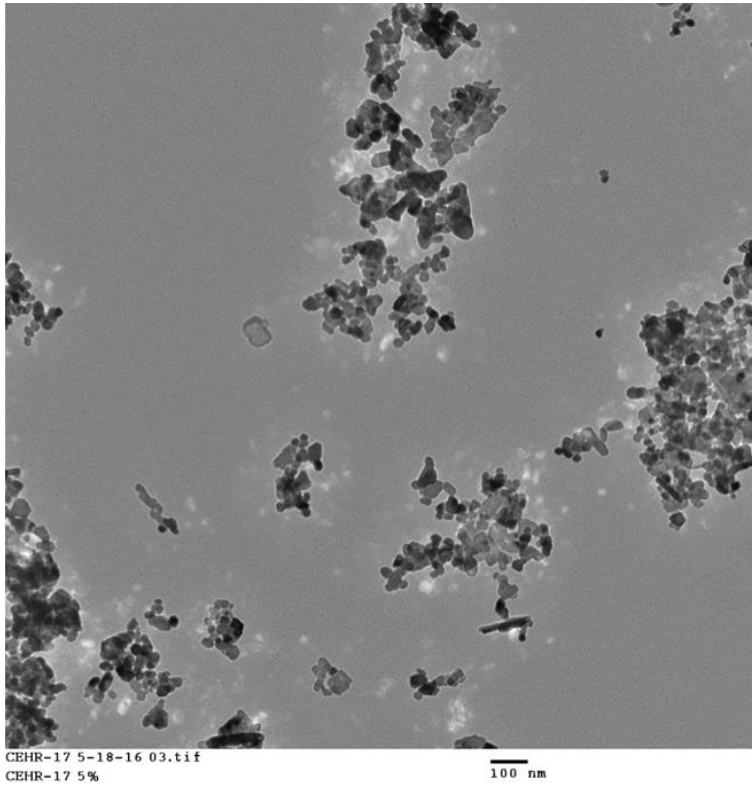

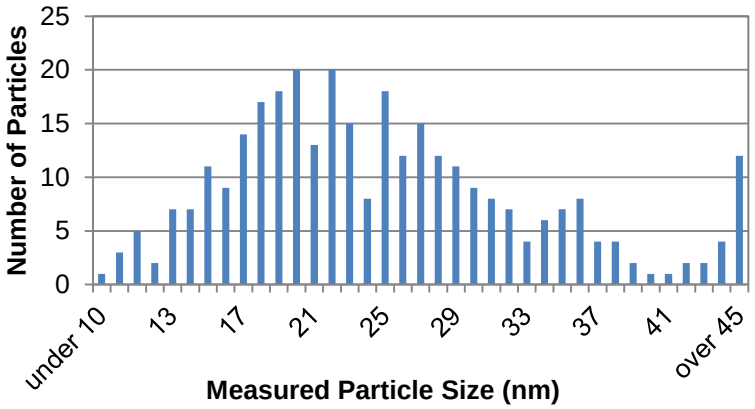

Figure V-2. Representative TEM Images of CEHR-17. Two representative images are shown for CEHR-17, showing the range of average diameters spanning 25 ± 9 nm (n = 315).

E. Hydrodynamic Size/Size Distribution via Dynamic Light Scattering

Design and Methods

A Malvern Zetasizer Nano ZS instrument (Southborough, MA) with back scattering detector (173°) was used for measuring the hydrodynamic size (diameter) in batch mode. NIST-NCL joint protocol PCC-1 was followed (https://ncl.cancer.gov/resources/assay-cascade-protocols). Stock samples of CEHR-16 and CEHR-17 were diluted 1000- and 10,000-fold in water. Measurements were made at 25°C in a quartz microcuvette. Traces in the figures represent the average of at least twelve measurements.

Hydrodynamic diameters are reported as the intensity-weighted average and as the volume-weighted average over a particular range of size populations corresponding to the most prominent peak. The Int-Peak value is used as the hydrodynamic diameter of a particular species. The Vol-Peak and %Vol values are used to approximate relative amounts of various species in the formulation. Z-Avg values are generally used to assess batch-to-batch variability of a sample.

Results and Discussion

The intensity and volume distribution plots for the zinc oxide nanoparticles from US Nano are provided in Figures V-3 to V-4. A summary of the sizes is provided in the corresponding tables below each figure. In brief, the zinc oxide samples were much larger in size than reported and may have aggregated in solution.

CEHR-16 has a manufacturer reported diameter range of 30-40 nm (believed to be a TEM diameter). The DLS measured size was considerably larger than the reported value, suggesting the sample has aggregated/agglomerated in solution. The intensity distribution size was 668 nm and the volume distribution size was 891 nm. Similarly, CEHR-17 was much greater in size as compared to the reported size, suggesting particle aggregation/agglomeration. The manufacturer reported size (believed to be TEM) was 50-80 nm. The intensity DLS distribution was 318 nm and the volume distribution was slightly larger at 347 nm.

While true that DLS hydrodynamic sizes are expected to be larger than TEM sizes, these very large differences are much greater than reasonably expected between DLS and TEM sizes for a monodisperse sample population. Both samples are believed to be aggregated/agglomerated in solution. The TEM images also showed evidence of particle aggregation/agglomeration (Figures V-1 and V-2). A comparison of the reported, TEM-measured and DLS-measured sizes is provided in Table V-4 below.

Table V-4. Comparison of TEM and DLS sizes.

Reference Number	Nominal size reported by manufacturer	TEM Measured Size	DLS Measured Size (Int-Peak)
CEHR-16	30-40 nm	35 ± 9 nm	668 ± 36 nm
CEHR-17	50-80 nm	25 ± 9 nm	318 ± 12 nm

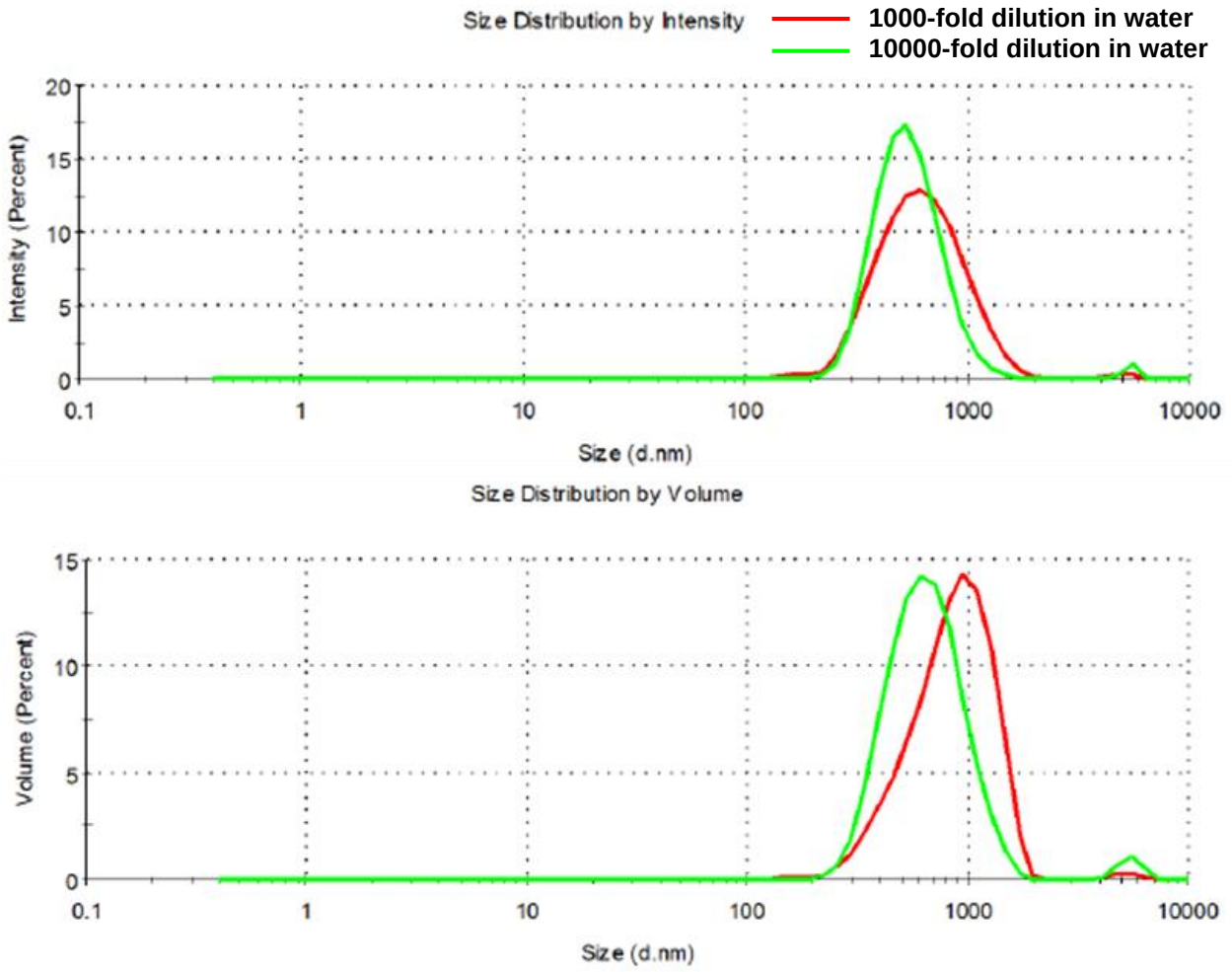

Figure V-3. The averaged intensity and volume distribution plots for CEHR-16 diluted in water.

Table V-5. Summary of the hydrodynamic size for CEHR-16 diluted in water

Dispersing Medium	Dilution	Z-Avg, nm	PdI	Int-Peak, nm	% Int	Vol-Peak, nm	% Vol
DI water	1000-fold	571 ± 11	0.17 ± 0.02	668 ± 36	99 ± 2	891 ± 59	99 ± 2
DI water	10,000-fold	586 ± 23	0.27 ± 0.04	563 ± 46	99 ± 1	680 ± 116	98 ± 2

Note: Results are the average of at least 12 measurements. Z-Avg is the intensity-weighted average. PdI is the polydispersity index. Int-Peak is the intensity-weighted average over the primary peak. % Int is the percentage of the intensity spectra occupied by the primary peak. Vol-Peak is the volume-weighted average over the primary peak. % Vol is the percentage of the volume spectra occupied by the primary peak.

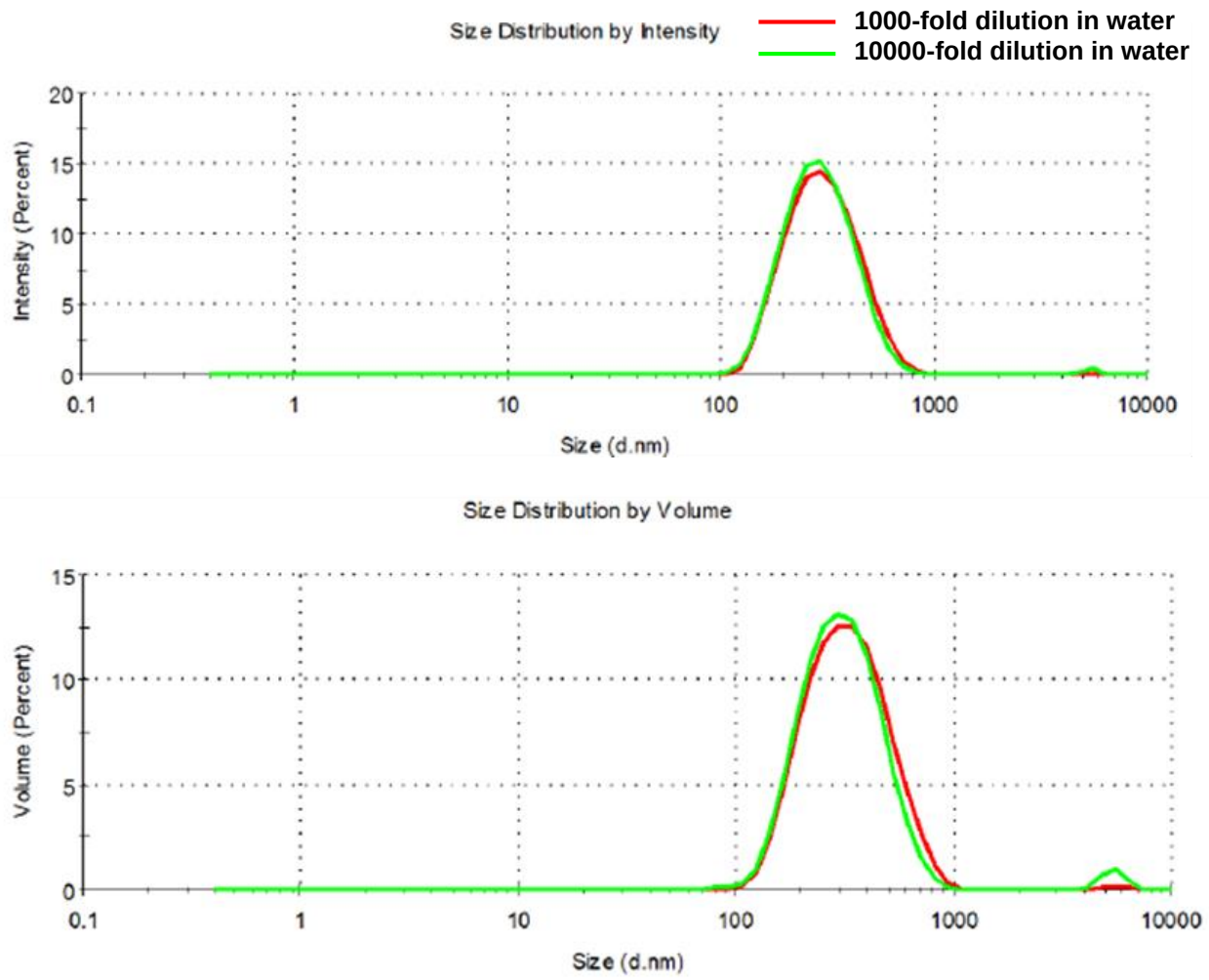

Figure V-4. The averaged intensity and volume distribution plots for CEHR-17 diluted in water.

Table V-6. Summary of the hydrodynamic size for CEHR-17 diluted in water

Dispersing Medium	Dilution	Z-Avg, nm	PdI	Int-Peak, nm	% Int	Vol-Peak, nm	% Vol
DI water	1000-fold	281 ± 3	0.14 ± 0.02	318 ± 12	100 ± 0	347 ± 22	99 ± 1
DI water	10,000-fold	283 ± 4	0.19 ± 0.02	304 ± 17	99 ± 1	325 ± 26	98 ± 2

F. Asymmetric-Flow Field Flow Fractionation

Design and Methods

The zinc oxide nanoparticles were separated using asymmetric-flow field-flow fractionation (AF4) with multiple in-line detectors to evaluate the polydispersity of the samples. AF4 provides a more thorough understanding of the various populations present in the sample over other batch-mode measurement techniques such as DLS alone. The AF4 system consisted of an isocratic pump (Agilent G1310A, Palo Alto, CA), well-plate autosampler (Agilent G1329A), AF4 separation channel (Eclipse DualTec; Wyatt Technology, Santa Barbara, CA), multi-angle light scattering detector (HELEOS II; Wyatt Technology), diode array detector (DAD, Agilent G1315B), and a DLS detector (Malvern Zetasizer Nano ZS; Southborough, MA). The separation channel had a length of 275 mm and a 350 µm spacer. A 10 kDa regenerated cellulose membrane was used for all separations.

The elution profile is provided in Table V-7. The cross flow was controlled by an Eclipse flow controller. CEHR-17 was diluted 500-fold in 15 mM NaCl and filtered through a 0.2 µm regenerated cellulose membrane prior to use. The elution was also run in 15 mM NaCl. This was chosen because the nanoparticles were stable in this dispersing media after dilution and did not interact/stick to the FFF membrane. A sample injection of volume of 100 µL was used for all samples and the chromatographic traces were monitored by DLS detection and UV at 210 nm. The hydrodynamic size is plotted across the eluted peaks. The UV absorbance at 210 nm was monitored to track relative abundance of each different size population.

Table V-7. AF4 elution profile.

Start Time (min)	End Time (min)	Duration (min)	Mode	Starting Cross-flow Rate (mL/min)	Ending Cross-flow Rate (mL/min)
0	2	2	Elution	1	1
2	4	2	Focus	-	-
4	9	5	Focus + Inject	-	-
9	19	10	Focus	-	-
19	29	10	Elution	1	1
29	31	2	Elution	1	0.5
31	41	10	Elution	0.5	0
41	61	20	Elution	0	0
61	63	2	Elution + Inject	0	0
63	64	1	Elution	0	0

Results and Discussion

The AF4 fractograms for CEHR-17 are shown in Figure V-5. The light scattering (top and bottom panel) signals showed a single peak (the first peak at roughly 20 minutes was the void peak). This peak had a polydispersed size distribution ranging from 127-215 nm. The tail end of this peak also contained a slightly larger size range of 260-290 nm. The flow-mode DLS results agreed reasonably well with the batch-mode DLS results. The single peak in batch-mode DLS was approximately 318 nm. Since larger particles will dominant the batch-mode light scattering signal, the 127-215 nm population seen by flow-mode DLS is likely masked by the larger-sized population in the batch-mode DLS measurement. Batch-mode DLS has limitations in resolving power and cannot separate these two populations.

CEHR-16 was not subjected to AF4 analysis due to the bacterial contamination detected in the formulation.

Table V-8. Comparison of Batch-mode and Flow-mode DLS sizes.

Reference Number	Batch-mode DLS Measured Size (Int-Peak)	Flow-mode DLS Measured Size: Major peak	Flow-mode DLS Measured Size: Minor peak
CEHR-16	668 ± 36 nm	Not Tested	
CEHR-17	318 ± 12 nm	127-215 nm	260-290 nm

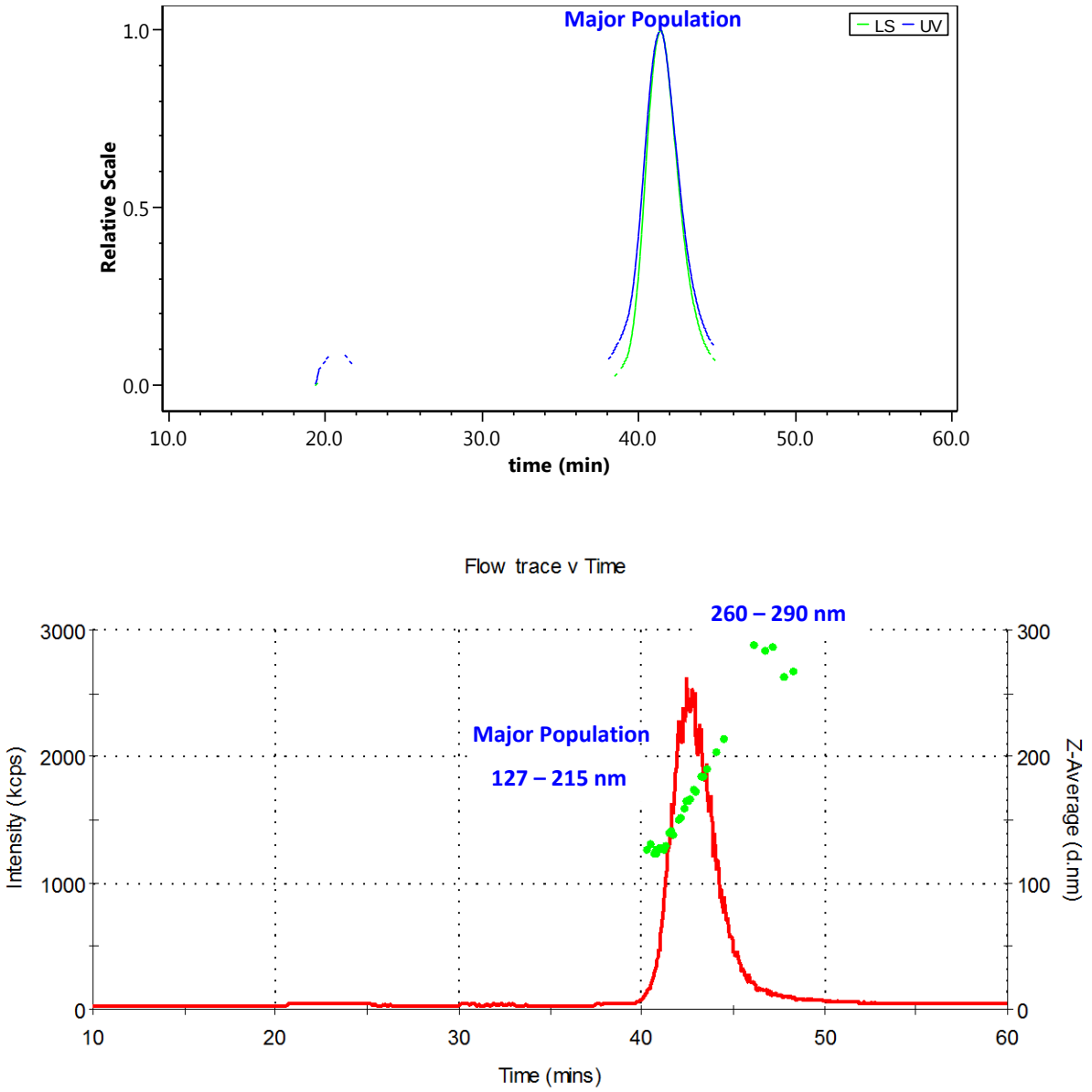

Figure V-5. AF4 fractograms for CEHR-17. The top panel shows the UV (210 nm) and LS (light scattering) signals while the bottom panel shows the hydrodynamic size distributions across the eluted peaks.

G. Inductively Coupled Plasma Mass Spectrometry

Design and Methods

The zinc concentrations of CEHR-16 and CEHR-17 were determined by inductively coupled plasma mass spectrometry (ICP-MS). An Agilent ICP-MS 7500CX equipped with a micro-mist nebulizer, standard sample introduction system, and integrated auto-sampler, operated in "no gas" mode in Agilent's proprietary ORS (Octopole Reaction System) was used. Tuning of the instrument was performed daily prior to sample testing.

Semi-Quantitative Analysis

A semi-quantitative analysis was performed on each sample prior to quantitative determination of the zinc concentrations. The semi-quantitative analysis was performed to help determine the proper dilution range for the samples, as well as to detect the presence of other metals in the sample. Only metals with counts two times greater than the background were denoted.

A 25 µL aliquot of the zinc stock solution was digested using 200 µL concentrated hydrochloric acid and 100 µL concentrated nitric acid. After 10 minutes, this digested sample was vortexed for 10 seconds and then diluted with water to target a 30 mL first dilution. A second dilution was performed by adding 10 mL of 2% nitric acid to 100 µL of the first dilution.

Total Metal Concentration

Using the data from the semi-quantitative analysis, the appropriate dilution was determined for the ICP-MS full quantitative analysis. The dilution target for the samples was 5 to 200 ppb. The total metal concentration was determined using the native formulation (i.e. not centrifuged or separated). Samples (10-100 µL) were initially digested with a 2:1 mixture of HCl:HNO_3. Typically, no more than a total of 1 mL of concentrated acid was used. The acid digested samples were then further diluted to approximately 30-50 mL total volume with 2% nitric acid. A second dilution was then performed in which 10-100 µL of the first dilution was diluted to 10-50 mL using 2% nitric acid. Samples were run in triplicate.

The metal concentration in samples was determined by comparing against a series of calibration standards prepared from NIST SRM 3168a. A dilution of 5000 ng Zn/g in 2% HNO_3 was used to make a 1000 ng Zn / g solution, which was then used to create standards for the calibration curve in a range of 5 to 200 ng/g in 10 mL volumes. The dilutions were made using 2% nitric acid. In addition, an internal standard, indium, was used to track the signal response of the ICP-MS. The internal standard was diluted to approximately 50 ppb and was mixed with the sample using a sample T. A simple linear regression was used for calculation of the metal concentrations.

The sequence for the ICP-MS runs consisted of five blanks, the calibration curve standards ordered from lowest to highest, five more blanks, then the zinc nanoparticle samples. Each sample was run in triplicate with three blanks between each sample. After the last zinc oxide sample was measured, five blanks were run, followed by the calibration standards once again. Within each sample set, the samples were run from highest dilution to lowest dilution. Three final blanks were run to flush the sample introduction system.

Free Metal Concentration and Metal Release with Time

In addition to determining the total metal concentration present in each sample, ICP-MS was also used to assess the amount of free metal ions present. The separation of free metal ions from the nanoparticles was carried out using stirred cell filtration as described in Section IV. The stirred cell separation was performed twice on each sample at different times to evaluate the release of free metal ions over time. The dates are noted for each analysis. The permeate dilutions were run first, followed by the reserved solution samples.

Results and Discussion

Semi-Quantitative Analysis

The results from the semi-quantitative analysis of CEHR-16 and CEHR-17 are shown in Figure V-6. The analysis showed zinc was the only species present in CEHR-16. For CEHR-17, zinc along with iron, strontium, and manganese were all detected. The origin of impurities is unknown. This was only an analysis to detect potential metal impurities. For an accurate determination of their concentrations, quantitative analysis compared to a standard would be required.

A. CEHR-16

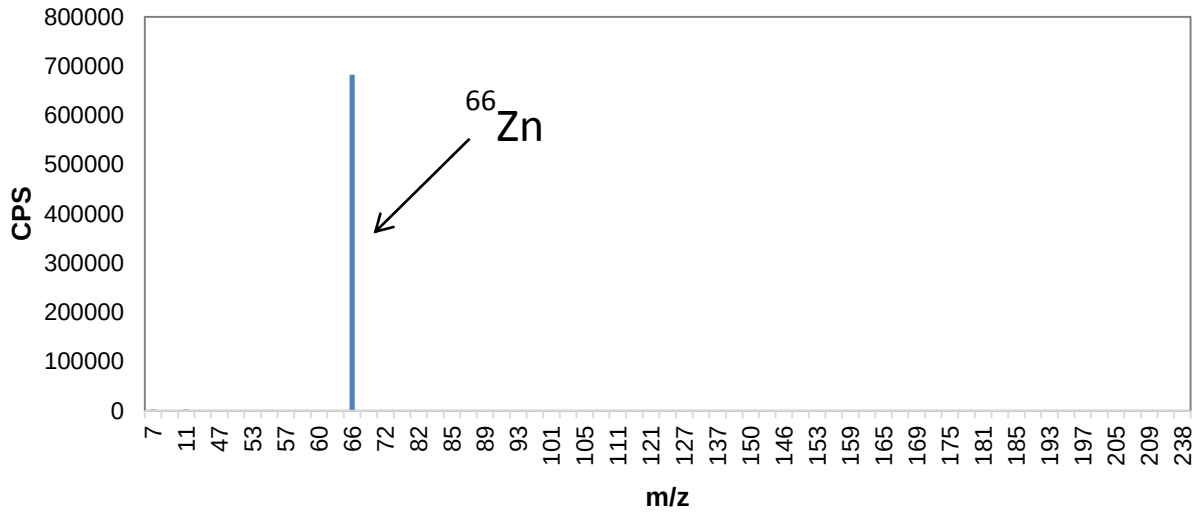

B. CEHR-17

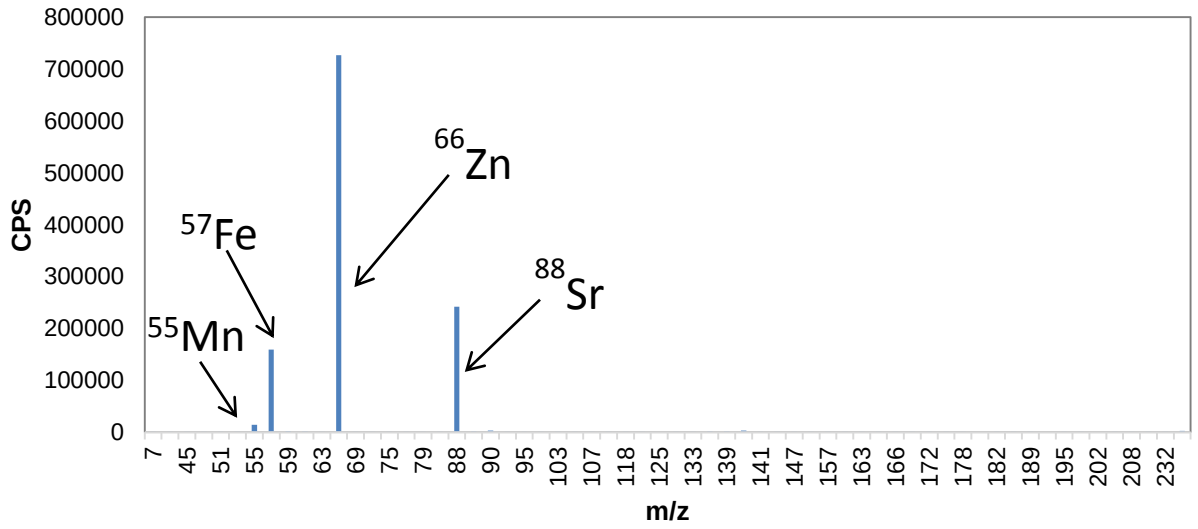

Figure V-6. Plots of CPS vs m/z. (A) CEHR-16 semi-quantitative analysis plot. **(B)** CEHR-17 semi-quantitative analysis plot. Both samples were analyzed on 8 November 2016. Note ^{12}C, ^{23}Na, ^{24}Mg, ^{27}Al, ^{29}Si, ^{31}P, ^{34}S, ^{35}Cl, ^{39}K, and ^{43}Ca were removed in both plots to better visualize the smaller peaks. The internal standard peak for ^{115}In was also omitted.

Full Quantitative Analysis: Total Zinc Concentration
The calibration curve used for total zinc quantitation was constructed from NIST SRM 3168a (Figure V-7). Quantitative total zinc concentrations for CEHR-16 and CEHR-17 are summarized in Table V-9. The ICP-MS zinc concentrations, in units of mg/g, were converted to zinc oxide weight percent using the ZnO molecular weight 81.408 g/mol. To calculate the ZnO percent, the ZnO mass was divided by the mass of the solution to output the nanoparticle percent. An average of five different runs was used to calculated the zinc and zinc oxide concentrations. The measured nanoparticle concentrations for CEHR-16 and CEHR-17 were 23% and 22% by weight, respectively. These values were in good agreement with the theoretical concentration of 20 wt%.

Of note, there was a considerable difference in total zinc concentration among the various runs, as alluded to by the large standard deviation. Both samples settled with time which likely led to inconsistent sampling. While an average of five runs did yield a nanoparticle concentration consistent with the theoretical value, the user is cautioned to ensure an adequate and thorough mixing to prior to sampling. The nanoparticle settling can be seen in the picture to the right.

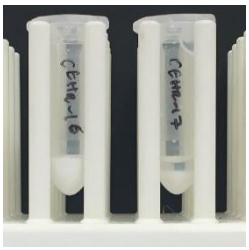

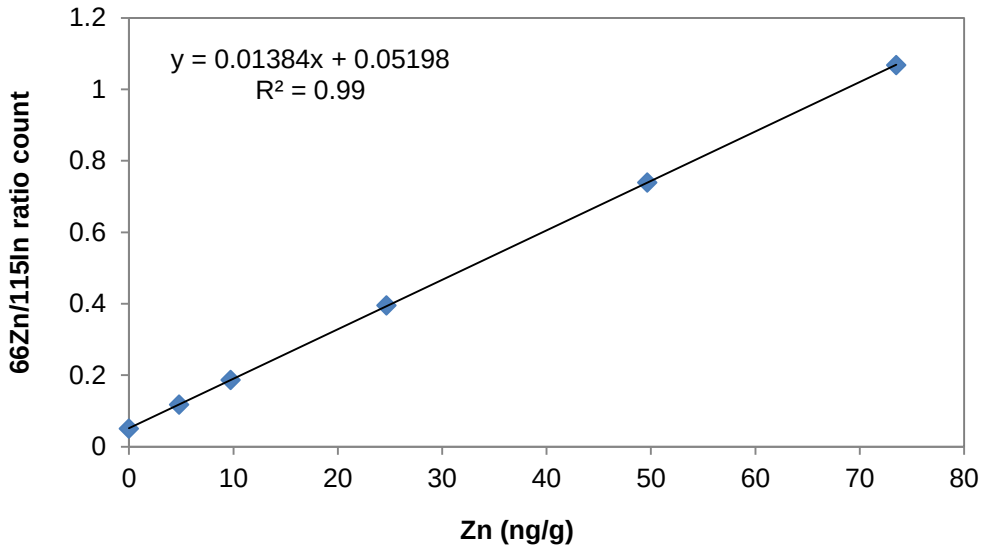

Figure V-7. Zinc Calibration Curve. A typical calibration curve ranging from 0 to 75 Zn ng/g, used to calculate the zinc concentration in CEHR-16 and CEHR-17. The calibration curve was constructed from NIST SRM 3168a zinc standard.

Table V-9. Summary of the total zinc oxide concentration in CEHR-16 and CEHR-17 as determined by ICP-MS. The total zinc oxide concentration was also converted to ZnO wt% for comparison to the reported concentrations.

Reference Number	Reported Concentration	Total [Zn]	Total ZnO
CEHR-16	20 wt%	187 ± 49 mg/g (n=5)	23% by wt.
CEHR-17	20 wt%	176 ± 49 mg/g (n=5)	22% by wt.

Free Zinc Concentration

Stirred cell filtration was employed to separate any free zinc ions from the zinc oxide nanoparticles. Repeat measurements were made approximately three months apart to assess zinc release kinetics/stability of the formulation. The stock sample (prior to stirred cell filtration; designated as Total [Zn] in Table V-10) was re-measured each time and used to calculate (normalize) the percent free zinc (free [Zn]/total [Zn]) in each formulation.

The free zinc concentrations in CEHR-16 and CEHR-17 at three time points are shown in Table V-10. Both CEHR-16 and CEHR-17 showed very little free zinc at the initial measurement, but had up to 1.3% free zinc at the later time points.

Of note, there was a considerable difference among the total zinc concentrations measured at the various time points. The large differences in concentrations may be attributed to non-homogeneity within the sample as described previously.

Table V-10. Summary of Free Zinc Concentrations. A summary of the free zinc detected by ICP-MS following stirred cell separation. Each sample was analyzed at three time points.

Reference Number	Date	Total [Zn] (Reserve)	Free [Zn] (Permeate)	% Free Zn
CEHR-16	06 June 2016	183 ± 1 mg/g	0.0085 ± 0.0003 mg/g	<0.1%
CEHR-16	07 Sept 2016	109 ± 3 mg/g	0.0005 ± 0.0002 mg/g	<0.1%
CEHR-16	30 Nov 2016	272 ± 2 mg/g	3.228 ± 0.007 mg/g	1.2%
CEHR-17	06 June 2016	221 ± 2 mg/g	0.0225 ± 0.0003 mg/g	<0.1%
CEHR-17	07 Sept 2016	121 ± 9 mg/g	1.57 ± 0.02 mg/g	1.3%
CEHR-17	30 Nov 2016	229 ± 7 mg/g	2.08 ± 0.01 mg/g	0.9%

H. Thermogravimetric Analysis

Design and Methods

Samples were analyzed via thermogravimetric analysis (TGA) to assess whether coatings were present on the nanoparticles and in what concentration. TGA was also used to determine the concentration of the metallic nanomaterial by measuring the residual material remaining after combustion of any coatings. For measurement of the metallic nanoparticle concentration, the samples were measured in their liquid (as-received) forms. For detection and measurement of coating concentrations, the samples were lyophilized prior to the TGA run. The signal from the water loss had the potential to swamp out a small amount of loss from any coating present, and thus was removed/minimized by lyophilization. Using lyophilized samples allowed for better sensitivity (total weight measured >1 mg) and hence a more accurate coating determination.

Nanoparticle Concentration

For each liquid sample, 50 µL was transferred to an aluminum oxide crucible (150 µL crucible with lid, Mettler Toledo) for TGA measurement (TGA/DSC 1, Mettler Toledo). Samples were held at 25˚C for 5 min, then ramped to 1000˚C at a heating rate of 20˚C/min under nitrogen gas. A new crucible was used for each sample. The empty crucible was subjected to the TGA method prior to loading the sample to serve as a background correction.

TGA cannot confirm the oxidation state of the material. Concentrations are reported using the manufacturer-reported oxidation state.

Coating Detection and Concentration

To determine coating content of the samples, samples were lyophilized overnight after being frozen in an ultra-low temperature freezer (-80˚C) for at least 3 hours. Typically, 250 µL of sample solution yielded 60 mg of lyophilized powder. About 12 mg was the typical amount added for TGA analysis, allowing for repeat runs, if necessary. The dried samples were added to aluminum oxide crucibles and subjected to the same temperature program as described above for the liquid samples.

Results and Discussion

Nanoparticle Concentration

The TGA curves (top panel; weight loss versus temperature) for CEHR-16 and CEHR-17 are shown in Figures V-8 and V-9, respectively. The first derivative of this curve (bottom panel) was used to highlight the weight loss events. For both samples, a single weight loss event was observed between 50-180˚C, corresponding to the loss of water. Any coating loss was too small relative to the water peak to be clearly seen. The total mass zinc oxide was determined by using the amount of mass remaining at the end of the TGA run. The TGA-measured nanoparticle concentrations for CEHR-16 and CEHR-17 were 20% and 16% (by weight), respectively. These results were in very good agreement with the vendor-specified values of 20% for both samples. Moreover, the TGA results also agreed with the ICP-MS results (Table V-11).

Note, this analysis assumes that, at the end of the run, all that remained was the zinc oxide nanoparticles; the water would have evaporated and any organic coating present would have combusted. In some instances, combustion of a coating may leave residual mass, which would increase the nanoparticle concentration. It is not possible to determine this without subjecting the coating alone (not in nanosolution) to the TGA method.

Table V-11. Comparison of TGA Measured Concentration to ICP-MS Measured and Reported Nanoparticle Concentrations.

Reference Number	Reported Concentration	Measured Concentration via ICP-MS	Measured Concentration via TGA of Liquid Sample
CEHR-16	20 wt%	23 wt%	20 wt%
CEHR-17	20 wt%	22 wt%	16 wt%

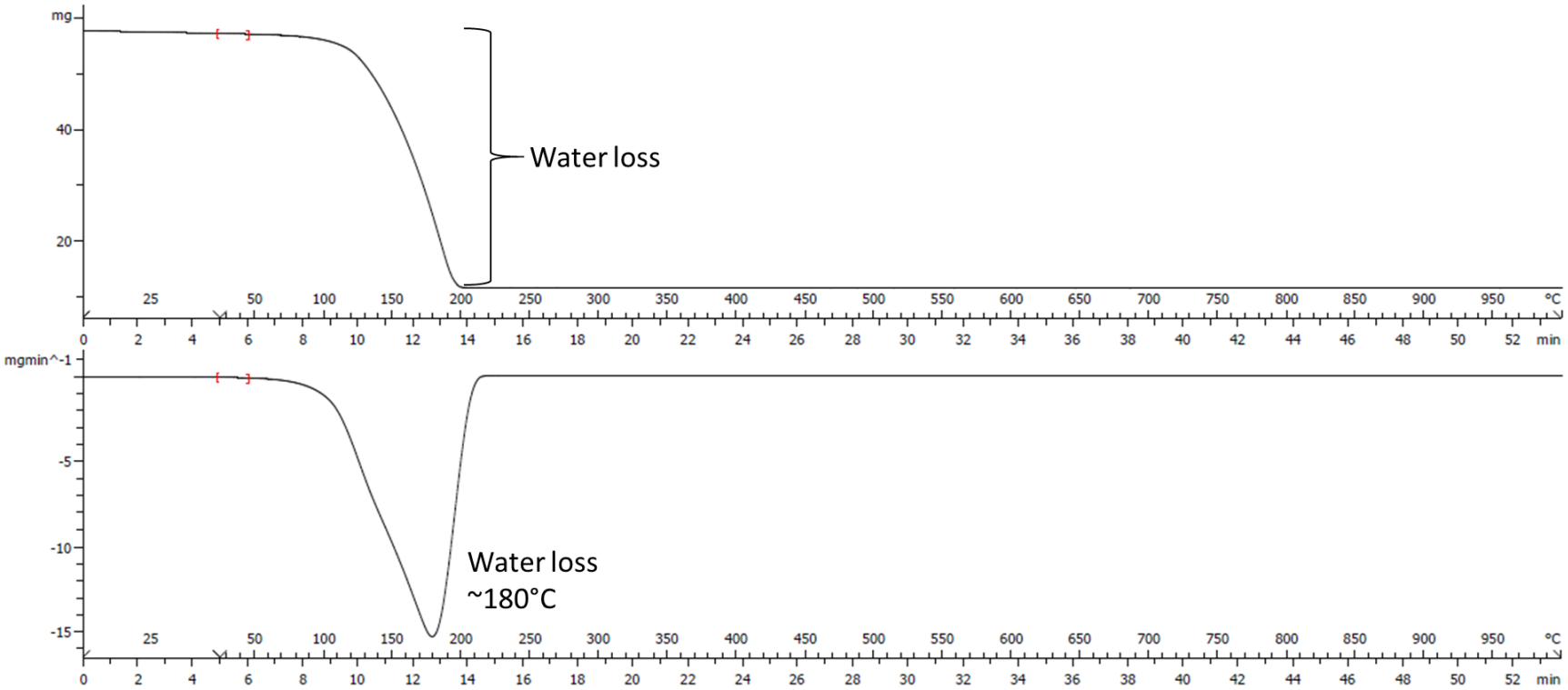

Reference Number	Volume (µL)	Starting Mass (mg)	Total Mass Loss (mg)	Residue mass (mg)
CEHR-16	50	57.644	46.201	11.443

Figure V-8. TGA thermogram of CEHR-16. The top panel is the weight loss versus temperature (and time) curve. The bottom panel is the first derivative of that curve.

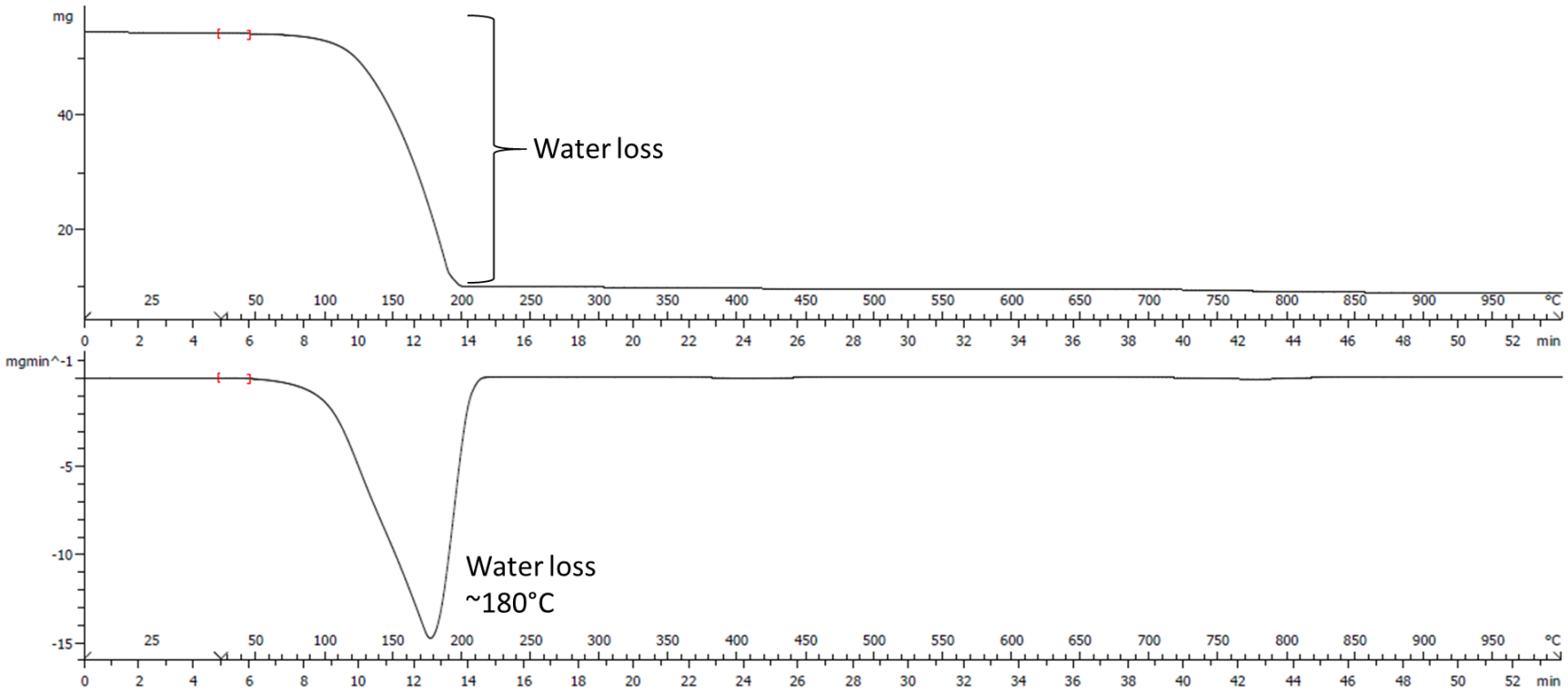

Reference Number	Volume (µL)	Starting Mass (mg)	Total Mass Loss (mg)	Residue mass (mg)
CEHR-17	50	54.353	45.550	8.803

Figure V-9. TGA thermogram of CEHR-17. The top panel is the weight loss versus temperature (and time) curve. The bottom panel is the first derivative of that curve.

Coating Detection and Concentration

TGA was also used to determine whether a surface coating was present. The manufacturers of the zinc oxide nanoparticles, US Nano, did not disclose a coating on the nanoparticles. Often however, especially for proprietary coatings, this information is omitted from sample descriptions. All samples were lyophilized to reduce the water peak and improve sensitivity for coating detection. The TGA curves for the lyophilized samples are shown in Figures V-10 and V-11, respectively.

Multiple weight loss events were observed for both CEHR-16 and CEHR-17. In both samples, the first weight loss event corresponded to the loss of residual water and occurred by 100˚C. Based off of the first derivative curves, decomposition temperatures of 275 and 440°C were seen for CEHR-16, while three decomposition temperatures, 300, 420, and 775°C, were observed for CEHR-17. These weight losses were assumed to result from decomposition of a surface coating and/or added excipients (possibly added to help with solubilization and stability). Given the different decomposition patterns, the coating and/or excipients are likely different between the two formulations.

For each run, the weight loss of coating was calculated by using the first derivative analysis to mark the beginning and end of the weight loss events. This translated to a starting and ending temperature range of 200 and 1000°C, respectively. The final weight at 1000°C was taken to be the zinc oxide amount, and assumed that the weight of any residual decomposed coating and/or excipients was negligible relative to the weight of the zinc oxide nanoparticles. The mass ratio of coating and/or excipients to zinc oxide nanoparticle was then calculated for each independent run. The calculated percent coatings were 2% and 8% for CEHR-16 and CEHR-17, respectively (Table V-12). Note, the identity of the coating and/or excipients could not be determined by TGA.

Table V-12. Summary of Percent Coating Mass per Mass Nanoparticle detected in each of the zinc oxide nanoparticles.

Reference Number	Reported Coating	%Mass Coating per Mass Nanoparticle
CEHR-16	None reported	2%
CEHR-17	None reported	8%

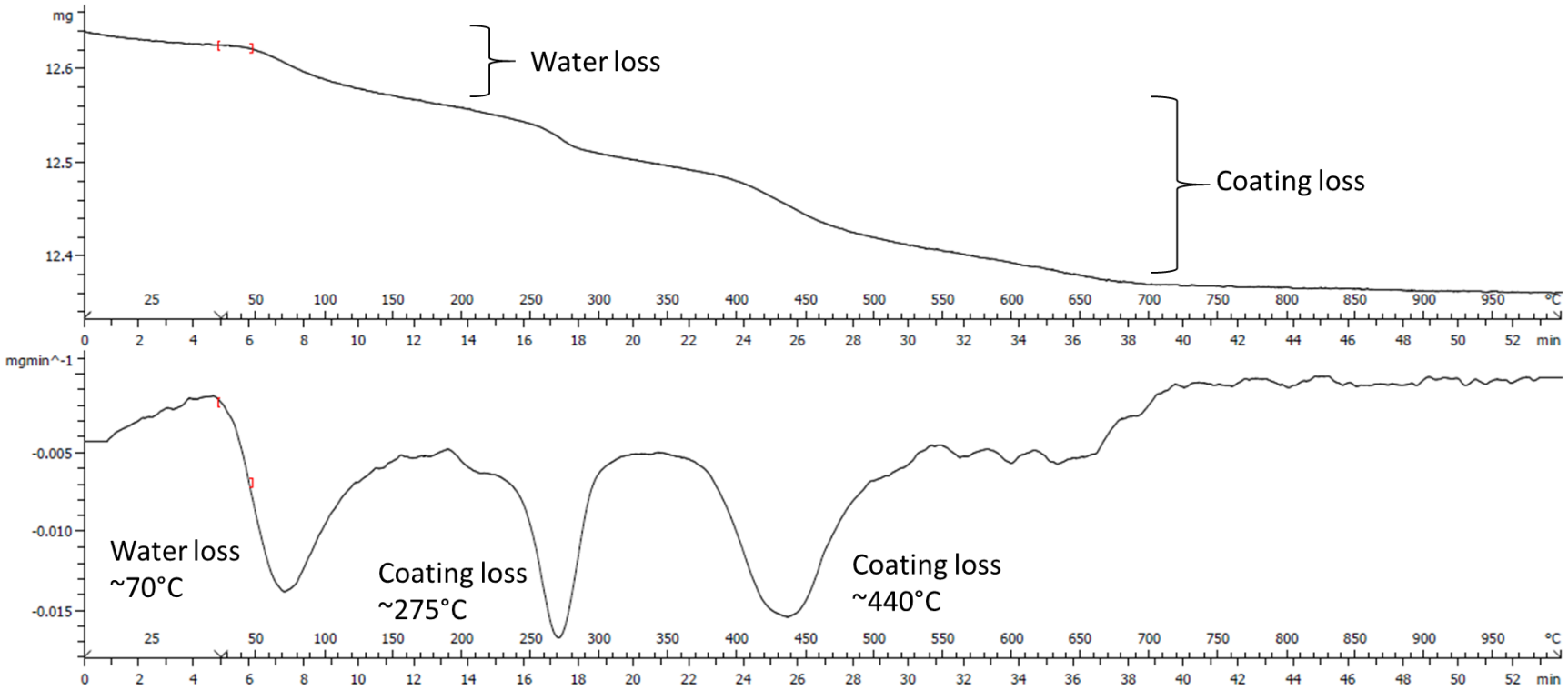

Reference Number	Starting Mass (mg)	Water Loss (mg)	Coating Loss (mg)	Residue (mg)	%Mass Coating per Mass Zinc Oxide Nanoparticles
CEHR-16	12.669	0.080	0.199	12.390	2%

Figure V-10. TGA thermogram of CEHR-16 (lyophilized). The top panel is the weight loss versus temperature (and time) curve. The bottom panel is the first derivative of that curve.

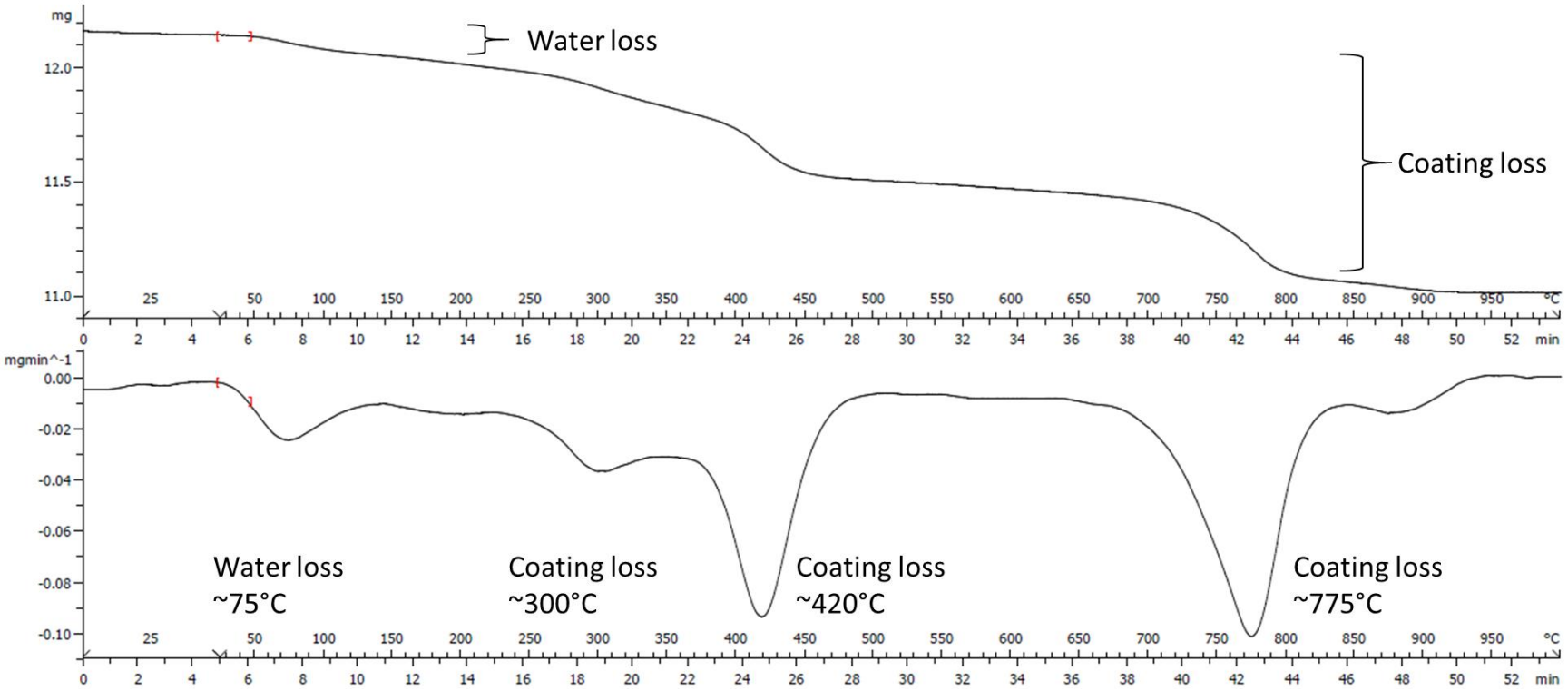

Reference Number	Starting Mass (mg)	Water Loss (mg)	Coating Loss (mg)	Residue (mg)	%Mass Coating per Mass Zinc Oxide Nanoparticles
CEHR-17	12.157	0.159	0.985	11.013	8%

Figure V-11. TGA thermogram of CEHR-17 (lyophilized). The top panel is the weight loss versus temperature (and time) curve. The bottom panel is the first derivative of that curve.

I. Zeta Potential

Design and Methods

A Malvern Zetasizer Nano ZS instrument was used to measure zeta potential at 25°C for all samples. NCL protocol PCC-2 was followed (https://ncl.cancer.gov/resources/assay-cascade-protocols). Samples were diluted 10,000-fold in water. Sample pH was measured before loading into a pre-rinsed folded capillary cell. Zeta potential measurement was made at native pH (approximately 7.0-7.5). An applied voltage of 150 V was used. Traces in the figures represent the average of four measurements.

The instrument was validated by running an appropriate standard (Zeta Potential Transfer Standard, DTS0050, zeta potential value of -42 ± 4 mV at 25˚C, Malvern Instruments) before all zeta potential measurements.

Results and Discussion

The zeta potential distributions for CEHR-16 and CEHR-17 are shown in Figures V-12 and V-13, respectively. Both samples, when dispersed in water and at native pH, exhibited negative zeta potential values (Table V-13). Negative zeta potentials would be anticipated for either uncoated zinc oxide nanoparticles, or those modified with a negatively charged surface coating.

Table V-13. Summary of the zeta potentials for CEHR-16 and CEHR-17.

Sample	pH	Zeta Potential
CEHR-16	7.5	-22 ± 1 mV
CEHR-17	7.0	-35 ± 1 mV

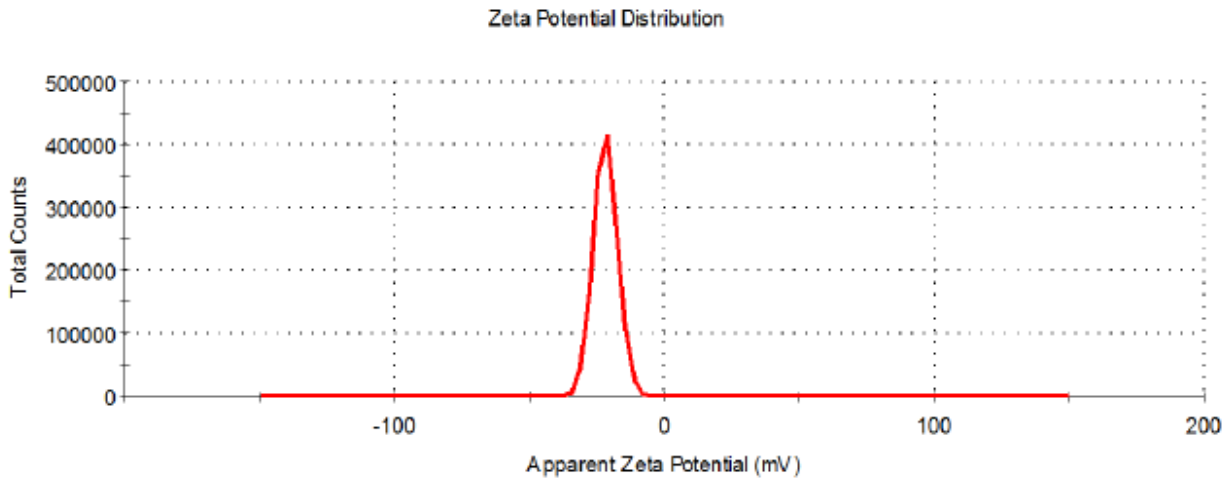

Sample	pH	Zeta Potential
CEHR-16	7.5	-22 ± 1 mV

Figure V-12. The averaged zeta potential distributions for CEHR-16 diluted 10,000-fold in deionized water.

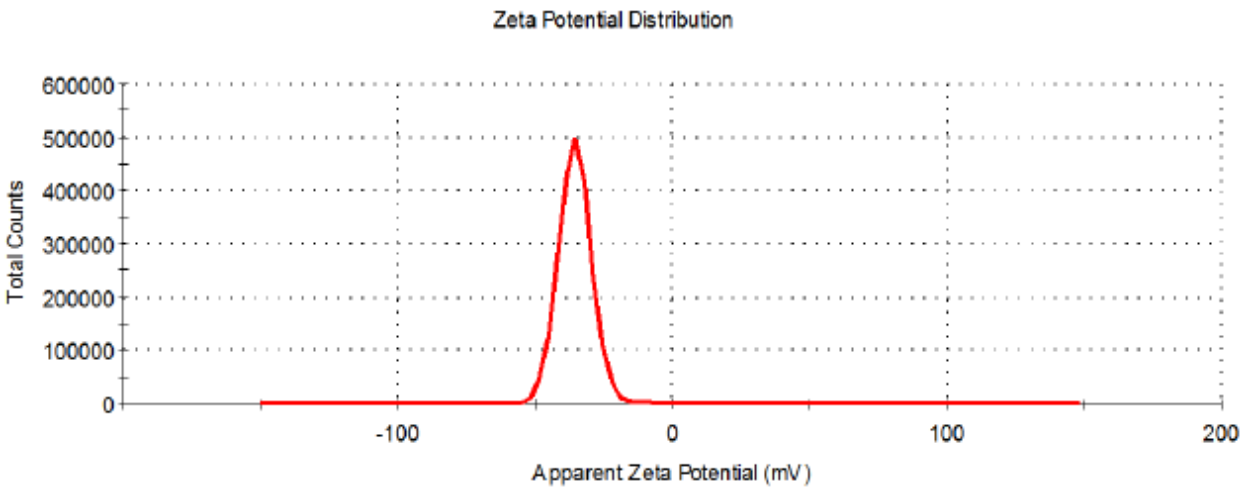

Sample	pH	Zeta Potential
CEHR-17	7.0	-35 ± 1 mV

Figure V-13. The averaged zeta potential distributions for CEHR-17 diluted 10,000-fold in deionized water.

VI. Iron Oxide

VI. Iron Oxide

A. Section Summary

Two iron oxide nanoparticles with a nominal size range of 15-20 nm and 20 nm (CEHR-18 and CEHR-19, respectively) were characterized for sterility and relevant physicochemical parameters. This included size (DLS and TEM) and polydispersity (AF4-DLS) measurements, zeta potential, total and free iron concentrations by inductively-coupled plasma mass spectrometry (ICP-MS), and detection and quantification of possible surface coatings on the nanoparticles (TGA). Note, the samples settled rapidly and required a very thorough mixing to ensure homogeneous sampling.

Sterility screening of the iron oxide nanoparticles showed that CEHR-18 was free of bacterial contamination, while CEHR-19 was contaminated with bacteria (Table VI-1). Endotoxin levels were quantitated by the Limulus Amebocyte Lysate (LAL) assay. Analysis revealed that CEHR-18 had endotoxin values ≤0.05 EU/mg, and CEHR-19 had an average endotoxin value of 6170 EU/mg, likely stemming from the noted bacterial contamination (Table VI-2). Therefore, CEHR-19 is not recommended for biological testing.

Size analysis of the two iron oxide nanomaterials was conducted by dynamic light scattering (DLS) and transmission electron microscopy (TEM). For both samples, significant agglomeration/aggregation can be seen. Individual particles could still be seen for CEHR-18, but not CEHR-19. The TEM measured diameter for the individual particles of CEHR-18 was 12 nm, slightly smaller than the reported size range of 15-20 nm (Table VI-3). The DLS measured sizes were considerably larger than the reported values. The hydrodynamic diameters for CEHR-18 and CEHR-19 were 238 and 242 nm, respectively (Table VI-4). In agreement with the TEM, the DLS data also suggests the sample has aggregated/agglomerated in solution. DLS also showed peaks >1 µm. Although DLS is not a reliable technique for accurate sizing greater than one micron, TEM images suggest populations >1 µm are present (Figures VI-1 and VI-2).

Asymmetric-flow field flow fractionation (AF4) was used to examine the size polydispersity of CEHR-18. A very broad size population was observed (Figure VI-5). The dominant size population was 34-100 nm. A second minor population was also noted, increasing in size up to approximately 260 nm. The flow-mode DLS results agreed with the batch-mode DLS results, both showing polydispersity. CEHR-19 was not analyzed by AF4 due to bacterial contamination in the sample.

Iron concentrations, both total and free iron, were measured by inductively coupled plasma-mass spectrometry (ICP-MS). These concentrations were converted to a weight percent of iron oxide for comparison to the manufacturer-reported sample concentrations. The total iron oxide nanoparticle concentrations for CEHR-18 and CEHR-19 were 9% and 15% by weight (Table VI-9), respectively. The total nanoparticle concentration was also determined using thermogravimetric analysis (TGA). The TGA-measured concentrations for CEHR-18 and CEHR-19 were 11 and 26%, respectively (Table V-11). These values did not align with the manufacturer specified values of 20 and 10 wt% for CEHR-18 and CEHR-19, respectively. CEHR-18 was approximately half the reported concentration, while CEHR-19 was 1.5-2.5X higher than the reported concentration. The free iron content for each formulation was also measured by ICP-MS. An increase in the free iron content can be an indication of particle instability. For CEHR-18 and CEHR-19, a maximum of 1.2% and 2.5% free iron, respectively, was detected over a six-month period (Table VI-10).

ICP-MS and TGA were also used to assess the purity of the formulations. ICP-MS was used to determine if any metal impurities were present in the samples. Both samples contained zinc and manganese, but exact concentrations of these impurities were not obtained (Figure VI-6). TGA revealed additional components thought to be a coating on the nanomaterial. The percent mass ratios of coating to iron oxide were approximately 15% and 17% for CEHR-18 and CEHR-19, respectively (Table VI-12). TGA could not confirm the identity of this material. The zeta potentials of the nanoparticles were negative (Tables VI-13). These values are consistent for either uncoated iron oxide nanoparticles or those coated with a negatively-charged surface moiety.

B. Sterility

Design and Methods

Sterility, i.e. bacterial contamination, of the two iron oxide nanoformulations was assessed using NCL protocol STE-2.2 (https://ncl.cancer.gov/resources/assay-cascade-protocols). In brief, samples were plated onto LB agar plates at several dilutions (10-, 100-, and 1000-fold) and allowed to incubate at 37°C for 72 hours. The plates were then visually inspected for colony formation.

Results & Conclusions

CEHR-18 showed no visible colony formation after the 72 hr incubation period. CEHR-19 was contaminated with bacteria, having shown 72,000 CFU/mg. A summary of the sterility testing results for these samples is provided in the table below.

Table VI-1. Summary of the sterility testing results for the iron oxide nanoparticles.

Reference Number	Nanoparticle Description	Nominal size reported by manufacturer	Sterility (agar plate)
CEHR-18	Fe_3O_4 nanopowder, 20 wt% water dispersion	15-20 nm	Negative
CEHR-19	Fe_2O_3 gamma, 10 wt% water dispersion	20 nm	**72,000 CFU/mg**

C. Endotoxin

Design and Methods

The objective of this experiment was to evaluate potential endotoxin contamination in the two iron oxide formulations. NCL's protocols for the kinetic turbidity Limulus Amebocyte Lysate (LAL) assay was used (STE-1.2; https://ncl.cancer.gov/resources/assay-cascade-protocols). All samples were initially diluted to 1 mg/mL theoretical concentration and tested at 1:5, 1:50, and 1:500 dilutions in water.

Results and Discussion

CEHR-18 had undetectable levels of endotoxin (i.e., below the assay's lower limit of detection, < 0.05). CEHR-19 interfered with the LAL assay. The results shown were obtained from testing of the supernatant only. That is, the sample was resuspended in water, the nanoparticle pelleted through centrifugation, and the supernatant removed for endotoxin testing. This supernatant sample had endotoxin levels > 6000 EU/mg. This finding was not unexpected and is likely explained by the bacterial contamination detected in CEHR-19. However, bacterial serotyping was not performed to verify this. It is recommended this formulation not be used in any biological testing.

Table IV-2. Endotoxin levels detected by the LAL assay. Results are shown as endotoxin units (EU) per mg of nanoparticle

Reference Number	Nanoparticle Description	Nominal size reported by manufacturer	Endotoxin Turbidity LAL
CEHR-18	Fe_3O_4 nanopowder, 20 wt% water dispersion	15-20 nm	<0.05 EU/mg
CEHR-19	Fe_2O_3 gamma, 10 wt% water dispersion	20 nm	**6170 EU/mg**

D. Transmission Electron Microscopy

Design and Methods

Transmission electron microscopy (TEM) was conducted to assess the size and morphology of the iron oxide nanomaterials. Stock solutions were diluted to 2% with ultrapure water, and 2 µL was applied to a glow discharged carbon film grid (Electron Microscopy Sciences). The grid was washed three times with ultrapure water, blotted, and allowed to air dry before imaging. Images were taken using a T-12 TEM (FEI) equipped with a LαB6 thermoionic gun at 80 V acceleration voltage.

Particle size analysis was performed using ImageJ (https://imagej.nih.gov/ij/). Only particles that were individually dispersed were included in the sizing analysis.

Results and Discussion

Figures VI-1 and VI-2 contain representative images for CEHR-18 and CEHR-19, which are Fe_3O_4 and Fe_2O_3 gamma, respectively. CEHR-18 was similar to CEHR-16 and CEHR-17, having distinct particles that appeared to have aggregated/agglomerated in solution. The measured size of the individual particles was slightly smaller than the reported size range of 15-20 nm. CEHR-19 was unable to be sized because of the extensive aggregation within the sample.

Table VI-3. Comparison of vendor reported size and TEM-measured size.

Reference Number	Nanoparticle Description	Nominal size reported by manufacturer	TEM Measured Size
CEHR-18	Fe_3O_4 nanopowder, 20 wt% water dispersion	15-20 nm	12 ± 4 nm
CEHR-19	Fe_2O_3 gamma, 10 wt% water dispersion	20 nm	Not Sized

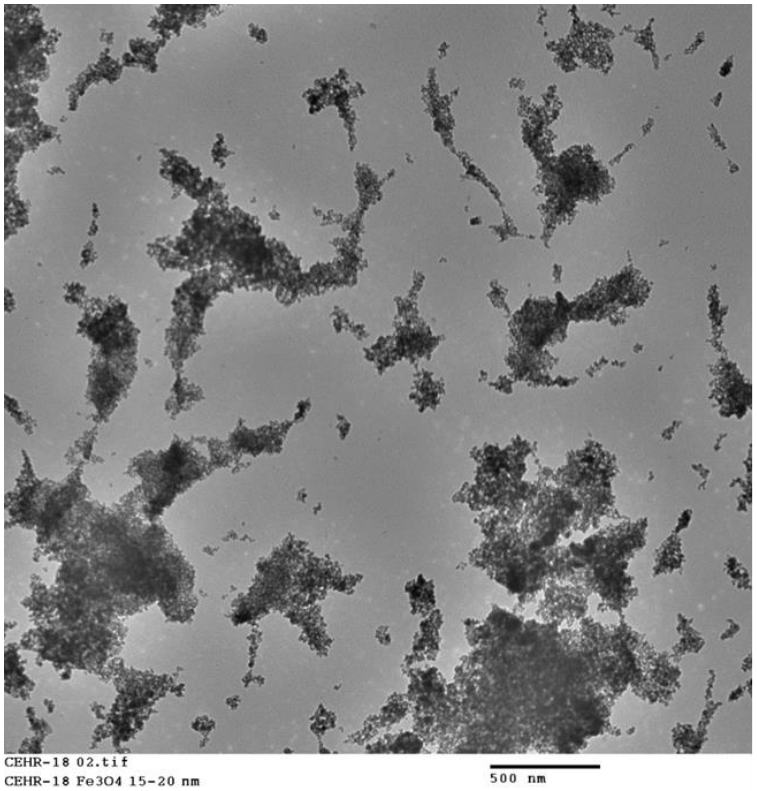

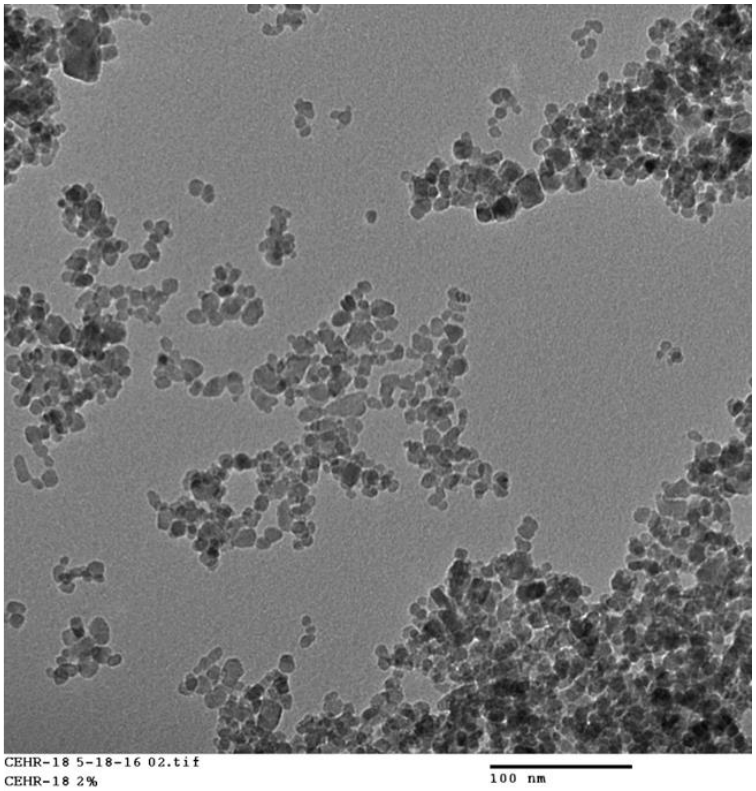

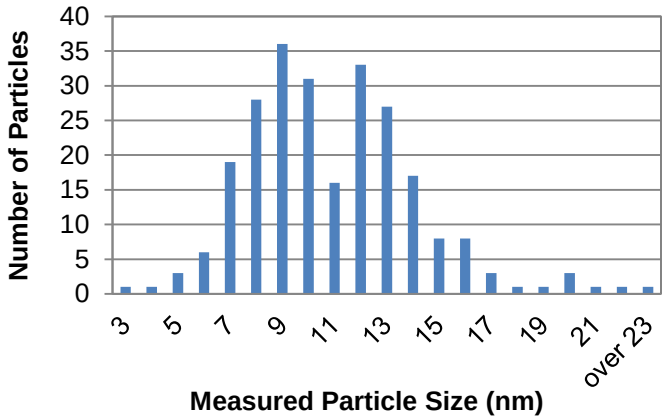

Figure VI-1. Representative TEM Images of CEHR-18. Two representative images are shown for CEHR-18, showing the range of average diameters spanning 12 ± 4 nm (n = 245).

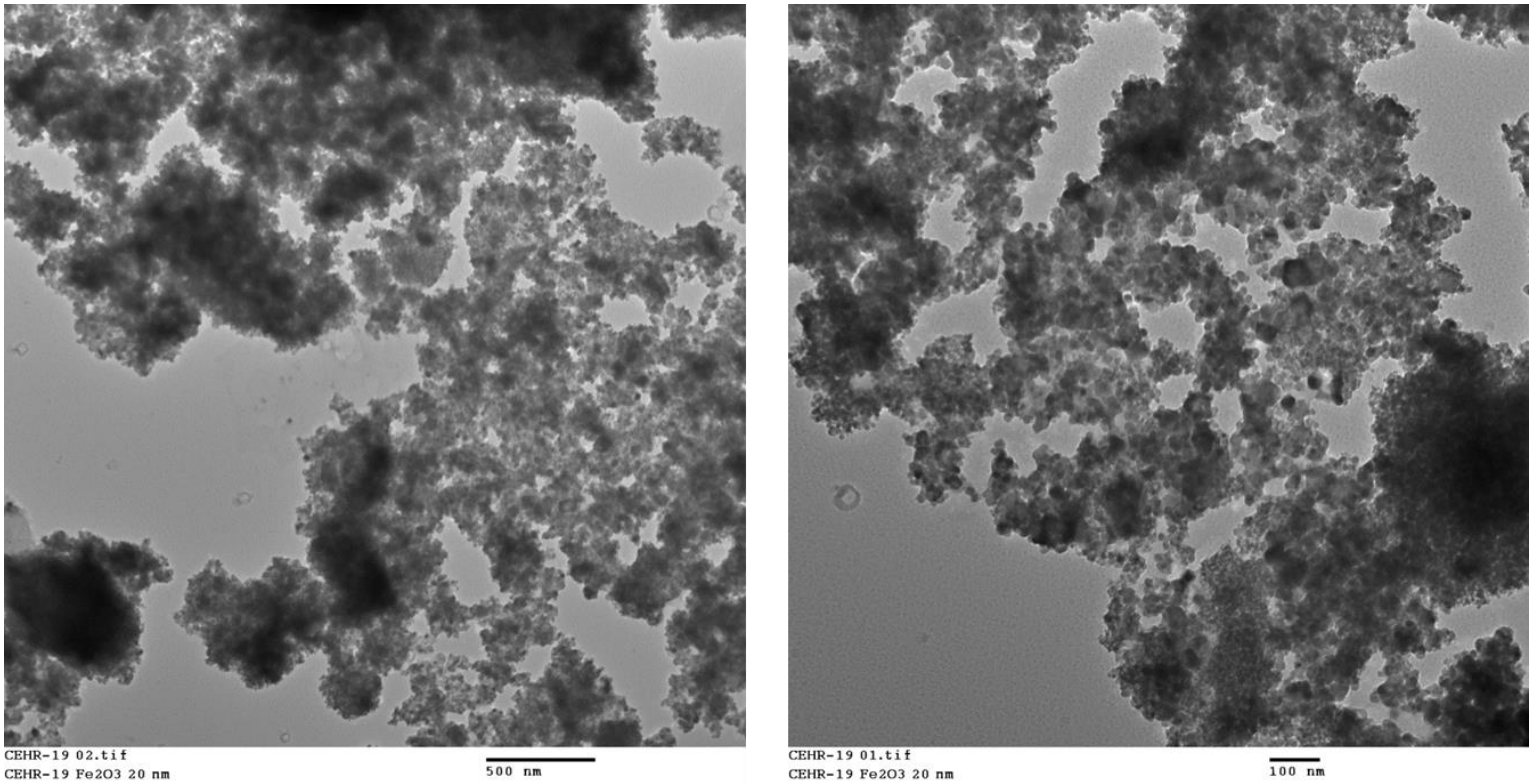

Figure VI-2. Representative TEM Images of CEHR-19. Two representative images are shown for CEHR-19, showing the severity of particle agglomeration within the sample. This sample could not be sized.

E. Hydrodynamic Size/Size Distribution via Dynamic Light Scattering

Design and Methods

A Malvern Zetasizer Nano ZS instrument (Southborough, MA) with back scattering detector (173°) was used for measuring the hydrodynamic size (diameter) in batch mode. NIST-NCL joint protocol PCC-1 was followed (https://ncl.cancer.gov/resources/assay-cascade-protocols). Stock samples of CEHR-18 and CEHR-19 were diluted 10,000- and 100,000-fold in water. Measurements were made at 25°C in a quartz microcuvette. Traces in the figures represent the average of at least twelve measurements.

Hydrodynamic diameters are reported as the intensity-weighted average and as the volume-weighted average over a particular range of size populations corresponding to the most prominent peak. The Int-Peak value is used as the hydrodynamic diameter of a particular species. The Vol-Peak and %Vol values are used to approximate relative amounts of various species in the formulation. Z-Avg values are generally used to assess batch-to-batch variability of a sample.

Results and Discussion

The iron oxide nanoparticles from US Nano were diluted in water and measured by DLS for hydrodynamic diameter. The intensity and volume distribution plots are provided in Figures VI-3 and VI-4, respectively.

CEHR-18 has a reported diameter of 15-20 nm, presumed to be a TEM diameter. The hydrodynamic diameter measured by DLS was significantly larger. Both the intensity and volume distributions were very broad, with average diameters of 238 nm and 166 nm, respectively. CEHR-19 showed a similar trend. The intensity and volume distributions were both very broad, with average diameters of 242 nm and 112 nm, respectively. Both samples appeared to have aggregated/agglomerated in solution, in agreement with the TEM images. Peaks were also noted above one micron in size; however, DLS is generally not accurate for size measurement above one micron. DLS relies on the Brownian motion of particles to calculate the size. Particles greater than one micron generally settle out of solution and are not accurately captured by DLS.

Table VI-4. Comparison of TEM and DLS sizes.

Reference Number	Nominal size reported by manufacturer	TEM Measured Size	DLS Measured Size (Int-Peak)
CEHR-18	15-20 nm	12 ± 4 nm	238 ± 15 nm
CEHR-19	20 nm	Not Sized	242 ± 26 nm

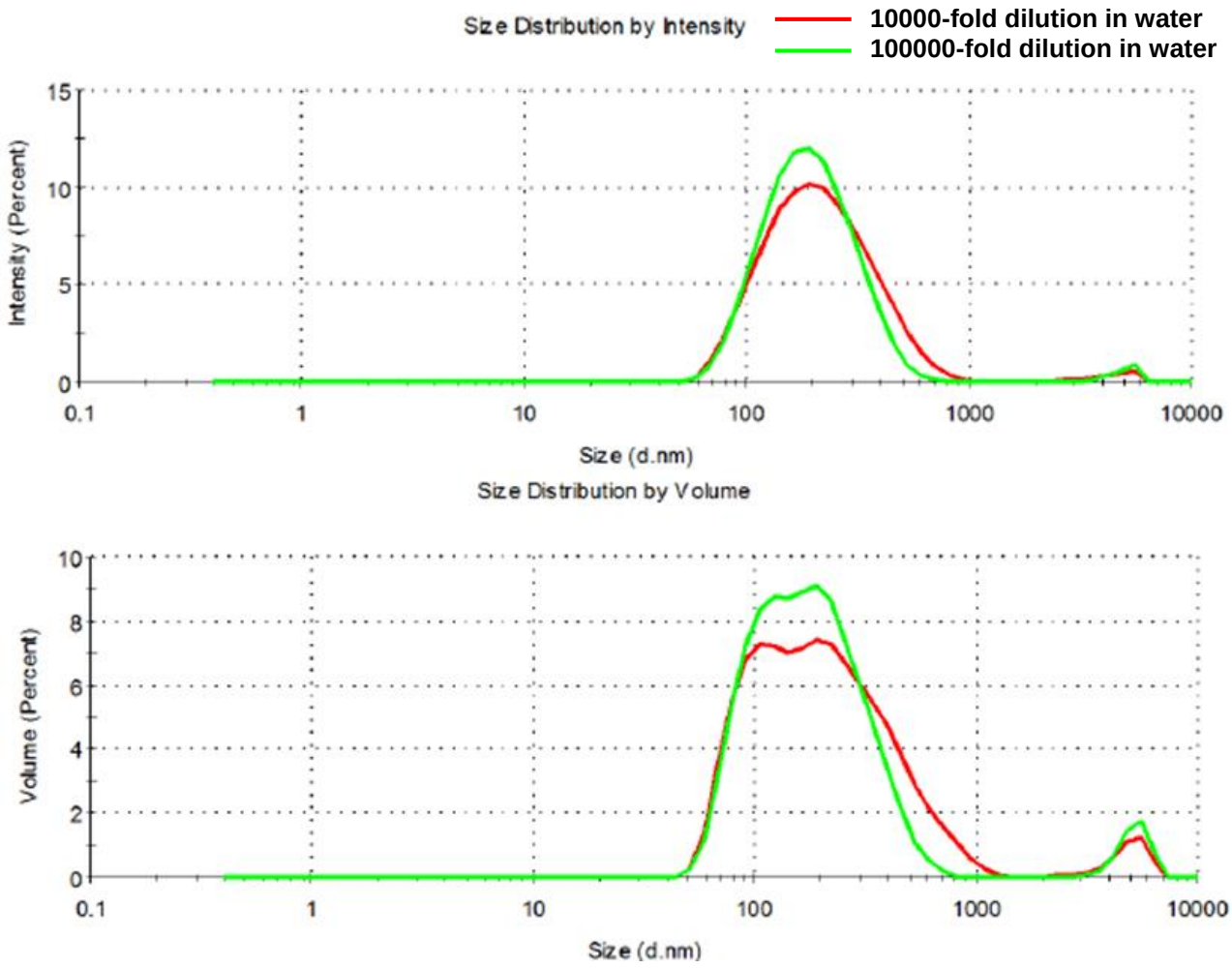

Figure VI-3. The averaged intensity and volume distribution plots for CEHR-18 diluted in water.

Table VI-5. Summary of the hydrodynamic size for CEHR-18 diluted in water

Dispersing Medium	Dilution	Z-Avg, nm	PdI	Int-Peak, nm	% Int	Vol-Peak, nm	% Vol
DI water	10,000-fold	189 ± 3	0.24 ± 0.01	238 ± 15	98 ± 1	166 ± 72	68 ± 28
DI water	100,000-fold	180 ± 5	0.23 ± 0.02	207 ± 15	98 ± 1	148 ± 44	70 ± 27

Note: Results are the average of at least 12 measurements. Z-Avg is the intensity-weighted average. PdI is the polydispersity index. Int-Peak is the intensity-weighted average over the primary peak. % Int is the percentage of the intensity spectra occupied by the primary peak. Vol-Peak is the volume-weighted average over the primary peak. % Vol is the percentage of the volume spectra occupied by the primary peak.

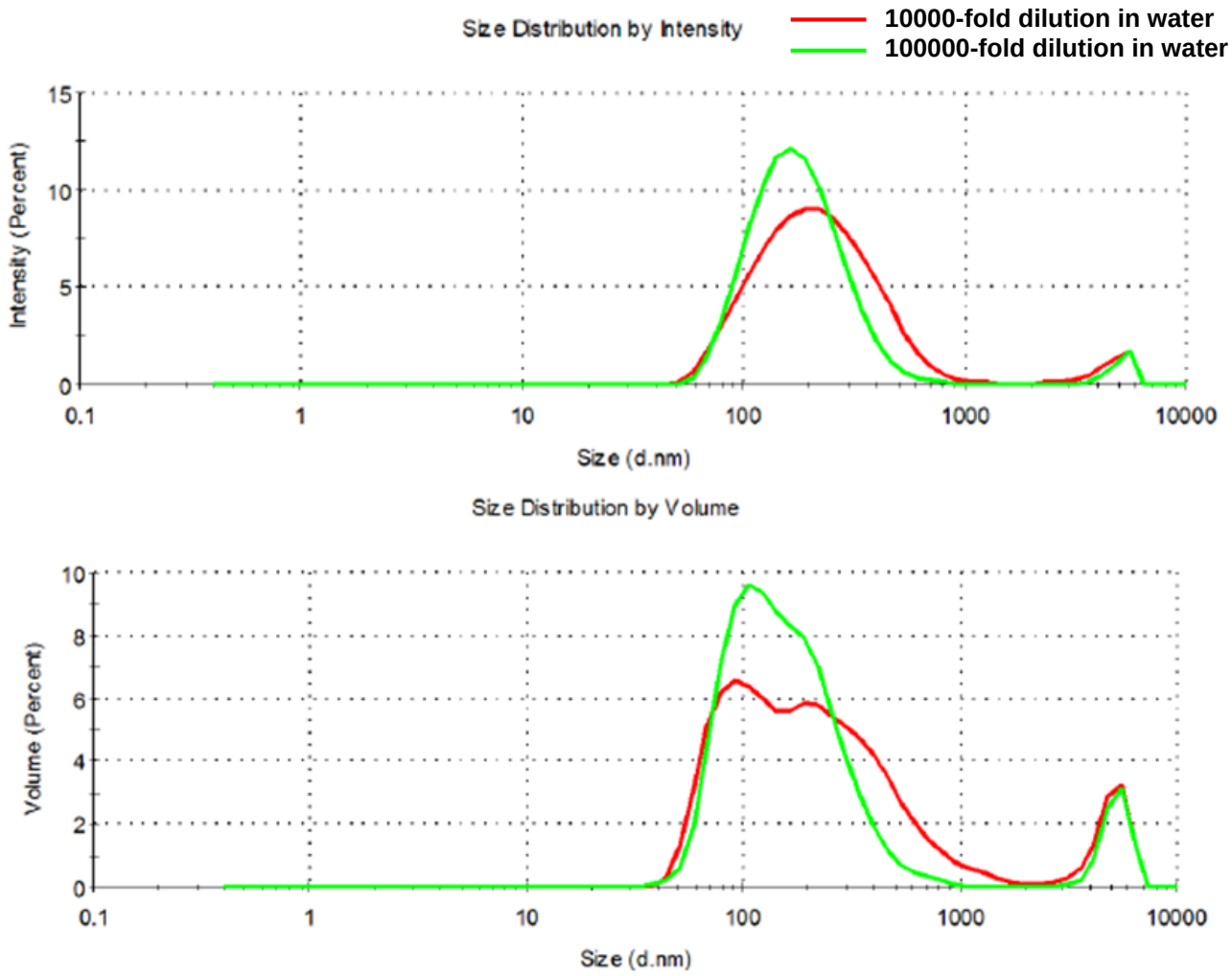

Figure VI-4. The averaged intensity and volume distribution plots for CEHR-19 diluted in water.

Table VI-6. Summary of the hydrodynamic size for CEHR-19 diluted in water

Dispersing Medium	Dilution	Z-Avg, nm	PdI	Int-Peak, nm	% Int	Vol-Peak, nm	% Vol
DI water	10,000-fold	200 ± 9	0.34 ± 0.02	242 ± 26	95 ± 3	112 ± 40	46 ± 15
DI water	100,000-fold	172 ± 14	0.22 ± 0.07	186 ± 13	97 ± 1	161 ± 25	88 ± 13

F. Asymmetric-Flow Field Flow Fractionation

Design and Methods

The iron oxide nanoparticles were separated using asymmetric-flow field-flow fractionation (AF4) with multiple in-line detectors to evaluate the polydispersity of the samples. AF4 provides a more thorough understanding of the various populations present in the sample over other batch-mode measurement techniques such as DLS alone. The AF4 system consisted of an isocratic pump (Agilent G1310A, Palo Alto, CA), well-plate autosampler (Agilent G1329A), AF4 separation channel (Eclipse DualTec; Wyatt Technology, Santa Barbara, CA), multi-angle light scattering detector (HELEOS II; Wyatt Technology), diode array detector (DAD, Agilent G1315B), and a DLS detector (Malvern Zetasizer Nano ZS; Southborough, MA). The separation channel had a length of 275 mm and a 350 µm spacer. A 10 kDa regenerated cellulose membrane was used for all separations.

The elution profile is provided in Table VI-7. The cross flow was controlled by an Eclipse flow controller. CEHR-18 was diluted 100-fold in 15 mM NaCl and filtered through a 0.2 µm regenerated cellulose membrane prior to use. The elution was also run in 15 mM NaCl. This was chosen because the nanoparticles were stable in this dispersing media after dilution and did not interact/stick to the FFF membrane. A sample injection of volume of 100 µL was used for all samples and the chromatographic traces were monitored by DLS detection and UV at 210 nm. The hydrodynamic size is plotted across the eluted peaks. The UV absorbance at 210 nm was monitored to track relative abundance of each different size population.

Table VI-7. AF4 elution profile.

Start Time (min)	End Time (min)	Duration (min)	Mode	Starting Cross-flow Rate (mL/min)	Ending Cross-flow Rate (mL/min)
0	2	2	Elution	1	1
2	4	2	Focus	-	-
4	9	5	Focus + Inject	-	-
9	19	10	Focus	-	-
19	29	10	Elution	1	1
29	31	2	Elution	1	0.5
31	41	10	Elution	0.5	0
41	61	20	Elution	0	0
61	63	2	Elution + Inject	0	0
63	64	1	Elution	0	0

Results and Discussion

The fractograms for CEHR-18 are shown in Figure VI-5. The light scattering (top and bottom panel) signals showed a very broad single peak. By UV, the majority of this sample (as evidenced by its strong UV signal) had a hydrodynamic size of 34-100 nm. Contained within this broad peak, was a second size population with sizes increasing up to 260 nm. The flow-mode DLS results agreed with the batch-mode DLS data, suggesting the sample was polydisperse. Batch-mode DLS cannot discern two populations this close in size. The larger sized population will dominate the batch-mode light scattering signal.

CEHR-19 was not subjected to AF4 analysis due to the bacterial contamination in the sample.

Table VI-8. Comparison of batch-mode and flow-mode DLS sizes.

Reference Number	Batch-mode DLS Measured Size (Int-Peak)	Flow-mode DLS Measured Size: Major peak	Flow-mode DLS Measured Size: Minor peak
CEHR-18	238 ± 15 nm	34-100 nm	200-260 nm
CEHR-19	242 ± 26 nm	Not Tested	

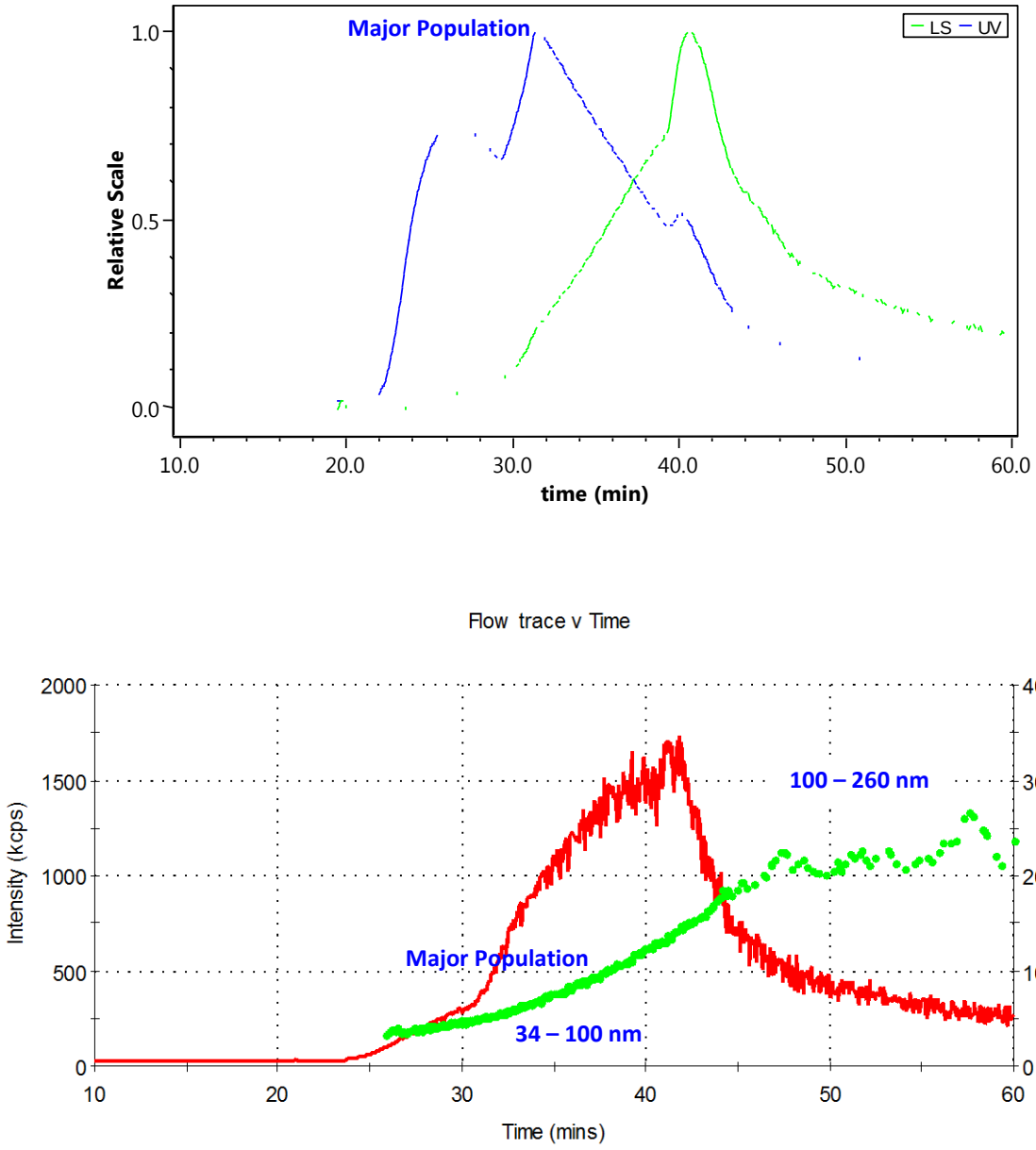

Figure VI-5. AF4 fractograms for CEHR-18. The top panel shows the UV (210 nm) and LS (light scattering) signals while the bottom panel shows the hydrodynamic size distributions across the eluted peaks.

G. Inductively Coupled Plasma Mass Spectrometry

Design and Methods

The iron concentrations of CEHR-18 and CEHR-19 were determined by inductively coupled plasma mass spectrometry (ICP-MS). An Agilent ICP-MS 7500CX equipped with a micro-mist nebulizer, standard sample introduction system, and integrated auto-sampler, operated in "no gas" mode in Agilent's proprietary ORS (Octopole Reaction System) was used. Tuning of the instrument was performed daily prior to sample testing.

Semi-Quantitative Analysis

A semi-quantitative analysis was performed on each sample prior to quantitative determination of the iron concentrations. The semi-quantitative analysis was performed to help determine the proper dilution range for the samples, as well as to detect the presence of other metals in the sample. Only metals with counts two times greater than the background were denoted.

A 15 µL aliquot of the iron stock solution was digested using 200 µL concentrated hydrochloric acid and 100 µL concentrated nitric acid. After 10 minutes, this digested sample was vortexed for 10 seconds and then diluted with 2% nitric acid to target a 30 mL first dilution. Next, a second dilution was performed by adding 10 mL of 2% nitric acid to 10 µL of the first dilution.

Total Metal Concentration

Using the data from the semi-quantitative analysis, the appropriate dilution was determined for the ICP-MS full quantitative analysis. The dilution target for the samples was 5 to 200 ppb. The total metal concentration was determined using the native formulation (i.e. not centrifuged or separated). Samples (10-100 µL) were initially digested with a 2:1 mixture of HCl:HNO_3. Typically, no more than 1 mL of concentrated acid was used. The acid digested samples were then further diluted to approximately 30-50 mL total volume with 2% nitric acid. A second dilution was then performed in which 10-100 µL of the first dilution was diluted to 10-50 mL using 2% nitric acid. Samples were run in duplicate.

The metal concentration was determined by comparing against a series of calibration standards prepared from NIST SRM 3126a. A series of concentrations ranging 5 to 200 ng/g (ppb) were prepared. The dilutions were made using 2% nitric acid. Specifically, a dilution of 5000 ng Fe / g in 2% HNO_3 was used to make a 1000 ng Fe / g solution, which was then used to create standards for the calibration curve in a range of 5 to 200 ng/g in 10 mL volumes. In addition, an internal standard, yttrium, was used to track the signal response of the ICP-MS. The internal standard was diluted to approximately 50 ppb and was mixed with the sample using a sample T. A simple linear regression was used for calculation of the metal concentrations.

The sequence for the ICP-MS runs consisted of five blanks, the calibration curve standards ordered from lowest to highest, five more blanks, then the iron oxide nanoparticle samples from highest dilution to lowest dilution. Each sample was run in duplicate with three blanks run between each sample. After the last sample was measured, five blanks were run, followed by the calibration standards, and three blanks to flush the sample introduction system.

Free Metal Concentration and Metal Release with Time

In addition to determining the total metal concentration present in each sample, ICP-MS was also used to assess the amount of free metal ions present. The separation of free metal ions from the nanoparticles was carried out using stirred cell filtration as described in Section IV-G. The stirred cell separation was performed twice on each sample at different times to evaluate the release of free metal ions over time. The dates are noted for each analysis. The permeate dilutions were run first, followed by the reserved solutions.

Results and Discussion

Semi-Quantitative Analysis

The results from the semi-quantitative analysis of CEHR-18 and -19 are shown in Figure VI-6. For both samples, iron, zinc, and manganese were present. The origin of the zinc and manganese impurities is not known. This was only an analysis to detect potential metal impurities. For an accurate determination of their concentrations, quantitative analysis compared to a standard would be required.

A. CEHR-18

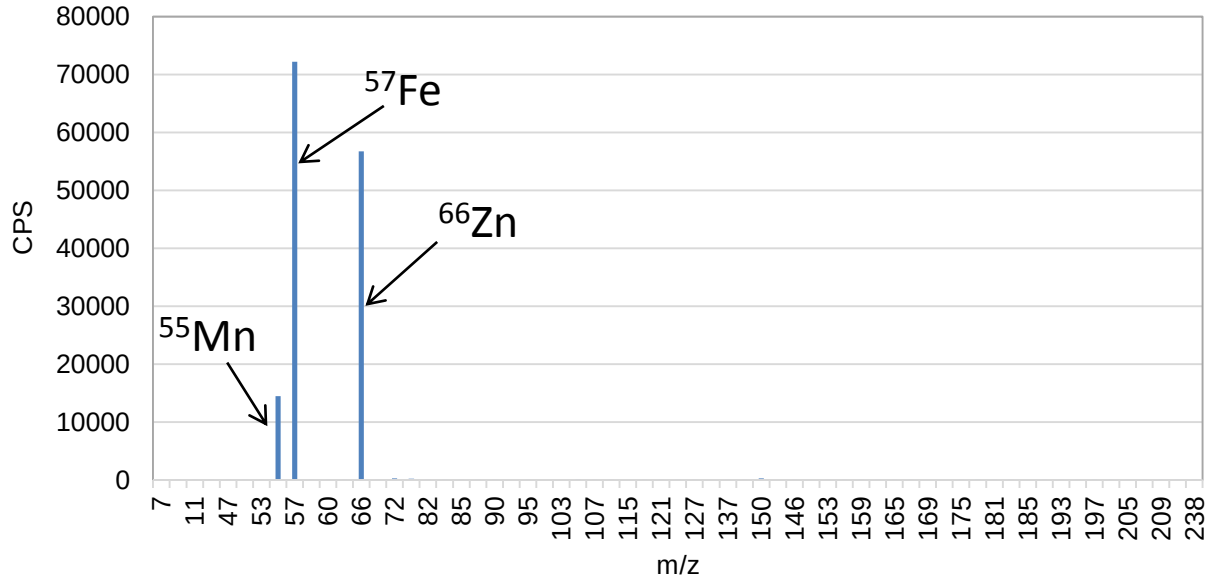

B. CEHR-19

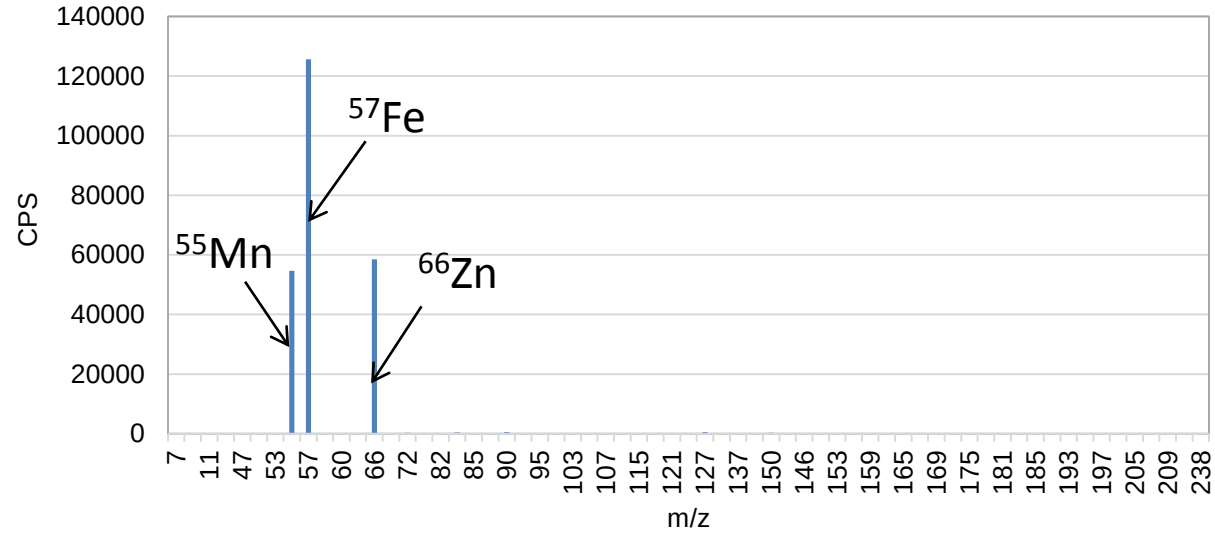

Figure VI-6. Plots of CPS vs m/z. (A) CEHR-18 semi-quantitative analysis plot. **(B)** CEHR-19 semi-quantitative analysis plot. Both samples were analyzed on 10 November 2016. Note ^{12}C, ^{23}Na, ^{24}Mg, ^{27}Al, ^{29}Si, ^{31}P, ^{34}S, ^{35}Cl, ^{39}K, and ^{43}Ca were removed in both plots to better visualize the smaller peaks. The internal standard peak for ^{89}Y was also omitted.

Full Quantitative Analysis: Total Iron Concentration

The calibration curve used for total iron quantitation was constructed from NIST SRM 3126a (Figure VI-7). Quantitative total iron concentrations for CEHR-18 and CEHR-19 are summarized in Table VI-9 and were 68 and 107 mg/g, respectively. The ICP-MS iron concentrations, in units of mg/g, were also converted to weight percents for comparison to the vendor reported values. The iron mass was converted to Fe_3O_4 for CEHR-18 and Fe_2O_3 for CEHR-19, using the molecular weights, 231.53 and 159.69 g/mol, respectively. To calculate the iron oxide weight percent, the iron oxide mass was divided by the mass of the solution to output the nanoparticle percent. The iron oxide concentrations for CEHR-18 and CEHR-19 were 9% and 15% by weight, respectively. The total iron oxide concentration for CEHR-18 was less than half of its vendor-specified value of 20 wt%, while that of CEHR-19 was 1.5X higher than its vendor-specified value 10 wt%.

Of note, there was a considerable difference in total iron concentration among the various runs, especially for CEHR-19. This is evident by the large standard deviation. Both samples settled with time which likely led to inconsistent sampling. The user is cautioned to ensure an adequate and thorough mixing to prior to sampling. The nanoparticle settling can be seen in the picture to the right.

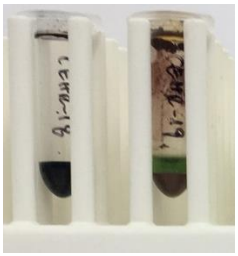

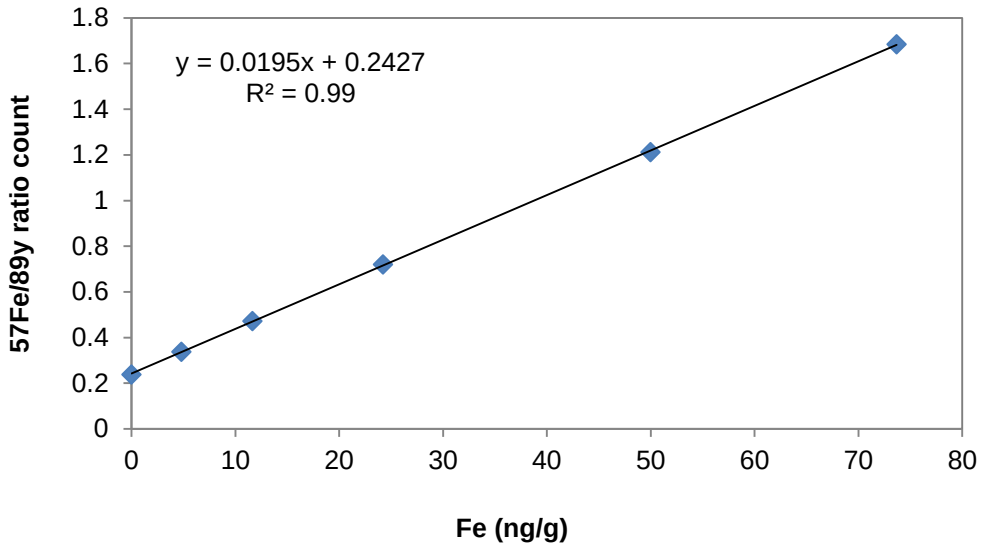

Figure VI-7. Iron Calibration Curve. A typical calibration curve ranging from 0 to 75 Fe ng/g, used to calculate the iron concentration in CEHR-18 and CEHR-19. The calibration curve was constructed from NIST SRM 3126a iron standard.

Table VI-9. Summary of the total iron concentration in CEHR-18 and CEHR-19 as determined by ICP-MS. The total iron concentration was also converted to Fe_3O_4 for CEHR-18 and Fe_2O_3 for CEHR-19, respectively, for comparison to the reported concentrations.

Reference Number	Reported Concentration	Total [Fe]	Total [Fe_xO_y]
CEHR-18	20 wt%	68 ± 12 mg/g (n=5)	9% by weight
CEHR-19	10 wt%	107 ± 38 mg/g (n=5)	15% by weight

Free Iron Concentration

Stirred cell filtration was employed to separate any free iron ions from the iron oxide nanoparticles. Repeat measurements were made approximately three months apart to assess iron release kinetics/stability of the formulation. The stock sample (prior to stirred cell filtration; designated as Total [Fe] in Table IV-10) was re-measured each time and used to calculate (normalize) the percent free iron (free [Fe] / total [Fe]) in each formulation.

The free iron concentrations in CEHR-18 and CEHR-19 at three time points are shown in Table VI-10. While somewhat variable over the six-month window, a maximum of 1.2% and 2.5% free iron was observed for CEHR-18 and CEHR-19, respectively. The differences in the total iron concentrations among the measurements reported in Table VI-10 are attributed to the non-homogeneity within the sample as described on the previous page.

Table VI-10. Summary of Free Iron Concentrations. A summary of the free iron detected by ICP-MS following stirred cell separation. Each sample was analyzed at three time points.

Reference Number	Date	Total [Fe] (Reserve)	Free [Fe] (Permeate)	% Free Fe
CEHR-18	09 June 2016	83 ± 2 mg/g	0.66 ± 0.01 mg/g	0.8%
CEHR-18	26 Aug 2016	50 ± 3 mg/g	0.61 ± 0.08 mg/g	1.2%
CEHR-18	21 Nov 2016	69.9 ± 0.7 mg/g	0.20 ± 0.02 mg/g	0.3%
CEHR-19	09 June 2016	64 ± 2 mg/g	1.60 ± 0.03 mg/g	2.5%
CEHR-19	26 Aug 2016	72 ± 6 mg/g	1.29 ± 0.02 mg/g	1.8%
CEHR-19	21 Nov 2016	134 ± 4 mg/g	2.35 ± 0.05 mg/g	1.8%

H. Thermogravimetric Analysis

Design and Methods

Samples were analyzed via thermogravimetric analysis (TGA) to assess whether coatings were present on the nanoparticles and in what concentration. TGA was also used to determine the concentration of the metallic nanomaterial by measuring the residual material remaining after combustion of any coatings. For measurement of the metallic nanoparticle concentration, the samples were measured in their liquid (as-received) forms. For detection and measurement of coating concentrations, the samples were lyophilized prior to the TGA run. The signal from the water loss had the potential to swamp out a small amount of loss from any coating present, and thus was removed/minimized by lyophilization. Using lyophilized samples allowed for better sensitivity (total weight measured >1 mg) and hence a more accurate coating determination.

Nanoparticle Concentration

For each liquid sample, 50 µL was transferred to an aluminum oxide crucible (150 µL crucible with lid, Mettler Toledo) for TGA measurement (TGA/DSC 1, Mettler Toledo). Samples were held at 25˚C for 5 min, then ramped to 1000˚C at a heating rate of 20˚C/min under nitrogen gas. A new crucible was used for each sample. The empty crucible was subjected to the TGA method prior to loading the sample to serve as a background correction.

TGA cannot confirm the oxidation state of the material. Concentrations are reported using the manufacturer-reported oxidation state.

Coating Detection and Concentration

To determine coating content of the samples, samples were lyophilized overnight after being frozen in an ultra-low temperature freezer (-80˚C) for at least 3 hours. Typically, 250 µL of sample solution yielded 45 mg of lyophilized powder. About 10 mg was the typical amount added for TGA analysis, allowing for repeat runs, if necessary. The dried samples were added to aluminum oxide crucibles and subjected to the same temperature program as described above for the liquid samples.

Results and Discussion

Nanoparticle Concentration

The TGA curves (top panel; weight loss versus temperature) for CEHR-18 and CEHR-19 are shown in Figures VI-8 and VI-9, respectively. The first derivative of this curve (bottom panel) was used to highlight the weight loss events. For both samples, a single weight loss event was observed between 50-180˚C, corresponding to the loss of water. The total mass iron oxide was determined by using the amount of mass left at the end of the TGA run. The TGA-measured values for CEHR-18 and CEHR-19 were 11% and 26 % by weight, respectively. CEHR-18 is roughly half the reported concentration, while CEHR-19 is more than double the reported concentration.

Despite being very different from the reported concentrations, the TGA measured concentrations aligned very well with the ICP-MS measured concentrations for CEHR-18 (Table VI-11). The TGA CEHR-19 concentration was higher than the ICP-MS concentration, but both showed a concentration higher than theoretical. As discussed in the ICP-MS section, both nanoparticle solutions were heterogeneous with visible particle sedimentation. This could result in inconsistent sampling which would influence nanoparticle concentrations.

Note, this analysis assumes that, at the end of the run, all that remained was the iron oxide nanoparticles; the water would have evaporated and any organic coating present would have combusted. In some instances, combustion of a coating may leave residual mass, which would increase the nanoparticle concentration. It is not possible to determine this without subjecting the coating alone (not in nanosolution) to the TGA method.

Table VI-11. Comparison of TGA Measured Concentration to ICP-MS Measured and Reported Nanoparticle Concentrations.

Reference Number	Reported Concentration	Measured Concentration via ICP-MS	Measured Concentration via TGA of Liquid Sample
CEHR-18	20 wt%	9%	11 wt%
CEHR-19	10 wt%	15%	26 wt%

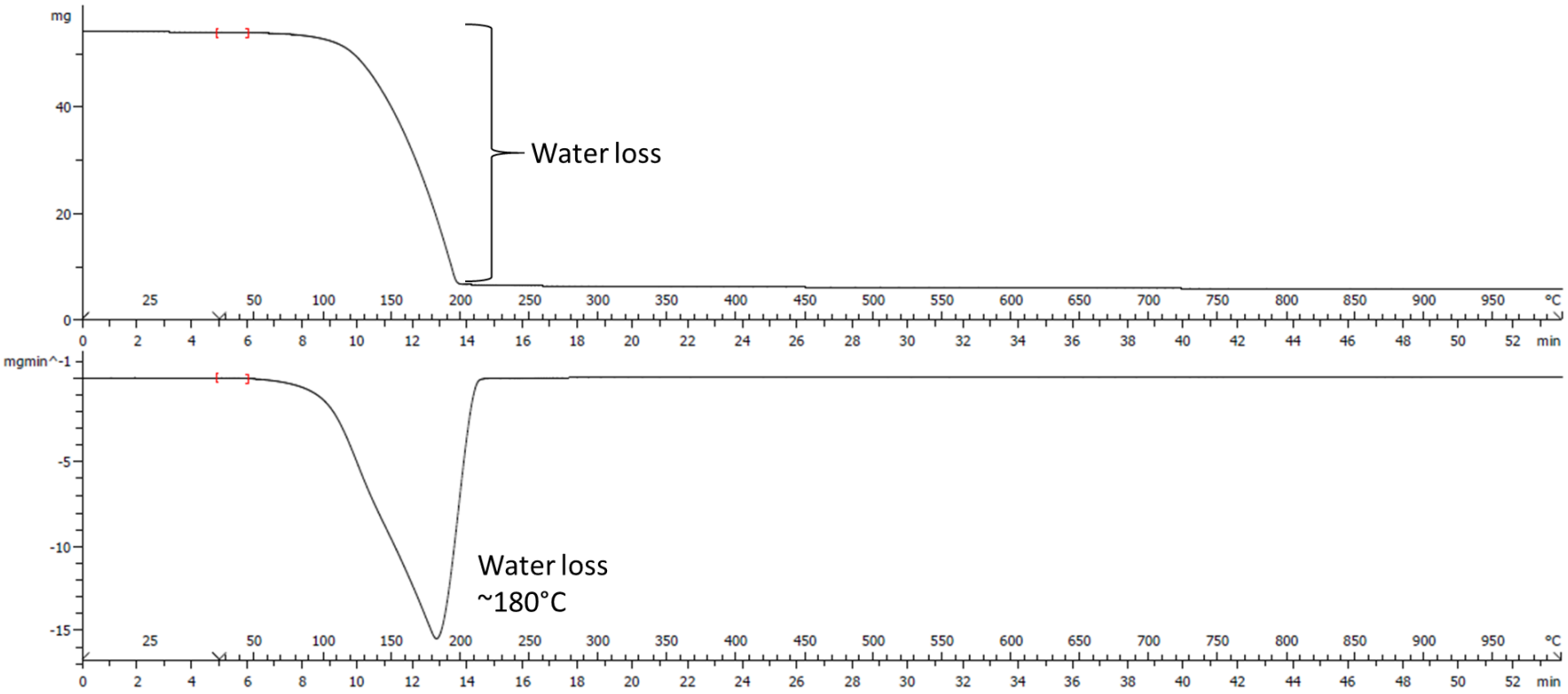

Reference Number	Volume (µL)	Starting Mass (mg)	Total Mass Loss (mg)	Residue mass (mg)
CEHR-18	50	54.1773	48.3748	5.8025

Figure VI-8. TGA thermogram of CEHR-18. The top panel is the weight loss versus temperature (and time) curve. The bottom panel is the first derivative of that curve.

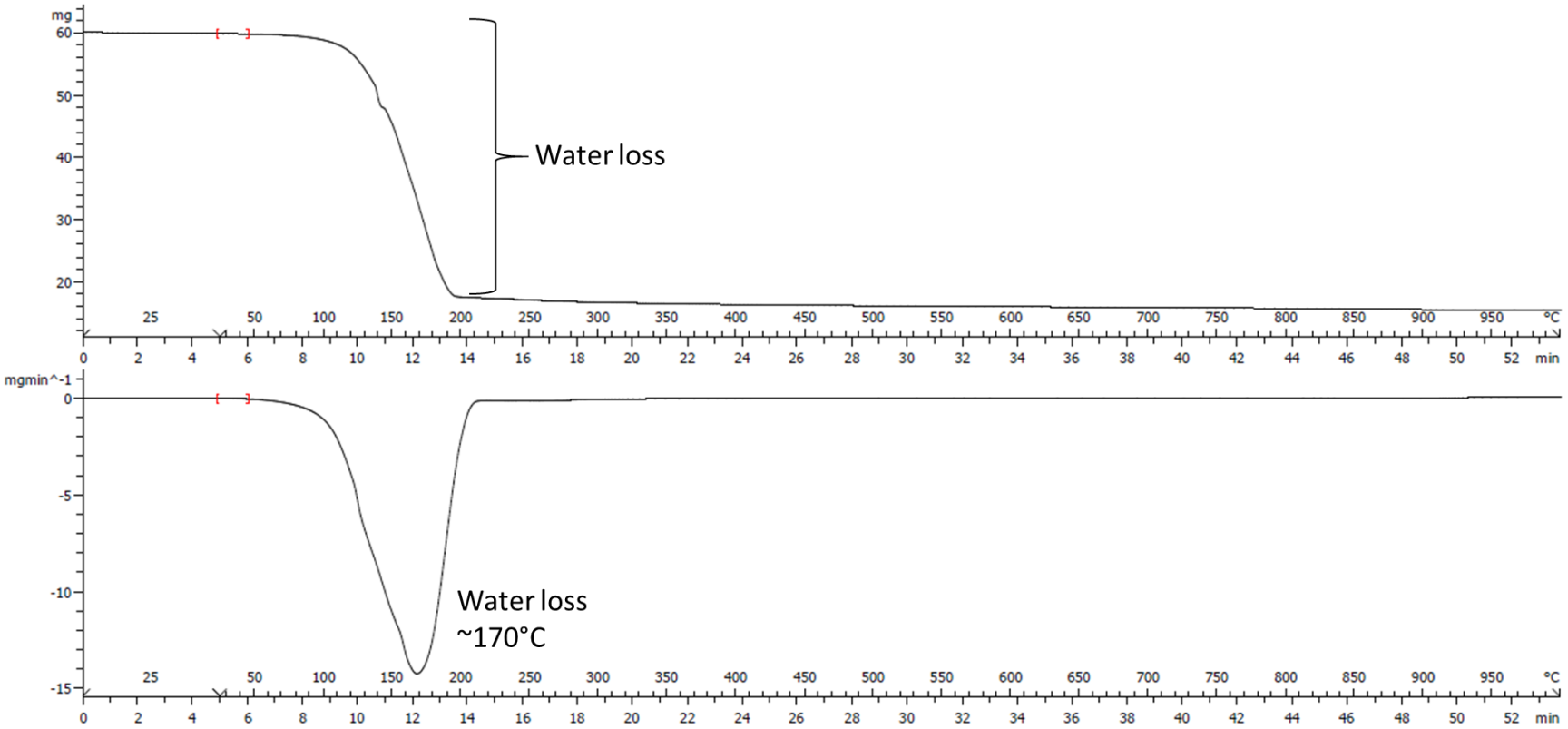

Reference Number	Volume (µL)	Starting Mass (mg)	Total Mass Loss (mg)	Residue mass (mg)
CEHR-19	50	59.8302	44.5592	15.271

Figure VI-9. TGA thermogram of CEHR-19. The top panel is the weight loss versus temperature (and time) curve. The bottom panel is the first derivative of that curve.

Coating Detection and Concentration

TGA was also used to determine whether a surface coating was present. The manufacturers of the iron oxide nanoparticles, US Nano, did not disclose whether a coating was used on the nanoparticles. Often however, especially for proprietary coatings, this information is omitted from sample descriptions. It was assumed that if any coating were present, it would be in very low quantities. Since the water peak dominated the TGA curves, all samples were lyophilized to remove the water and improve sensitivity for coating detection. Typical TGA curves for the lyophilized iron oxide samples are shown in Figures VI-10 and VI-11, respectively.

Multiple weight loss events were observed for both CEHR-18 and CEHR-19. In both samples, the first weight loss event corresponded to the loss of residual water and occurred by 150˚C. Two decomposition temperatures, 240 and 725°C, were observed for CEHR-18. Similar decomposition temperatures of 260 and 725°C, were observed for CEHR-19.It was assumed that these weight losses were due to surface coating and/or added excipients (possibly to help with solubilization and stability).

For each run, the weight loss of coating was calculated by using the first derivative analysis to mark the beginning and end of each weight loss event. The beginning and end was chosen where the derivative was constant (essentially zero). The final weight, as measured after the TGA run, was taken to be the iron oxide amount. This translated to a starting and ending temperature range of 200 and 1000°C, respectively. This assumes that the weight of any residual decomposed coating and/or excipients is negligible relative to the weight of iron oxide nanoparticles. The mass ratio of coating to iron oxide nanoparticles was then calculated for each independent run. The calculated percent coatings were 15% and 17% for CEHR-18 and CEHR-19, respectively (Table VI-12). Note, the identity of the coating and/or excipients could not be determined by TGA and was not reported by the vendor.

Table VI-12. Summary of Percent Coating Mass per Mass Nanoparticle detected in each of the iron oxide nanoparticles.

Reference Number	Reported Coating	%Mass Coating per Mass Nanoparticle
CEHR-18	None reported	15%
CEHR-19	None reported	17%

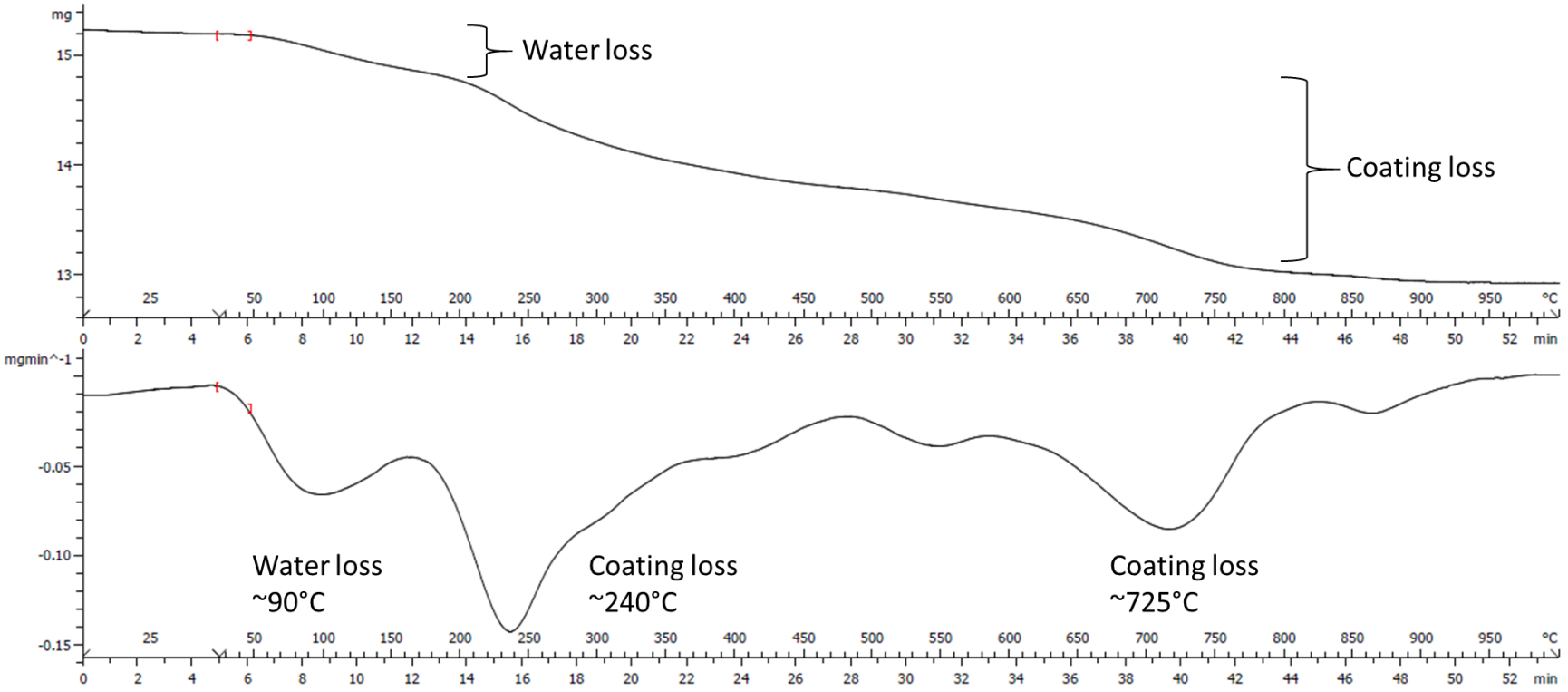

Reference Number	Starting Mass (mg)	Water Loss (mg)	Coating Loss (mg)	Residue (mg)	%Mass Coating per Mass Iron Oxide Nanoparticles
CEHR-18	15.238	0.334	1.977	12.922	15%

Figure VI-10. TGA thermogram of CEHR-18 (lyophilized). The top panel is the weight loss versus temperature (and time) curve. The bottom panel is the first derivative of that curve.

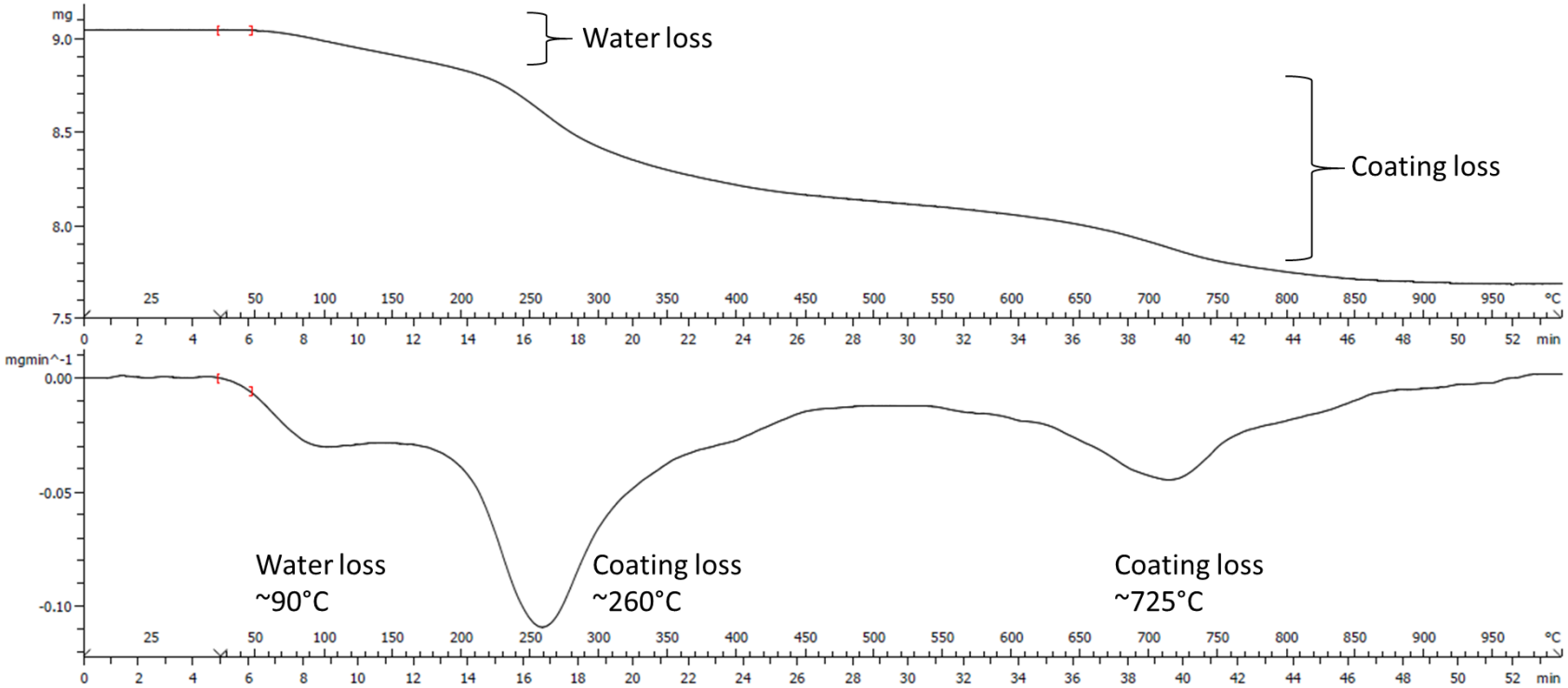

Reference Number	Starting Mass (mg)	Water Loss (mg)	Coating Loss (mg)	Residue (mg)	%Mass Coating per Mass Iron Oxide Nanoparticles
CEHR-19	9.053	0.091	1.268	7.684	17%

Figure VI-11. TGA thermogram of CEHR-19 (lyophilized). The top panel is the weight loss versus temperature (and time) curve. The bottom panel is the first derivative of that curve.

I. Zeta Potential

Design and Methods

A Malvern Zetasizer Nano ZS instrument was used to measure zeta potential at 25°C for all samples. NCL protocol PCC-2 was followed (https://ncl.cancer.gov/resources/assay-cascade-protocols). Both iron oxide samples were diluted 10,000-fold in deionized water. Sample pH was measured before loading into a pre-rinsed folded capillary cell. An applied voltage of 150 V was used. Traces in the figures represent the average of four measurements.

The instrument was validated by running an appropriate standard (Zeta Potential Transfer Standard, DTS0050, zeta potential value of -42 ± 4 mV at 25°C, Malvern Instruments) before all zeta potential measurements.

Results and Discussion

The iron oxide nanomaterials, CEHR-18 and CEHR-19, both had negative zeta potentials, at -36 mV (Table VI-13). Negative zeta potentials would be anticipated for either uncoated iron oxide nanoparticles or those modified with a negatively charged surface coating.

Table VI-13. Summary of the zeta potentials for CEHR-18 and CEHR-19.

Sample	pH	Zeta Potential
CEHR-18	7.6	-36 ± 0 mV
CEHR-19	7.4	-36 ± 1 mV

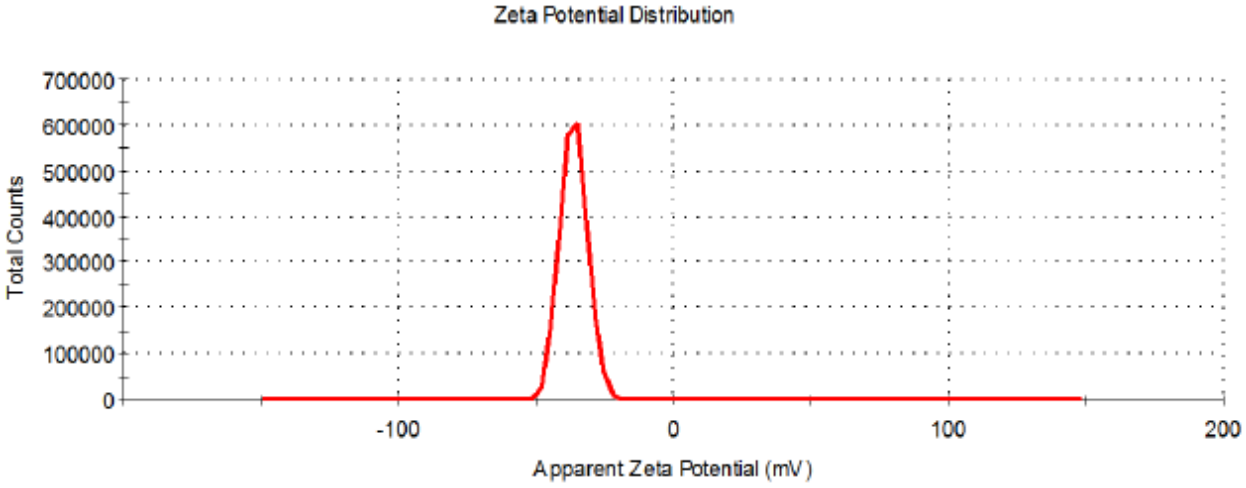

Sample	pH	Zeta Potential
CEHR-18	7.6	-36 ± 0 mV

Figure VI-12. The averaged zeta potential distributions for CEHR-18 diluted 10,000-fold in deionized water.

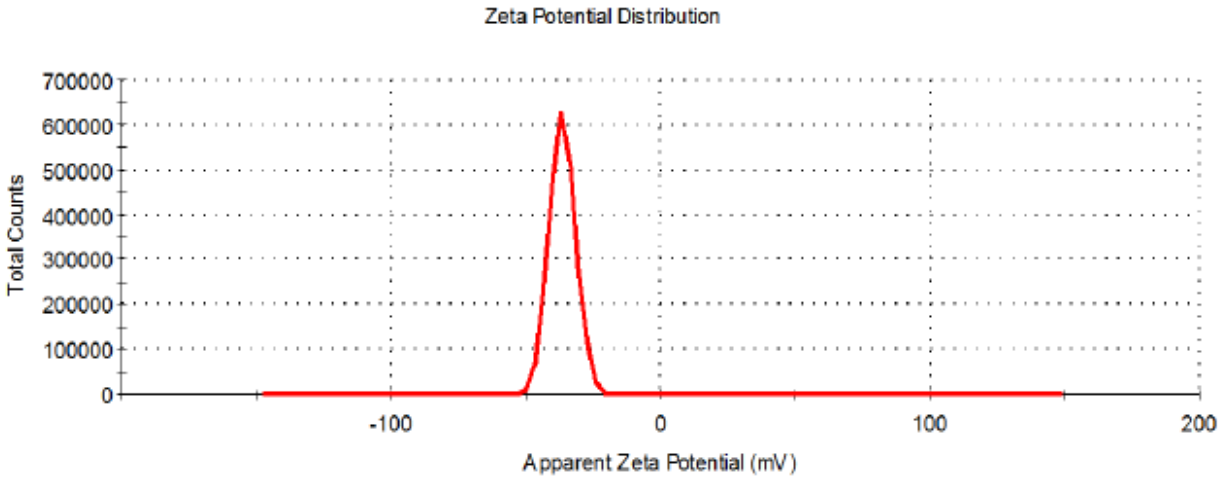

Sample	pH	Zeta Potential
CEHR-19	7.4	-36 ± 1 mV

Figure VI-13. The averaged zeta potential distributions for CEHR-19 diluted 10,000-fold in deionized water.

VII. Aluminum Oxide

VII. Aluminum Oxide

A. Section Summary

Three aluminum oxide nanoparticles with nominal sizes of 10, 30 and 30 nm (CEHR-20, CEHR-21, and CEHR-22, respectively) were characterized for sterility and relevant physicochemical parameters. This included size (DLS and TEM) measurements, zeta potential, total and free aluminum concentrations by inductively-coupled plasma mass spectrometry (ICP-MS) and detection and quantification of possible surface coatings on the nanoparticles (TGA).

Sterility screening of the aluminum oxide nanoparticles showed that all three samples were free of bacterial contamination. Endotoxin levels were quantitated by the Limulus Amebocyte Lysate (LAL) assay. Analysis revealed that all three samples had endotoxin levels below the assay limit of detection. For CEHR-20 and CEHR-21 this translated to endotoxin values ≤ 0.5 EU/mg, and for CEHR-22 this was ≤ 5 EU/mg (Table VII-2). The difference in the reported values for CEHR-22 was due to a different dilution factor for this sample. CEHR-22 interfered with the LAL assay at the lower dilution.

Size analysis of the three aluminum oxide nanomaterials was conducted by dynamic light scattering (DLS) and transmission electron microscopy (TEM). By TEM, CEHR-20 appeared to consist of longer, rod-like particles, measuring 24 nm (along the longest axis). This is more than double the reported size of 10 nm (Table VII-3). CEHR-21 had an average measured size of 30 nm, consistent with the reported size. CEHR-22 was half of the reported size, measuring only 15 nm. Both CEHR-21 and CEHR-22 appeared to have flake or plate-like particles rather than spheres. For all three samples, the DLS measured sizes were considerably larger than their reported values suggesting possible aggregation/agglomeration in solution. The intensity DLS distribution was 122, 194, and 171 nm, for CEHR-20, CEHR-21, and CEHR-22, respectively (Tables III-4 to III-6).

Asymmetric-flow field flow fractionation (AF4) was attempted to examine the size polydispersity of the aluminum oxide nanoparticles; however, these samples could not be measured reliably. All three samples are positively-charged (Table VII-12) and interacted strongly with the membranes. Two membranes, regenerated cellulose and polyethersulfone (10 kDa MWCO for both) were tested, but the samples stuck to the membranes. As a result, the light scattering (DLS and MALS) signals were unreliable. Additional attempts to reduce the membrane interactions with PBS or 0.05 % (v/v) SDS resulted in nanoparticle instability (i.e. precipitation) when diluted with either dispersant. Therefore, no AF4 data is presented for the aluminum oxide materials.

Aluminum concentrations, both total and free aluminum were measured by inductively coupled plasma-mass spectrometry (ICP-MS). These concentrations were converted to a weight percent of aluminum oxide for comparison to the manufacturer-reported sample concentrations. The total aluminum oxide nanoparticle concentrations for CEHR-20, CEHR-21, and CEHR-22 were 10%, 15%, and 22% by weight, respectively (Table VII-8). The total nanoparticle concentration was also determined using thermogravimetric analysis (TGA). The TGA-measured concentrations for CEHR-20, CEHR-21, and CEHR-22 were 16, 19, and 19% by weight, respectively (Table VII-10). The TGA results agreed with the manufacturer-specified value of 20 wt% (for all three samples) better than the ICP-MS results. Sample heterogeneity is a likely reason for the differences in values. CEHR-20, for example, was gelatinous which makes it difficult to ensure consistent sampling. The free aluminum content for each formulation was also measured by ICP-MS. An increase in the free aluminum content can be an indication of particle

instability. For CEHR-20, CEHR-21, and CEHR-22, a maximum of 0.1%, 0.3% and 0.1% free aluminum, respectively, was detected over a six-month window (Table VII-9).

ICP-MS and TGA were also used to assess the purity of the formulations. ICP-MS was used to determine if any metal impurities were present in the samples. No metal impurities were found in CEHR-22. CEHR-20 contained zinc and CEHR-21 contained yttrium, zirconium, and hafnium (Figure VII-7). TGA revealed additional components thought to be a coating on the nanomaterial. The percent mass ratios of coating to aluminum oxide were approximately 23%, 5%, and 14% for CEHR-20, CEHR-21, and CEHR-22, respectively (Table VII-11). TGA could not confirm the identity of this material, although a difference in decomposition temperatures indicates the coating and/or added excipients is different for CEHR-20 versus CEHR-21 and CEHR-22. The zeta potentials for all three aluminum oxide nanoparticles were positive (Table VII-12). These values are inconsistent for uncoated aluminum oxide nanoparticles and suggest they may be coated with a positively-charged surface moiety.

B. Sterility

Design and Methods

Sterility, i.e. bacterial contamination, of the three aluminum oxide nanoparticles was assessed using NCL protocol STE-2.2 (https://ncl.cancer.gov/resources/assay-cascade-protocols). In brief, samples were plated onto LB agar plates at several dilutions (10-, 100-, and 1000-fold) and allowed to incubate at 37°C for 72 hours. The plates were then visually inspected for colony formation.

Results & Conclusions

None of the three tested samples, CEHR-20, CEHR-21, or CEHR-22, showed visible colony formation after the 72 hr incubation period. A summary of the results is provided in the table below.

Table VII-1. Summary of the sterility testing results for the aluminum oxide nanoparticles.

Reference Number	Nanoparticle Description	Nominal size reported by manufacturer	Sterility (agar plate)
CEHR-20	Al_2O_3 gamma, 20 wt% dispersion	10 nm	Negative
CEHR-21	Al_2O_3 alpha, 20 wt% dispersion	30 nm	Negative
CEHR-22	Al_2O_3 gamma, 20 wt% dispersion	30 nm	Negative

C. Endotoxin

Design and Methods

The objective of this experiment was to evaluate potential endotoxin contamination in the three aluminum oxide formulations. NCL's protocol for the kinetic turbidity Limulus Amebocyte Lysate (LAL) assay was used (STE-1.2; https://ncl.cancer.gov/resources/assay-cascade-protocols). All samples were initially diluted to 1 mg/mL theoretical concentration and tested at 1:5, 1:50, and 1:500 dilutions in water. CEHR-22 interfered with the assay at all initial dilutions and was re-tested at a 1:5000 dilution.

Results and Discussion

All three samples had undetectable levels of endotoxin, i.e., below the assay's lower limit of detection (0.001 EU/mL). Results are reported from the lowest dilution which did not interfere with the LAL assay, and are corrected for the appropriate dilution factor. The endotoxin levels were below 0.5 EU/mg for CEHR-20 and CEHR-21, and below 5 EU/mg for CEHR-22. Analysis of CEHR-22 at lower dilutions (5-, 50-, and 500-fold) was invalid due to sample interference with the LAL assay. Therefore, this sample was re-tested at a dilution of 5000-fold. This is the reason for the different sensitivity reported for CEHR-22.

Also of note, CEHR-20 and CEHR 22 interfered with the LAL assay. Results for these materials were obtained by testing the supernatant only. Briefly, the sample was resuspended in water, the nanoparticle pelleted through centrifugation, and the supernatant removed for endotoxin testing. A caveat to this approach is that any endotoxin that remains bound to the centrifuged and removed nanoparticle is not quantified.

Table VII-2. Endotoxin levels detected by the LAL assay. Results are shown as endotoxin units (EU) per mg of nanoparticle.

Reference Number	Nanoparticle Description	Nominal size reported by manufacturer	Endotoxin Turbidity LAL
CEHR-20	Al_2O_3 gamma, 20 wt% dispersion	10 nm	< 0.5 EU/mg
CEHR-21	Al_2O_3 alpha, 20 wt% dispersion	30 nm	< 0.5 EU/mg
CEHR-22	Al_2O_3 gamma, 20 wt% dispersion	30 nm	< 5 EU/mg

D. Transmission Electron Microscopy

Design and Methods

Transmission electron microscopy (TEM) was conducted to assess the size and morphology of the aluminum oxide nanomaterials. Stock solutions of the CEHR-20, CEHR-21 and CEHR-22 samples were diluted to 0.25%, 0.5%, and 0.1%, respectively, with ultrapure water. A 2 µL aliquot was applied to a glow discharged carbon film grid (Electron Microscopy Sciences). The grid was washed three times with ultrapure water, blotted, and allowed to air dry before imaging. Images were taken using a T-12 TEM (FEI) equipped with a LαB6 thermoionic gun at 80 V acceleration voltage.

Particle size analysis was performed using ImageJ (https://imagej.nih.gov/ij/). Only particles that were individually dispersed were included in the sizing analysis.

Results and Discussion

Representative TEM images for the three aluminum oxide samples are provided in Figures VII-1 to VII-3. CEHR-20 appeared to have more rod-like structures, whereas CEHR-21 and CEHR-22 appeared to have more flake-like structures. CEHR-20 was measured along the longest axis for sizing and gave an average diameter of 24 nm, more than double the manufacturer reported size (presumed to be a TEM diameter). The average diameter of CEHR-21 was 30 nm, in agreement with the reported nominal size. However, the standard deviation was more than 50% of the particle size. CEHR-22 had a TEM diameter of 15 nm, half the reported size.

These differences in sizes highlight the challenge in specifying a particle diameter for a sample that is heterogeneous in nature, has the potential to aggregate/agglomerate in solution, and has different shapes.

Table VII-3. Comparison of vendor reported size and TEM-measured size.

Reference Number	Nanoparticle Description	Nominal size reported by manufacturer	TEM Measured Size
CEHR-20	Al_2O_3 gamma, 20 wt% dispersion	10 nm	24 ± 7 nm (Rod-like)
CEHR-21	Al_2O_3 alpha, 20 wt% dispersion	30 nm	30 ± 17 nm (Flakes)
CEHR-22	Al_2O_3 gamma, 20 wt% dispersion	30 nm	15 ± 5 nm (Flakes)

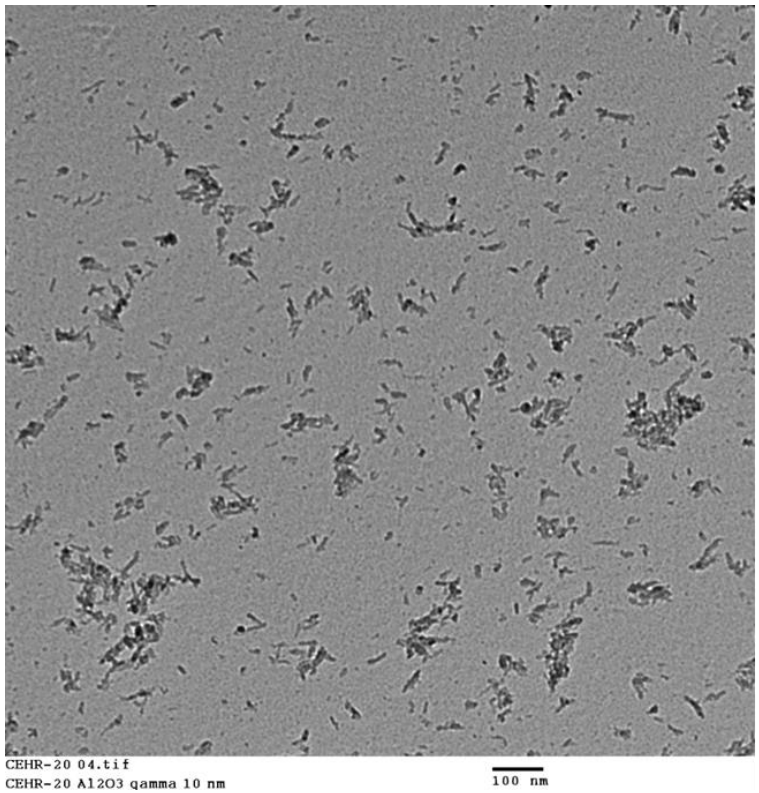

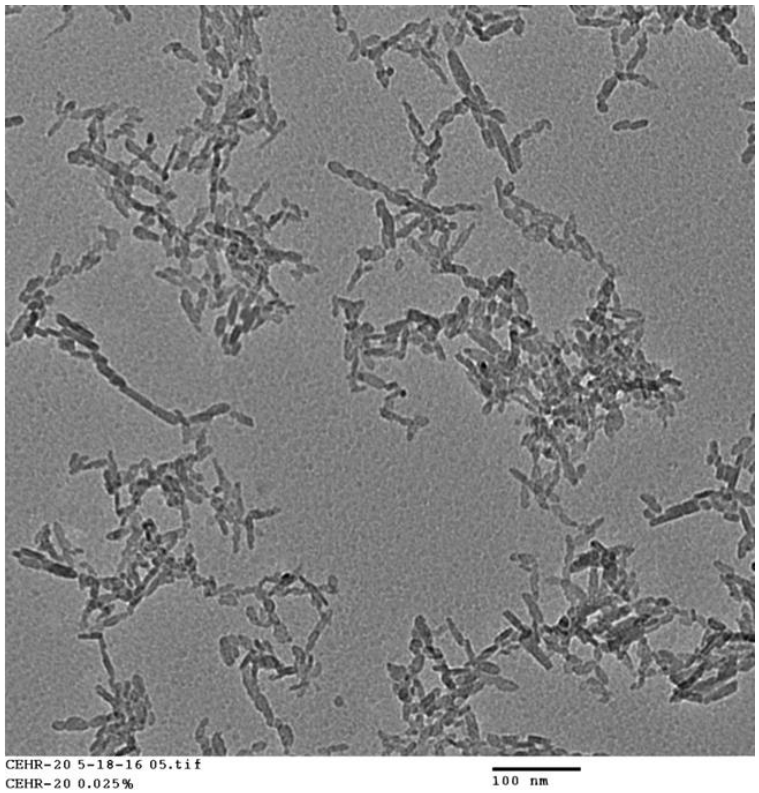

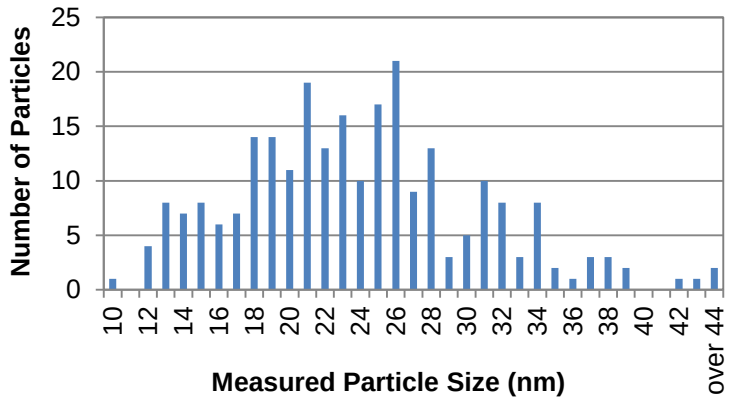

Figure VII-1. Representative TEM Images of CEHR-20. Two representative images are shown for CEHR-20, showing the range of average diameters spanning 24 ± 7 nm (n = 250). Many rod-like structures were observed for this material.

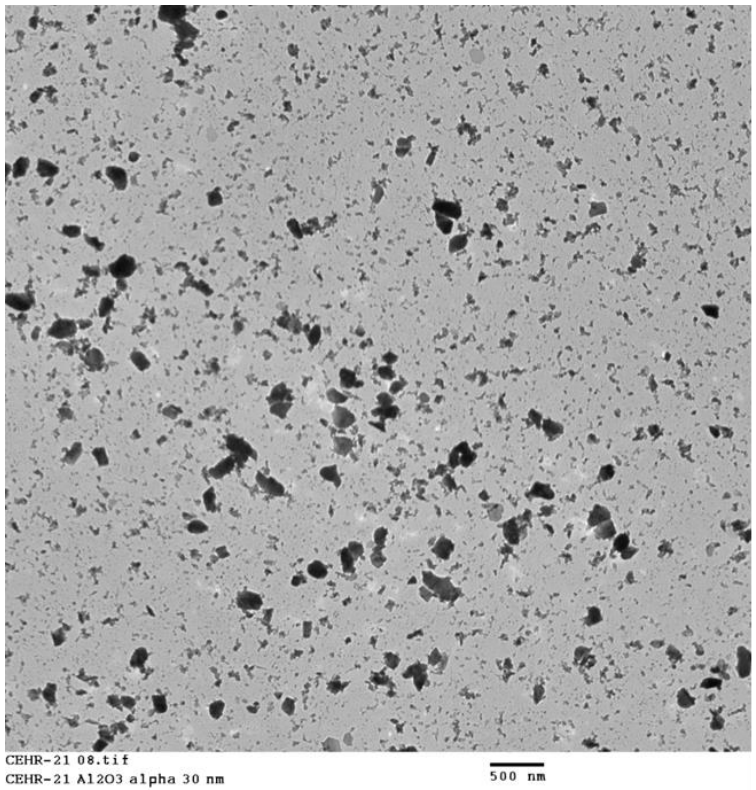

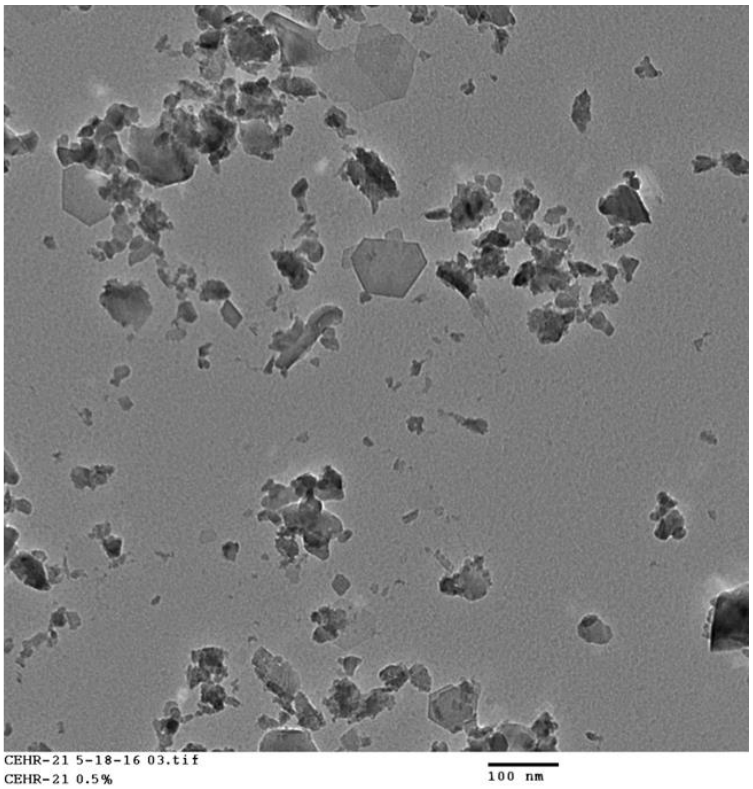

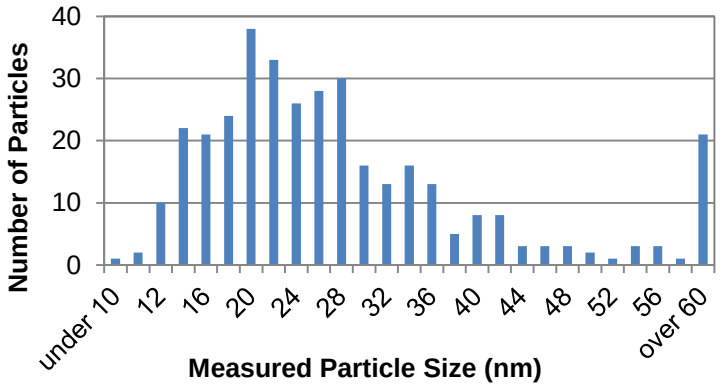

Figure VII-2. Representative TEM Images of CEHR-21. Two representative images are shown for CEHR-21, showing the range of average diameters spanning 30 ± 17 nm (n = 354). Many flake-like structures were observed for this material.

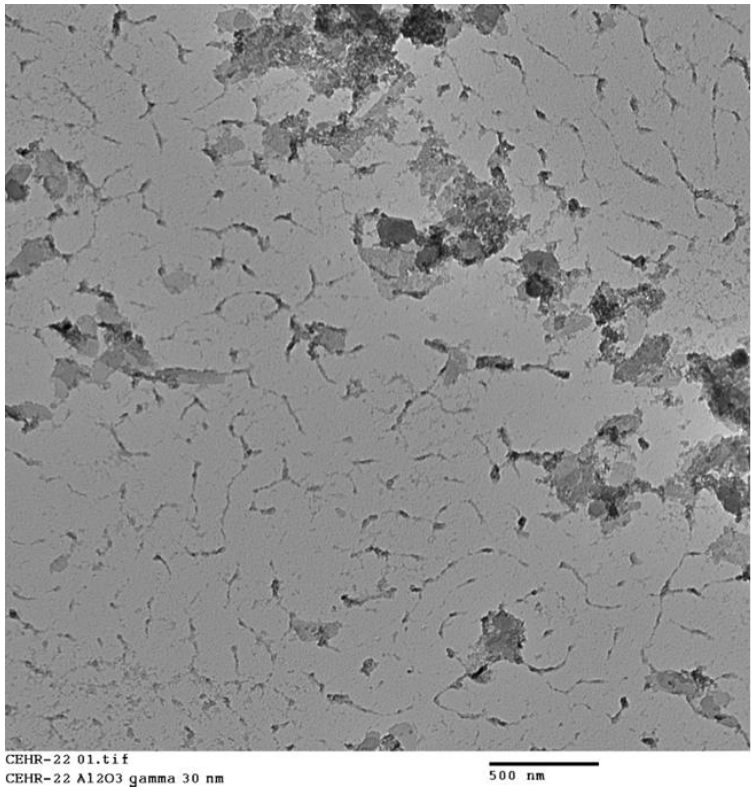

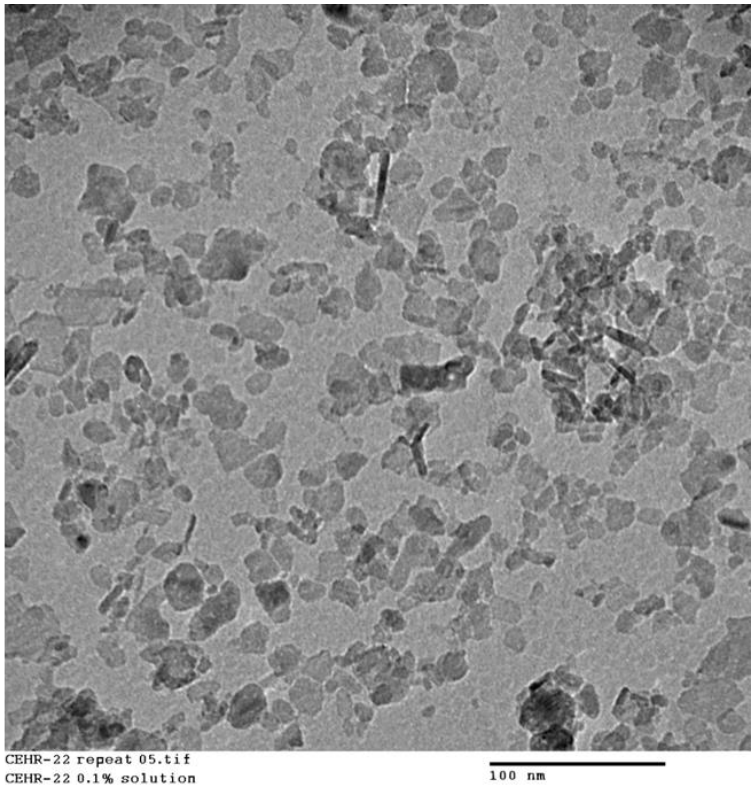

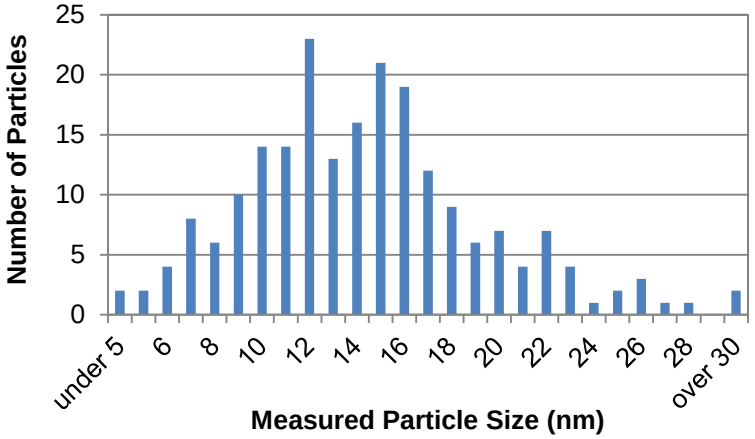

Figure VII-3. Representative TEM Images of CEHR-22. Two representative images are shown for CEHR-22, showing the range of average diameters spanning 15 ± 5 nm (n = 211). Many flake-like structures were observed for this material.

E. Hydrodynamic Size/Size Distribution via Dynamic Light Scattering

Design and Methods

A Malvern Zetasizer Nano ZS instrument (Southborough, MA) with back scattering detector (173°) was used for measuring the hydrodynamic size (diameter) in batch mode. NIST-NCL joint protocol PCC-1 was followed (https://ncl.cancer.gov/resources/assay-cascade-protocols). Stock samples of CEHR-20 through CEHR-22 were diluted 100-, 1000-, or 10,000-fold in water. At least two dilutions were measured for each sample. Measurements were made at 25°C in a quartz microcuvette. Traces in the figures represent the average of at least twelve measurements.

Hydrodynamic diameters are reported as the intensity-weighted average and as the volume-weighted average over a particular range of size populations corresponding to the most prominent peak. The Int-Peak value is used as the hydrodynamic diameter of a particular species. The Vol-Peak and %Vol values are used to approximate relative amounts of various species in the formulation. Z-Avg values are generally used to assess batch-to-batch variability of a sample.

Results and Discussion

The intensity and volume distribution plots for the aluminum oxide nanoparticles are provided in Figures VII-4 to VII-6. A summary of the sizes is provided in the corresponding tables below each figure and in Table VII-4 below. In general, these samples were much larger than reported and may have aggregated in solution.

CEHR-20 has a 10 nm reported diameter (presumed to be TEM). The DLS measured diameter was more than 10 times larger, with an Int-Peak of 122 nm and a Vol-Peak of 92 nm. While the sample was relatively monodisperse based on the measured PdI, and did not change upon dilution, it is likely to have aggregated in solution as was observed in the TEM images (Figure VII-1). A similar trend was seen with CEHR-21. The DLS hydrodynamic diameter was 194 nm, more than six times the reported diameter, but was monodisperse as indicated by the low PdI. TEM shows some degree of aggregation/agglomeration as well (Figure VII-2)

CEHR-22 also has a reported diameter of 30 nm. Like the other two aluminum oxide samples, the measured DLS size was much larger than the reported size. The intensity distribution was bimodal with a major peak at 171 nm. The averaged volume distribution was closer to the reported size; however, the peak was extremely broad, spanning approximately 1-500 nm. This suggests a wide range of size populations exist in the sample.

Table VII-4. Comparison of TEM and DLS sizes.

Reference Number	Nominal size reported by manufacturer	TEM Measured Size	DLS Measured Size (Int-Peak)
CEHR-20	10 nm	24 ± 7 nm	122 ± 2 nm
CEHR-21	30 nm	30 ± 17 nm	194 ± 2 nm
CEHR-22	30 nm	15 ± 5 nm	171 ± 2 nm

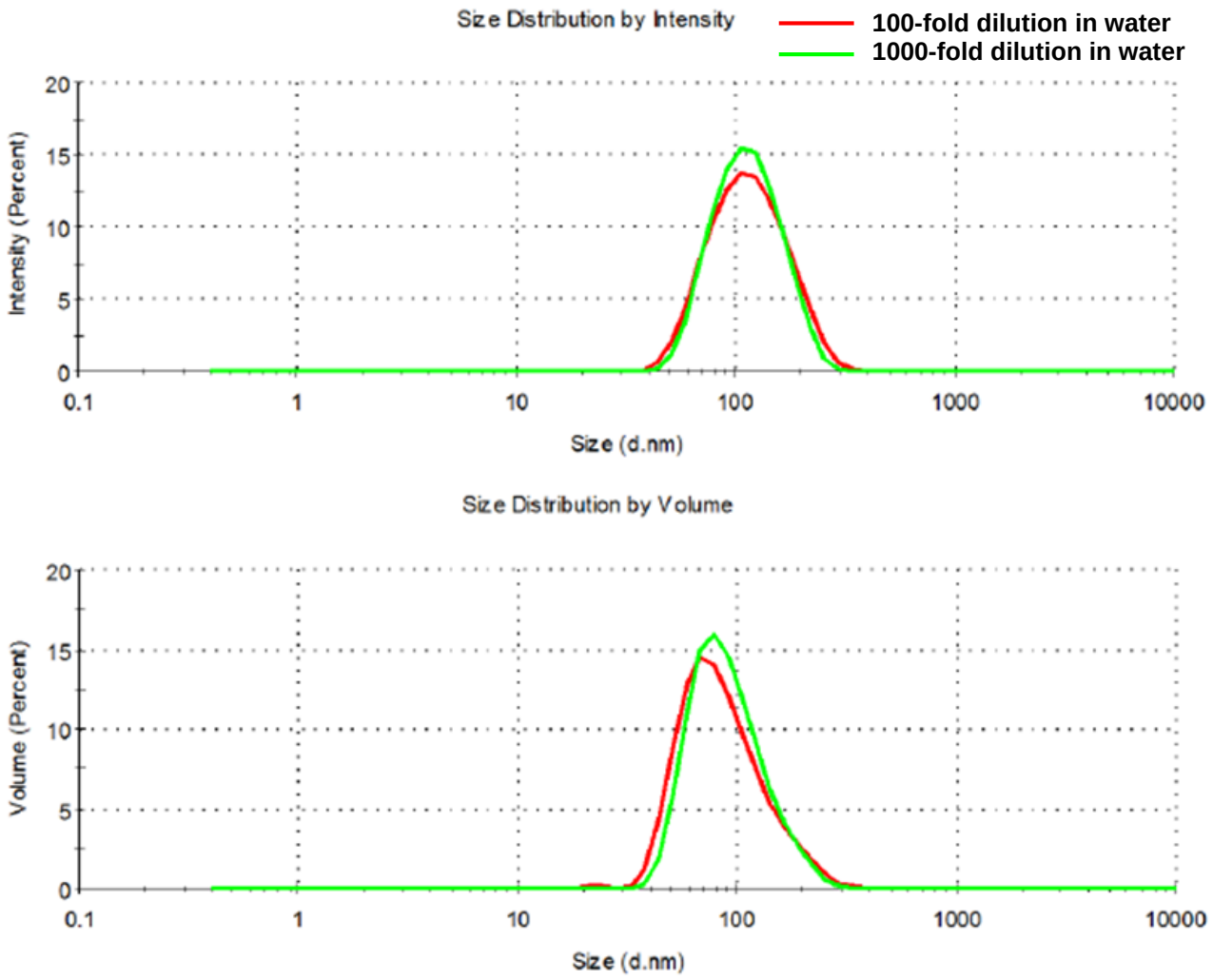

Figure VII-4. The averaged intensity and volume distribution plots for CEHR-20 diluted in water.

Table VII-5. Summary of the hydrodynamic size for CEHR-20 diluted in water

Dispersing Medium	Dilution	Z-Avg, nm	PdI	Int-Peak, nm	% Int	Vol-Peak, nm	% Vol
DI water	100-fold	104 ± 1	0.14 ± 0.01	122 ± 2	100 ± 0	92 ± 3	99 ± 1
DI water	1000-fold	105 ± 0	0.11 ± 0.02	119 ± 2	100 ± 0	95 ± 2	100 ± 0

Note: Results are the average of at least 12 measurements. Z-Avg is the intensity-weighted average. PdI is the polydispersity index. Int-Peak is the intensity-weighted average over the primary peak. % Int is the percentage of the intensity spectra occupied by the primary peak. Vol-Peak is the volume-weighted average over the primary peak. % Vol is the percentage of the volume spectra occupied by the primary peak.

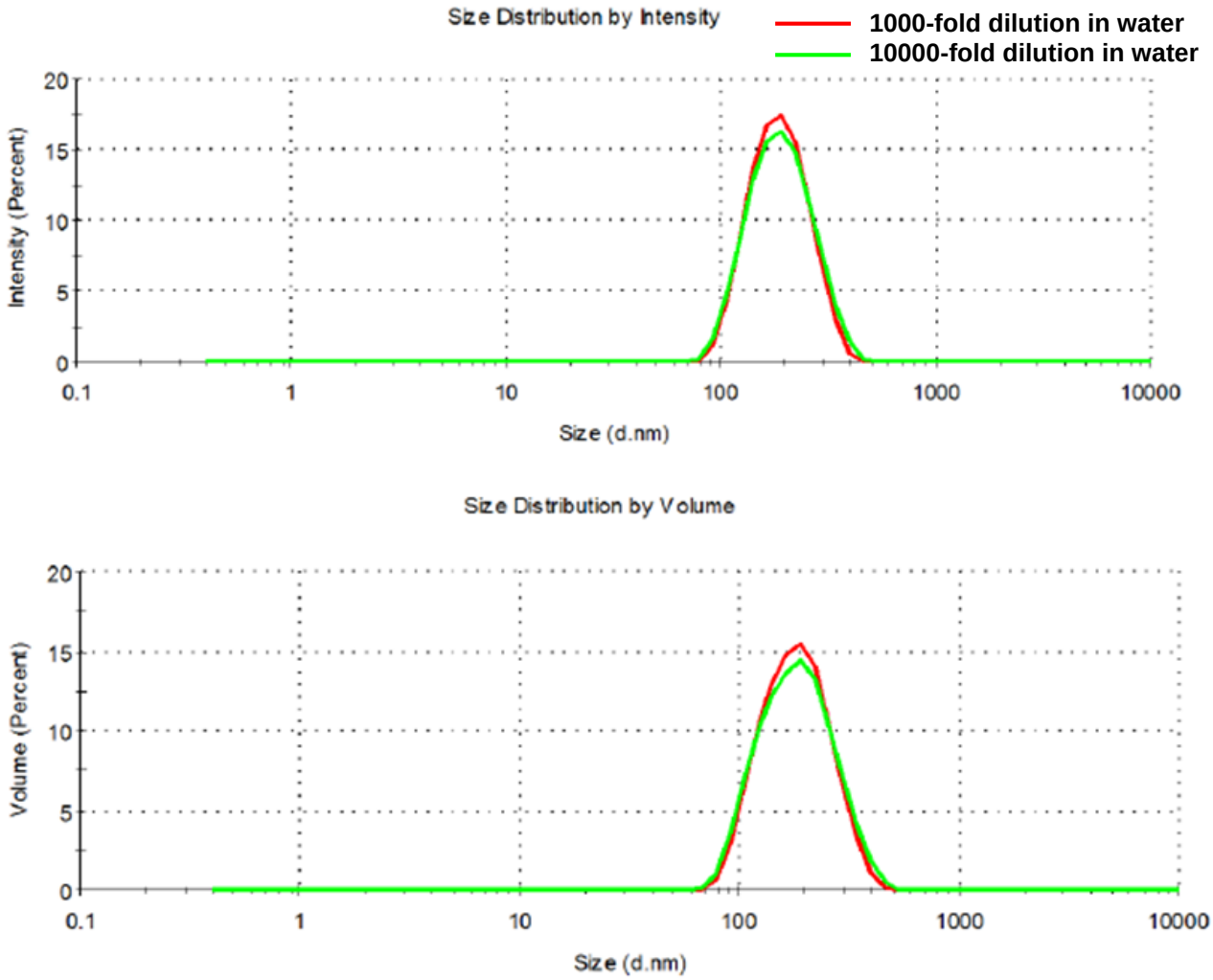

Figure VII-5. The averaged intensity and volume distribution plots for CEHR-21 diluted in water.

Table VII-6. Summary of the hydrodynamic size for CEHR-21 diluted in water

Dispersing Medium	Dilution	Z-Avg, nm	PdI	Int-Peak, nm	% Int	Vol-Peak, nm	% Vol
DI water	1000-fold	177 ± 1	0.07 ± 0.01	194 ± 2	100 ± 0	189 ± 1	100 ± 0
DI water	10,000-fold	178 ± 1	0.09 ± 0.02	198 ± 3	100 ± 0	193 ± 2	100 ± 0

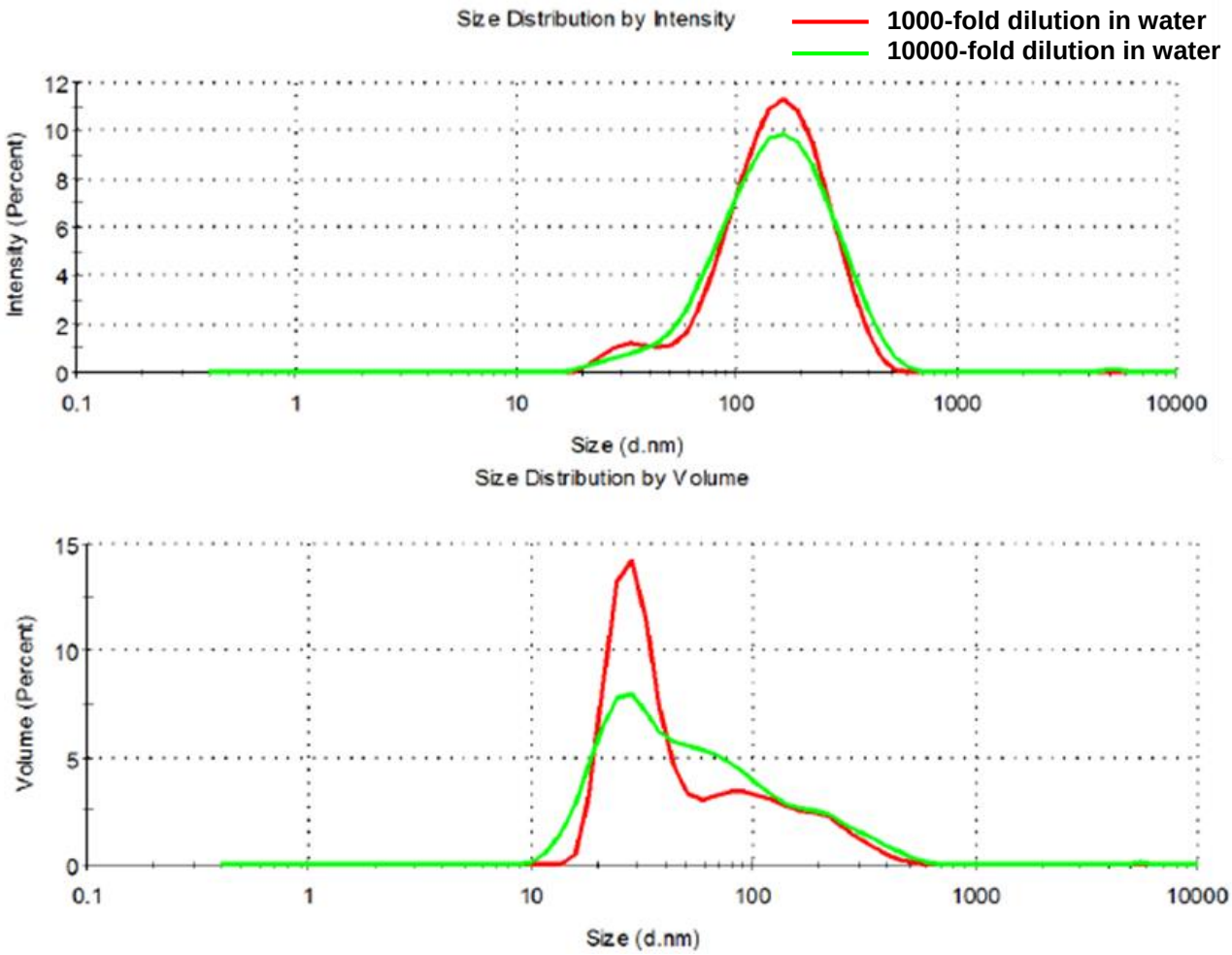

Figure VII-6. The averaged intensity and volume distribution plots for CEHR-22 diluted in water.

Table VII-7. Summary of the hydrodynamic size for CEHR-22 diluted in water

Dispersing Medium	Dilution	Z-Avg, nm	PdI	Int-Peak, nm	% Int	Vol-Peak, nm	% Vol
DI water	1000-fold	125 ± 1	0.25 ± 0.01	171 ± 2	96 ± 3	36 ± 16	70 ± 11
DI water	10,000-fold	126 ± 2	0.26 ± 0.01	176 ± 7	98 ± 3	25 ± 6	64 ± 8

F. Inductively Coupled Plasma Mass Spectrometry

Design and Methods

The aluminum concentrations of CEHR-20 through CEHR-22 were determined by inductively coupled plasma mass spectrometry (ICP-MS). An Agilent ICP-MS 7500CX equipped with a micro-mist nebulizer, standard sample introduction system, and integrated auto-sampler, operated in “no gas” mode in Agilent’s proprietary ORS (Octopole Reaction System) was used. Tuning of the instrument was performed daily prior to sample testing.

Semi-Quantitative Analysis

A semi-quantitative analysis was performed on each sample prior to quantitative determination of the aluminum concentrations. The semi-quantitative analysis was performed to help determine the proper dilution range for the samples, as well as to detect the presence of other metals in the sample. Only metals with counts two times greater than the background were denoted.

A 20 µL aliquot of the aluminum stock solution was digested using 300 µL concentrated hydrochloric acid and 150 µL concentrated nitric acid. After 10 minutes, this digested sample was vortexed for 10 seconds and then diluted with 2% nitric acid to target a 50 mL first dilution. A second dilution was performed by adding 10 mL of 2% nitric acid to 10 µL of the first dilution.

Total Metal Concentration

Using the data from the semi-quantitative analysis, the appropriate dilution was determined for the ICP-MS full quantitative analysis. The dilution target for the samples was 5 to 200 ppb. The total metal concentration was determined using the native formulation (i.e. not centrifuged or separated). Samples (10-100 µL) were initially digested with hydrochloric acid. Typically, no more than a total of 1 mL of concentrated acid was used. The acid digested samples were then further diluted to approximately 30-50 mL total volume with 2% nitric acid. A second dilution was then performed in which 10-100 µL of the first dilution was diluted to 10-50 mL using 2% nitric acid. Samples were run in duplicate.

The aluminum concentration in the samples was determined by comparing against a series of calibration standards prepared from NIST SRM 3101a. A series of concentrations ranging from 5 to 200 ng/g (ppb) were prepared. The dilutions were made using 2% nitric acid. Specifically, a dilution of 5000 ng Al / g in 2% HNO_3 was used to make a 1000 ng Al / g solution, which was then used to create standards for the calibration curve in a range of 5 to 200 ng/g in 10 mL volumes. In addition, an internal standard, scandium, was used to track the signal response of the ICP-MS. The internal standard was diluted to approximately 50 ppb and was mixed with the sample using a sample T. A simple linear regression was used for calculation of the metal concentrations.

The sequence for the ICP-MS runs consisted of five blanks, the calibration curve standards ordered from lowest to highest, five more blanks, then the aluminum oxide nanoparticle samples. Each sample was run in duplicate with three blanks in between. Within each sample set, the samples were run from highest dilution to lowest dilution. After the last aluminum oxide sample was measured, five blanks were run, followed by the calibration standards once again. Three blanks were run to flush the sample introduction system.

Free Metal Concentration and Metal Release with Time

In addition to determining the total metal concentration present in each sample, ICP-MS was also used to assess the amount of free metal ions present. The separation of free metal ions from the nanoparticles was carried out using stirred cell filtration as described in Section IV. The stirred cell separation was performed twice on each sample at different times to evaluate the release of free metal ions over time. The dates are noted for each analysis. The permeate dilutions were run first, followed by the reserved solution samples.

Results and Discussion

Semi-Quantitative Analysis

The results from the semi-quantitative analysis of CEHR-20, CEHR-21 and CEHR-22 are shown in Figure VII-7. All three samples showed aluminum. Zinc was detected in CEHR-20. CEHR-21 showed traces of zirconium, yttrium, and hafnium. No other metal impurities were found in CEHR-22. The origin of these metal impurities is not known. This was only an analysis to detect potential metal impurities. For an accurate determination of their concentrations, quantitative analysis compared to a standard would be required.

A. CEHR-20

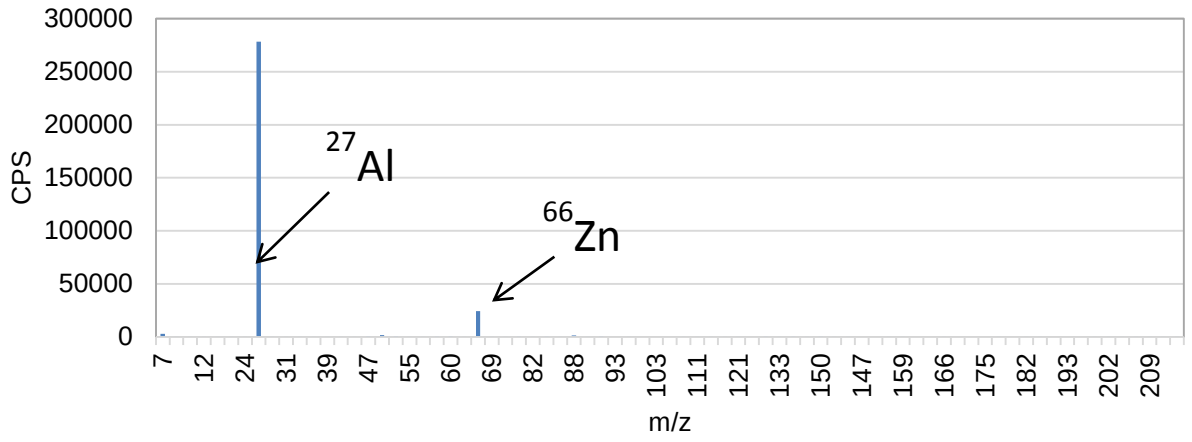

B. CEHR-21

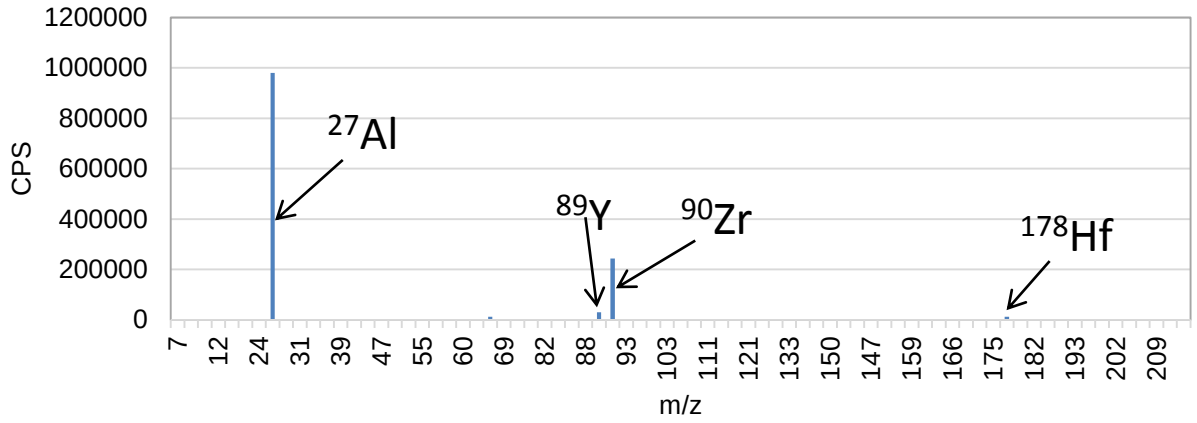

C. CEHR-22

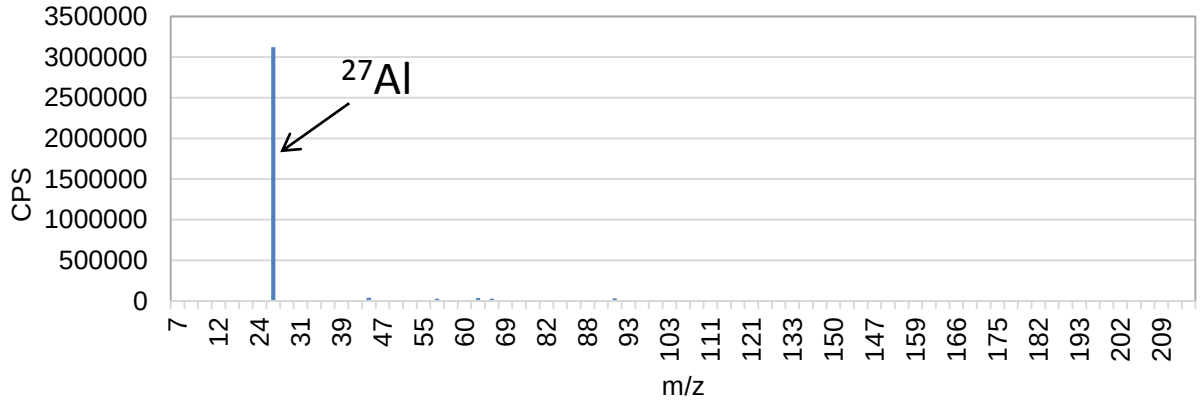

Figure VII-7. Plots of CPS vs m/z. (A) CEHR-20 semi-quantitative analysis plot. **(B)** CEHR-21 semi-quantitative analysis plot. **(C)** CEHR-22 semi-quantitative analysis plot. All three samples were analyzed on 10 November 2016. Note ^{12}C, ^{23}Na, ^{24}Mg, ^{27}Al, ^{29}Si, ^{31}P, ^{34}S, ^{35}Cl, ^{39}K, and ^{43}Ca were removed in all three plots to better visualize the smaller peaks. The internal standard peak for ^{45}Sc was also omitted.

Full Quantitative Analysis: Total Aluminum Concentration

The calibration curve used for total aluminum quantitation was constructed from NIST SRM 3101a (Figure VII-8). Quantitative total aluminum concentrations for CEHR-20, CEHR-21 and CEHR-22 are summarized in Table VII-8. The ICP-MS aluminum concentrations, in units of mg/g, were converted to aluminum oxide weight percent. To do so, the aluminum mass was converted to Al_2O_3, using an aluminum oxide molecular weight of 101.96 g/mol. To calculate the aluminum oxide weight percent, the aluminum oxide mass was divided by the mass of the solution to output the nanoparticle percent. The aluminum concentrations for CEHR-20, CEHR-21 and CEHR-22 were 10%, 15%, and 22% by weight, respectively. The theoretical concentration was 20% wt. for all three samples. Thus, the total aluminum oxide concentrations for CEHR-20 and CEHR-21 were lower, while CEHR-22 agreed with the vendor specified value.

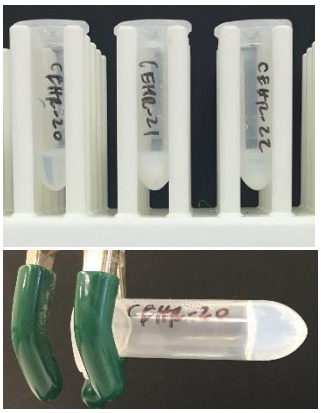

One possible reason for the variable aluminum concentrations, as noted by the large standard deviation, is settling of the sample which can lead to inconsistent sampling. Of note, CEHR-20 is almost gel-like in texture. The picture to the rights shows CEHR-20 held sideways; the gel-like sample does not flow when tipped.

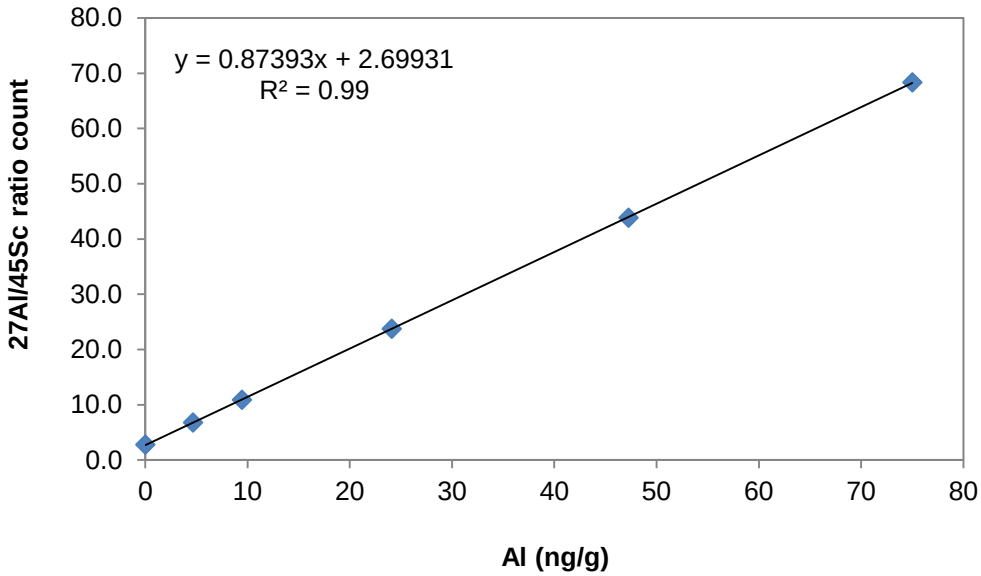

Figure VII-8. Aluminum Calibration Curve. A typical calibration curve ranging from 0 to 75 Al ng/g, used to calculate the aluminum concentration in CEHR-20, CEHR-21, and CEHR-22. The calibration curve was constructed from NIST SRM 3101a aluminum standard.

Table VII-8. Summary of the total aluminum concentration in CEHR-20, CEHR-21, and CEHR-22 as determined by ICP-MS.

Reference Number	Reported Concentration	Total [Al]	Total Al_2O_3
CEHR-20	20 wt%	53 ± 28 mg/g (n=5)	10% by weight
CEHR-21	20 wt%	79 ± 20 mg/g (n=5)	15% by weight
CEHR-22	20 wt%	119 ± 71 mg/g (n=5)	22% by weight

Free Aluminum Concentration

Stirred cell filtration was employed to separate any free aluminum ions from the aluminum oxide nanoparticles. Repeat measurements were made approximately two to three months apart to assess aluminum release kinetics/stability of the formulation. The stock sample (prior to stirred cell filtration; designated as Total [Al] in Table VII-9) was re-measured each time and used to calculate (normalize) the percent free aluminum (free [Al] / total [Al]) in each formulation.

The free aluminum concentrations in all three samples at three time points are shown in Table VII-9. While somewhat variable over the six-month window, a maximum of 0.1%, 0.3%, and 0.1% free aluminum for CEHR-20, CEHR-21, and CEHR-22, respectively, was observed. The differences in total aluminum concentrations among the measurements is attributed to the non-homogeneity within the sample.

Table VII-9. Summary of Free Aluminum Concentrations. A summary of the free aluminum detected by ICP-MS following stirred cell separation. Each sample was analyzed at three time points.

Reference Number	Date	Total [Al] (Reserve)	Free [Al] (Permeate)	% Free Al
CEHR-20	15 June 2016	76.8 ± 0.8 mg/g	0.087 ± 0.002 mg/g	0.1%
CEHR-20	30 Aug 2016	36.9 ± 2.8 mg/g	0.020 ± 0.001 mg/g	<0.1%
CEHR-20	30 Nov 2016	87 ± 7 mg/g	0.079 ± 0.003 mg/g	<0.1%
CEHR-21	15 June 2016	111 ± 4 mg/g	0.0104 ± 0.0006 mg/g	<0.1%
CEHR-21	30 Aug 2016	59 ± 8 mg/g	0.030 ± 0.009 mg/g	<0.1%
CEHR-21	30 Nov 2016	83 ± 6 mg/g	0.25 ± 0.02 mg/g	0.3%
CEHR-22	15 June 2016	64 ± 2 mg/g	0.027 ± 0.001 mg/g	<0.1%
CEHR-22	30 Aug 2016	72 ± 7 mg/g	0.008 ± 0.001 mg/g	<0.1%
CEHR-22	30 Nov 2016	153 ± 2 mg/g	0.030 ± 0.002 mg/g	<0.1%

G. Thermogravimetric Analysis

Design and Methods

Samples were analyzed via thermogravimetric analysis (TGA) to assess whether coatings were present on the nanoparticles and in what concentration. TGA was also used to determine the concentration of the metallic nanomaterial by measuring the residual material remaining after combustion of any coatings. For measurement of the metallic nanoparticle concentration, the samples were measured in their liquid (as-received) forms. For detection and measurement of coating concentrations, the samples were lyophilized prior to the TGA run. The signal from the water loss had the potential to swamp out a small amount of loss from any coating present, and thus was removed/minimized by lyophilization. Using lyophilized samples allowed for better sensitivity (total weight measured >1 mg) and hence a more accurate coating determination.

Nanoparticle Concentration

For each liquid sample, 50 µL was transferred to an aluminum oxide crucible (150 µL crucible with lid, Mettler Toledo) for TGA measurement (TGA/DSC 1, Mettler Toledo). Samples were held at 25˚C for 5 min, then ramped to 1000˚C at a heating rate of 20˚C/min under nitrogen gas. A new crucible was used for each sample. The empty crucible was subjected to the TGA method prior to loading the sample to serve as a background correction.

TGA cannot confirm the oxidation state of the material. Concentrations are reported using the manufacturer-reported oxidation state.

Coating Detection and Concentration

To determine coating content of the samples, samples were lyophilized overnight after being frozen in an ultra-low temperature freezer (-80˚C) for at least 3 hours. Typically, 150 µL of sample solution yielded 40 mg of lyophilized powder. About 15 mg was the typical amount added for TGA analysis, allowing for repeat runs, if necessary. The dried samples were added to aluminum oxide crucibles and subjected to the same temperature program as described above for the liquid samples.

Results and Discussion

Nanoparticle Concentration

The TGA curves (top panel; weight loss versus temperature) for CEHR-20, CEHR-21, and CEHR-22 are shown in Figures VII-9 to VII-11, respectively. The first derivative of this curve (bottom panel) was used to highlight the weight loss events. The major weight loss event in each sample corresponded to the loss of water, between 50-190˚C. The total mass aluminum oxide was determined by using the amount of mass left at the end of the TGA run. A comparison of the vendor-reported concentrations to the TGA-measured concentrations is provided in Table VII-10. The TGA-measured values for CEHR-20, CEHR-21, and CEHR-22 were 16, 19, and 19% wt., respectively.

For CEHR-21 and CEHR-22, the TGA measured concentrations matched the vendor-specified concentration of 20% wt. For CEHR-20, the TGA measured concentration was approximately 20% lower than the vendor-specified value. The TGA results were in closer agreement to the vendor-specified values as compared to the ICP-MS results. Typically, ICP-MS is a more accurate and sensitive technique. However, the variability in these values lies in the fact that all three samples are very heterogeneous, especially CEHR-20 which was gelatinous.

Note, this analysis assumes that, at the end of the run, all that remained was the aluminum oxide nanoparticles; the water would have evaporated and any organic coating present would have combusted. In some instances, combustion of a coating may leave residual mass, which would increase the nanoparticle concentration. It is not possible to determine this without subjecting the coating alone (not in nanosolution) to the TGA method.

Table VII-10. Comparison of TGA Measured Concentration to ICP-MS Measured and Reported Nanoparticle Concentrations.

Reference Number	Reported Concentration	Measured Concentration via ICP-MS	Measured Concentration via TGA of Liquid Sample
CEHR-20	20% wt.	10% wt.	16% wt.
CEHR-21	20% wt.	15% wt.	19% wt.
CEHR-22	20% wt.	22% wt.	19% wt.

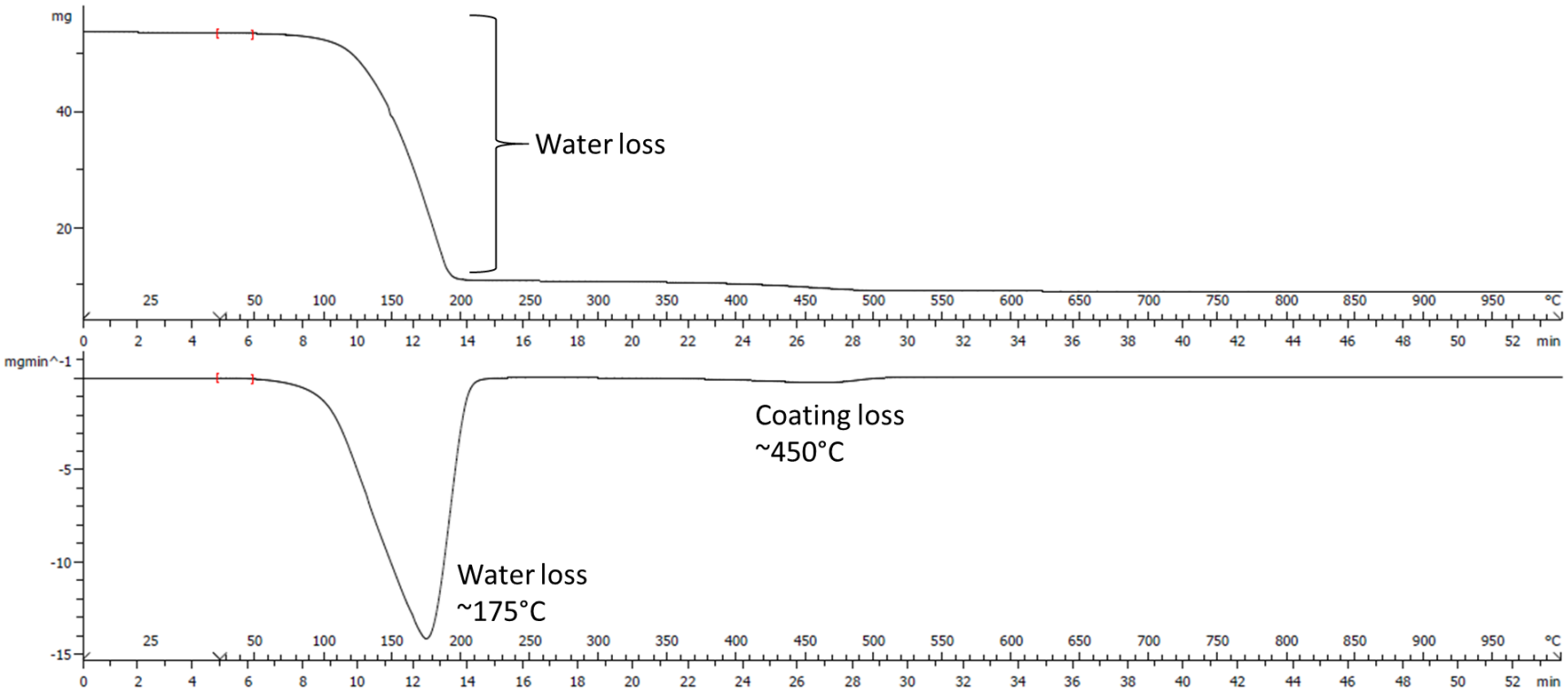

Reference Number	Volume (µL)	Starting Mass (mg)	Total Mass Loss (mg)	Residue mass (mg)
CEHR-20	50	53.600	42.940	2.032

Figure VII-9. TGA thermogram of CEHR-20. The top panel is the weight loss versus temperature (and time) curve. The bottom panel is the first derivative of that curve.

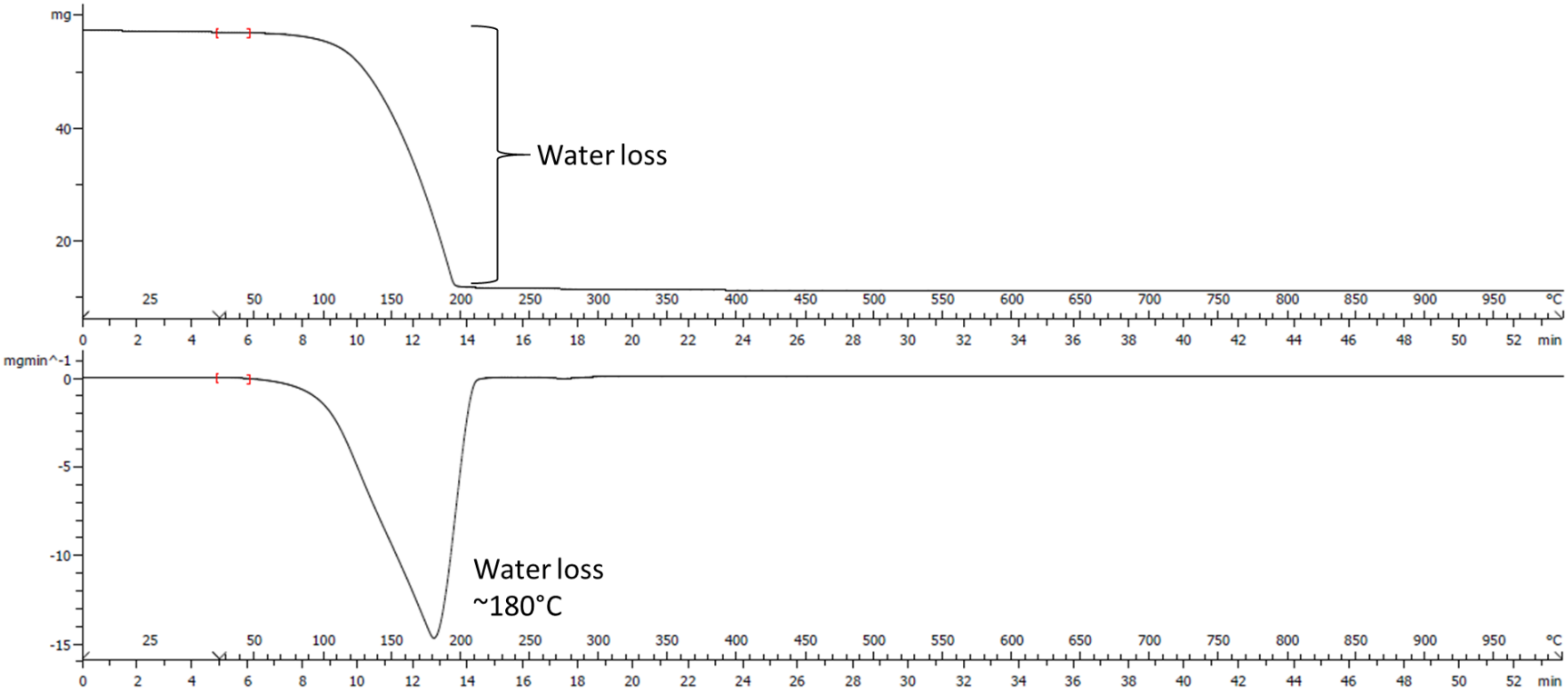

Reference Number	Volume (µL)	Starting Mass (mg)	Total Mass Loss (mg)	Residue mass (mg)
CEHR-21	50	57.280	45.677	0.573

Figure VII-10. TGA thermogram of CEHR-21. The top panel is the weight loss versus temperature (and time) curve. The bottom panel is the first derivative of that curve.

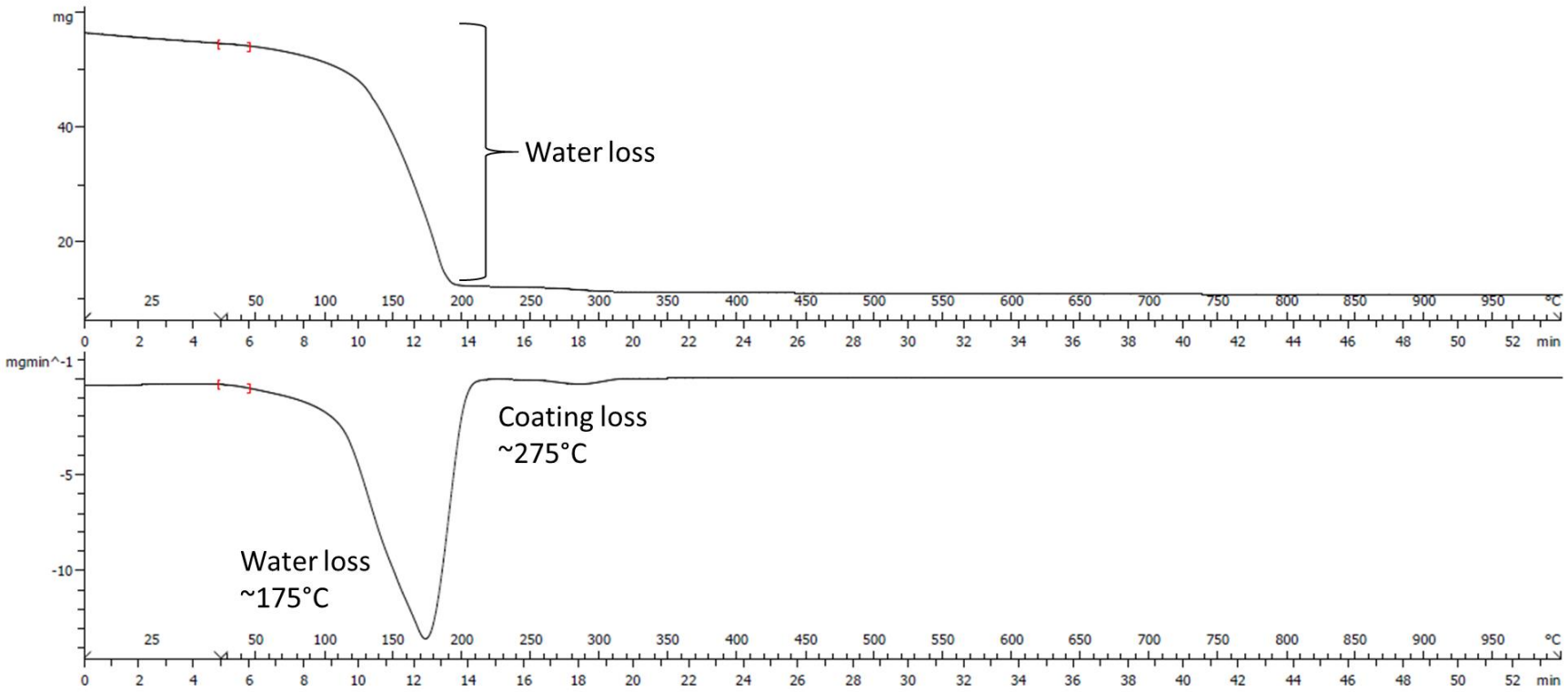

Reference Number	Volume (µL)	Starting Mass (mg)	Total Mass Loss (mg)	Residue mass (mg)
CEHR-22	50	56.222	44.246	1.371

Figure VII-11. TGA thermogram of CEHR-22. The top panel is the weight loss versus temperature (and time) curve. The bottom panel is the first derivative of that curve.

Coating Detection and Concentration

The manufacturers of the aluminum oxide nanoparticles, US Nano, did not disclose whether a coating was present on the nanoparticles. It was assumed that if any coating were present, it would be very low in concentration. Since the water peak dominated the TGA curves, all samples were lyophilized to remove the water and improve sensitivity for coating detection. Typical TGA curves for the lyophilized samples are shown in Figures VII-12 to VII-14, respectively. In CEHR-20 and CEHR-22, the first weight loss event corresponded to the loss of residual water and occurred by 180˚C. For CEHR-21, a second weight loss event overlapped with the water loss. Further weight loss events were observed for all three samples. It was assumed that these weight losses were due to coating and/or added excipients (possibly added to help with solubilization and stability). From the second derivative curves, a decomposition temperature of 470°C was noted for CEHR-20, while a decomposition of 280°C was observed for CEHR-21 and CEHR-22.

For each run, the weight loss of coating was calculated by using the first derivative analysis to mark the beginning and end of each weight loss event. The beginning and end was chosen where the derivative was constant (essentially zero). The final weight, as measured after the TGA run, was taken to be the aluminum oxide amount. This translated to a starting and ending temperature range of 200 and 1000°C, respectively. This assumes that the weight of any residual decomposed coating is negligible relative to the weight of aluminum oxide. The mass ratio of coating to aluminum oxide was then calculated for each independent run and is summarized in Table VII-11. The calculated percent coatings were 23%, 5%, and 14% for CEHR-20, CEHR-21, and CEHR-22, respectively. Note, the identity of the coating could not be determined by TGA, and was not reported by the vendor. The different decomposition temperature for CEHR-20 as compared to CEHR-21 and CEHR-22 suggests a different coating and/or excipients were used in this solution.

Table VII-11. Summary of Percent Coating Mass per Mass Nanoparticle detected in each of the aluminum oxide nanoparticles.

Reference Number	Reported Coating	%Mass Coating per Mass Nanoparticle
CEHR-20	None reported	23%
CEHR-21	None reported	5%
CEHR-22	None reported	14%

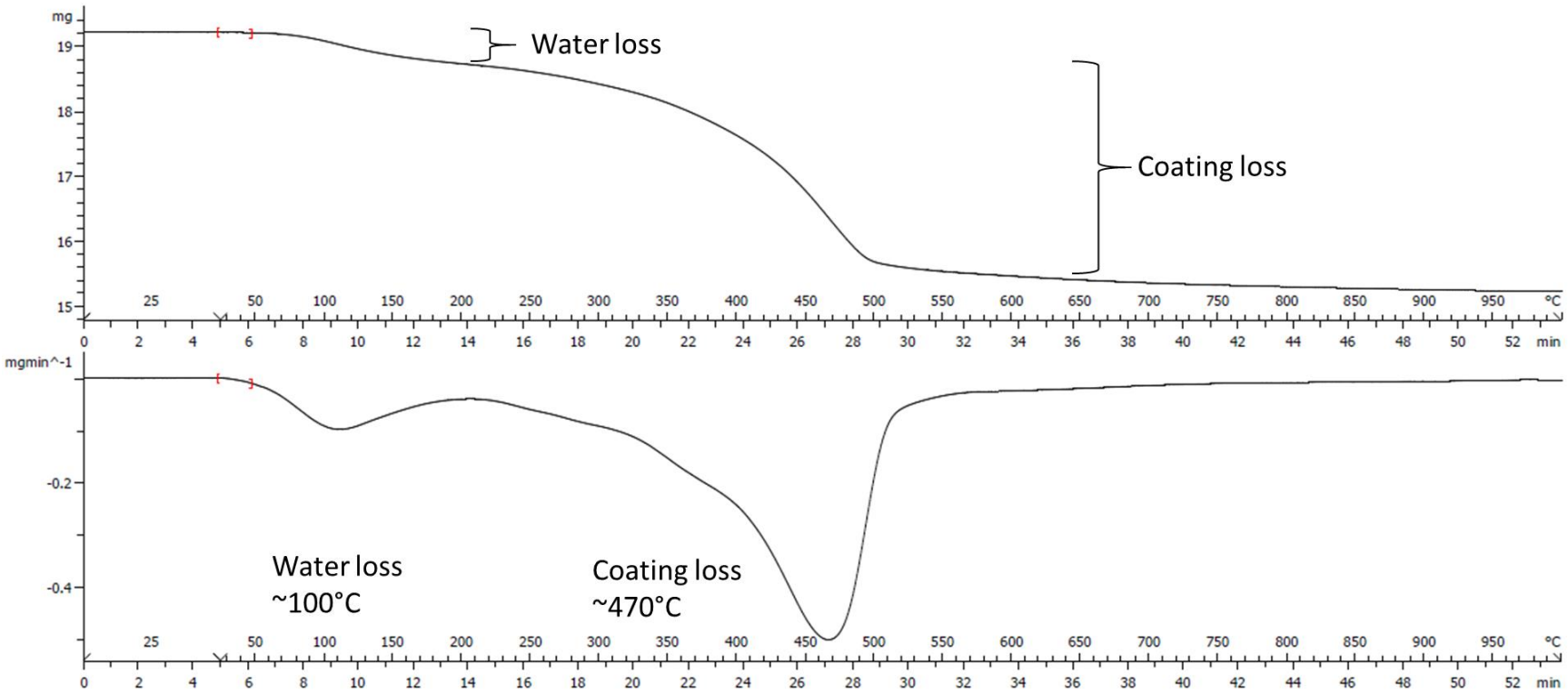

Reference Number	Starting Mass (mg)	Water Loss (mg)	Coating Loss (mg)	Residue (mg)	%Mass Coating per Mass Aluminum Oxide Nanoparticles
CEHR-20	19.200	0.497	3.502	15.201	23%

Figure VII-12. TGA thermogram of CEHR-20 (lyophilized). The top panel is the weight loss versus temperature (and time) curve. The bottom panel is the first derivative of that curve.

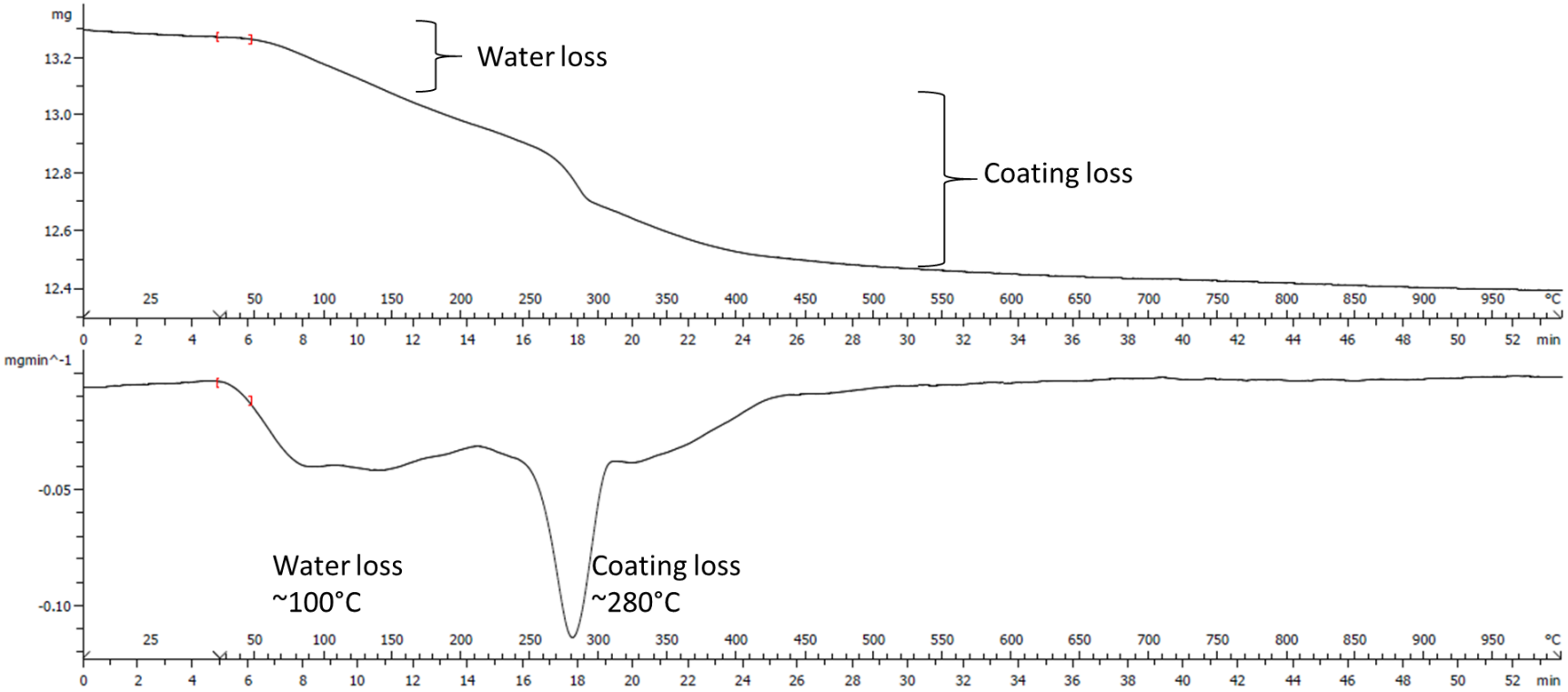

Reference Number	Starting Mass (mg)	Water Loss (mg)	Coating Loss (mg)	Residue (mg)	%Mass Coating per Mass Aluminum Oxide Nanoparticles
CEHR-21	13.290	0.313	0.589	12.388	5%

Figure VII-13. TGA thermogram of CEHR-21 (lyophilized). The top panel is the weight loss versus temperature (and time) curve. The bottom panel is the first derivative of that curve.

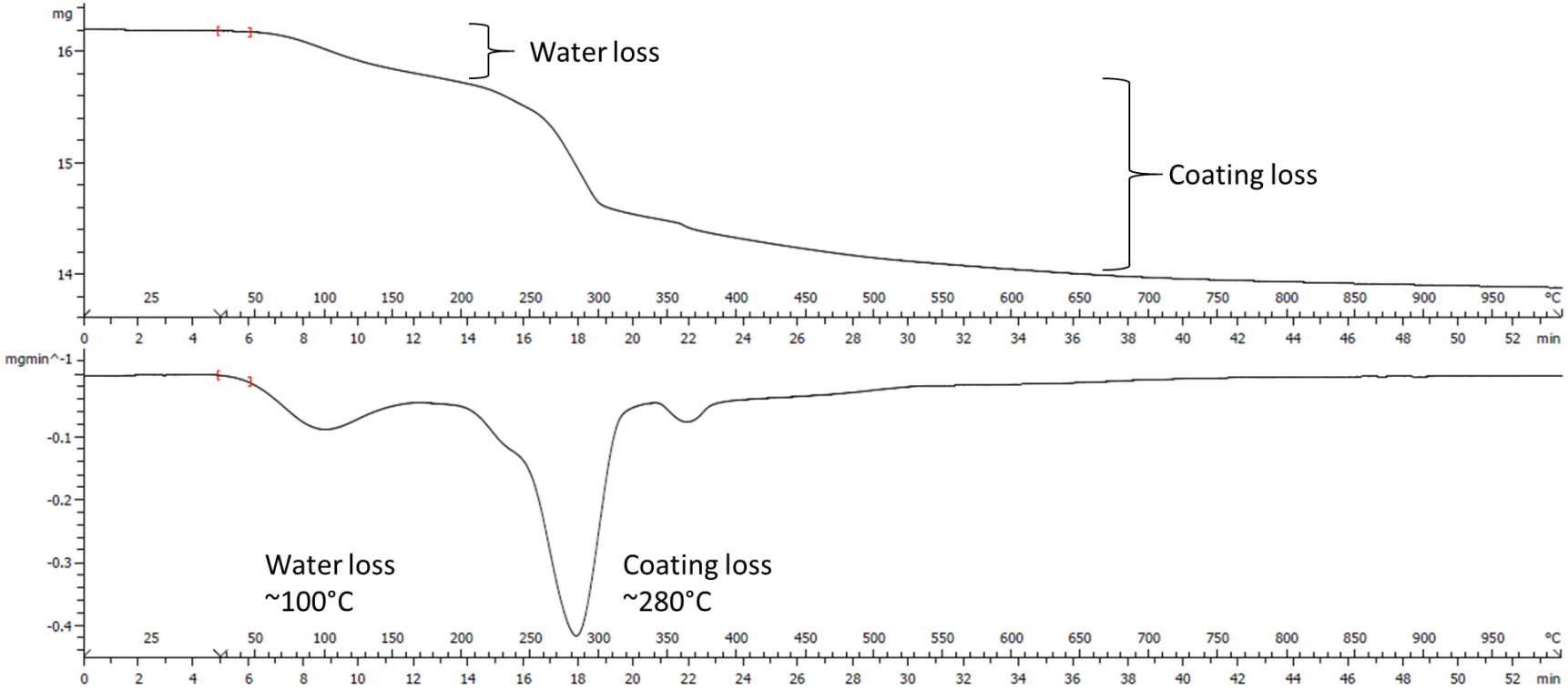

Reference Number	Starting Mass (mg)	Water Loss (mg)	Coating Loss (mg)	Residue (mg)	%Mass Coating per Mass Aluminum Oxide Nanoparticles
CEHR-22	16.197	0.433	1.894	13.870	14%

Figure VII-14. TGA thermogram of CEHR-22 (lyophilized). The top panel is the weight loss versus temperature (and time) curve. The bottom panel is the first derivative of that curve.

H. Zeta Potential

Design and Methods

A Malvern Zetasizer Nano ZS instrument was used to measure zeta potential at 25°C for all samples. NCL protocol PCC-2 was followed (https://ncl.cancer.gov/resources/assay-cascade-protocols). Samples were diluted 100- or 1000-fold in deionized water. Sample pH was measured before loading into a pre-rinsed folded capillary cell. An applied voltage of 150 V was used. Traces in the figures represent the average of four measurements.

The instrument was validated by running an appropriate standard (Zeta Potential Transfer Standard, DTS0050, zeta potential value of -42 ± 4 mV at 25°C, Malvern Instruments) before all zeta potential measurements.

Results and Discussion

CEHR-20 through CEHR-22, the three aluminum oxide nanomaterials, all had positive zeta potential values (Table VII-12). This is in contrast to the expected range for these materials and could indicate the presence of an undisclosed positively-charged coating on the nanoparticles. TGA analysis of these materials confirmed the presence of another species in the formulation (see Figures VII-12 to VII-14). Tests conducted at NCL could not identify the coating.

Table VII-12. Summary of the zeta potentials for CEHR-20 to CEHR-21.

Sample	pH	Zeta Potential
CEHR-20	4.2	45 ± 1 mV
CEHR-21	5.3	25 ± 2 mV
CEHR-22	5.4	48 ± 1 mV

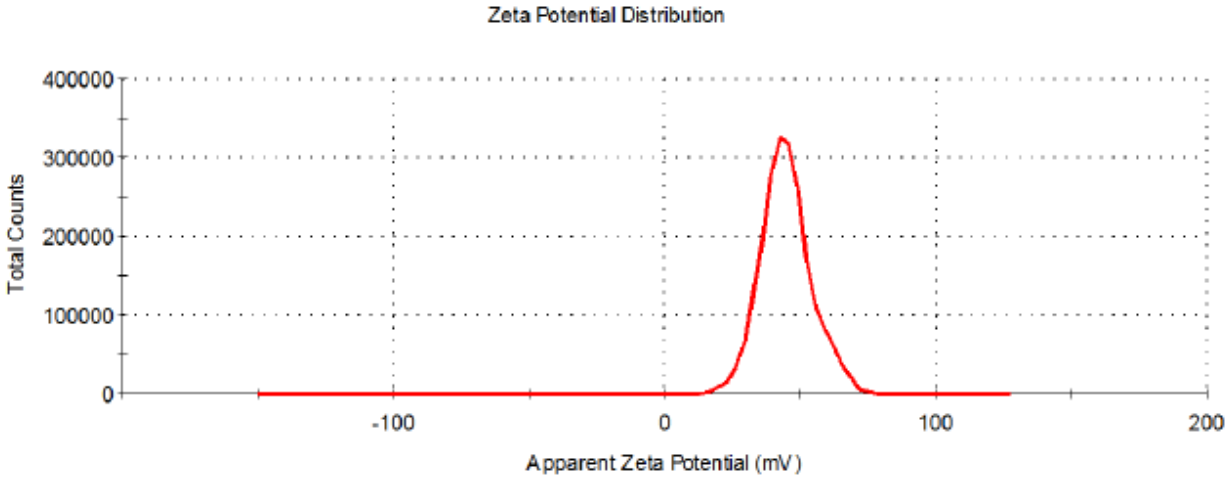

Sample	pH	Zeta Potential
CEHR-20	4.2	45 ± 1 mV

Figure VII-15. The averaged zeta potential distributions for CEHR-20 diluted 100-fold in deionized water.

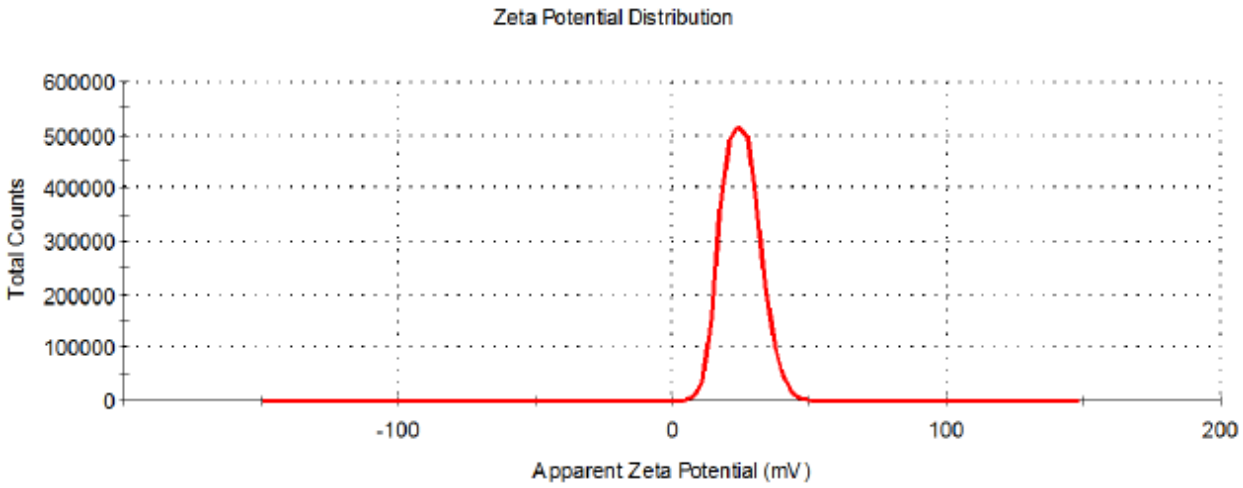

Sample	pH	Zeta Potential
CEHR-21	5.3	25 ± 2 mV

Figure VII-16. The averaged zeta potential distributions for CEHR-21 diluted 100-fold in deionized water.

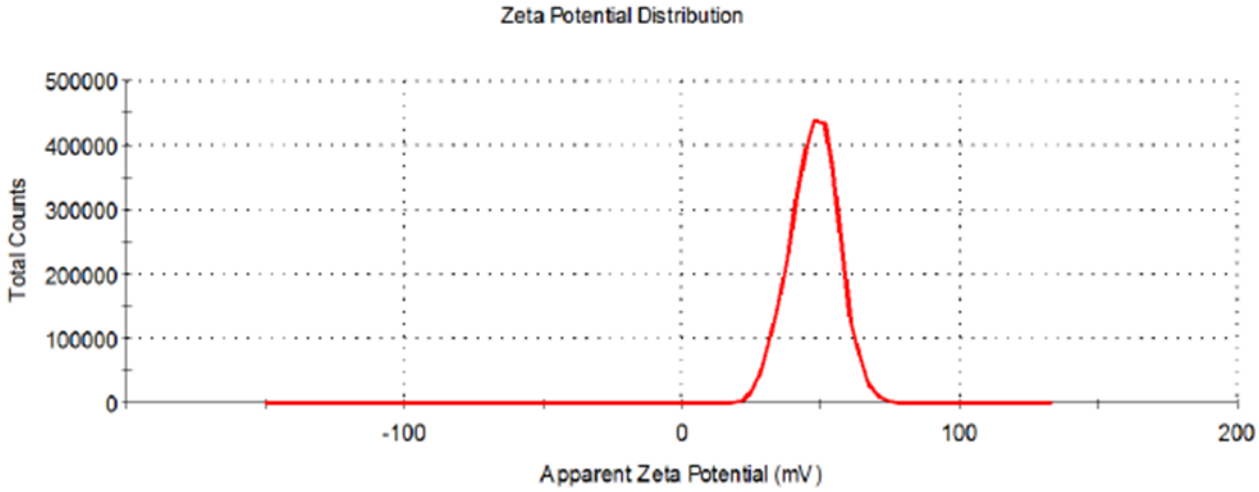

Sample	pH	Zeta Potential
CEHR-22	5.4	48 ± 1 mV

Figure VII-17. The averaged zeta potential distributions for CEHR-22 diluted 1000-fold in deionized water.

VIII. Titanium Oxide

VIII. Titanium Oxide

A. Section Summary

Four titanium oxide nanoparticles with nominal size ranges of 5-15 nm for CEHR-23 and CEHR-24 and 30-50 nm CEHR-25 and CEHR-26 were characterized for sterility and relevant physicochemical parameters. CEHR-23 and CEHR-25 are anatase TiO_2 while CEHR-24 and CEHR-26 are rutile TiO_2. Characterization included size (DLS and TEM) and polydispersity (AF4-DLS) measurements, zeta potential, total and free titanium concentrations by inductively-coupled plasma mass spectrometry (ICP-MS), and detection and quantification of possible surface coatings on the nanoparticles (TGA).

Sterility screening of the titanium oxide nanoparticles showed that CEHR-23, CEHR-25, and CEHR-26 were free of bacterial contamination. CEHR-24, however, was contaminated with bacteria; therefore, this sample is not recommended for biological testing (Table VIII-1). Endotoxin analysis revealed that CEHR-23, CEHR-25, and CEHR-26 had endotoxin values <5, <0.5, and <0.05 EU/mg, respectively (Table VIII-2). CEHR-24 had an average endotoxin value of 28.2 EU/mg. The bacterial contamination in CEHR-24 may have contributed to the endotoxin levels in this sample.

Size analysis of the four titanium oxide nanomaterials was conducted by dynamic light scattering (DLS) and transmission electron microscopy (TEM). The TEM measured diameters for CEHR-25 and CEHR-26 were 41 and 55 nm, respectively (Table VIII-3). Both of these were close to the reported sizes. However, CEHR-24 was much larger, by nearly 5 times, than the reported size. Accurate sizing for CEHR-23 was not possible by TEM. There were not enough clearly discernable individual particles. The DLS measured diameters for all particles were considerably larger than the TEM sizes, suggesting the samples have aggregated/agglomerated in solution in agreement with the TEM images. The DLS diameters (Int-Peak) were 47, 683, 219, and 780 nm for CEHR-23, CEHR-24, CEHR-25, and CEHR-26, respectively (Figures VIII-5 to VIII-8).

Asymmetric-flow field flow fractionation (AF4) was used to examine the size polydispersity of CEHR-25. A very broad size distribution was observed (Figure VIII-9). The dominant size population within this very broad peak was approximately 43-200 nm. A second, minor population was also present with sizes increasing up to 320 nm. This is in agreement with the batch-mode DLS which showed an average diameter >200 nm and a polydispersed sample population. AF4 analysis of CEHR-23 and CEHR-26 could not be measured reliably due to strong interaction with the membrane. CEHR-24 was not analyzed by AF4 due to the bacterial contamination in the sample.

Titanium concentrations, both total and free titanium, were measured by inductively coupled plasma-mass spectrometry (ICP-MS). These concentrations were converted to a weight percent of titanium oxide for comparison to the manufacturer-reported sample concentrations. The total titanium oxide nanoparticle concentrations for CEHR-23, CEHR-24, CEHR-25, and CEHR-26 were 11%, 12%, 39%, and 7% by weight (Table VIII-11), respectively. These measured values were similar, although slightly lower, to the theoretical concentration for CEHR-23, CEHR-24 and CEHR-25. The concentration for CEHR-26 was substantially lower, and was less than half the reported concentration. The total nanoparticle concentration was also determined using thermogravimetric analysis (TGA). The TGA-measured concentrations for CEHR-23, CEHR-24, CEHR-25, and CEHR-26 were 13%, 15%, 36%, and 9% by weight, respectively (Table VIII-13). In agreement with the ICP-MS results, CEHR-23, CEHR-24, and CEHR-25 were reasonably

similar to the reported concentrations, while CEHR-26 was only about half the reported concentration. The free titanium content for each formulation was also measured by ICP-MS. A maximum of only 0.1% free titanium was detected by November 2016 (Table VIII-12).

ICP-MS and TGA were also used to assess the purity of the formulations. ICP-MS was used to determine if any metal impurities were present in the samples. CEHR-23 and CEHR-24 contained zinc and hafnium (Figure VIII-10). CEHR-26 contained zinc, zirconium, and tin. CEHR-25 contained the most metal impurities with zinc, iron, strontium, manganese, vanadium, lead, uranium, and cerium all detected. TGA revealed additional components thought to be a coating on the nanomaterial. The percent mass ratios of coating to titanium oxide were 9%, 10%, 10%, and 1% for CEHR-23, CEHR-24, CEHR-25, and CEHR-26, respectively (Table VIII-14). TGA could not confirm the identity of this material. The zeta potentials of the nanoparticles were negative for CEHR-24, positive for CEHR-23, borderline neutral for CEHR-25, and neutral for CEHR-26 (Table VIII-15). The negative values are consistent for uncoated titanium oxide nanoparticles or those coated with a negatively-charged surface moiety. The different zeta potential ranges and different decomposition patterns in TGA suggest the coatings/excipients may be different among the four samples.

B. Sterility

Design and Methods

Sterility, i.e. bacterial contamination, of the four titanium oxide nanoparticles was assessed using NCL protocol STE-2.2 (https://ncl.cancer.gov/resources/assay-cascade-protocols). In brief, samples were plated onto LB agar plates at several dilutions (10-, 100-, and 1000-fold) and allowed to incubate at 37°C for 72 hours. The plates were then visually inspected for colony formation.

Results & Conclusions

CEHR-23, CEHR-25, and CEHR-26 did not show visible colony formation after 72 hr. CEHR-24 was contaminated with bacteria, and showed 310 CFU/mg. Therefore, it is recommended CEHR-24 not be used in any biological assays. A summary of these findings is provided in the table below.

Table VIII-1. Summary of the sterility testing results for the titanium oxide nanoparticles.

Reference Number	Nanoparticle Description	Nominal size reported by manufacturer	Sterility (agar plate)
CEHR-23	TiO_2 anatase, 15 wt% dispersion	5 -15 nm	Negative
CEHR-24	TiO_2 rutile, 15 wt% dispersion	5 -15 nm	**310 CFU/mg**
CEHR-25	TiO_2 anatase, 40 wt% dispersion	30 -50 nm	Negative
CEHR-26	TiO_2 rutile, 20 wt% dispersion	30 -50 nm	Negative

C. Endotoxin

Design and Methods

The objective of this experiment was to evaluate potential endotoxin contamination in the four titanium oxide formulations. NCL's protocols for the kinetic turbidity Limulus Amebocyte Lysate (LAL) assay was used (STE-1.2; https://ncl.cancer.gov/resources/assay-cascade-protocols). All samples were initially diluted to 1 mg/mL theoretical concentration and tested at 1:5, 1:50, and 1:500 dilutions in water. CEHR-23 interfered with the assay at all initial dilutions and was re-tested at a 1:5000 dilution.

Results and Discussion

Three of the four samples, CEHR-23, CEHR-25, and CEHR-26, had undetectable levels of endotoxin, i.e., below the assay's lower limit of detection (0.001 EU/mL). Results are reported from the lowest dilution which did not interfere with the LAL assay. The reported values are corrected by the corresponding dilution factor for each sample. CEHR-23 interfered with the LAL assay at the lower dilutions. Therefore, the results from the 1:5000 dilution were reported. Similarly, CEHR-25 and CEHR-26 values were obtained from the lowest non-interfering dilutions of 500- and 50-fold, respectively. This is the reason for the different sensitivities reported among CEHR-23, CEHR-25, and CEHR-26.

CEHR-24 had 28.2 EU/mg endotoxin. This contamination may have originated from the bacterial contamination detected in this sample. However, bacterial serotyping was not performed to verify this. Regardless of the serotype, the presence of live bacteria in this sample should preclude its use in biological assays.

Table VIII-2. Endotoxin levels detected by the LAL assay. Results are shown as endotoxin units (EU) per mg of nanoparticle.

Reference Number	Nanoparticle Description	Nominal size reported by manufacturer	Endotoxin, Turbidity LAL
CEHR-23	TiO_2 anatase, 15 wt% dispersion	5 -15 nm	<5 EU/mg
CEHR-24	TiO_2 rutile, 15 wt% dispersion	5 -15 nm	**28 EU/mg**
CEHR-25	TiO_2 anatase, 40 wt% dispersion	30 -50 nm	<0.5 EU/mg
CEHR-26	TiO_2 rutile, 20 wt% dispersion	30 -50 nm	<0.05 EU/mg

D. Transmission Electron Microscopy

Design and Methods

Transmission electron microscopy (TEM) was conducted to assess the size and morphology of the nanomaterials. Stock solutions of each sample were diluted to 1% with ultrapure water, and 2 µL was applied to a glow discharged carbon film grid (Electron Microscopy Sciences). The grid was washed three times with ultrapure water, blotted, and allowed to air dry before imaging. Images were taken using a T-12 TEM (FEI) equipped with a LαB6 thermoionic gun at 80 V acceleration voltage.

Particle size analysis was performed using ImageJ (https://imagej.nih.gov/ij/). Only particles that were individually dispersed were included in the sizing analysis.

Results and Discussion

Figures VIII-1 to VIII-4 contain representative images of the four titanium dioxide particles, CEHR-23 through CEHR-26, respectively. There were not enough clearly discernable individual particles for sizing analysis of CEHR-23. The measured size of CEHR-24 disagreed greatly with the reported size (presumed to be a TEM diameter); the average measured diameter (63 nm) was approximately 5 times greater than the reported size. CEHR-25 had an average measured diameter of 41 nm and fell within the reported size range. These particles had a somewhat different appearance than the other titanium dioxide particles. The surface of the CEHR-25 particles appeared to have more ridges; whereas the surface of the other particles appeared more smooth. The measured size of CEHR-26 was 55 nm, in agreement with the high end of the reported size range.

Table VIII-3. Comparison of vendor reported size and TEM-measured size.

Reference Number	Nanoparticle Description	Nominal size reported by manufacturer	TEM Measured Size nm
CEHR-23	TiO_2 anatase, 15 wt% dispersion	5 -15 nm	N/A
CEHR-24	TiO_2 rutile, 15 wt% dispersion	5 -15 nm	63 ± 19 nm
CEHR-25	TiO_2 anatase, 40 wt% dispersion	30 -50 nm	41 ± 14 nm
CEHR-26	TiO_2 rutile, 20 wt% dispersion	30 -50 nm	55 ± 15 nm

N/A = Not Available

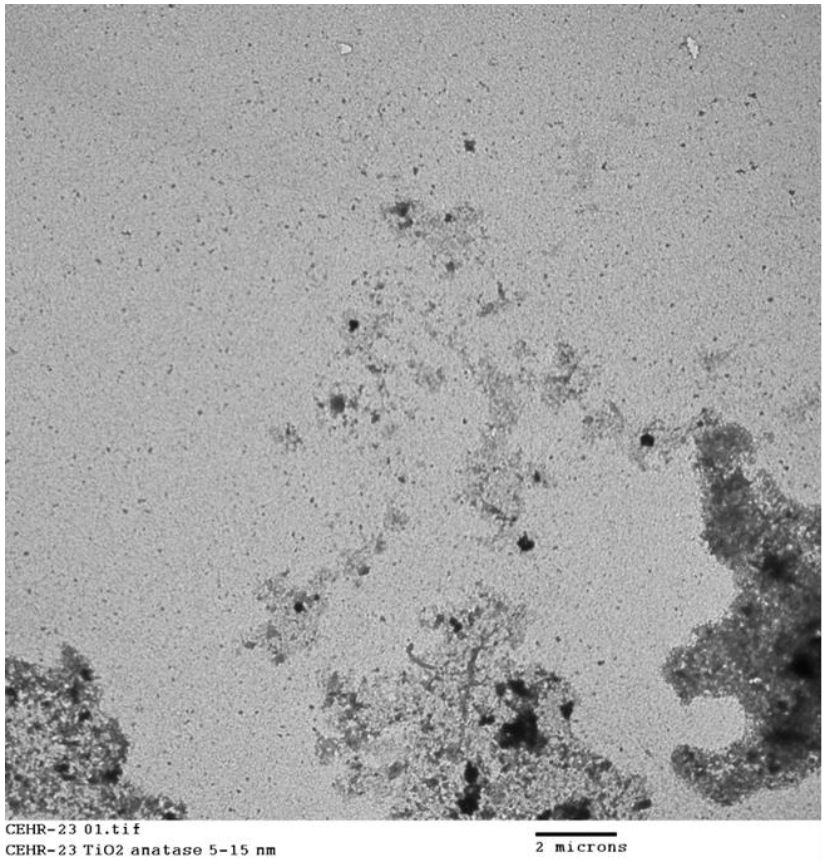

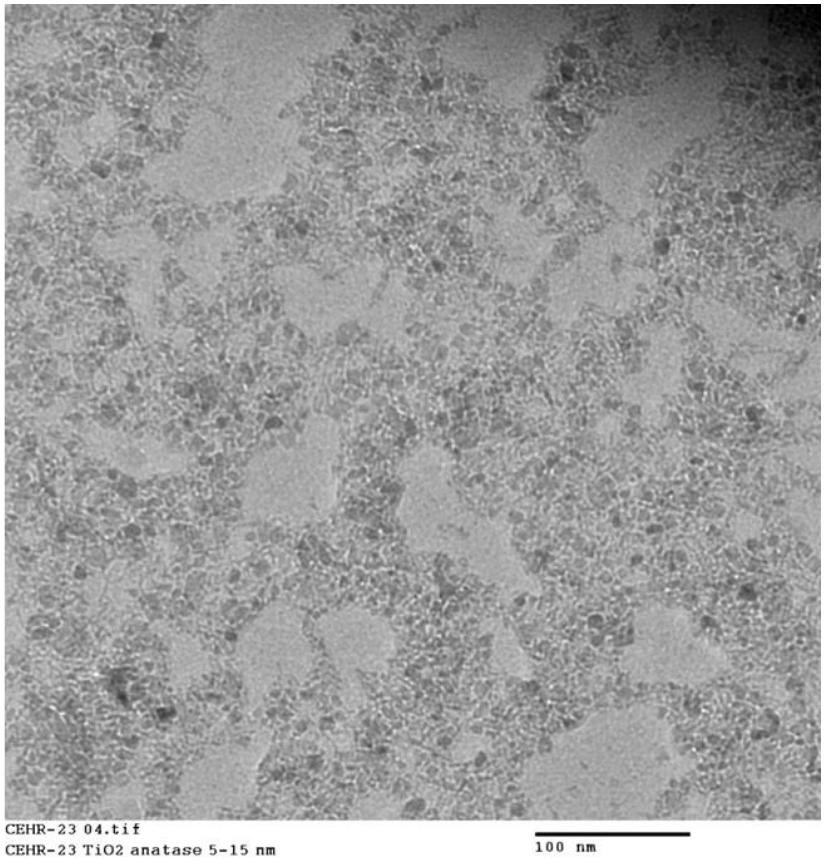

Figure VIII-1. Representative TEM Images of CEHR-23. Two representative images are shown for CEHR-23. There were not enough clearly discernable individual particles for sizing analysis.

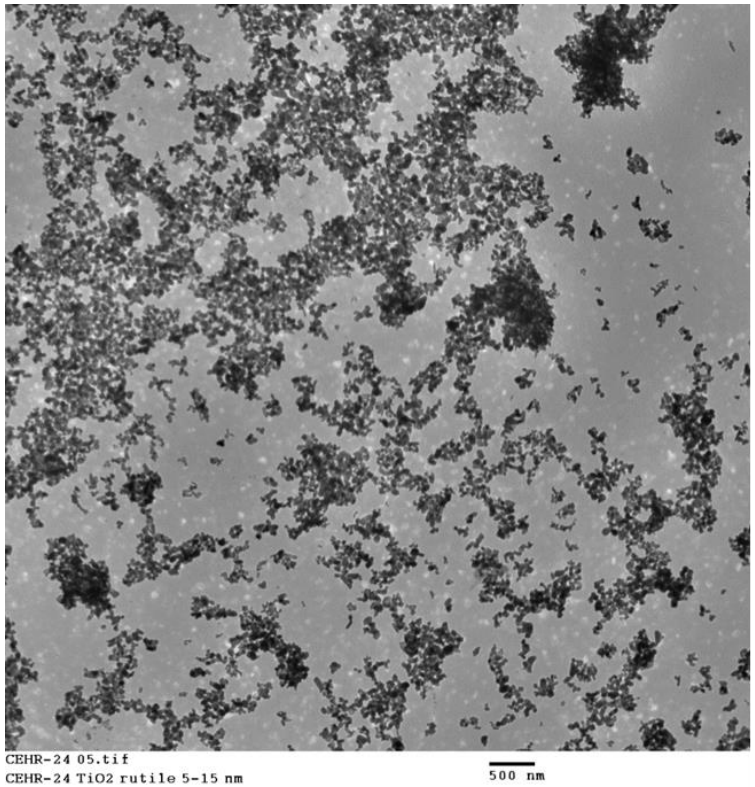

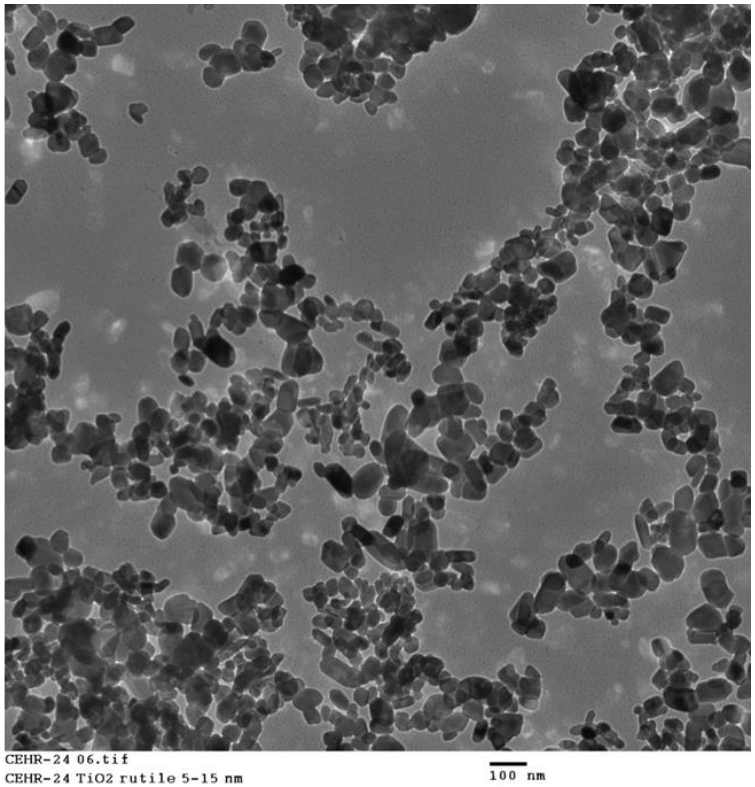

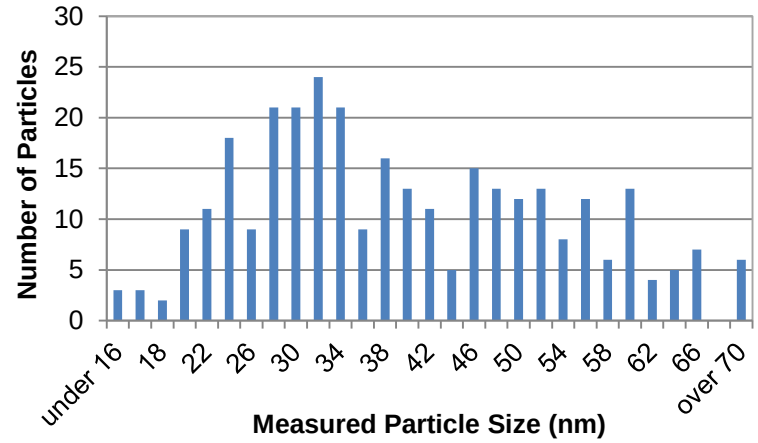

Figure VIII-2. Representative TEM Images of CEHR-24. Two representative images are shown for CEHR-24, showing the range of average diameters spanning 63 ± 19 nm (n = 312).

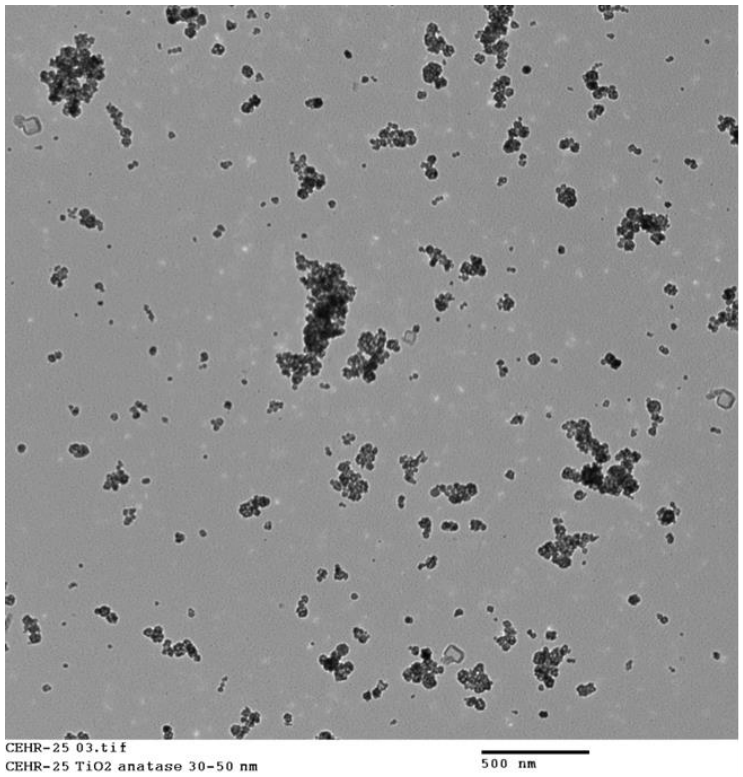

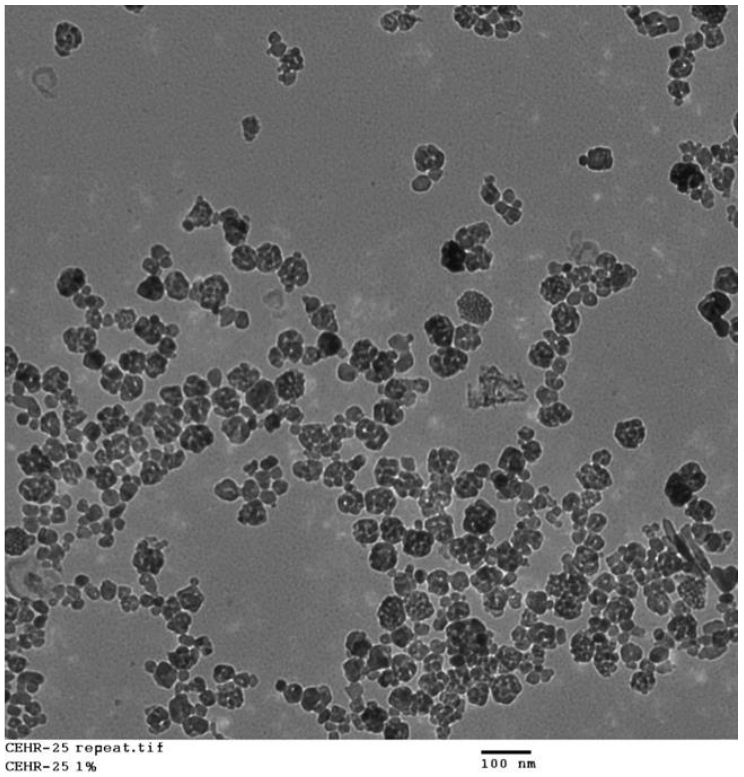

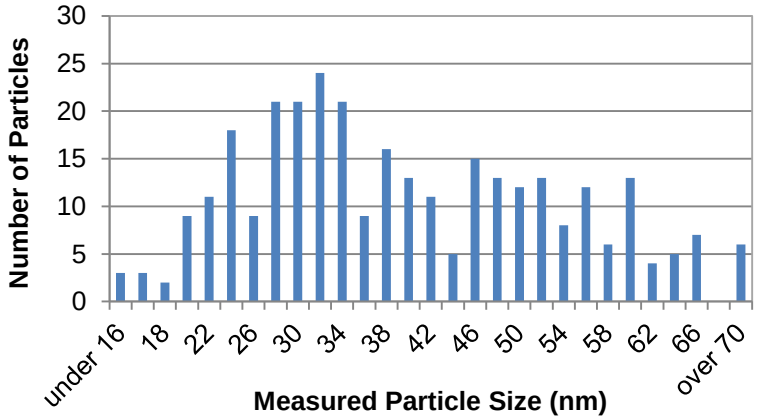

Figure VIII-3. Representative TEM Images of CEHR-25. Two representative images are shown for CEHR-25, showing the range of average diameters spanning 41 ± 14 nm (n = 310).

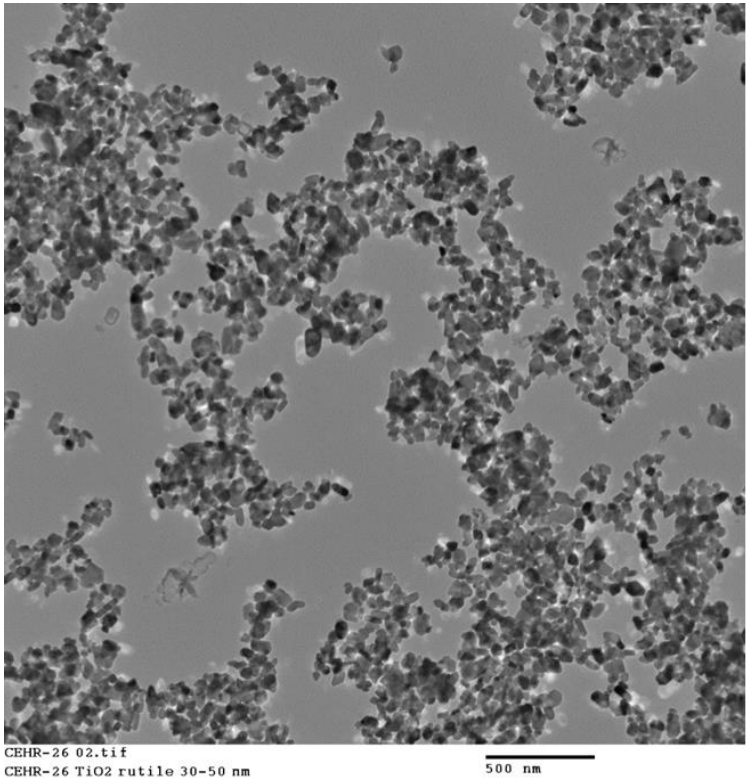

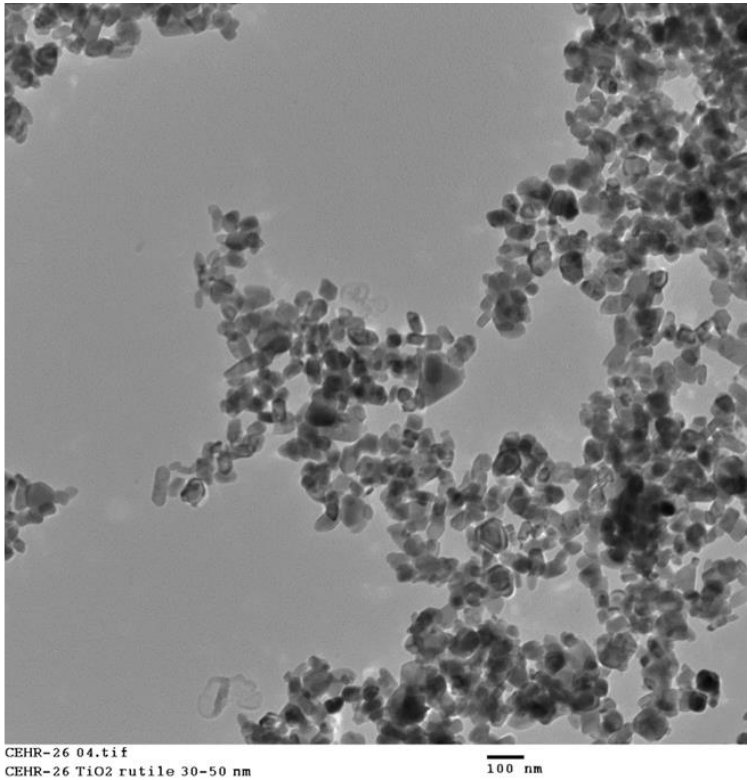

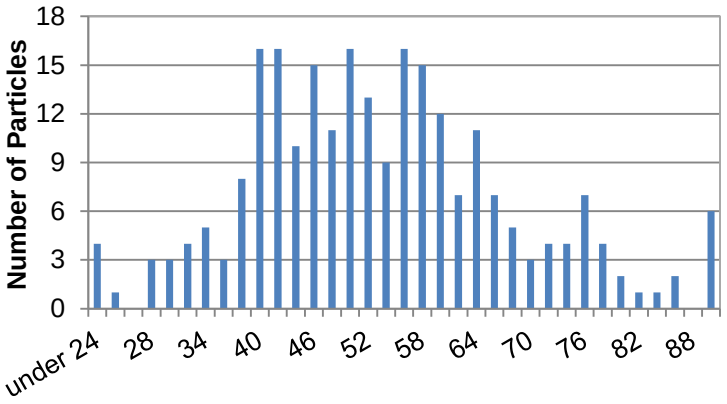

Figure VIII-4. Representative TEM Images of CEHR-26. Two representative images are shown for CEHR-26, showing the range of average diameters spanning 55 ± 15 nm (n = 244).

E. Hydrodynamic Size/Size Distribution via Dynamic Light Scattering

Design and Methods

A Malvern Zetasizer Nano ZS instrument (Southborough, MA) with back scattering detector (173°) was used for measuring the hydrodynamic size (diameter) in batch mode. NIST-NCL joint protocol PCC-1 was followed (https://ncl.cancer.gov/resources/assay-cascade-protocols). Stock samples of CEHR-23 through CEHR-26 were measured at two dilutions ranging 100-fold to 1,000,000-fold in water. Measurements were made at 25°C in a quartz microcuvette. Traces in the figures represent the average of at least twelve measurements.

Hydrodynamic diameters are reported as the intensity-weighted average and as the volume-weighted average over a particular range of size populations corresponding to the most prominent peak. The Int-Peak value is used as the hydrodynamic diameter of a particular species. The Vol-Peak and %Vol values are used to approximate relative amounts of various species in the formulation. Z-Avg values are generally used to assess batch-to-batch variability of a sample.

Results and Discussion

The intensity and volume distribution plots for CEHR-23 through CEHR-26 are provided in Figures VIII-5 to VIII-8. A summary of the sizes is provided in the corresponding tables below each figure. A comparison of the DLS hydrodynamic diameters to the TEM measured and reported nominal sizes is provided in Table VIII-4 below.

CEHR-23 had a hydrodynamic diameter of 47 nm. However, the sample had a PdI >0.2 (meaning the sample was polydisperse) and the broad peak spanned <10 nm to >100 nm. The volume distribution showed a bimodal distribution with an average size of 16 nm. The smaller size for the volume distribution compared to the intensity distribution is typically indicative of sample aggregation, as was evident in the TEM images (Figure VIII-1). CEHR-24, which has a similar reported size range as CEHR-23, displayed an intensity and volume peak of 683 nm and 885 nm, respectively. Upon dilution, the diameters were significantly reduced to 236 nm and 239 nm, respectively. This could be the result of agglomerates in solution which fall apart upon dilution. At either dilution, however, the measured diameters were significantly larger than the reported values.

CEHR-25 and CEHR-26 have reported size ranges of 30-50 nm, but displayed a significant difference by DLS compared to the reported size. The Int-Peak for CEHR-25 was 219 nm and the Vol-Peak was 103 nm. The peaks also shifted upon dilution and the PdI was >0.2. The Int-Peak for CEHR-26 was 780 nm and the Vol-Peak was 953 nm. Both distributions showed a minor (<10%) peak <100 nm at the greater sample dilution. These samples contained particles of the intended size, as evidenced by TEM (Figure VIII-3 and VIII-4), but they appear to aggregate/agglomerate in solution.

Table VIII-4. Comparison of TEM and DLS sizes.

Reference Number	Nominal size reported by manufacturer	TEM Measured Size	DLS Measured Size (Int-Peak)
CEHR-23	5 -15 nm	N/A	47 ± 4 nm
CEHR-24	5 -15 nm	63 ± 19 nm	683 ± 209 nm
CEHR-25	30 -50 nm	41 ± 14 nm	219 ± 36 nm
CEHR-26	30 -50 nm	55 ± 15 nm	780 ± 68 nm

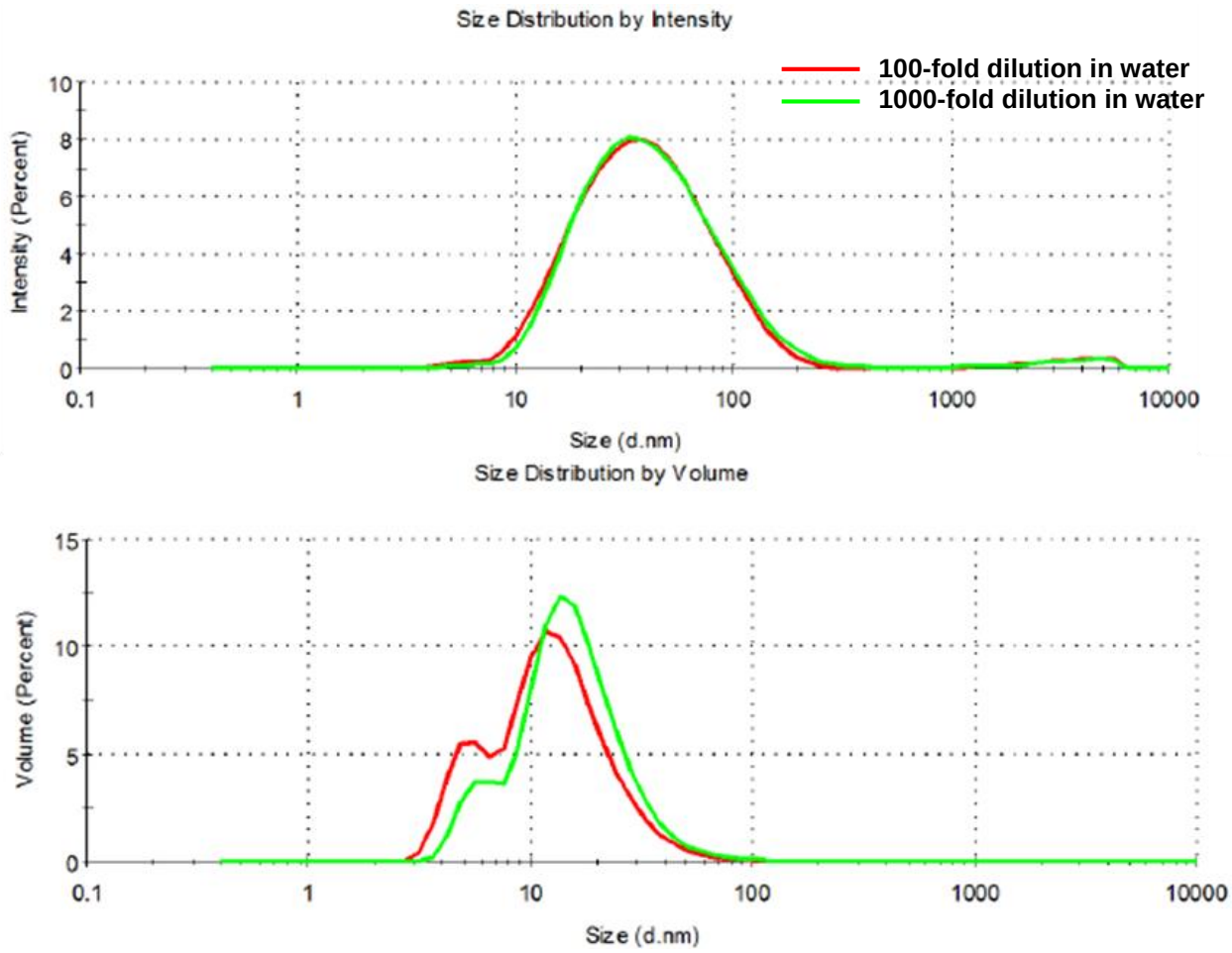

Figure VIII-5. The averaged intensity and volume distribution plots for CEHR-23 diluted in water.

Table VIII-5. Summary of the hydrodynamic size for CEHR-23 diluted in water

Dispersing Medium	Dilution	Z-Avg, nm	PdI	Int-Peak, nm	% Int	Vol-Peak, nm	% Vol
DI water	100-fold	33 ± 0	0.29 ± 0.02	47 ± 4	96 ± 3	16 ± 3	77 ± 30
DI water	1000-fold	34 ± 0	0.30 ± 0.03	51 ± 6	97 ± 2	17 ± 4	93 ± 16

Note: Results are the average of at least 12 measurements. Z-Avg is the intensity-weighted average. PdI is the polydispersity index. Int-Peak is the intensity-weighted average over the primary peak. % Int is the percentage of the intensity spectra occupied by the primary peak. Vol-Peak is the volume-weighted average over the primary peak. % Vol is the percentage of the volume spectra occupied by the primary peak.

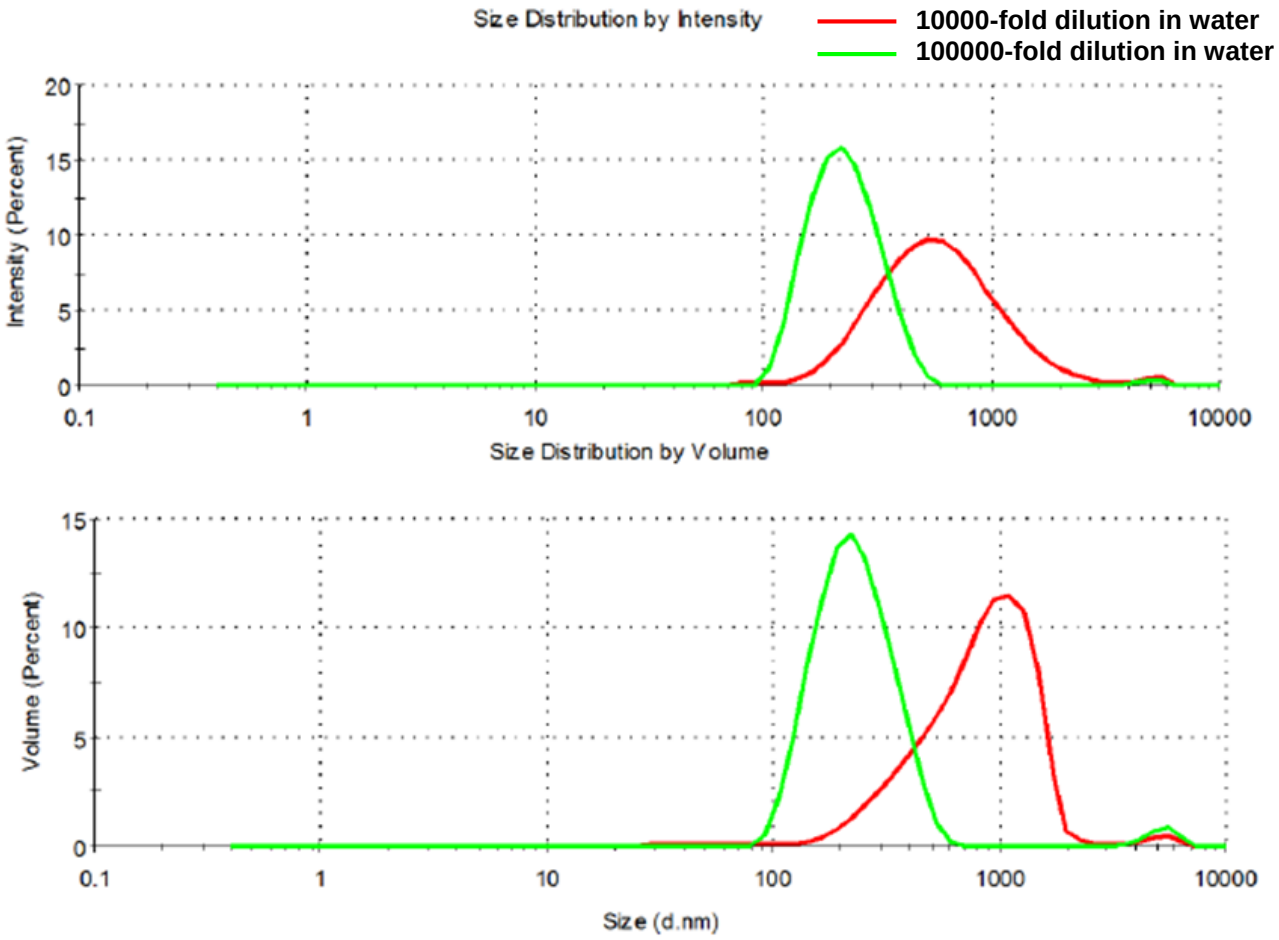

Figure VIII-6. The averaged intensity and volume distribution plots for CEHR-24 diluted in water.

Table VIII-6. Summary of the hydrodynamic size for CEHR-24 diluted in water

Dispersing Medium	Dilution	Z-Avg, nm	PdI	Int-Peak, nm	% Int	Vol-Peak, nm	% Vol
DI water	10,000-fold	501 ± 108	0.29 ± 0.06	683 ± 209	98 ± 2	885 ± 217	98 ± 3
DI water	100,000-fold	217 ± 11	0.15 ± 0.03	236 ± 9	99 ± 1	239 ± 11	98 ± 4

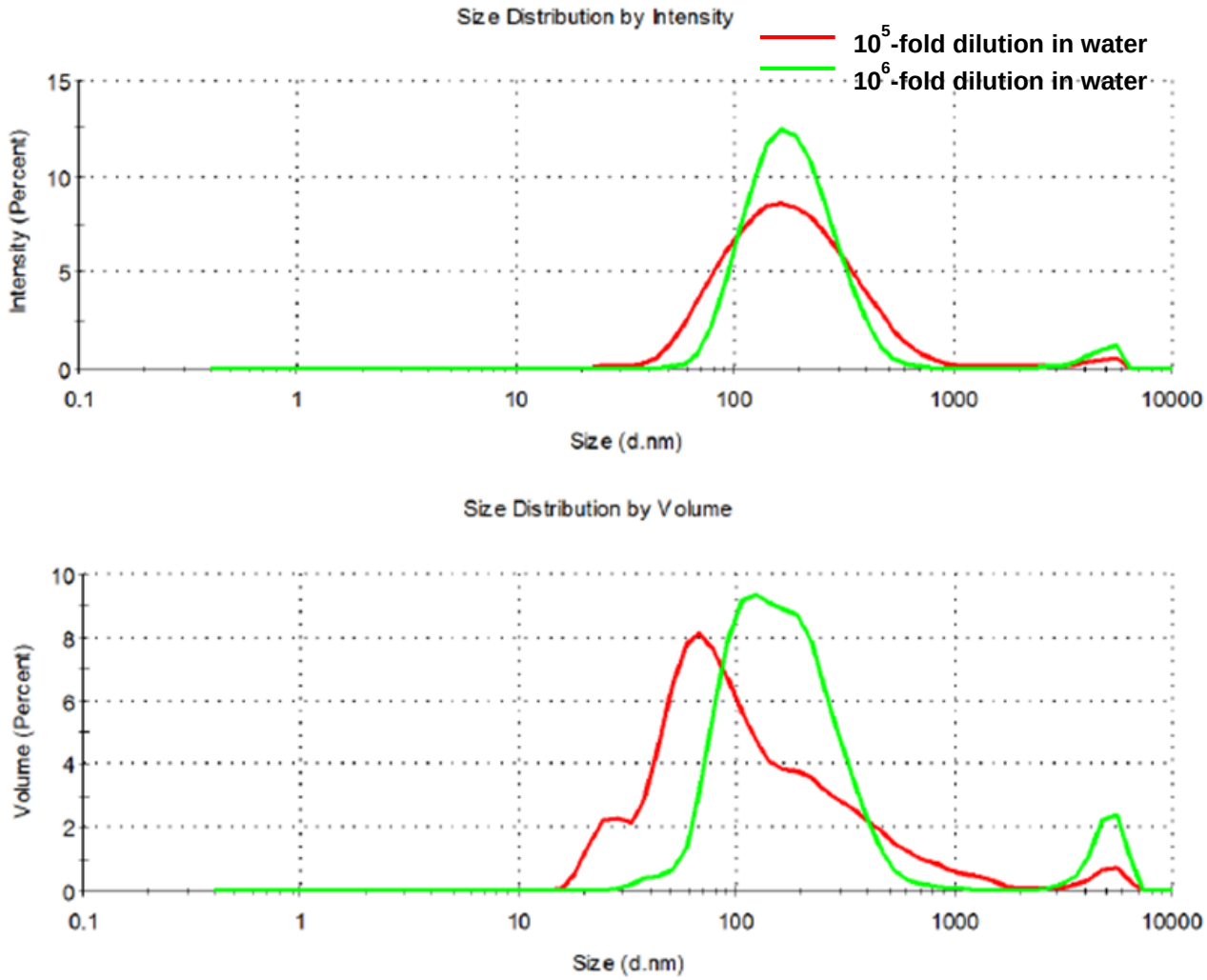

Figure VIII-7. The averaged intensity and volume distribution plots for CEHR-25 diluted in water.

Table VIII-7. Summary of the hydrodynamic size for CEHR-25 diluted in water

Dispersing Medium	Dilution	Z-Avg, nm	PdI	Int-Peak, nm	% Int	Vol-Peak, nm	% Vol
DI water	100,000-fold	153 ± 3	0.28 ± 0.03	219 ± 36	98 ± 1	103 ± 45	66 ± 19
DI water	1,000,000-fold	174 ± 11	0.24 ± 0.04	195 ± 16	97 ± 3	158 ± 39	80 ± 20

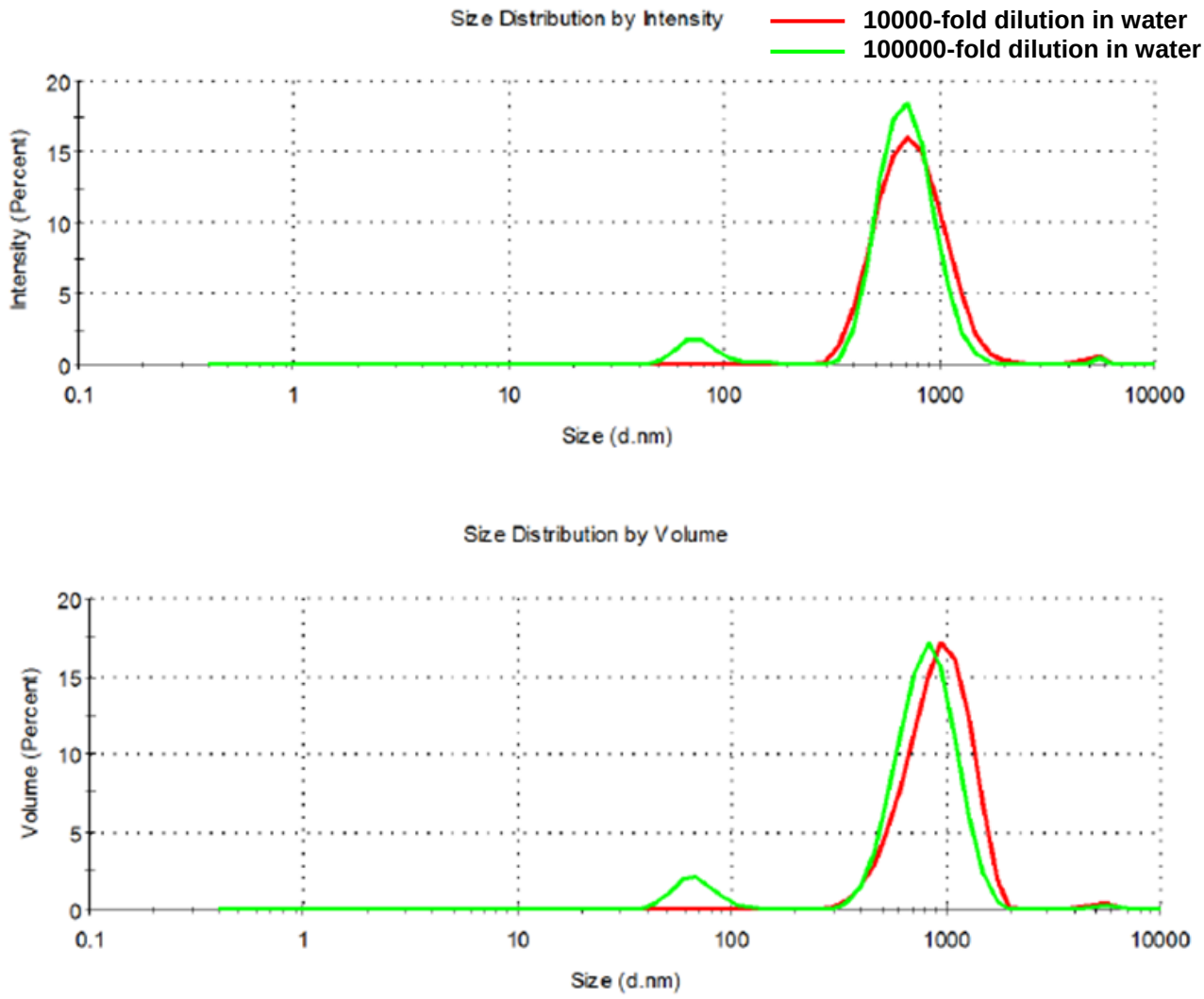

Figure VIII-8. The averaged intensity and volume distribution plots for CEHR-26 diluted in water.

Table VIII-8. Summary of the hydrodynamic size for CEHR-26 diluted in water

Dispersing Medium	Dilution	Z-Avg, nm	PdI	Int-Peak, nm	% Int	Vol-Peak, nm	% Vol
DI water	10,000-fold	754 ± 51	0.22 ± 0.03	780 ± 68	99 ± 1	953 ± 73	99 ± 1
DI water	100,000-fold	697 ± 130	0.57 ± 0.09	734 ± 96	93 ± 6	844 ± 123	91 ± 8

F. Asymmetric-Flow Field Flow Fractionation

Design and Methods

The titanium oxide nanoparticles were separated using asymmetric-flow field-flow fractionation (AF4), with multiple in-line detectors, to evaluate the polydispersity of the samples. AF4 provides a more thorough understanding of the various populations present in the sample over other batch-mode measurement techniques such as DLS alone. The AF4 system consisted of an isocratic pump (Agilent G1310A, Palo Alto, CA), well-plate autosampler (Agilent G1329A), AF4 separation channel (Eclipse DualTec; Wyatt Technology, Santa Barbara, CA), multi-angle light scattering detector (HELEOS II; Wyatt Technology), diode array detector (DAD, Agilent G1315B), and a DLS detector (Malvern Zetasizer Nano ZS; Southborough, MA). The separation channel had a length of 275 mm and a 350 µm spacer. A 10 kDa regenerated cellulose membrane was used for all separations.

The elution profile is provided in Table VIII-9. The cross flow was controlled by an Eclipse flow controller. CEHR-25 was diluted 1000-fold in 15 mM NaCl and filtered through a 0.2 µm regenerated cellulose membrane prior to use. The elution was also run in 15 mM NaCl. This was chosen because the nanoparticles were stable in this dispersing media after dilution and did not interact/stick to the FFF membrane. A sample injection of volume of 100 µL was used for all samples and the chromatographic traces were monitored by DLS detection and UV at 210 nm. The hydrodynamic size is plotted across the eluted peaks. The UV absorbance at 210 nm was monitored to track relative abundance of each different size population.

Table VIII-9. AF4 elution profile.

Start Time (min)	End Time (min)	Duration (min)	Mode	Starting Cross-flow Rate (mL/min)	Ending Cross-flow Rate (mL/min)
0	2	2	Elution	1	1
2	4	2	Focus	-	-
4	9	5	Focus + Inject	-	-
9	19	10	Focus	-	-
19	29	10	Elution	1	1
29	31	2	Elution	1	0.5
31	41	10	Elution	0.5	0
41	61	20	Elution	0	0
61	63	2	Elution + Inject	0	0
63	64	1	Elution	0	0

Results and Discussion

The fractograms for CEHR-25 are shown in Figure VIII-9. The light scattering (top and bottom panel) signals showed a very broad single peak. By UV, the majority of this sample (as evidenced by its strong UV signal) had a hydrodynamic size range of 43-200 nm. Contained within this broad peak, was a second size population with sizes increasing up to 320 nm. The flow-mode DLS results agreed with the batch-mode DLS which showed polydispersity with an average size of 219 nm. In both cases, the sizes measured were much larger than the nominal size range (presumably TEM) of 30-50 nm.

CEHR-24 was not subjected to AF4 analysis due to the bacterial contamination. AF4 separation for CEHR-23 and CEHR-26 was unsuccessful. Both samples are positively-charged (Table VIII-15) and interacted highly with the membranes. Two membranes, regenerated cellulose and polyethersulfone (10 kDa MWCO for both) were tested using 15 mM NaCl as the mobile phase. In both cases, the samples stuck to the membrane and resulted in very little sample recovery. As a result, the light scattering (DLS and MALS) signals were unreliable. Additional attempts to reduce the membrane interactions with PBS or 0.05 % (v/v) SDS resulted in nanoparticle instability (i.e. precipitation).

Table VIII-10. Comparison of batch-mode and flow-mode DLS sizes.

Reference Number	Batch-mode DLS Measured Size (Int-Peak)	Flow-mode DLS Measured Size: Major peak	Flow-mode DLS Measured Size: Minor peak
CEHR-23	47 ± 4 nm	Separation unsuccessful	
CEHR-24	683 ± 209 nm	Not Tested	
CEHR-25	219 ± 36 nm	43-200 nm	285-320 nm
CEHR-26	780 ± 68 nm	Separation unsuccessful	

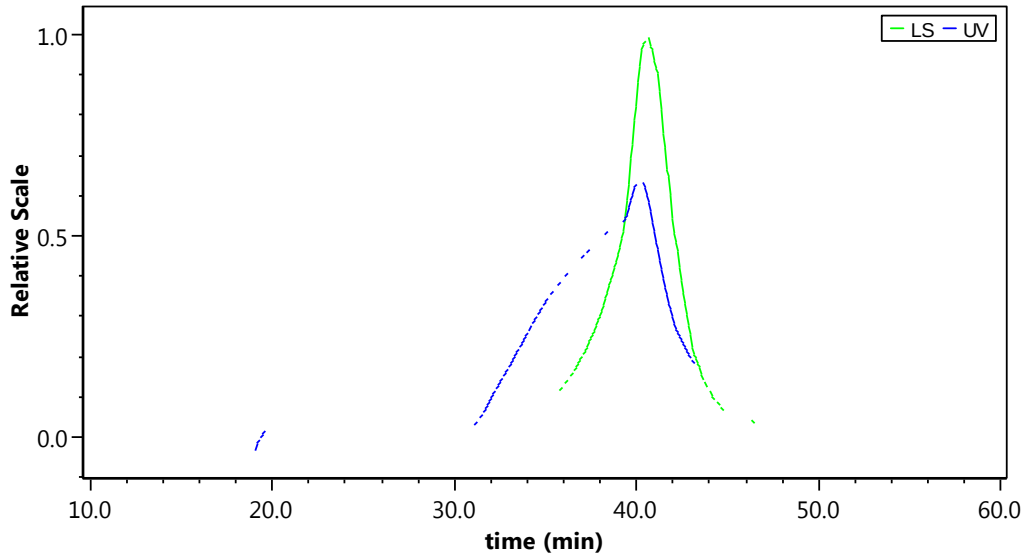

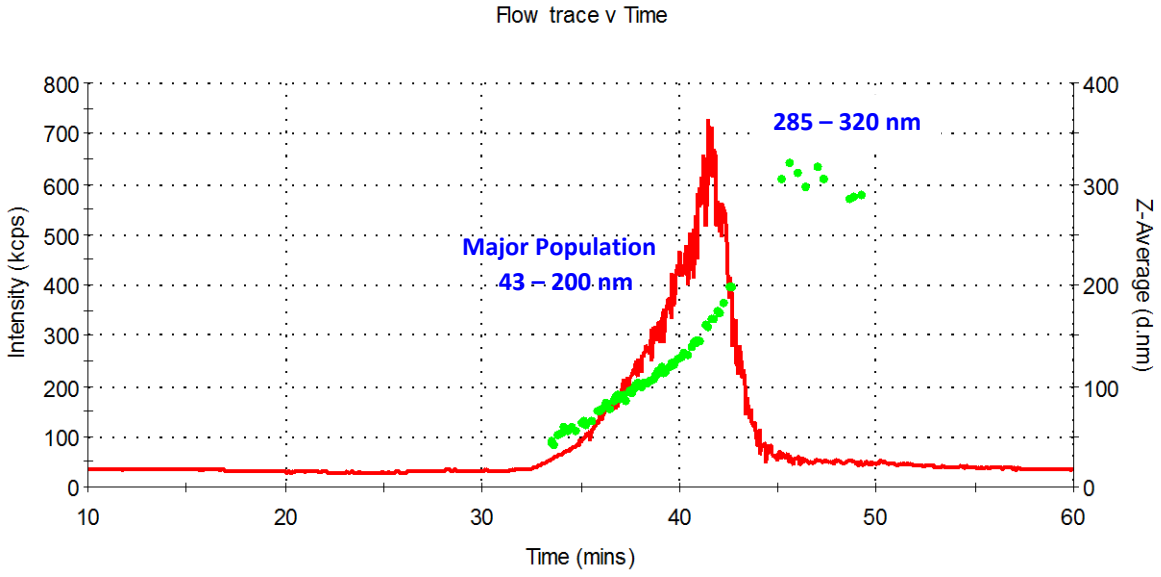

Figure VIII-9. AF4 fractograms for CEHR-25. The top panel shows the UV (210 nm) and LS (light scattering) signals while the bottom panel shows the hydrodynamic size distributions across the eluted peaks.

G. Inductively Coupled Plasma Mass Spectrometry

Design and Methods

The titanium concentrations of CEHR-23 through CEHR-26 were determined by inductively coupled plasma mass spectrometry (ICP-MS). An Agilent ICP-MS 7500CX equipped with a micro-mist nebulizer, standard sample introduction system, and integrated auto-sampler, operated in “no gas” mode in Agilent’s proprietary ORS (Octopole Reaction System) was used. Tuning of the instrument was performed daily prior to sample testing.

NOTE: If attempting to reproduce this method, please use extreme caution. Hydrofluoric acid (HF), used for digestion of the titanium nanoparticles, is an extremely dangerous acid. Ensure that proper protection measures are taken to avoid any exposure or skin contact. Hydrofluoric acid should be handled inside a chemical fume hood. In addition, appropriate personal protective equipment including a lab coat, a lab apron, nitrile gloves, acid resistant thick gloves, arm gaiters, safety glasses, and face shield should be used.

Semi-Quantitative Analysis

A semi-quantitative analysis was performed on each sample prior to quantitative determination of the titanium concentrations. The semi-quantitative analysis was performed to help determine the proper dilution range for the samples, as well as to detect the presence of other metals in the sample. Only metals with counts two times greater than the background were denoted.

Each titanium oxide sample (25 µL) was digested using concentrated hydrofluoric acid (100 µL). Then the sample was diluted to 50 mL of 2% nitric acid.

Total Metal Concentration

Using the data from the semi-quantitative analysis, the appropriate dilution was determined for the ICP-MS full quantitative analysis. The dilution target for the samples was 5 to 200 ppb. The total metal concentration was determined using the native formulation (i.e. not centrifuged or separated). Samples (10-100 µL) were initially digested with hydrofluoric acid. Typically, no more than a total of 1 mL of concentrated acid was used. The acid digested samples were then further diluted to approximately 30-50 mL total volume with 2% nitric acid. A second dilution was then performed in which 10-100 µL of the first dilution was diluted to 10-50 mL using 2% nitric acid. Samples were run in triplicate.

The metal concentration in the samples was determined by comparing against a series of calibration standards prepared from NIST SRM 3162a. A series of concentrations ranging from 5 to 200 ng/g (ppb) were prepared. The dilutions were made using 2% nitric acid. Specifically, a dilution of 5000 ng Ti / g in 2% HNO_3 was used to make a 1000 ng Ti / g solution, which was then used to create standards for the calibration curve in a range of 5 to 200 ng/g in 10 mL volumes. In addition, an internal standard, yttrium, was used to track the signal response of the ICP-MS. The internal standard was diluted to approximately 50 ppb and was mixed with the sample using a sample T. A simple linear regression was used for calculation of the metal concentrations.

The sequence for the ICP-MS runs consisted of five blanks, the calibration curve standards ordered from lowest to highest, five more blanks, then the titanium oxide nanoparticle samples. Each sample was run in triplicate with three blanks in between. Within each sample set, the samples were run from highest dilution to lowest dilution. After the last titanium oxide sample

was measured in triplicate, five blanks were run, followed by the calibration standards again. Three blanks were run to flush the sample introduction system.

Free Metal Concentration and Metal Release with Time
In addition to determining the total metal concentration present in each sample, ICP-MS was also used to assess the amount of free metal ions present. The separation of free metal ions from the nanoparticles was carried out using stirred cell filtration as described in Section IV. The stirred cell separation was performed twice on each sample at different times to evaluate the release of free metal ions over time. The dates are noted for each analysis. Within each set of samples, the permeate dilutions were run first, followed by the reserved solution samples.

Results and Discussion

Semi-Quantitative Analysis
The results from the semi-quantitative analysis of CEHR-23, CEHR-24, CEHR-25, and CEHR-26 are shown in Figure VIII-10. Titanium was found in all four samples, as expected. CEHR-23 and CEHR-24 also contained zinc and hafnium. CEHR-26 contained zinc, zirconium, and tin. CEHR-25 contained the most metal impurities: zinc, iron, strontium, manganese, vanadium, lead, uranium, and cerium. The origins of these metal impurities are unknown. This was only an analysis to detect potential metal impurities. For an accurate determination of their concentrations, quantitative analysis compared to a standard would be required.

A. CEHR-23

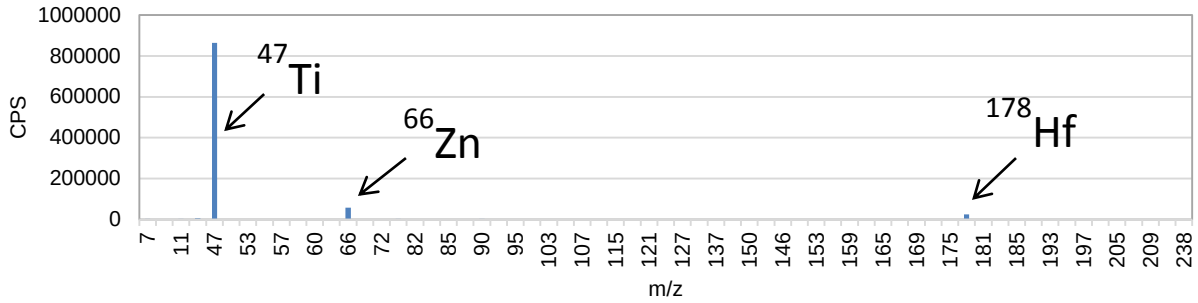

B. CEHR-24

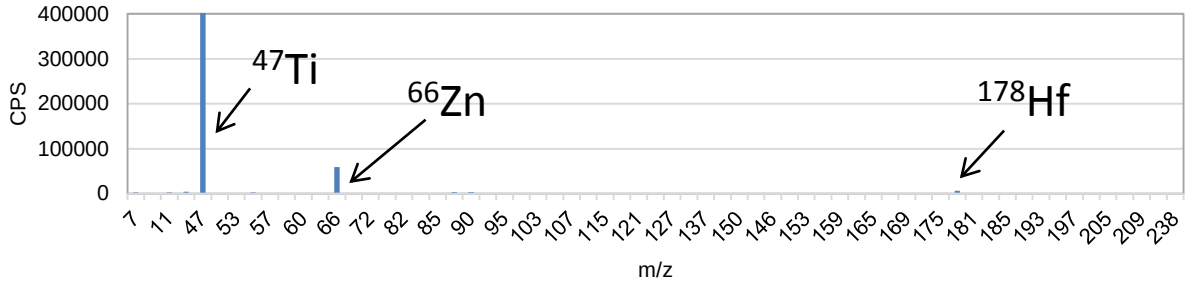

C. CEHR-25

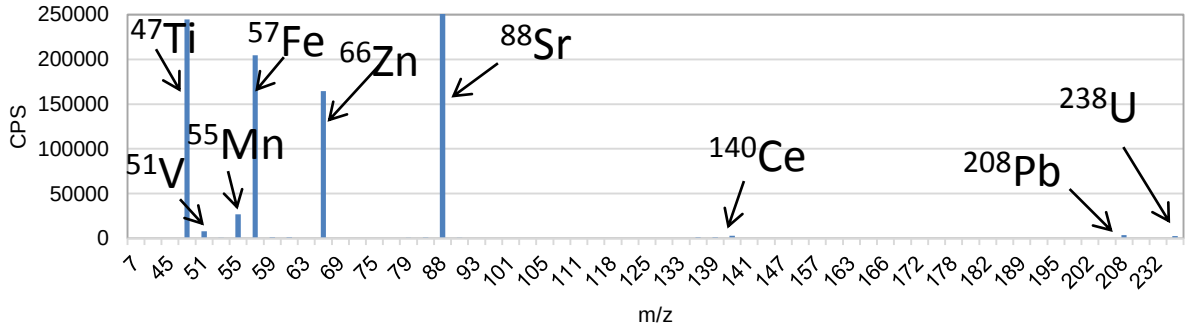

D. CEHR-26

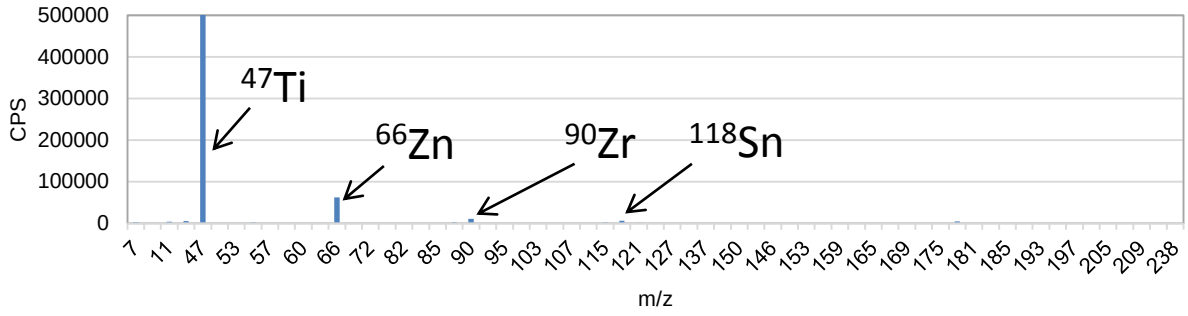

Figure VIII-10. Plots of CPS vs m/z. (A) CEHR-23 semi-quantitative analysis plot. **(B)** CEHR-24 semi-quantitative analysis plot. **(C)** CEHR-25 semi-quantitative analysis plot. **(D)** CEHR-26 semi-quantitative analysis plot. All samples were analyzed on 9 November 2016. Note ^{12}C, ^{23}Na, ^{24}Mg, ^{27}Al, ^{29}Si, ^{31}P, ^{34}S, ^{35}Cl, ^{39}K, and ^{43}Ca were removed in all three plots to better visualize the smaller peaks. The internal standard peak for ^{89}Y was also omitted.

Full Quantitative Analysis: Total Titanium Concentration

The calibration curve used for total titanium quantitation was constructed from NIST SRM 3162a. Quantitative total titanium concentrations for CEHR-23, CEHR-24, CEHR-25, and CEHR-26 are summarized in Table VIII-11. The ICP-MS titanium concentrations, in units of mg/g, were converted to weight percent. To do so, the titanium mass was converted to TiO_2, using titanium oxide's molecular weight of 79.866 g/mol. To calculate the titanium oxide weight percent, the titanium oxide mass was divided by the mass of the solution to output the nanoparticle percent. The percent weights of the nanoparticles were 11%, 12%, 39%, and 7% by weight for CEHR-23, CEHR-24, CEHR-25, and CEHR-26 respectively. The theoretical concentrations were 15, 15, 40, and 20%, respectively. CEHR-23, CEHR-24 and CEHR-25 were reasonably close to the theoretical concentrations, considering the sample heterogeneity issues. CEHR-26 was significantly lower than the theoretical value, with less than half the reported nanoparticle concentration. Sample settling was the most evident with CEHR-26 as shown in the photograph.

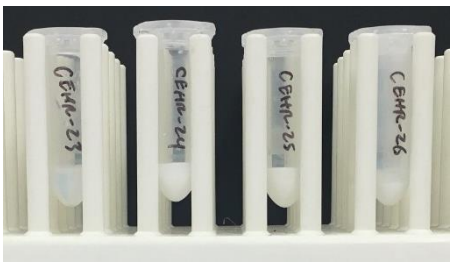

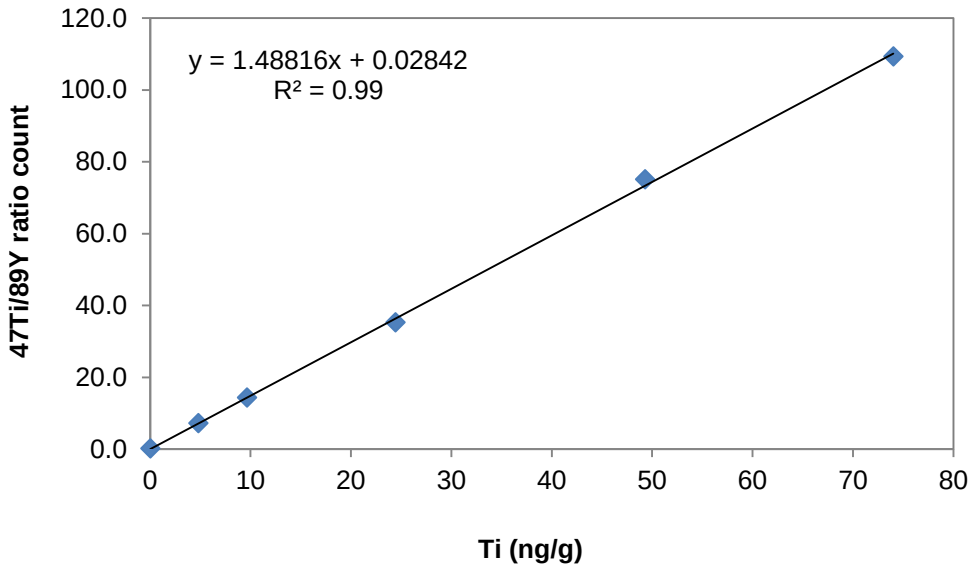

Figure VIII-11. Titanium Calibration Curve. A typical calibration curve ranging from 0 to 75 Ti ng/g, used to calculate the titanium concentration in CEHR-23, CEHR-24, CEHR-25, and CEHR-26. The calibration curve was constructed from NIST SRM 3162a titanium standard.

Table VIII-11. Summary of the total titanium concentration in CEHR-23, CEHR-24, CEHR-25, and CEHR-26 as determined by ICP-MS.

Reference Number	Reported Concentration	Total [Ti]	Total [TiO_2]
CEHR-23	15 wt%	63 ± 8 mg/g (n=5)	11% by weight
CEHR-24	15 wt%	72 ± 20 mg/g (n=5)	12% by weight
CEHR-25	40 wt%	231 ± 66 mg/g (n=5)	39% by weight
CEHR-26	20 wt%	42 ± 22 mg/g (n=5)	7% by weight

Free Titanium Concentration
Stirred cell filtration was employed to separate any free titanium ions from the titanium oxide nanoparticles. Repeat measurements were made approximately two months apart to assess titanium release kinetics/stability of the formulation. The stock sample (prior to stirred cell filtration; designated as Total [Ti] in Table VIII-12) was re-measured each time and used to calculate (normalize) the percent free titanium (free [Ti] / total [Ti]) in each formulation. The free titanium concentrations in all four samples at two time points are shown in Table VIII-33. A maximum of 0.1% free titanium was observed for all four samples.

The differences in the total titanium concentrations among the measurements reported, most notably for CEHR-24, CEHR-25 and CEHR-26, can be attributed to non-homogeneity within the sample. All samples showed visible settling over time.

Table VIII-12. Summary of Free Titanium Concentrations. A summary of the free titanium detected by ICP-MS following stirred cell separation. Each sample was analyzed at two time points.

Reference Number	Date	Total [Ti] (Stir Cell Reserve)	Free [Ti] (Permeate)	% Free Ti
CEHR-23	28 Sept 2016	64 ± 9 mg/g	BLOQ	-
CEHR-23	29 Nov 2016	63 ± 1 mg/g	0.040 ± 0.002 mg/g	<0.1%
CEHR-24	28 Sept 2016	54 ± 8 mg/g	BLOQ	-
CEHR-24	29 Nov 2016	75.4 ± 0.9 mg/g	0.038 ± 0.001 mg/g	<0.1%
CEHR-25	28 Sept 2016	346 ± 7 mg/g	BLOQ	-
CEHR-25	29 Nov 2016	194 ± 3 mg/g	0.0393 ± 0.0005 mg/g	<0.1%
CEHR-26	28 Sept 2016	43 ± 1 mg/g	BLOQ	-
CEHR-26	29 Nov 2016	75 ± 1 mg/g	0.0815 ± 0.0010 mg/g	0.1%

H. Thermogravimetric Analysis

Design and Methods

Samples were analyzed via thermogravimetric analysis (TGA) to assess whether coatings were present on the nanoparticles and in what concentration. TGA was also used to determine the concentration of the metallic nanomaterial by measuring the residual material remaining after combustion of any coatings. For measurement of the metallic nanoparticle concentration, the samples were measured in their liquid (as-received) forms. For detection and measurement of coating concentrations, the samples were lyophilized prior to the TGA run. The signal from the water loss had the potential to swamp out a small amount of loss from any coating present, and thus was removed/minimized by lyophilization. Using lyophilized samples allowed for better sensitivity (total weight measured >1 mg) and hence a more accurate coating determination.

Nanoparticle Concentration

For each liquid sample, 50 μL was transferred to an aluminum oxide crucible (150 μL crucible with lid, Mettler Toledo) for TGA measurement (TGA/DSC 1, Mettler Toledo). Samples were held at 25˚C for 5 min, then ramped to 1000˚C at a heating rate of 20˚C/min under nitrogen gas. A new crucible was used for each sample. The empty crucible was subjected to the TGA method prior to loading the sample to serve as a background correction.

TGA cannot confirm the oxidation state of the material. Concentrations are reported using the manufacturer-reported oxidation state.

Coating Detection and Concentration

To determine coating content of the samples, samples were lyophilized overnight after being frozen in an ultra-low temperature freezer (-80˚C) for at least 3 hours. Typically, 250 μL of sample solution yielded 40 mg of lyophilized powder. About 12 mg was the typical amount added for TGA analysis, allowing for repeat runs, if necessary. The dried samples were added to aluminum oxide crucibles and subjected to the same temperature program as their liquid forms.

Results and Discussion

Nanoparticle Concentration

The TGA curves (top panel; weight loss versus temperature) for CEHR-23, CEHR-24, CEHR-25, and CEHR-26 are shown in Figures VIII-12 through VIII-15, respectively. The first derivative of this curve (bottom panel) was used to highlight the weight loss events. For all samples, the major weight loss event was observed between 50-180˚C, corresponding to the loss of water and possible coating. All samples seemed to show two peaks under this water loss peak. Small peaks at 375 and 325˚C, presumably from a coating, were also noted for CEHR-24 and CEHR-25, respectively.

The total mass titanium oxide was determined by using the amount of mass remaining at the end of the TGA run. However, this analysis assumes that, at the end of the run, all that remained was the titanium oxide; the water would have evaporated and any organic coating present would have combusted. The TGA-measured nanoparticle concentrations for CEHR-23, CEHR-24, CEHR-25, and CEHR-26 were 13%, 15%, 36%, and 9% (by weight), respectively (Table VIII-13). These results were in good agreement with the vendor reported concentrations for CEHR-23, CEHR-24, and CEHR-25. CEHR-26, however, was only half the reported concentration. The TGA results were in agreement with the ICP-MS measured concentrations (Table VIII-13).

Table VIII-13. Comparison of TGA Measured Concentration to ICP-MS Measured and Reported Nanoparticle Concentrations.

Reference Number	Reported Concentration	Measured Concentration via ICP-MS	Measured Concentration via TGA of Liquid Sample
CEHR-23	15 wt%	11% wt.	13% wt.
CEHR-24	15 wt%	12% wt.	15% wt.
CEHR-25	40 wt%	39% wt.	36% wt.
CEHR-26	20 wt%	7% wt.	9% wt.

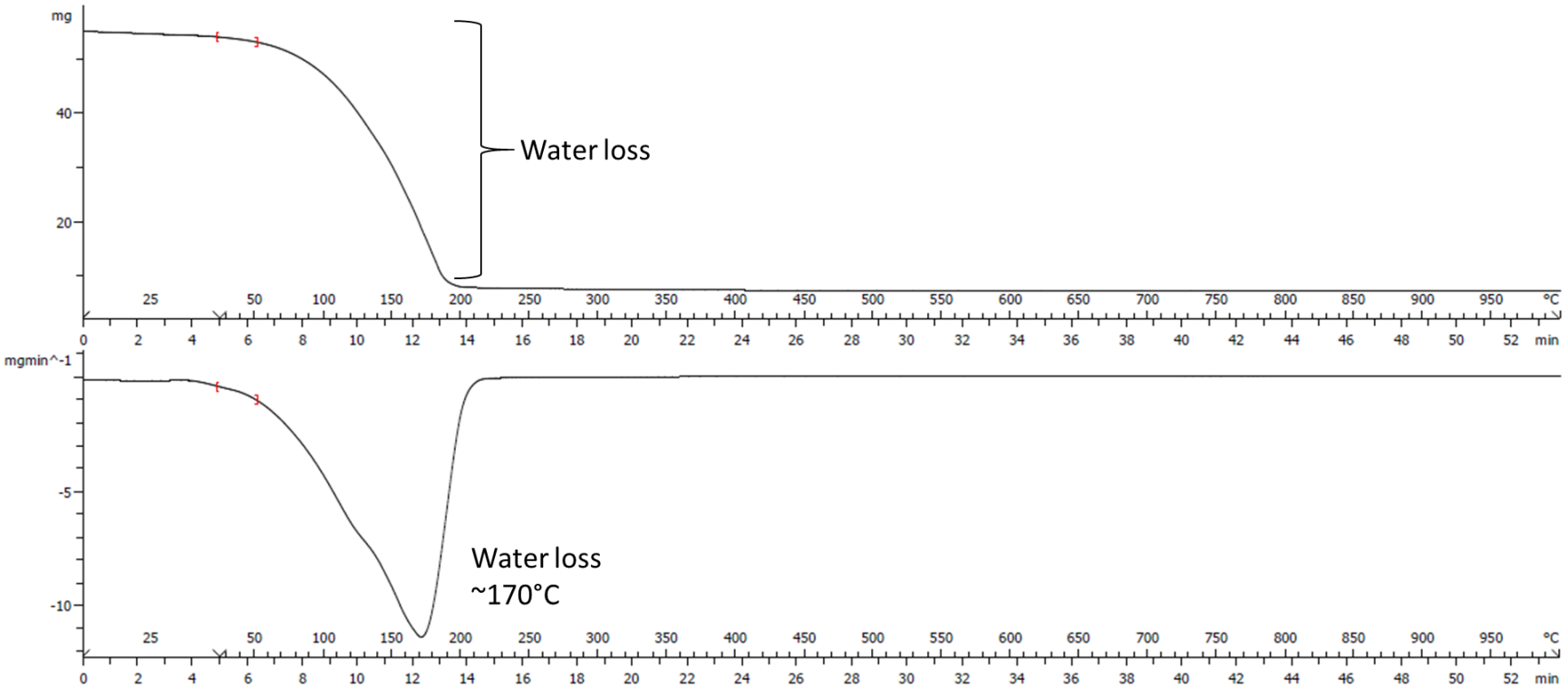

Reference Number	Volume (µL)	Starting Mass (mg)	Total Mass Loss (mg)	Residue mass (mg)
CEHR-23	50	54.803	47.631	7.172

Figure VIII-12. TGA thermogram of CEHR-23. The top panel is the weight loss versus temperature (and time) curve. The bottom panel is the first derivative of that curve.

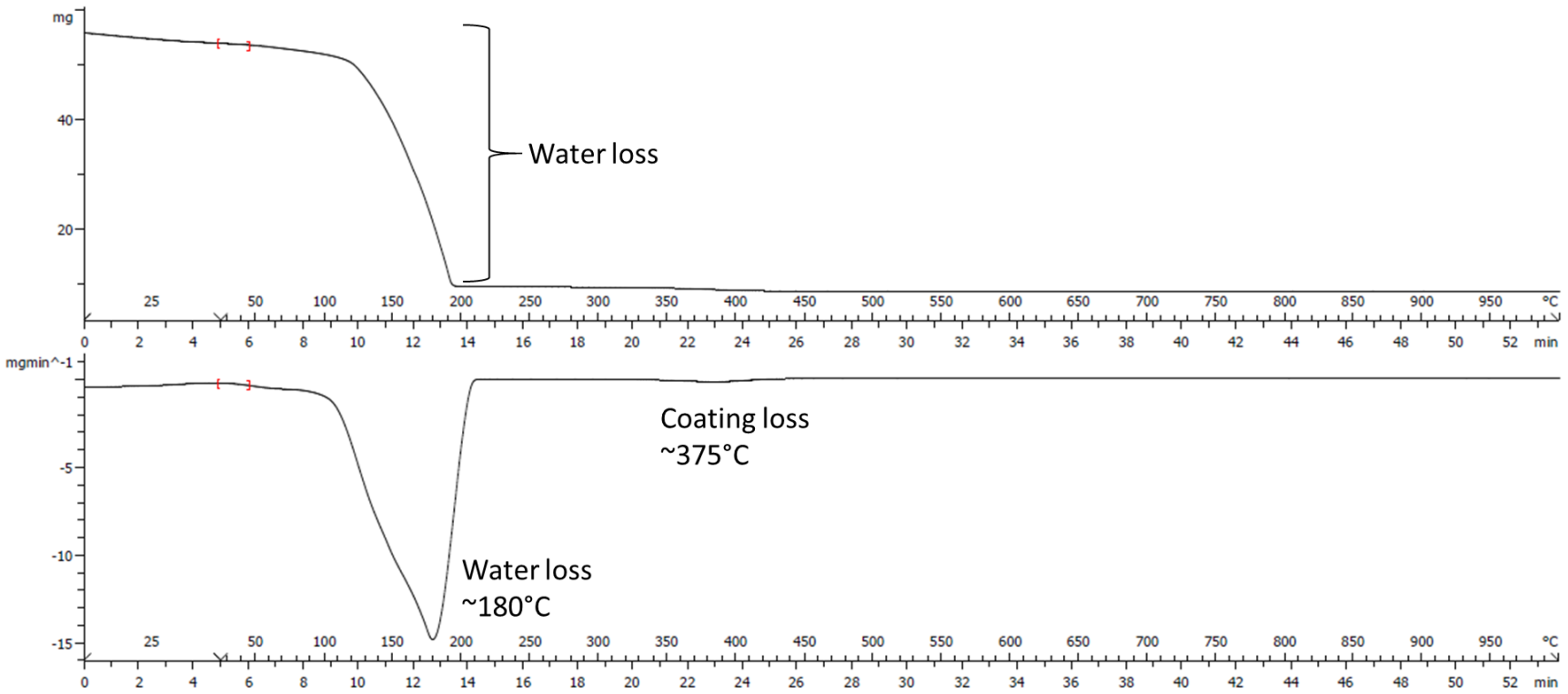

Reference Number	Volume (µL)	Starting Mass (mg)	Total Mass Loss (mg)	Residue mass (mg)
CEHR-24	50	55.746	47.286	8.459

Figure VIII-13. TGA thermogram of CEHR-24. The top panel is the weight loss versus temperature (and time) curve. The bottom panel is the first derivative of that curve.

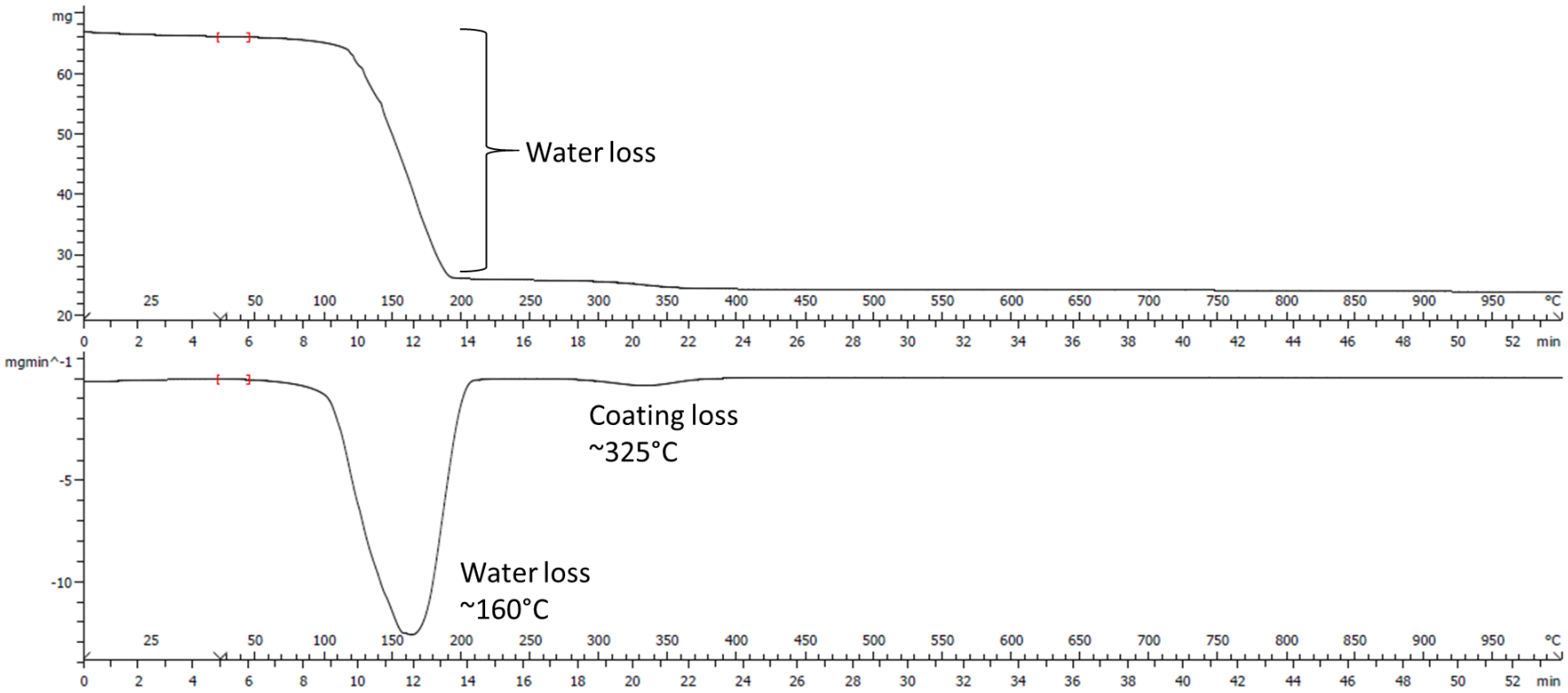

Reference Number	Volume (µL)	Starting Mass (mg)	Total Mass Loss (mg)	Residue mass (mg)
CEHR-25	50	66.676	42.950	23.727

Figure VIII-14. TGA thermogram of CEHR-25. The top panel is the weight loss versus temperature (and time) curve. The bottom panel is the first derivative of that curve.

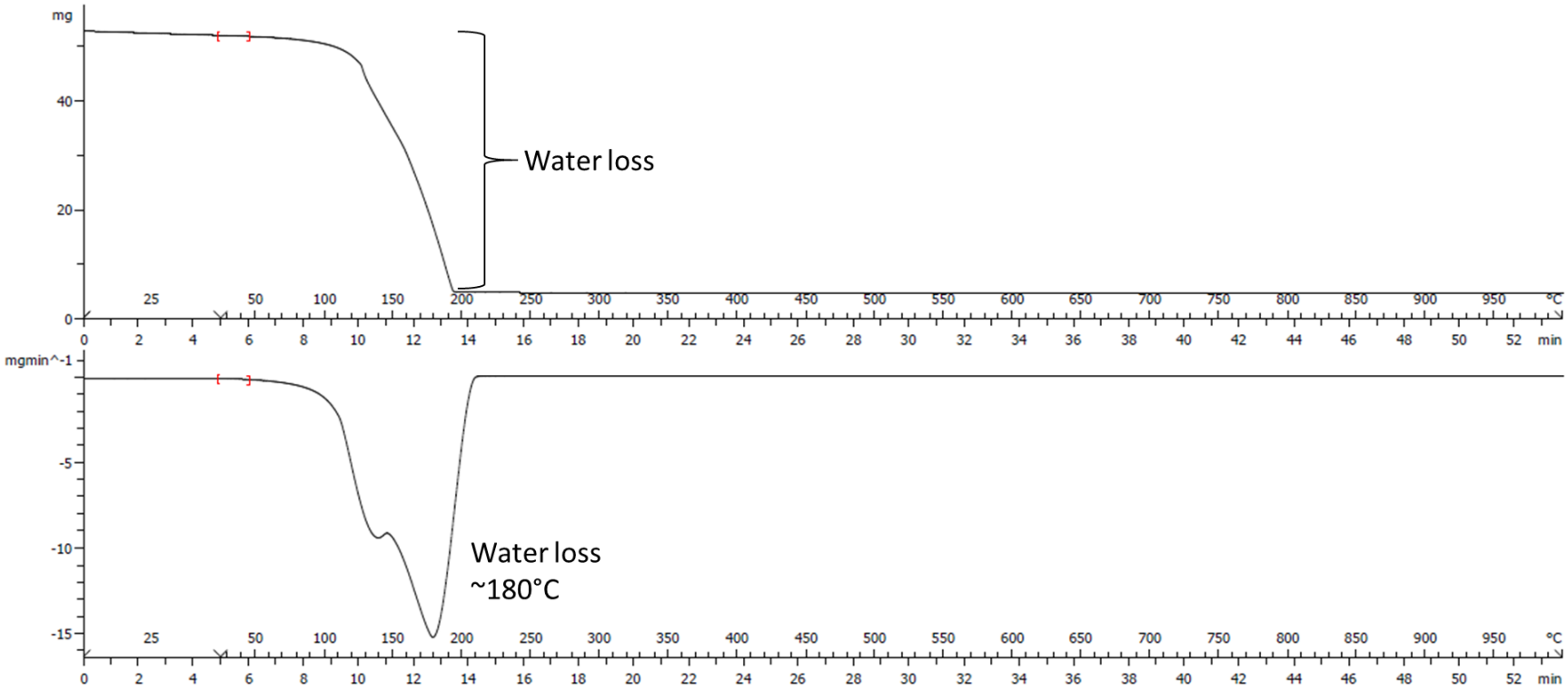

Reference Number	Volume (µL)	Starting Mass (mg)	Total Mass Loss (mg)	Residue mass (mg)
CEHR-26	50	52.612	47.923	4.689

Figure VIII-15. TGA thermogram of CEHR-26. The top panel is the weight loss versus temperature (and time) curve. The bottom panel is the first derivative of that curve.

Coating Detection and Concentration

TGA was also used to determine whether a surface coating was present. The manufacturers of the titanium oxide nanoparticles, US Nano, did not disclose a coating on the nanoparticles. Often however, especially for proprietary coatings, this information is omitted from sample descriptions. All samples were lyophilized to reduce the water peak and improve sensitivity for coating detection. The TGA curves for the lyophilized samples are shown in Figures VIII-16 to VIII-19, respectively.

Multiple weight loss events were observed for CEHR-23, CEHR-24, CEHR-25, and CEHR-26. In all samples, the first minor weight loss event corresponded to the loss of residual water and occurred by 100˚C. The second weight loss events were attributed to the decomposition of surface coating and/or added excipients (possibly added to help with solubilization and stability). From the first derivative curves, decomposition temperatures of 275, 390, 350, and 250°C were observed for CEHR-23, CEHR-24, CEHR-25, and CEHR-26, respectively.

For each run, the weight loss of coating was calculated by using the first derivative analysis to mark the beginning and end of the weight loss events. This translated to a variable starting temperature (100°C for CEHR-23 and CEHR-24, 200°C for CEHR-25, and 130°C for CEHR-26) and ending temperature of 1000°C. The final weight at 1000°C was taken to be the titanium oxide amount, and assumed that the weight of any residual decomposed coating and/or excipients was negligible relative to the weight of the titanium oxide nanoparticles. The mass ratio of coating and/or excipients to titanium oxide nanoparticle was then calculated for each independent run. The calculated percent coatings were 9%, 10%, 10%, and 1% for CEHR-23, CEHR-24, CEHR-25, and CEHR-26, respectively (Table VIII-14). Note, the identity of the coating and/or excipients could not be determined by TGA. The different decomposition patterns suggest a different coating and/or excipients were used in each solution.

Table VIII-14. Summary of Percent Coating Mass per Mass Nanoparticle detected in each of the aluminum oxide nanoparticles.

Reference Number	Reported Coating	%Mass Coating per Mass Nanoparticle
CEHR-23	None reported	9%
CEHR-24	None reported	10%
CEHR-25	None reported	10%
CEHR-26	None reported	1%

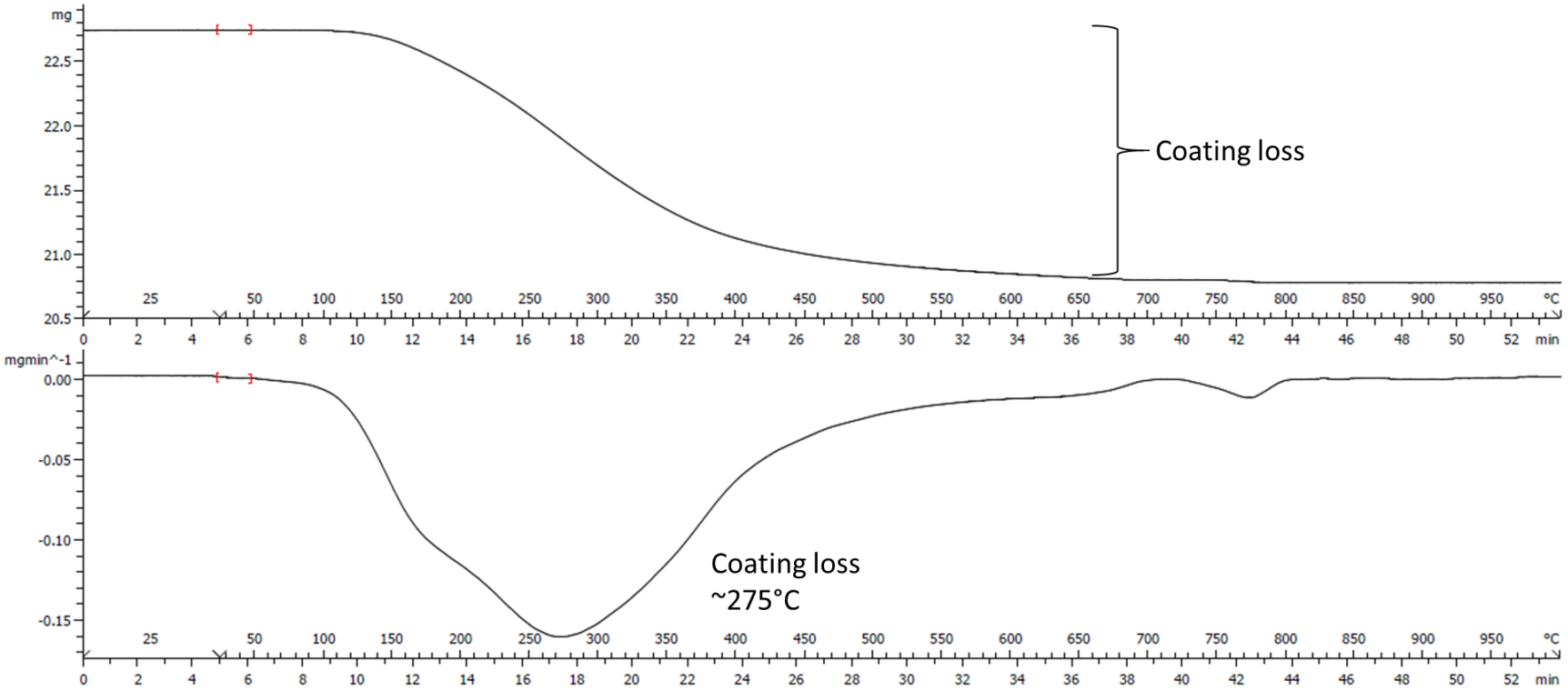

Reference Number	Starting Mass (mg)	Water Loss (mg)	Coating Loss (mg)	Residue (mg)	%Mass Coating per Mass Titanium Oxide Nanoparticles
CEHR-23	22.733	0	1.956	20.777	9%

Figure VIII-16. TGA thermogram of CEHR-23 (lyophilized). The top panel is the weight loss versus temperature (and time) curve. The bottom panel is the first derivative of that curve.

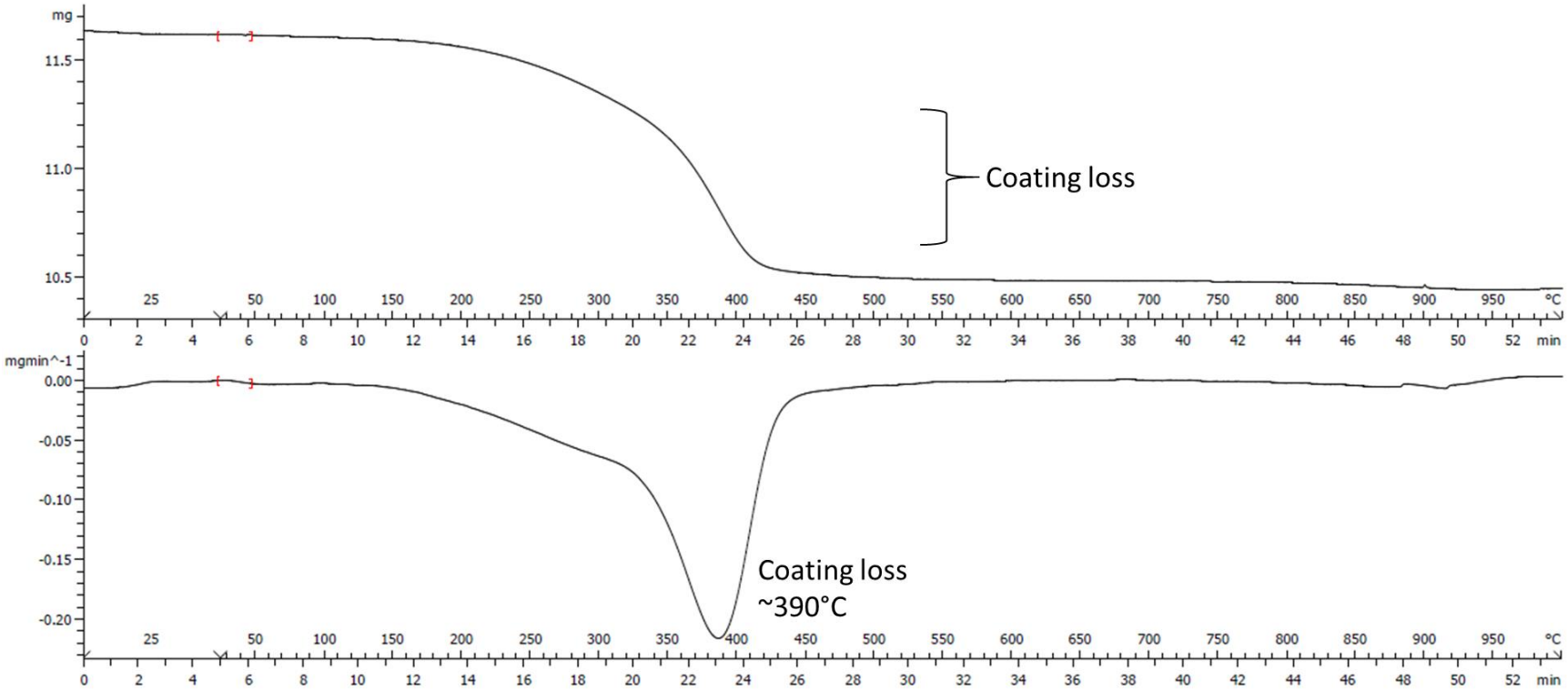

Reference Number	Starting Mass (mg)	Water Loss (mg)	Coating Loss (mg)	Residue (mg)	%Mass Coating per Mass Titanium Oxide Nanoparticles
CEHR-24	11.635	0	1.194	10.441	10%

Figure VIII-17. TGA thermogram of CEHR-24 (lyophilized). The top panel is the weight loss versus temperature (and time) curve. The bottom panel is the first derivative of that curve.

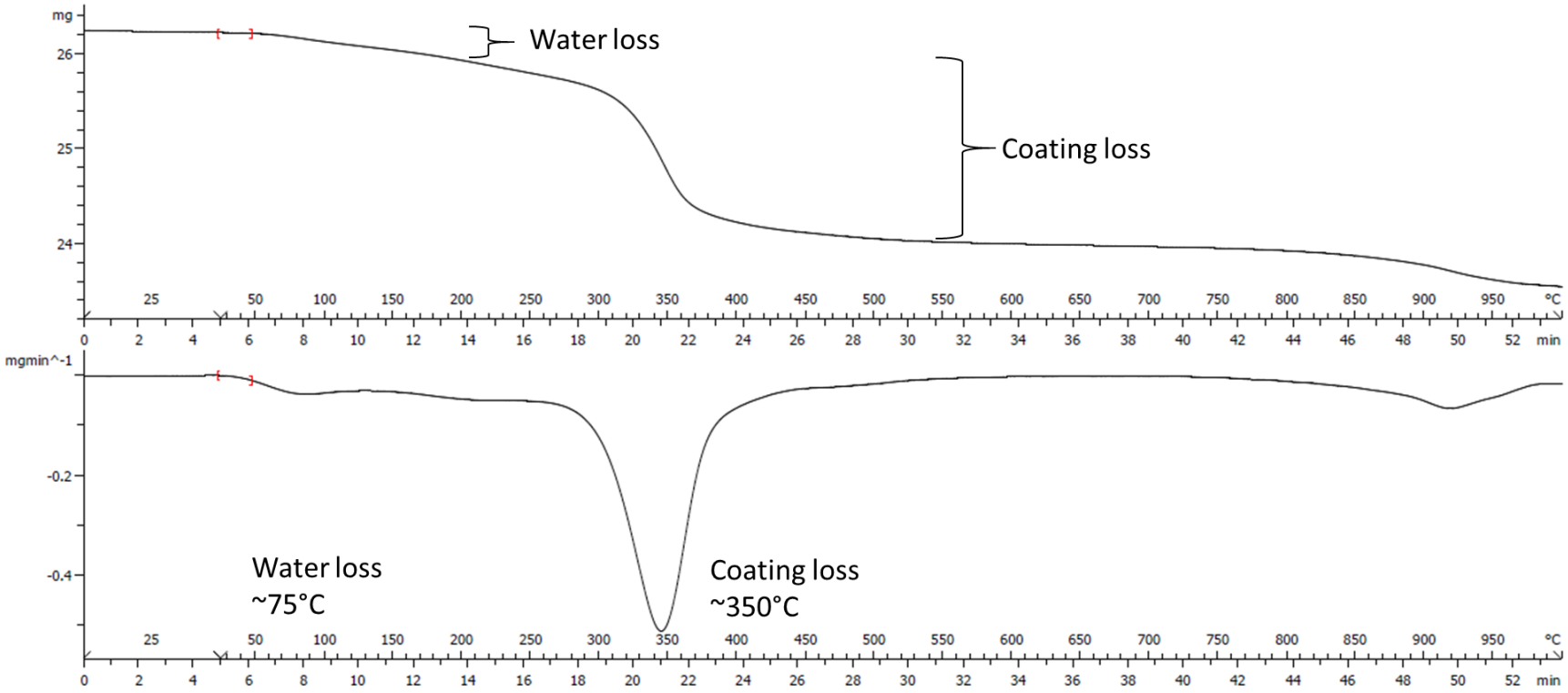

Reference Number	Starting Mass (mg)	Water Loss (mg)	Coating Loss (mg)	Residue (mg)	%Mass Coating per Mass Titanium Oxide Nanoparticles
CEHR-25	26.237	0.205	2.490	23.542	10%

Figure VIII-18. TGA thermogram of CEHR-25 (lyophilized). The top panel is the weight loss versus temperature (and time) curve. The bottom panel is the first derivative of that curve.

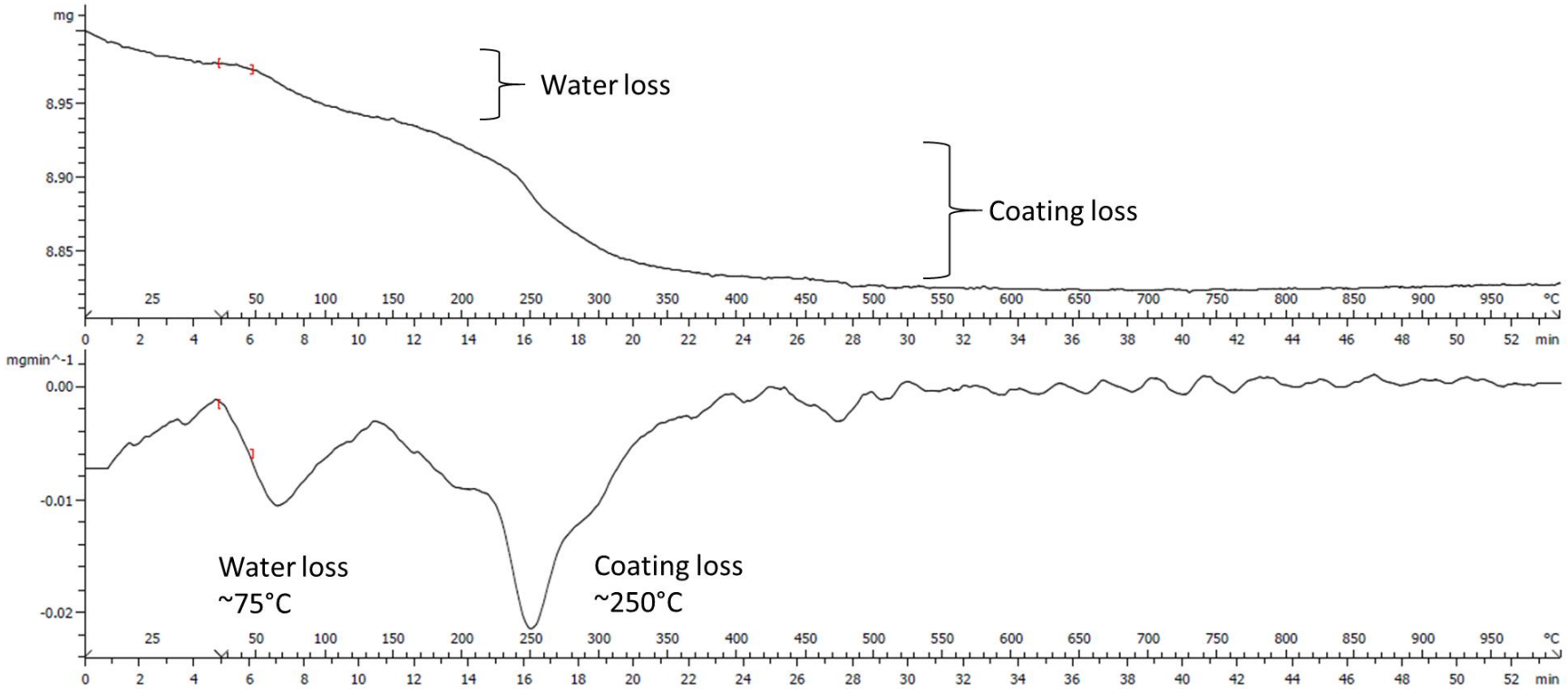

Reference Number	Starting Mass (mg)	Water Loss (mg)	Coating Loss (mg)	Residue (mg)	%Mass Coating per Mass Titanium Oxide Nanoparticles
CEHR-26	8.999	0.062	0.110	8.827	1 %

Figure VIII-19. TGA thermogram of CEHR-26 (lyophilized). The top panel is the weight loss versus temperature (and time) curve. The bottom panel is the first derivative of that curve.

I. Zeta Potential

Design and Methods

A Malvern Zetasizer Nano ZS instrument was used to measure zeta potential at 25°C for all samples. NCL protocol PCC-2 was followed (https://ncl.cancer.gov/resources/assay-cascade-protocols). Samples were 100- or 10,000-fold in deionized water. Sample pH was measured before loading into a pre-rinsed folded capillary cell. An applied voltage of 150 V was used. Traces in the figures represent the average of four measurements.

The instrument was validated by running an appropriate standard (Zeta Potential Transfer Standard, DTS0050, zeta potential value of -42 ± 4 mV at 25°C, Malvern Instruments) before all zeta potential measurements.

Results and Discussion

The titanium oxide nanomaterials showed a range of zeta potential values (Table VIII-15). CEHR-23 was highly positive with a value of 40 mV. CEHR-24 was negative with a value of -20 mV. CEHR-25 was borderline neutral, and CEHR-26 was neutral. Generally, zeta potential values ranging +10 mV to -10 mV are considered neutral.

Unmodified or uncoated titanium dioxide nanoparticles are expected to have a negative zeta potential. The range of zeta potential values observed for these formulations indicates unknown coatings are likely present. In fact, TGA analysis confirmed the presence coatings or other excipients (see Figures VIII-16 to VIII-19), but could not identify the composition of the coatings. The range in zeta potential values also suggests different coatings/excipients may be used in each of the formulations, as was suggested by the different decomposition patterns in TGA.

Table VIII-15. Summary of the zeta potentials for CEHR-23 to CEHR-26.

Sample	pH	Zeta Potential
CEHR-23	2.7	40 ± 2 mV
CEHR-24	5.4	-20 ± 1 mV
CEHR-25	5.7	-12 ± 0 mV
CEHR-26	5.7	7 ± 1 mV

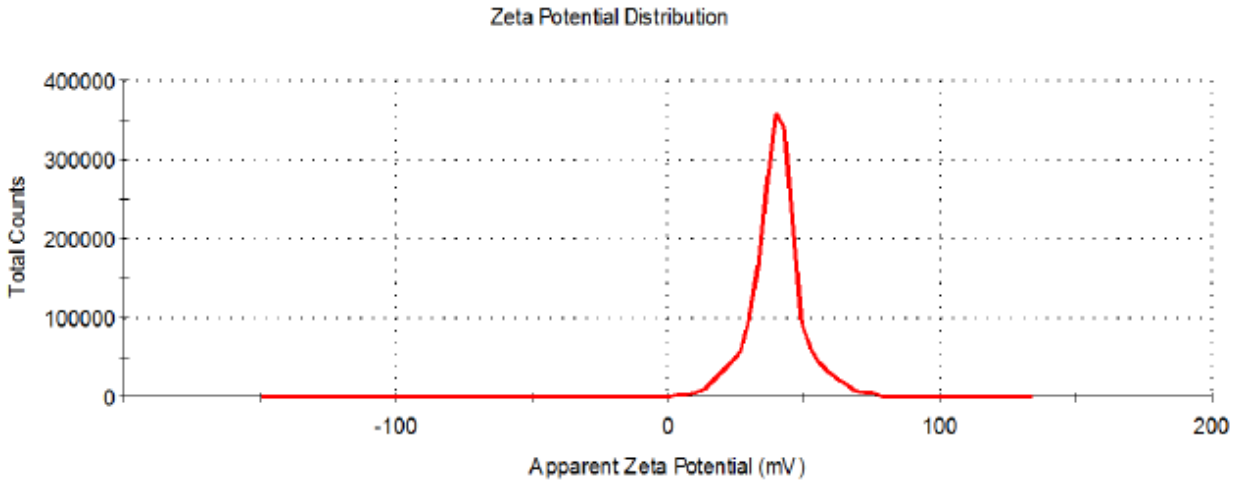

Sample	pH	Zeta Potential
CEHR-23	2.7	40 ± 2 mV

Figure VIII-20. The averaged zeta potential distributions for CEHR-23 diluted 100-fold in deionized water.

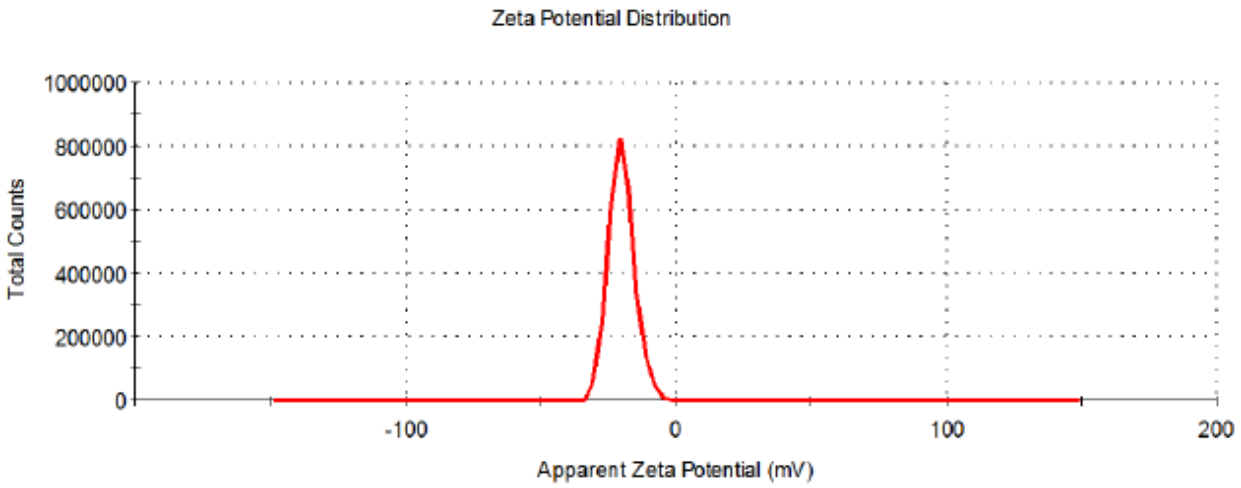

Sample	pH	Zeta Potential
CEHR-24	5.4	-20 ± 1 mV

Figure VIII-21. The averaged zeta potential distributions for CEHR-24 diluted 10,000-fold in deionized water.

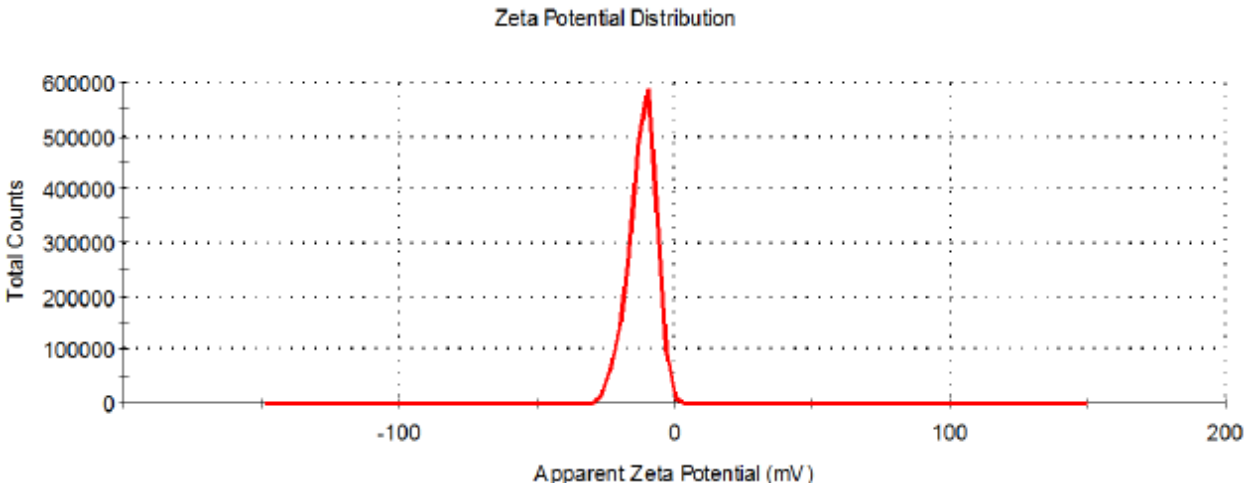

Sample	pH	Zeta Potential
CEHR-25	5.7	-12 ± 0 mV

Figure VIII-22. The averaged zeta potential distributions for CEHR-25 diluted 10,000-fold in deionized water.

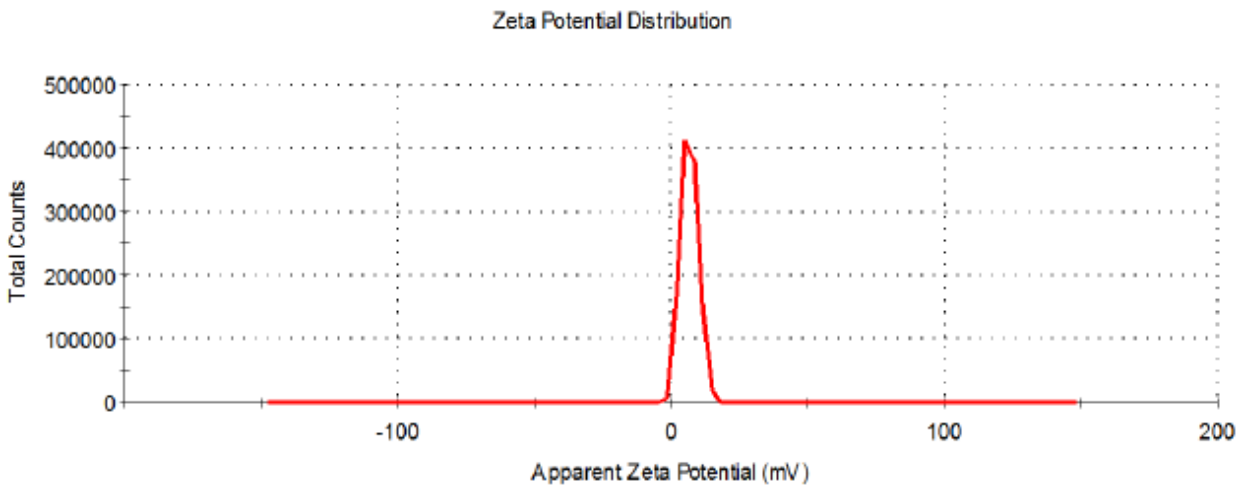

Sample	pH	Zeta Potential
CEHR-26	5.7	7 ± 1 mV

Figure VIII-23. The averaged zeta potential distributions for CEHR-26 diluted 10,000-fold in deionized water.

ABBREVIATIONS

AF4	asymmetric flow field-flow fractionation
BET	Brunauer, Emmett and Teller
BLOQ	below limit of quantitation
CEHR	US Army Center for Environmental Health Research
d.nm	diameter, in nanometers
DLS	dynamic light scattering
EU	endotoxin unit
ICP-MS	inductively coupled plasma mass spectrometry
LAL	limulus amebocyte lysate
MWCO	molecular weight cut-off
NCL	Nanotechnology Characterization Laboratory
NIST-SRM	National Institute of Standards and Technology, Standard Reference Material
PCC	physicochemical characterization
PdI	polydispersity index
PVP	polyvinylpyrrolidone
STE	sterility
TEM	transmission electron microscopy
TGA	thermogravimetric analysis
UV	ultraviolet

Nanotechnology Characterization Laboratory

Scott E. McNeil
Jeffrey D. Clogston
Marina A. Dobrovolskaia
Rachael M. Crist
Jiewei Wu
Barry Neun
Sonny Man
Alpana Dongargaonkar
Alison Vermilya
Cassandra Mankus

Electron Microscopy Laboratory

Ulrich Baxa
